



Title	Studies on Structural and Magnetic Properties of Perovskite-Related Compounds $\text{Sr}_2\text{LnRuO}_6$, $\text{Ba}_3\text{LnRu}_2\text{O}_9$ (Ln = Y, Lanthanides)
Author(s)	Doi, Yoshihiro
Citation	北海道大学. 博士(理学) 甲第6096号
Issue Date	2002-09-25
DOI	10.14943/doctoral.k6096
Doc URL	http://hdl.handle.net/2115/28097
Type	theses (doctoral)
File Information	thesis2002.pdf



[Instructions for use](#)

**Studies on Structural and Magnetic Properties
of Perovskite-Related Compounds
 $\text{Sr}_2\text{LnRuO}_6$, $\text{Ba}_3\text{LnRu}_2\text{O}_9$ (Ln = Y, Lanthanides)**

Yoshihiro Doi

Division of Chemistry
Graduate School of Science
Hokkaido University

2002

Contents

Chapter 1. General introduction

1.1 Introduction	1
1.1.1 Perovskite-related compounds.....	3
1.1.1.1 Flexibility in the chemical composition	3
1.1.1.2 Flexibility in the crystal structure.....	3
1.1.2 Characteristics of 4f electrons of lanthanide elements	4
1.1.3 Magnetic properties of ruthenium-containing oxides.....	5
1.2 Purpose and scope of this thesis	9
1.3 References	14

Chapter 2. Experimental

2.1 X-ray diffraction	16
2.1.1 Measurement of X-ray diffraction.....	16
2.2 Neutron diffraction	16
2.2.1 Advantage of using neutron diffraction	16
2.2.2 Measurement of neutron diffraction	17
2.2.3 Magnetic structure amplitude factor	18
2.3 Rietveld analysis.....	21
2.3.1 Model function	21
2.3.1.1 Symmetric profile-shape function	21
2.3.1.2 Profile asymmetry and peak shift	22
2.3.1.3 Preferred-orientation function	23
2.3.1.4 Absorption factor	23
2.3.1.5 Criteria of fit	24
2.4 Magnetic property measurements.....	25
2.5 Specific heat	26
2.6 Electrical resistivity	27
2.7 Mössbauer spectrum.....	27
2.7.1 Mössbauer spectroscopy.....	27
2.7.1.1 Mössbauer effect.....	27

2.7.1.2 Recoil-free fraction.....	28
2.7.2 Measurement of Mössbauer spectrum.....	29
2.7.3 Hyperfine interactions	29
2.7.3.1 Isomer shift.....	30
2.7.3.2 Second order Doppler shift.....	30
2.7.3.3 Electric quadrupole interaction.....	31
2.8 References	36

Chapter 3. Crystal structures and magnetic properties of the ordered perovskites $\text{Sr}_2\text{LnRuO}_6$

3.1 Introduction	37
3.1.1 Double perovskites $\text{A}_2\text{BB}'\text{O}_6$	37
3.1.2 Magnetic interaction in ordered perovskites	38
3.2 Crystal structures and magnetic properties of ordered perovskites $\text{Sr}_2\text{LnRuO}_6$ (Ln = Eu–Lu).....	41
3.2.1 Introduction	41
3.2.2 Experimental.....	41
3.2.3 Results and discussion.....	42
3.2.3.1 Crystal structure.....	42
3.2.3.2 Magnetic properties	42
3.2.4 Summary.....	45
3.3 Magnetic and neutron diffraction study on ordered perovskite $\text{Sr}_2\text{HoRuO}_6$	56
3.3.1 Introduction	56
3.3.2 Experimental.....	56
3.3.3 Results and discussion.....	57
3.3.3.1 Crystal structure.....	57
3.3.3.2 Magnetic properties	58
3.3.3.3 Magnetic structure	59
3.3.4 Summary.....	60
3.4 Magnetic properties and crystal structures of ordered perovskites $\text{Sr}_2\text{TbRu}_{1-x}\text{Ir}_x\text{O}_6$ 68	
3.4.1 Introduction	68
3.4.2 Experimental.....	68
3.4.3 Results and discussion.....	69
3.4.3.1 Crystal structure of $\text{Sr}_2\text{TbRu}_{1-x}\text{Ir}_x\text{O}_6$	69
3.4.3.2 Magnetic properties of $\text{Sr}_2\text{TbRuO}_6$ and $\text{Sr}_2\text{TbRu}_{1-x}\text{Ir}_x\text{O}_6$	71

3.4.3.3 Neutron diffraction measurements for $\text{Sr}_2\text{TbRuO}_6$	72
3.4.4 Summary.....	74
3.5 Magnetic properties of ordered perovskites $\text{Ba}_2\text{LnTaO}_6$ (Ln = Y, Lanthanides).....	83
3.5.1 Introduction	83
3.5.2 Experimental.....	83
3.5.3 Results and discussion	84
3.5.3.1 Crystal structures	84
3.5.3.2 Magnetic properties	85
3.5.3.3 ^{151}Eu Mössbauer spectrum	89
3.5.4 Summary.....	91
3.6 References	105

Chapter 4. Crystal structures and magnetic properties of 6H-perovskites $\text{Ba}_3\text{LnRu}_2\text{O}_9$

4.1 Introduction	108
4.1.1 6H-perovskites $\text{Ba}_3\text{LnRu}_2\text{O}_9$	108
4.1.2 Magnetic susceptibilities of the magnetic dimer	109
4.2 Crystal structures and electrical resistivity of $\text{Ba}_3\text{LnRu}_2\text{O}_9$	113
4.2.1 Experimental.....	113
4.2.1.1 Sample preparation	113
4.2.1.2 X-ray diffraction measurements	113
4.2.1.3. Electrical resistivity measurements	113
4.2.2 Results and discussion	114
4.2.2.1 Crystal structure of $\text{Ba}_3\text{LnRu}_2\text{O}_9$	114
4.2.2.2 Electrical resistivity	116
4.2.3 Summary.....	116
4.3 Magnetic properties of 6H-perovskites $\text{Ba}_3\text{LnRu}_2\text{O}_9$ (Ln = Y, In, La, Sm, Eu, and Lu)	128
4.3.1 Introduction	128
4.3.2 Experimental.....	128
4.3.3 Results and discussion	129
4.3.3.1 Magnetic susceptibility.....	129
4.3.3.2 Specific heat	130
4.3.4 Summary.....	131

4.4 Magnetic and neutron diffraction studies on 6H-perovskites $\text{Ba}_3\text{Ln}^{4+}\text{Ru}^{4+}_2\text{O}_9$ (Ln = Ce, Pr, and Tb).....	137
4.4.1 Introduction	137
4.4.2 Experimental.....	137
4.4.3 Results and discussion	138
4.4.3.1 Crystal structure of $\text{Ba}_3\text{TbRu}_2\text{O}_9$ at low temperatures	138
4.4.3.2 Magnetic susceptibilities	138
4.4.3.3 Specific heat	141
4.4.3.4 Magnetic structure of $\text{Ba}_3\text{TbRu}_2\text{O}_9$	142
4.4.4 Summary.....	142
4.5 Ferromagnetic transition and structural phase transition of $\text{Ba}_3\text{NdRu}_2\text{O}_9$	151
4.5.1 Introduction	151
4.5.2. Experimental.....	151
4.5.2.1 Sample preparation.....	151
4.5.2.1 X-ray and neutron diffraction measurements	151
4.5.2.3 Magnetic and thermal measurements	152
4.5.3 Results and discussion	152
4.5.3.1 Crystal structure at low temperatures	152
4.5.3.2 Magnetic properties of $\text{Ba}_3\text{NdRu}_2\text{O}_9$	154
4.5.3.3 Discussion on the magnetic properties of $\text{Ba}_3\text{NdRu}_2\text{O}_9$	155
4.5.4 Summary.....	157
4.6 Magnetic and calorimetric studies on $\text{Ba}_3\text{LnRu}_2\text{O}_9$ (Ln = Gd, Ho–Yb)	168
4.6.1 Introduction	168
4.6.2 Experimental.....	168
4.6.3 Results and discussion	169
4.6.3.1 Magnetic susceptibilities	169
4.6.3.2 Specific heats	170
4.6.4 Summary.....	172
4.7 References	181
Chapter 5. Concluding remarks.....	183
Acknowledgements	188
List of publications	189

Chapter 1.

General introduction

1.1 Introduction

Inorganic chemistry has become a very important field of chemistry, because most high technological materials have an inorganic origin. For the last several decades, many interesting physical properties have been found in inorganic compounds, especially in solid-state compounds, and they are applied to various uses and bearing the present-day technology. The continuous research of the material chemistry and the discovery of new materials and functions are needed for the development of the technology.

An important factor to determine the physical properties of the solid compounds is the crystal structure. The crystal structure is a definite arrangement and linkage of atoms in a periodic orderly array, where the periodicity results from infinite translations in three-dimensions. Each individual structure can be described by its symmetry (space group), unit cell parameters, chemical composition, the positions of atoms, the coordination of atoms, and the kind of the bonds between them. Consequently, a crystal structure is not merely a geometric arrangement of atoms, since the particular characteristics of the chemical elements involved, the way of their linkage and the kind of interatomic bonds play an important role in the physical properties of compounds. As results of long years of research, enormous kinds of solid compounds have been found, and their crystal structures have been systematized in many kinds of structural groups [1.1-3].

Among those structural groups, one of the most important groups is that of the perovskite-related compounds. The perovskites have the flexibility of a chemical composition and crystal structure; hence, the combination of many kinds of ions and the control of their crystal structures are possible. By this flexibility, the perovskite-related

compounds can show a variety of physical properties such as the superconductivity (e.g. $\text{YBa}_2\text{Cu}_3\text{O}_{7-\delta}$ [1.4]), electronic conductivity (e.g. ReO_3 [1.5]), ionic conductivity (e.g. $\text{SrCe}_{0.95}\text{Yb}_{0.05}\text{O}_{3-\delta}$ [1.6]), ferroelectricity (e.g. BaTiO_3 [1.7]), giant magnetic resistance (e.g. $\text{La}_{1-x}\text{Ca}_x\text{MnO}_3$ [1.8]), etc. Therefore, the perovskite-related compounds are an advantageous group of compounds to find new interesting physical properties.

The physical properties of the solid compounds are also determined by the electronic behavior. Magnetism is one of the basic properties of electrons and essentially a quantum phenomenon. Despite its old history of the research, the magnetism is a remarkably developing research field in both experimental and theoretical interests at now. The contents of this research field are spreading widely by the discovery of many new phenomena and theories. Particularly, since the discovery of the high-temperature superconductivity in copper containing oxides [1.9], many studies for the transition metal oxides have been performed to elucidate the mechanism of high-temperature superconductivity and to search new superconductors. Besides the superconductivity, many interesting magnetic properties were found out in the transition metal oxides, for example, the spin glass, magnetoresistance, metal-insulator transition, and low-dimensional magnetism etc. In order to understand these magnetic properties, it is required to investigate the electronic state of many solid compounds.

In this thesis, the author has focused his attention to perovskite-related oxides containing both lanthanide and ruthenium ions, and have investigated their structural and magnetic properties. These compounds are very attractive on the point of the magnetic features: the magnetic properties of 4f electrons of lanthanide ions, and those of 4d electrons of ruthenium ions, and magnetic cooperative phenomena due to the magnetic interaction between them. The principal motivation of this investigation is to elucidate the magnetic properties of these compounds.

In the following sections, the perovskite and its flexibility in the chemical composition and crystal structure (section 1.1.1), characteristics of 4f electrons of the lanthanide elements (section 1.1.2), and magnetic properties of ruthenium-containing oxides (section 1.1.3) will be described.

1.1.1 Perovskite-related compounds [1.10-13]

1.1.1.1 Flexibility in the chemical composition

The perovskites form a family of compounds having a crystal structure similar to that of the mineral perovskite, CaTiO_3 . The perovskites have the general formula, ABX_3 , in which A represents a large electropositive cation and B represents a small transition metal ion. The perovskite structure can be described as a framework of corner-shared BO_6 octahedra, which contain A cations at 12-coordinate sites. Generally, the A sites are occupied by the alkaline earth metal, alkaline metal, or rare earth metal ions, and the X sites are occupied by oxide ions or halide ions (F^- , Cl^- , Br^-). Depending on the choice of the A and X ions, the B sites can be occupied by many kinds of cations. In addition, the combination of the charge contribution and the solid solution are possible in the wide range. In the case of oxides, there exist not only the simple combinations ($\text{A}^+\text{B}^{5+}\text{O}_3$, $\text{A}^{2+}\text{B}^{4+}\text{O}_3$, $\text{A}^{3+}\text{B}^{3+}\text{O}_3$) but also more complex combinations (e.g. $\text{A}^{2+}\text{B}^{3+}_{1/2}\text{B}'^{3+}_{1/2}\text{O}_3$, $\text{A}^{2+}\text{B}^{2+}_{1/3}\text{B}'^{5+}_{2/3}\text{O}_3$, $\text{A}^{2+}_{1/2}\text{A}'^{3+}_{1/2}\text{B}^{3+}_{1/2}\text{B}'^{4+}_{1/2}\text{O}_3$) and the solid solution (e.g. $\text{A}_{1-x}\text{A}'_x\text{B}_{1-y}\text{B}'_y\text{O}_3$).

1.1.1.2 Flexibility in the crystal structure

The structures of the perovskites ABX_3 are possible when A ions are comparable in size with X ions and the value of tolerance factor t lies between approximately 0.75 and 1.0 [1.10]. The tolerance factor is represented by

$$t = (r_A + r_X) / \sqrt{2}(r_B + r_X) \quad (1.1)$$

where r_A , r_B , r_X are ionic radii of the respective ions. By geometry, the ideal cubic structure should have $t = 1$. The schematic structure of ideal cubic ABX_3 perovskite is shown in Fig. 1.1. The perovskites with the cubic symmetry at room temperature is actually rare case; most perovskites, which have relatively small A ions ($t = 1$), adopt more distorted structures with a lower symmetry (e.g. rhombohedral LaAlO_3 -type structure and orthorhombic GdFeO_3 -type structure).

On the other hand, too large A ions ($t > 1$) tend to change the stacking sequence of closed packing AX_3 layers, consequently, some polymorphic structures are brought out.

Figure 1.2 shows stable structures of polymorphic structures for ABX_3 perovskites [1.14]. Figures 1.2(a) and (b) are a normal cubic perovskite with all-cubic stacking mode (CCC...) and hexagonal $CsNiCl_3$ -type structure with all-hexagonal stacking mode (HH...), respectively. Figures 1.2(c)–(e) show intermediate polymorphic structures between these two structures, and they are respectively the hexagonal $BaTiO_3$ structure (HCCH'C'C'...) (c), hexagonal $BaMnO_3$ structure (HCH'C'...) (d), and hexagonal $BaRuO_3$ structure (HHCH'H'C'H''H''C''...) (e).

1.1.2 Characteristics of 4f electrons of lanthanide elements [1.15, 16]

The configuration of the neutral lanthanide atom amounts to $[Xe] 4f^n$ ($[Xe]$: xenon electronic core) with three electrons in the higher energy 5d and 6s orbitals ($5d^1 6s^2$). The most stable oxidation state of lanthanide elements is trivalent. In addition to this trivalent state, it is known for some elements to adopt the tetravalent state (cerium, praseodymium, and terbium) and divalent state (samarium, europium, and ytterbium).

The magnetic properties of the lanthanide ions are fascinating for the reason of their systematic variety and intelligible complexity. Their magnetic properties are determined by the unpaired 4f electrons. They are compacted in the inner shell with a radius of $\sim 0.3 \text{ \AA}$ and shielded by the surrounding occupied 5s and 5p electrons. Therefore, they are highly localized electrons, and the orbital contributions to their magnetic moments are significant. The energy states of the $4f^n$ configurations are usefully approximated by the Russell-Saunders scheme and spin-orbit coupling constants are comparatively large, nearly every one of the trivalent ions is characterized by a ground state with a single value of resultant total angular momentum J and a first excited state at an energy larger by a number of times the quantity $k_B T$ (k_B : Boltzmann constant) [1.15-17]. These features are contrastive compared with those of d electrons: the orbitals located in the valency shell and essentially quenched orbital contributions. The electronic configurations, ground state term, and other information for the trivalent lanthanide ions are summarized in Table 1.1. The net effect for each of lanthanide ions is that the first excited state is essentially unpopulated by electrons except at very high

temperatures. The Sm^{3+} and Eu^{3+} ions, however, differ from the others in that the upper excited states in each lies sufficiently close to the ground state to be somewhat populated even at room temperature. These two ions may be expected to differ from the other Ln^{3+} ions in properties that depend upon population of J states.

In addition, these J states having the $(2J + 1)$ -fold degeneracy are split into some energy levels by the crystal field effect. The way of this splitting depends upon the symmetry of the crystal field and the number of 4f electrons. These energy levels are very important when the magnetic properties of lanthanide ions at low temperatures are discussed. In the case that a lanthanide ion having a half-integral J value, it has a doublet (Kramer's doublet) as a ground state no matter how low the symmetry of the crystal field becomes and unless a magnetic field is applied. Therefore, the magnetic properties of the lanthanide ions differ from each other whether its number of 4f electrons is even or odd.

In the solid compounds as the condensed matter, it is expected to observe various magnetic properties due to the magnetic interaction between lanthanide ions. Generally, the shielding by the surrounding electrons in outer shell makes the magnetic interactions between 4f electrons weak compared to those between d electrons. In fact, many of the lanthanide oxides order magnetically at < 4 K [1.18, 19]. However, it is possible to make their magnetic interactions strong by selecting a crystal structure, e.g., a ferromagnet EuO (T_C (Curie temperature) = ~ 70 K) [1.20] and antiferromagnets ATbO_3 ($A = \text{Sr, Ba}$; T_N (Néel temperature) = ~ 33 K) [1.21].

1.1.3 Magnetic properties of ruthenium-containing oxides

In recent years, the solid-state chemistry of mixed-metal oxides containing platinum group metals has attracted a great deal of interest. These materials adopt a diverse range of structures and show a wide range of magnetic and electrical properties. Especially, the ruthenium-containing oxides are most attractive. For example, the layered perovskite Sr_2RuO_4 (unconventional spin-triplet superconductivity below > 1 K) [1.22], the perovskite SrRuO_3 (metallic, and ferromagnetic behavior below 160 K)

[1.23], 9R-BaRuO₃ (nine layer structure; metallic behavior) [1.23], a pyrochlore Tl₂Ru₂O₇ (metal-insulator transition at 125 K) [1.24], pyrochlores Ln₂Ru₂O₇ (spin-glass like behavior) [1.25], and RuSr₂GdCu₂O₈ (coexistence ferromagnetism and superconductivity) [1.26] are known. Some of these intriguing physical phenomena of the Ru containing oxides are derived from the characters of the Ru ion itself, such as the variety of the crystal structure adopted by the Ru ion, relatively strong correlation effects in 4d orbitals, strong hybridization between 4d orbital of the Ru ion and 2p orbital of the O²⁻ ion.

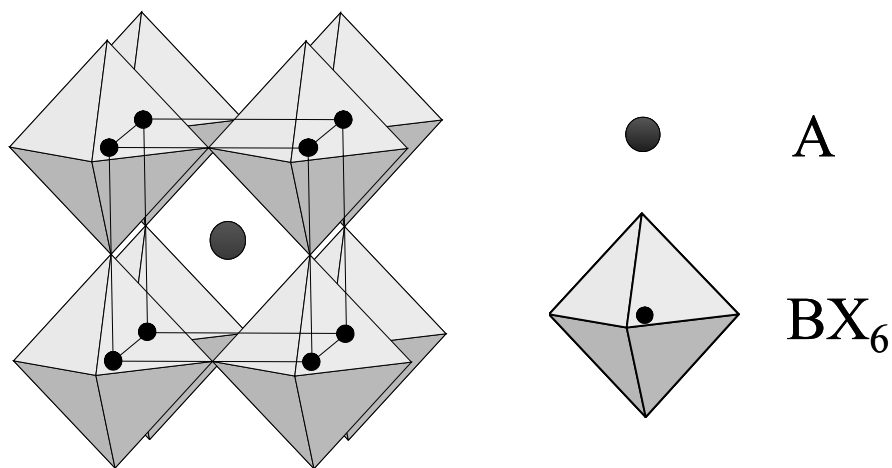


Figure 1.1 The schematic structure of ideal cubic ABX_3 perovskite.

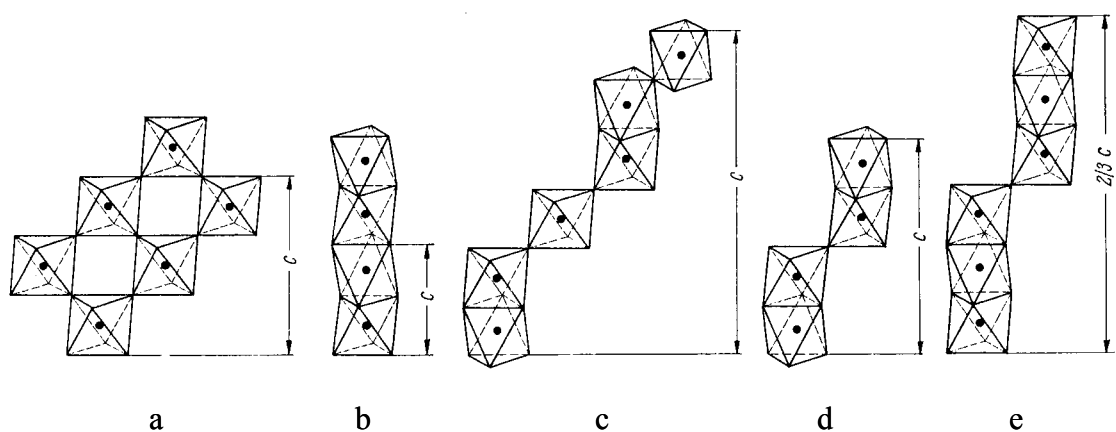


Figure 1.2 The schematic structure of ABX_3 : a) cubic perovskite structure, b) two-layer hexagonal $CsNiCl_3$ structure, c) six-layer $BaTiO_3$ structure, d) four-layer $BaMnO_3$ structure, and e) nine-layer hexagonal $BaRuO_3$ structure. [1.14]

Table 1.1 Some properties of lanthanide ions

Lanthanide ion	$4f^n$	g.s.	S	L	J	g_J	μ_{Ln}
La ³⁺ , Ce ⁴⁺	$4f^0$	1S_0	0	0	0	—	—
Ce ³⁺ , Pr ⁴⁺	$4f^1$	$^2F_{5/2}$	1/2	3	5/2	6/7	2.54
Pr ³⁺	$4f^2$	3H_4	1	5	4	4/5	3.58
Nd ³⁺	$4f^3$	$^4J_{9/2}$	3/2	6	9/2	8/11	3.62
Pm ³⁺	$4f^4$	5I_4	2	6	4	3/5	2.68
Sm ³⁺	$4f^5$	$^6H_{5/2}$	5/2	5	5/2	2/7	0.845
Eu ³⁺ , Sm ²⁺	$4f^6$	7F_0	3	3	0	—	—
Gd ³⁺ , Eu ²⁺ , Tb ⁴⁺	$4f^7$	$^8S_{7/2}$	7/2	0	7/2	2	7.94
Tb ³⁺	$4f^8$	7F_6	3	3	6	3/2	9.72
Dy ³⁺	$4f^9$	$^6H_{15/2}$	5/2	5	15/2	4/3	10.63
Ho ³⁺	$4f^{10}$	5I_8	2	6	8	5/4	10.58
Er ³⁺	$4f^{11}$	$^4I_{15/2}$	3/2	6	15/2	6/5	9.59
Tm ³⁺	$4f^{12}$	3H_6	1	5	6	7/6	7.55
Yb ³⁺	$4f^{13}$	$^2F_{7/2}$	1/2	3	7/2	8/7	4.54
Lu ³⁺ , Yb ²⁺	$4f^{14}$	1S_0	0	0	0	—	—

Note. g.s.: ground state; g_J : Landé g factor; μ_{Ln} : effective magnetic moment.

1.2 Purpose and scope of this thesis

As the subject of the study, this thesis describes the structural and magnetic properties of some perovskite-related oxides containing both lanthanide and ruthenium ions, i.e., $\text{Sr}_2\text{LnRuO}_6$, $\text{Ba}_3\text{LnRu}_2\text{O}_9$, and related compounds. The lanthanide ion is relatively large, and tends to adopt high coordination numbers. Therefore, the lanthanide ion sits at the A site of the perovskite-oxide ABO_3 . As described in section 1.1, the perovskites have the flexibility of a chemical composition and the combination of many kinds of ions are possible. By selecting large alkaline earth elements such as Sr and Ba as the A site atoms, lanthanides occupy the 6-coordinate B site. This is of advantage to investigate the magnetic properties of the lanthanide ions, because not the A site ions but the B site ions normally determine the physical properties of the perovskites ABO_3 . Furthermore, the introduction of the Ru ion to the B site as another magnetic ion brings the magnetic interactions between d–f electrons and between d–d electrons in addition to the interactions between f–f electrons. By these interactions, more interesting magnetic properties are expected to be found.

This thesis aims at investigating systematically the structural and magnetic properties of these compounds and elucidating their physical properties.

This thesis is composed of five Chapters.

Chapter 1 describes general features of perovskite-related compounds, magnetic features of 4f electrons of the lanthanide ions, and various magnetic properties of ruthenium-containing oxides.

In Chapter 2, the principles and methods of the experimental and analysis technique used in this work are summarized.

In Chapter 3, the crystal structures and magnetic properties of the ordered perovskites $\text{Sr}_2\text{LnRuO}_6$ are described. Generally, the mechanism of the magnetic interaction between magnetic ions in the localized electron system is the superexchange interaction via an intermediate anion between them. Due to the structural feature of the

perovskite, the superexchange pathway between the nearest neighbor B site ions is only $\sim 180^\circ$ B–O–B. The strength of the magnetic interaction between B ions changes greatly with the kinds of B site ions, and the order is generally d–d electrons > d–f electrons > f–f electrons. If the B site cations of $\text{Sr}_2\text{LnRuO}_6$, Ru and Ln, adopt the alternative ordered arrangement, there exists only a 180° Ru–O–Ln superexchange pathway. In that case, it is considered that the magnetic properties of these compounds reflect the magnetic interaction between Ru and Ln ions. Therefore, the ordered perovskites $\text{Sr}_2\text{LnRuO}_6$ are suitable for investigating the magnetic interaction between d and f electrons. The contents of Chapter 3 are divided into following six sections:

Section 3.1. As the introduction of this chapter, the general information about ordered perovskites is described.

Section 3.2. The synthesis, determination of the crystal structure by the X-ray diffraction measurement, and magnetic susceptibility measurement of ordered perovskites $\text{Sr}_2\text{LnRuO}_6$ (Ln = Eu–Lu) are described. The X-ray diffraction measurement will elucidate the order/disorder arrangement of B site ions and the change in the crystal structure with the ionic size of the lanthanide ions. In addition, the magnetic susceptibility measurements will give the knowledge about the magnetic interaction between d and f electrons.

Section 3.3 Neutron diffraction study on $\text{Sr}_2\text{HoRuO}_6$ and its detailed magnetic properties are described. In order to elucidate the complex magnetic behavior observed for this compound, the neutron diffraction, detailed magnetic susceptibility, and specific heat measurements were carried out. The magnetic properties at low temperatures were elucidated, and the magnetic structure has been determined.

Section 3.4 Neutron diffraction study on $\text{Sr}_2\text{TbRuO}_6$, and crystal structures and magnetic properties of a solid solution $\text{Sr}_2\text{Tb}(\text{Ru}_{1-x}\text{Ir}_x)\text{O}_6$ are described. The neutron diffraction measurement for $\text{Sr}_2\text{TbRuO}_6$ was performed,

and its magnetic structure has been determined.

In addition, the author extended the magnetic studies on the related ordered perovskites. The magnetic properties of the solid solutions $\text{Sr}_2\text{Tb}(\text{Ru}_{1-x}\text{Ir}_x)\text{O}_6$ are also studied. The end compounds, $\text{Sr}_2\text{Tb}^{3+}\text{Ru}^{5+}\text{O}_6$ and $\text{Sr}_2\text{Tb}^{4+}\text{Ir}^{4+}\text{O}_6$, have a similar crystal structure; however, their charge configurations of B site ions are different from each other. The X-ray diffraction and magnetic susceptibility measurements for the solid solutions will clarify the variation of the valence state of the B site ions with compositions and their magnetic properties.

Section 3.5 The crystal structures and magnetic properties of ordered perovskites $\text{Ba}_2\text{LnTaO}_6$ ($\text{Ln} = \text{Y}$, lanthanides) are described. The $\text{Ba}_2\text{LnTaO}_6$ is appropriate for the basic study of the magnetic behavior of lanthanide ions in the ordered perovskites, because only Ln^{3+} ions are magnetic (i.e., Ta^{5+} is nonmagnetic). The magnetic susceptibility measurements will give the knowledge about the magnetic properties of Ln^{3+} ions. In addition, the ^{151}Eu Mössbauer measurement for $\text{Ba}_2\text{EuTaO}_6$ is carried out. From this measurement, the information about the local environment and the valence state of Eu ions will be obtained.

Section 3.6 References in this chapter are listed.

In Chapter 4, the crystal structures and magnetic properties of the 6H-perovskites $\text{Ba}_3\text{LnRu}_2\text{O}_9$ ($\text{Ln} = \text{Y}$, In , lanthanides) are described. The 6H-perovskite structure is one of polymorphic structures of perovskite, and has two kinds of the B site ions; one occupies the corner-sharing octahedral site and another occupies the face-sharing octahedral site (see Fig. 1.2(c)). In the case of $\text{Ba}_3\text{LnRu}_2\text{O}_9$, Ln and Ru ions occupy the corner-sharing and face-sharing sites, respectively. Particularly, the latter forms a polyhedral unit “ Ru_2O_9 dimer”, in which two Ru ions have a short Ru–Ru distance (2.48–2.69 Å). Therefore, it is expected to show the strong magnetic interaction in the

dimer, i.e., the formation of a magnetic dimer. A previous study on the analogous compounds $\text{Ba}_3\text{M}^{2+}\text{Ru}^{5+}\text{O}_9$ ($\text{M} = \text{Mg}, \text{Ca}, \text{Cd}, \text{and Sr}$) shows an interesting magnetic behavior due to the antiferromagnetic coupling of Ru^{5+} ions in the Ru_2O_9 dimer isolated magnetically by diamagnetic M^{2+} ions [1.24]. Here, the electronic configuration of $\text{Ba}_3\text{LnRu}_2\text{O}_9$ is expected to be $\text{Ba}_3\text{Ln}^{3+}\text{Ru}^{4.5+}_2\text{O}_9$. If the magnetic moments of Ru ions in the dimer coupled antiferromagnetically, each dimer has one unpaired electron. In addition, if the lanthanide ions are magnetic, there exists a 180° Ru–O–Ln superexchange pathway. Therefore, this series of $\text{Ba}_3\text{LnRu}_2\text{O}_9$ compounds is considered to bring about interesting magnetic behavior due to the Ru_2O_9 dimer itself, the effect of one unpaired electron in each dimer, and the magnetic interaction between Ru and Ln ions. The contents of Chapter 4 are divided into the following seven sections:

Section 4.1. As the introduction of this chapter, the general information about 6H-perovskites and the magnetic dimer is described.

Section 4.2 The synthesis, determination of the crystal structure by the X-ray diffraction measurement, and electrical resistivity of 6H-perovskites $\text{Ba}_3\text{LnRu}_2\text{O}_9$ ($\text{Ln} = \text{Y}, \text{In}, \text{lanthanides}$) are described. The detailed crystal structures of $\text{Ba}_3\text{LnRu}_2\text{O}_9$ and the change in the crystal structure with the ionic size of lanthanide ions were elucidated by the X-ray diffraction measurement.

Section 4.3 The magnetic properties of $\text{Ba}_3\text{Ln}^{3+}\text{Ru}^{4.5+}_2\text{O}_9$ ($\text{Ln} = \text{Y}, \text{In}, \text{La}, \text{Sm}, \text{Eu}, \text{and Lu}$) are described. These compounds are appropriate for the study of the magnetic behavior of the $\text{Ru}^{4.5+}_2\text{O}_9$ dimers, because these Ln^{3+} ions are nonmagnetic or weak magnetic. The magnetic susceptibility and specific heat measurements will clarify the magnetic properties of the $\text{Ru}^{4.5+}_2\text{O}_9$ dimers.

Section 4.4 Neutron diffraction study on $\text{Ba}_3\text{TbRu}_2\text{O}_9$ and magnetic properties of $\text{Ba}_3\text{Ln}^{4+}\text{Ru}^{4+}_2\text{O}_9$ ($\text{Ln} = \text{Ce}, \text{Pr}, \text{and Tb}$) are described. In these three compounds, both Ln and Ru ions are tetravalent. The magnetic

susceptibility and specific heat measurements will elucidate their magnetic properties. Attempts to explain their observed susceptibilities using a magnetic dimer model were carried out. For $\text{Ba}_3\text{TbRu}_2\text{O}_9$, the magnetic structure was determined by the neutron diffraction measurement.

Section 4.5 The study on the ferromagnetic transition and structural phase transition of $\text{Ba}_3\text{NdRu}_2\text{O}_9$ are described. This ferromagnetic behavior was clarified by the magnetic susceptibility, magnetization, and specific heat measurements, and the crystal and magnetic structure at low temperatures was determined by the X-ray and neutron diffraction measurements.

Section 4.6 The magnetic properties of $\text{Ba}_3\text{LnRu}_2\text{O}_9$ ($\text{Ln} = \text{Gd}, \text{Ho}–\text{Yb}$) are described. In these compounds, the Ln^{3+} ions are magnetic and have large magnetic moments. Therefore, these compounds are appropriate for the study of the magnetic interaction between Ln^{3+} ions and the $\text{Ru}^{4.5+}_2\text{O}_9$ dimers. The magnetic susceptibility and specific heat measurements will clarify their magnetic properties.

Section 4.7 References in this chapter are listed.

Conclusion remarks of this thesis are given in Chapter 5.

1.3 References

- [1.1] R. W. G. Wyckoff, "Crystal Structures", Interscience, New York.
- [1.2] A. F. Wells, "Structural Inorganic Chemistry", 3rd ed, Clarendon Press, Oxford (1962).
- [1.3] F. S. Galasso, "Structure and Properties of Inorganic Solids", 2nd ed, Pergamon Press, Oxford (1970).
- [1.4] M. K. Wu, J. R. Ashburn, C.J. Torng, P. H. Hor, R. L. Meng, L. Gao, Z. J. Huang, Y. Q. Wang, and C. W. Chu, *Phys. Rev. Lett.* **58**, 908 (1987).
- [1.5] T. Tanaka, T. Akahane, E. Bannai, S. Kawai, N. Tsuda, and Y. Ishizawa, *J. Phys. C* **9**, 1235 (1976).
- [1.6] H. Iwahara, T. Esaka, H. Uchida, and N. Maeda, *Solid State Ionics* **3**, 359 (1981).
- [1.7] L. E. Cross, "Ferroelectric Ceramics", Birkhauser Verlag, Basel (1993).
- [1.8] G. H. Jonker and J. H. Von Santen, *Physica* **16**, 337 (1950).
- [1.9] J. B. Bednorz and K. A. Müller, *Z. Phys. B* **64**, 189 (1986).
- [1.10] J. B. Goodenough and J. M. Longo, "Landolt-Börnstein", New Series, Vol. III/4a, Springer, Berlin (1970).
- [1.11] H. P. J. Wijn, "Perovskites I" in "Landolt-Börnstein", New Series, Vol. III/27f1 β , Springer, Berlin (1996).
- [1.12] Y. Endoh, "Perovskites II" in "Landolt-Börnstein", New Series, Vol. III/27f3, Springer, Berlin (1994).
- [1.13] K. Koumoto et al. "Perovskite-Related Compounds: Storehouse of Functions", Japan Scientific Societies Press, Tokyo (1997), in Japanese.
- [1.14] J. M. Longo and J. A. Kafalas, *J. Solid State Chem.* **1**, 103 (1969).
- [1.15] R. L. Carlin, "Magnetochemistry", Springer Verlag, Berlin (1986).
- [1.16] C. Kittel, "Introduction to Solid State Physics", John Wiley & Sons Inc., New York (1986).
- [1.17] J. H. Van Vleck, "The Theory of Electric and Magnetic Susceptibilities",

- Oxford Univ. Press, Oxford (1931).
- [1.18] H. P. J. Wijn, "Hydride, Oxide (Teil C 1. Sc, Y, und Lanthanide)" in "Gmelins Handbuch der anorganischen Chemie", Springer, Berlin (1974).
- [1.19] H. P. J. Wijn, "Binary lanthanide oxides" in "Landolt-Börnstein", New Series, Vol. III/27c1, Springer, Berlin (1997).
- [1.20] A. Mauger and C. Godart, *Phys. Rep.* **141**, 51 (1986).
- [1.21] K. Tezuka, Y. Hinatsu, Y. Shimojo, and Y. Morii, *J. Phys.: Condens. Mater.* **10**, 11703 (1998).
- [1.22] Y. Maeno, H. Hashimoto, K. Yoshida, S. Nishizaki, T. Fujita, J. G. Bednorz, and F. Lichtenberg, *Nature* **372**, 532 (1994).
- [1.23] A. Callaghan, C. W. Moeller, and R. Ward, *Inorg. Chem.* **5**, 1572 (1966).
- [1.24] A. W. Sleight and R. J. Bouchard, *Solid State Chemistry, Proceedings of 5th Materials Research Symposium*, NBS Spec. Publ. 364, 227 (1972).
- [1.25] N. Taira, M. Wakeshima, and Y. Hinatsu, *J. Solid State Chem.* **144**, 216 (1999).
- [1.26] C. Bernhard, J. L. Tallon, Ch. Niedermayer, Th. Blasius, A. Golnik, E. Brücher, R. K. Kremer, D. R. Noakes, C. E. Stronach, and E. J. Ansaldo, *Phys. Rev. B* **59**, 14099 (1999).
- [1.27] J. Darriet, M. Drillon, G. Villeneuve, and P. Hagenmuller, *J. Solid State Chem.* **19**, 213 (1976).

Chapter 2. Experimental

2.1 X-ray diffraction

2.1.1 Measurement of X-ray diffraction

X-ray diffraction profiles at room temperature were measured with Cu- $K\alpha$ radiation (40 kV, 20 mA) on a RINT2200 diffractometer or MultiFlex diffractometer (Rigaku) equipped with a curve graphite monochromator. The data were collected in a step-scanning mode over the 2θ range of 10–120°. The step width and step time are 0.02° and 7.5 s, respectively. The samples were well ground, and then were put on the glass holder in measurement. The crystal structures of samples were determined by the Rietveld analysis method (section 2.3).

X-ray diffraction measurements at lower temperatures were carried out using a RINT2200 diffractometer. The sample was cooled by a variable temperature cryostat system, CryoMini (Iwatani Industrial Gases Co.). The sample holder was copper; the powdered sample was filled in this holder and was bound using a small amount of varnish.

2.2 Neutron diffraction

2.2.1 Advantage of using neutron diffraction

There are many similarities between X-ray and neutron diffraction, but there are also significant differences. Differences stem from the distinctive properties of thermal neutrons themselves.

The neutron is an electrically neutral particle and has a magnetic moment of spin

1/2. By the former feature, neutrons can penetrate deeply into most materials. This is an important advantage in studies of bulk materials and also facilitates the use of furnaces, cryostats and pressure cells for studies of materials under conditions encountered in real applications. By the latter feature, it becomes possible to probe the magnetic structure and magnetic dynamics of atomic systems. For magnetically ordered materials, the magnetic powder diffraction pattern may be separated from the nuclear one by comparing patterns above and below the magnetic ordering temperature and thus allowing the determination of the magnetic structure.

The difference in the scattering cross-section is also important. X-rays are scattered by the electron clouds of atoms, and the X-ray scattering cross-section decreases with scattering angle. On the other hand, neutrons are scattered by the nuclei of atoms, and the neutron scattering cross-sections are independent of scattering angle. Further, X-ray scattering cross-sections increase monotonically with atomic number, while neutron cross-sections vary erratically with atomic number. These features of neutrons result in useful contrastive effects, including high sensitivity to light elements, the ability to distinguish neighboring elements in the periodic table and scattering powers which can be manipulated by isotopic substitution.

2.2.2 Measurement of neutron diffraction

Powder neutron diffraction profiles were measured with two powder neutron diffractometers at the JRR-3M reactor of Japan Atomic Energy Research Institute (JAERI). One is a High Resolution Powder Diffractometer (HRPD) of JAERI [2.1]. The Ge (331) monochromator ($\lambda = 1.82268 \text{ \AA}$) or Si (533) monochromator ($\lambda = 1.1624 \text{ \AA}$) were used. The collimators used were 6'-20'-6', which were placed before and after the monochromator, and between the sample and each detector. The set of 64 detector and collimators, which were placed every 2.5 degrees, rotate around the sample. Another diffractometer is the Kinken powder diffractometer for High Efficiency and high Resolution MEaSurements (HERMES) of the Institute for Materials Research (IMR), Tohoku University [2.2]. The wavelength of neutron is 1.8196 \AA . The quantity of

powder samples is 6–10 g; the samples were contained in vanadium cans. The measurements were made at several temperatures (8–300 K for HRPD; 2–300 K for HERMES). The crystal and magnetic structures were determined by the Rietveld method.

2.2.3 Magnetic structure amplitude factor [2.3]

At first, it is supposed that the magnetic moments of atoms are in fixed orientations, e.g., in the simple case that the moments are parallel or antiparallel. The differential magnetic scattering cross-section per unit solid angle is expressed by

$$d\sigma_m = q^2 g^2 J^2 \left(\frac{e^2 \gamma}{2mc^2} \right) f^2 = p^2 q^2, \quad (2.1)$$

where e and m are the electron charge and mass, c is the velocity of light, J is the total angular momentum, g is the Landé splitting factor, γ is the magnetic moment of the neutron expressed in nuclear magnetons, and f is an amplitude form factor. The \mathbf{q} is the magnetic interaction vector defined by

$$\mathbf{q} = \boldsymbol{\varepsilon}(\boldsymbol{\varepsilon} \cdot \mathbf{K}) - \mathbf{K}, \quad (2.2)$$

where \mathbf{K} is a unit vector in the direction of the atomic magnetic spin and $\boldsymbol{\varepsilon}$ is a unit vector in the direction perpendicular to the effective reflecting planes, i.e., the so-called scattering vector, as indicated in Fig. 2.1. It follows from the definition of \mathbf{q} provided by Eq. (2.2) that \mathbf{q} lies in the plane of $\boldsymbol{\varepsilon}$ and \mathbf{K} and is perpendicular to $\boldsymbol{\varepsilon}$ and of magnitude $\sin\alpha$. Thus

$$|\mathbf{q}| = \sin \alpha, \quad (2.3)$$

and \mathbf{K} is the direction of the spins in the magnetic materials. The vector is in the opposite direction to that of the applied field or the magnetization in the material, simply because the spin moment arises from negative electrons.

It is of crucial importance to consider the interplay of the magnetic and nuclear scattering. The general effect of the polarization can be seen from Halpern and Johnson's expression for the differential scattering cross-section in the case of a

magnetic system in which all the magnetic moments are aligned parallel or antiparallel to a single direction, i.e., in a ferromagnetic or a simple antiferromagnetic material. This cross-section is given by

$$d\sigma = b^2 + 2bp\lambda \cdot \mathbf{q} + p^2q^2, \quad (2.4)$$

where b is the nuclear scattering length and λ is a unit vector in the direction of the spin of the incident neutron. When the neutron beam is unpolarized, i.e., when the unit vector λ can take all possible directions, then the middle term in this expression will average to zero. Therefore, for an unpolarized beam, the cross-section is given by

$$d\sigma = b^2 + p^2q^2. \quad (2.5)$$

In the more usual case where the neutron beam contains all directions of spin, the nuclear-magnetic interference term averages to zero, and the square of the structure amplitude factor F_{hkl} for (hkl) reflection is given by the sum of two terms, which represents respectively the nuclear and magnetic intensity.

Thus

$$|F_{hkl}|^2 = \left| \sum_n b_n \exp \left\{ 2\pi i \left(\frac{hx_n}{a} + \frac{ky_n}{b} + \frac{lz_n}{c} \right) \right\} \right|^2 + \left| \sum_n \mathbf{q}_n p_n \exp \left\{ 2\pi i \left(\frac{hx_n}{a} + \frac{ky_n}{b} + \frac{lz_n}{c} \right) \right\} \right|^2, \quad (2.6)$$

where the first term is the 2nd power of nuclear structure amplitude factor, and the quantity

$$\mathbf{F}_{\text{magn}} = \sum_n \mathbf{q}_n p_n \exp \left\{ 2\pi i \left(\frac{hx_n}{a} + \frac{ky_n}{b} + \frac{lz_n}{c} \right) \right\} \quad (2.7)$$

can be regarded as the magnetic structure amplitude factor. Particularly in relation to cooperative magnetic materials in which the magnetic moments point to more than one direction, it should be noted that \mathbf{F}_{magn} is a vector quantity. More correctly, the terms in Eqs. (2.6) and (2.7) should include a Debye-Waller factor. The essential feature of Eq. (2.6) is that there is no coherence between the nuclear and magnetic scattering with unpolarized neutrons and the two intensity components are additive.

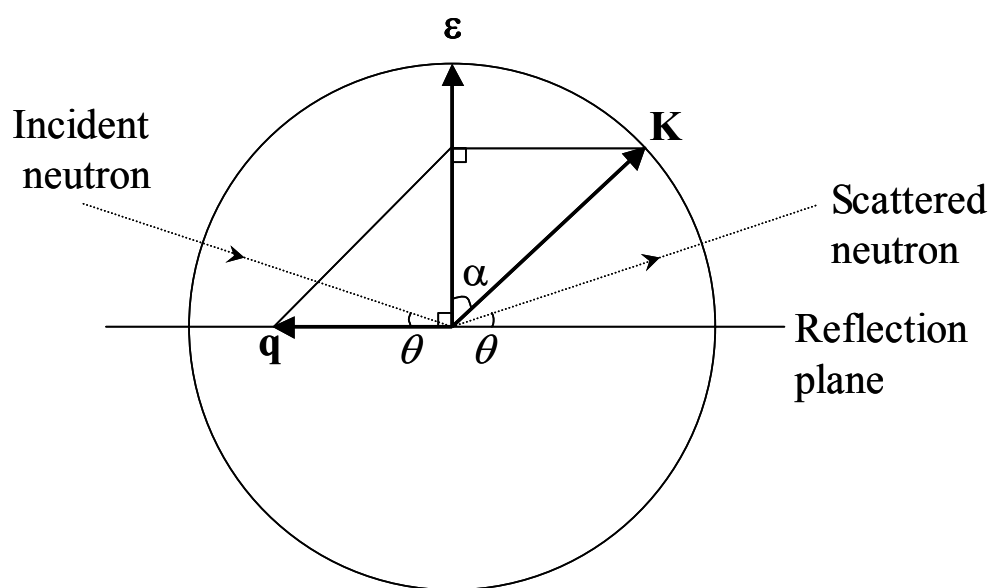


Figure 2.1 Identification of the unit vectors $\boldsymbol{\varepsilon}$ and \mathbf{K} , and the magnetic interaction vector \mathbf{q} .

2.3 Rietveld analysis

The Rietveld method is a technique for refining structural parameters (fractional coordinates, thermal parameters, occupation factors, and magnetic moments, etc.) directly from whole powder diffraction profiles without separating reflections. Variable parameters in Rietveld analysis are much more than those in single-crystal structural refinement in spite of less structural information contained in powder diffraction data. Peak-shift, background, profile-shape, preferred-orientation, and lattice parameters must be refined in addition to scale factors and structural parameters in the Rietveld analysis.

2.3.1 Model function [2.4]

2.3.1.1 Symmetric profile-shape function

The pseudo-Voigt function was used as a symmetric profile-shape function. The Voigt function, i.e., a convolution of the Lorentz function with the Gauss function, can be satisfactorily approximated by a linear combination of the two functions:

$$\begin{aligned}\phi(\Delta 2\theta) &= \eta\phi_L(\Delta 2\theta) + (1-\eta)\phi_G(\Delta 2\theta) \\ &= \eta \frac{2}{\pi H_k} \left\{ 1 + 4 \left(\frac{\Delta 2\theta}{H_k} \right)^2 \right\}^{-1} + (1-\eta) \frac{2\sqrt{\ln 2}}{\sqrt{\pi} H_k} \exp \left\{ -4 \ln 2 \left(\frac{\Delta 2\theta}{H_k} \right)^2 \right\}\end{aligned}\quad (2.8)$$

with

$$\eta = 1.36603 \left(\frac{H_{kL}}{H_k} \right) - 0.47719 \left(\frac{H_{kL}}{H_k} \right)^2 + 0.11116 \left(\frac{H_{kL}}{H_k} \right)^3 \quad (2.9)$$

and

$$\begin{aligned}H_k &= (H_{kG}^5 + 2.69269 H_{kG}^4 H_{kL} + 2.42843 H_{kG}^3 H_{kL}^2 + 4.47163 H_{kG}^2 H_{kL}^3 \\ &\quad + 0.07842 H_{kG} H_{kL}^4 + H_{kL}^5)^{0.2}\end{aligned}\quad (2.10)$$

Here, $\Delta 2\theta = 2\theta_i - 2\theta_k$ (i : step number, k : reflection number, $2\theta_i$: diffraction angle at the

i th step, and θ_k : Bragg angle for the k th reflection), ϕ_L is the normalized Lorentz function, ϕ_G is the normalized Gauss function, η is the fraction of the Lorentzian component, H_k is the full-width-at-half-maximum (FWHM) of ϕ_L and ϕ_G , and H_{kL} and H_{kG} are respectively the Lorentzian and Gaussian FWHM's for the Voigt function corresponding to the above pseudo-Voigt function. H_{kG} is related to the variance of the Gaussian component, σ^2 , by

$$H_{kG} = \sqrt{8\sigma^2 \ln 2} \quad (2.11)$$

with

$$\sigma^2 = U \tan^2 \theta_k + V \tan \theta_k + W. \quad (2.12)$$

Thus, H_{kG} is a function of the three Gaussian FWHM parameters, U , V , W . The first term in Eq. (2.12) contains a component of Gaussian microstrain broadening. H_{kL} varies with θ_k as

$$H_{kL} = X \sec \theta_k + Y \tan \theta_k \quad (2.13)$$

The first part proportional to $\sec \theta_k$ has the angular dependence associated with Scherrer approximation for crystallite-size broadening. X and Y are isotropic-broadening coefficients.

2.3.1.2 Profile asymmetry and peak shift

Profile asymmetry is introduced by employing a multi-term Simpson's rule integration devised. In this method, n symmetric profile-shape functions with different Simpson's coefficients for weights, g_j , and shifts, f_j , are positioned asymmetrically and superimposed with each other:

$$\phi'(\Delta 2\theta) = \frac{1}{3(n-1)} \sum_{j=1}^n g_j \phi(\Delta 2\theta') \quad (2.14)$$

with

$$\Delta 2\theta' = \Delta 2\theta + f_i A_s \cot 2\theta_k + Z + D_s \cos \theta_k + T_s \sin 2\theta_k \quad (2.15)$$

Here, $\phi'(\Delta 2\theta)$ is the asymmetric pseudo-Voigt function, and $\Delta 2\theta'$ is the 2θ difference modified for profile asymmetry, A_s , and peak shifts for each component profile:

zero-point shift, Z , specimen displacement, D_s , and specimen transparency, T_s . The corresponding Simpson's coefficients are:

$$n = 3: g_1 = g_3 = 1; g_2 = 4$$

$$n = 5: g_1 = g_5 = 1; g_2 = g_4 = 4; g_3 = 2$$

$$n = 7: g_1 = g_7 = 1; g_2 = g_4 = g_6 = 4; g_3 = 2$$

$$f_i = \left(\frac{j-1}{n-1} \right)^2 \quad (2.16)$$

The number of terms, n ($= 3, 5$, or 7), in Eq. (2.14) is automatically adjusted for each reflection using its FWHM and A_s must be positive to give reasonable tendencies of peak symmetry.

2.3.1.3 Preferred-orientation function

Preferred orientation is corrected with the March-Dollase function, P_k , which is independent of the diffraction geometry and applicable to both plate and acicular crystallites. The March-Dollase function is expressed by

$$P_k = \frac{1}{m_k} \sum_{j=1}^{m_k} (r^2 \cos^2 \alpha_j + r^{-1} \sin^2 \alpha_j)^{-3/2}, \quad (2.17)$$

where r is an adjustable parameter, and α_j is the angle between the preferred-orientation direction and the j th member of the symmetry-equivalent set of m_k diffraction planes. The March-Dollase function displays the best overall performance for structural studies. It conserves scattering matter, thereby allowing its use in the quantitative analysis of mixtures.

The refinable parameter, r , represents the effective sample compression or extension due to preferred orientation. Its value depends on both the diffraction geometry and the crystallite shape. For samples exhibiting no preferred orientation, r is equal to one.

2.3.1.4 Absorption factor

No absorption correction is needed in Bragg-Brentano-type X-ray powder

diffraction using flat-plate samples because the absorption factor is constant regardless of 2θ . On the other hand, absorption correction is indispensable in the Debye-Scherrer geometry, e.g., neutron powder diffraction using cylindrical containers. Rouse et al. [2.5] gave an analytical approximation of the absorption factor, $A(\theta_i)$, for cylindrical samples with the radius, r_c :

$$A(\theta_i) = \exp\left\{-(a_1 + a_2 \sin^2 \theta_i)\mu r_c - (a_3 + a_4 \sin^2 \theta_i)(\mu r_c)^2\right\} \quad (2.18)$$

with $a_1 = 1.7133$, $a_2 = -0.0368$, $a_3 = -0.0927$, and $a_4 = -0.3750$. The value of the linear absorption coefficient, μ , is calculated from the density of a sample.

2.3.1.5 Criteria of fit

The Rietveld refinement process will adjust the refinable parameters until the residual

$$S_y = \sum_i w_i (y_i - y_{ci})^2, \quad (2.19)$$

where

$$w_i = 1/y_i,$$

y_i = observed (gross) intensity at the i th step,

y_{ci} = calculated intensity at the i th step,

is minimized in some sense. In order to judge the result, there are some of R -factors as follows:

$$R_{wp} = \left\{ \frac{\sum_i w_i (y_i - y_{ci})^2}{\sum_i w_i y_i^2} \right\}^{1/2}, \quad (2.20)$$

$$R_1 = \frac{\sum_k |I_k(\text{obs}) - I_k(\text{calc})|}{\sum_k I_k(\text{obs})}, \quad (2.21)$$

$$R_F = \frac{\sum_k |(I_k(\text{obs}))^{1/2} - (I_k(\text{calc}))^{1/2}|}{\sum_k (I_k(\text{obs}))^{1/2}}. \quad (2.22)$$

Here, I_k is the intensity assigned to k th Bragg reflection at the end of the refinement

cycles. The goodness-of-fit indicator, S , is

$$S = \left\{ \frac{S_y}{(N - P)} \right\}^{1/2} = R_{wp} / R_e, \quad (2.23)$$

where

$$R_e = \left\{ \frac{(N - P)}{\sum_i w_i y_i^2} \right\}^{1/2}, \quad (2.24)$$

N is the number of observations (e.g. the number of y_i 's used) and P is the number of parameters adjusted.

2.4 Magnetic property measurements

Most of the magnetic property measurements in this thesis were carried out using a SQUID (superconducting quantum interference device) magnetometer. The SQUID consists of two superconductors separated by thin insulating layers to form two parallel Josephson junctions. The device is configured as a magnetometer to detect incredibly small magnetic fields. The Quantum Design Magnetic Property Measurement System (MPMS5S model) was used as a SQUID magnetometer. This magnetometer is a sophisticated analysis instrument configured for the study of the magnetic properties of small experimental samples over the temperature range of 1.8–400 K and the magnetic field up to 5.5 T.

The magnetic property measurements performed in this thesis are (a) the temperature-dependence of the magnetic susceptibility, (b) the field-dependence of the magnetization, and (c) the temperature-dependence of the remnant magnetization. The concrete measurement procedures are as follows:

(a) Magnetic susceptibility. The magnetic susceptibilities were measured after zero field cooling (ZFC) and field cooling (FC) conditions. In the ZFC condition, the samples were cooled in a zero field down to a minimum temperature of each measurement, and then, a magnetic field was applied and their magnetic susceptibilities were measured in a heating-up process. After the ZFC measurement had ended at a higher temperature than the magnetic transition temperature of the samples, the FC magnetic susceptibility was measured in a cooling-down process, in which the applied magnetic field was left as it was.

(b) Magnetization. The magnetization was measured at several temperatures by changing the magnetic field strength in the range between -5 and 5 T or between 0 and 5 T. Normally the sample was cooled down to a temperature for the measurement in a zero field (the ZFC condition). In some cases, the magnetization measurements also in the FC condition were carried out.

(c) Remnant magnetization. The temperature dependence of the remnant magnetization was carried out as follows. The samples were cooled down to a minimum temperature of each measurement (below the magnetic transition temperature of the sample) in a zero field. The magnetic field was applied up to 5 T and then reduced to 0 T, and the magnetization measurement was started in a heating-up process.

The samples were contained in the diamagnetic capsules of the medical use. The measured susceptibilities were corrected by extracting the contribution from diamagnetic ionic susceptibilities [2.6].

2.5 Specific heat

Specific heat measurements were performed by the Physical Property Measurement System (Quantum Design, PPMS model). This system uses a relaxation

technique. After each measurement cycle, which is a heating period followed by a cooling period, the heat capacity measurements fit the entire temperature response of the sample platform to a model that accounts for both the thermal relaxation of the sample platform to the bath temperature and the relaxation between the sample platform and sample must be considered when the thermal connection shared by the sample and sample platform is poor. The sample in the form of pellet was mounted on a thin alumina plate with apiezon for better thermal contact.

2.6 Electrical resistivity

Temperature dependence of the electrical resistivity was measured using a DC four-probe technique with the same measurement system (PPMS model). The sample was sintered, and then was cut into a piece of approximately $9 \times 3 \times 1 \text{ mm}^3$. Four contacts were painted onto the sample using silver paste. The measurements were performed in the temperature range 100–400 K for both cooling and heating processes.

2.7 Mössbauer spectrum

2.7.1 Mössbauer spectroscopy

2.7.1.1 Mössbauer effect

At the case of electron in atom and molecule systems, the energy levels and resonant absorption of nucleus exist. However, the energy differences between nuclear levels are about 1000 times larger than those between electron levels in the atom and molecule systems. The energy differences between nuclear levels are equivalent to the energy of the γ -ray (~ 10 – 100 keV). In the case of the emission and absorption of the

γ -ray, the free atomic nucleus recoils, and this recoil energy is large compared with the energy of the γ -ray. When the γ -ray is emitted from the nucleus, the conservation law of the energy gives the following relation,

$$E = E_{\gamma} + E_{\text{R}} \quad (2.25)$$

where E is the difference in energy between the ground and the excited levels in a gamma transition, E_{γ} is the energy of the emitted γ -ray, and E_{R} is the recoil energy in the emission process of the γ -ray. In the absorption process of the γ -ray, the absorbed nucleus recoils towards incident direction of the γ -ray and the γ -ray needs to have the recoil energy E_{R} in addition to the energy E . Therefore, the loss of the emission and absorption energy of the γ -ray is $2E_{\text{R}}$.

In general, the E_{R} is much smaller than E and is negligible. However, in the case of atomic nucleus, E_{R} is not so small compared with E . Thus, the atomic nuclear recoil resonant phenomenon of γ -ray is hard to occur.

The recoil energy E_{R} is written by

$$E_{\text{R}} = \frac{p^2}{2M} = \frac{(E_{\gamma}/c)^2}{2M} \quad (2.26)$$

where M is the mass of the emitting nucleus, p is the momentum of emitted or absorbed atoms. Actually atomic nucleus in solid state is not free but is restrained at lattice point and the recoil can be received by many atoms in solid state. Thus M is very large and the probability of $E_{\text{R}} = 0$ occurs, i.e., recoil-free resonance occurs. This recoil-free resonance is called Mössbauer effect associated with discoverer.

2.7.1.2 Recoil-free fraction

Considering the case of the excitation of the phonon in the emission process of the γ -ray, f is defined as the probability of the emission of the γ -ray without the excitation of the phonon. The recoil energy of ^{57}Fe Mössbauer transition is 10^{-3} eV, comparable to the energy of the phonon. Therefore, the relation between the recoil energy E_{R} and the probability f is given by

$$E_{\text{R}} = (1 - f)\hbar\omega. \quad (2.27)$$

This probability f is called the recoil-free fraction Zero phonon absorption, and indicates the probability of Mössbauer effect.

The recoil-free fraction depends on three factors, which are the free-atom recoil energy (which is proportional to E_γ^2), the properties of the solid lattice, and the ambient temperature. Thus f will be greater, the smaller the probability of excitation of the phonon, i.e., the smaller the γ -ray energy, the firmer the binding of the atom in the lattice, and the lower the temperature. Particularly, the relationship between f and last two factors is expressed by using the Debye model [2.7]:

$$f = \exp \left[\frac{-6E_R}{k_B \theta_D} \left\{ \frac{1}{4} + \left(\frac{T}{\theta_D} \right)^2 \int_0^{\theta_D/T} \frac{x dx}{e^x - 1} \right\} \right] \quad (2.28)$$

where k_B is the Boltzmann constant and θ_D is the Debye temperature.

2.7.2 Measurement of Mössbauer spectrum

Figure 2.2 shows the schematic drawing of the Mössbauer spectroscopy. The source vibrates against the sample and the energy of the γ -ray having only one wavelength is modulated by Doppler effect. The transmission of the γ -ray vs. the Doppler velocity is a Mössbauer spectrum.

The ^{151}Eu Mössbauer spectrum was measured with a Mössbauer spectrometer VT-6000 (Laboratory Equipment Co.) in the constant acceleration mode. The spectrometer was calibrated with a ^{57}Fe Mössbauer spectrum of $\alpha\text{-Fe}$ at room temperature. A $^{151}\text{SmF}_3$ radiation source (1.85 GBq) was used and the γ -rays were detected with a NaI scintillation counter. EuF_3 was used as a reference standard for the chemical isomer shift. The sample lapped in an aluminum foil was cooled down to each temperature by using a variable temperature cryostat system CryoMini (Iwatani Industrial Gases Co.).

2.7.3 Hyperfine interactions [2.8]

The nuclear transitions are very sensitive to the local environment of the atom, and Mössbauer spectroscopy is a sensitive probe of the different environments at an atom

occupies in a solid material. With the change of electron state, the nuclear levels change in which causes the peak shift and/or splitting in Mössbauer spectrum. Therefore, the spectrum gives the hyperfine structure. Isomer shift, second order Doppler shift, and electric quadrupole interaction related to this study, are explained as follows.

2.7.3.1 Isomer shift

The nucleus is surrounded by electronic charge with which it interacts electrostatically. The energy of interaction can be computed classically by considering a uniformly charged spherical nucleus imbedded in its s-electron charge cloud. Since there exists the Coulomb interaction between the electron and nucleus, a change in the chemical state will result as a shift of the nuclear levels.

In the Mössbauer spectrum, this effect is observed as the shift of the spectrum. Such an energy shift due to the chemical state is called as an isomer shift, δ , which is written by

$$\delta = \frac{4\pi}{5} Z e^2 R_n^2 \left(\frac{\Delta R_n}{R_n} \right) \left\{ |\psi_A(0)|^2 - |\psi_S(0)|^2 \right\} \quad (2.29)$$

where Z is the atomic number, R_n is the radius of the nucleus, $|\psi_A(0)|^2$ and $|\psi_S(0)|^2$ are the density of electron at the nucleus of absorber and source, respectively. Isomer shift depends on two factors. One is the difference between the radius of the ground state and excited state. Another is the electronic charge density at the nucleus, which is basically an atomic or chemical parameter, since it is affected by the valence state of the atom.

2.7.3.2 Second order Doppler shift

There exists the relativistic temperature-dependence contribution to the isomer shift. The emitting or absorbing atom is vibrating on its lattice site in the crystal. The frequency of oscillation about the mean position is of the order of 10^{12} sec^{-1} , so that the time-averaged displacement during the Mössbauer event is zero. However, there is a

term in the Doppler shift, which depends on v^2 , so that the mean value $\langle v^2 \rangle$ is not zero. The relativistic equation for the Doppler effect on an emitting photon gives the observed frequency ν' for a closing velocity v as

$$\nu' = \nu \left(1 - \frac{v}{c} \right) \left(1 - \frac{v^2}{c^2} \right)^{-1/2} \approx \nu \left(1 - \frac{v}{c} + \frac{v^2}{2c^2} \right) \quad (2.30)$$

where ν is the frequency for a stationary system. The first order term in velocity is a function of the velocity of the atom vibrating on its lattice site to the direction of the γ -ray and will average to zero over the lifetime of the state. The second order term with v^2 will not average to zero and is therefore independent of the direction of the γ -ray radiation. This term is usually referred to as a second order Doppler shift and expressed as

$$\nu' = \nu \left(1 + \frac{\langle v^2 \rangle}{2c^2} \right). \quad (2.31)$$

The $\langle v^2 \rangle$ term in this equation can be connected with $\langle v^2 \rangle$ in terms of the lattice dynamics of the solid. According to the Debye model of the solid, the second order Doppler shift δ_{SOD} in the velocity unit is written as follows [2.9],

$$\delta_{\text{SOD}} = \frac{-9k_{\text{B}}T}{2Mc} \left\{ \frac{1}{8} \frac{\theta_{\text{D}}}{T} + \left(\frac{T}{\theta_{\text{D}}} \right)^3 \int_0^{\theta_{\text{D}}/T} \frac{x^3 dx}{(e^x - 1)} \right\}. \quad (2.32)$$

2.7.3.3 Electric quadrupole interaction

When the nuclear spin I is 0 or 1/2, the nuclear charge is spherical symmetric and has zero quadrupole moment. When $I \geq 1$, on the other hand, the charge distribution of the nucleus is distorted from spherical symmetry, and the nucleus has non-zero quadrupole moment. The magnitude of the charge deformation of a nucleus is described as the nuclear quadrupole moment Q , given by

$$eQ = \int \rho_{\text{d}} r^2 (3 \cos^2 \theta - 1) d\tau \quad (2.33)$$

where ρ_d is the charge density in a volume element $d\tau$, which is at a distance r from the center of the nucleus and making an included angle θ to the nuclear spin quantization axis. The sign of Q depends on the shape of the deformation. A negative quadrupole moment indicates that the nucleus is oblate or flattened along the spin axis, whereas for a positive moment it is prolate or elongated.

In a chemical bonded atom, the electronic charge distribution is usually not spherically symmetric. The electric field gradient at the nucleus is defined as a tensor,

$$E_{ij} = -V_{ij} = \left(-\partial^2 V / \partial x_i \partial x_j \right) \quad (x_i, x_j = x, y, z), \quad (2.34)$$

where V is the electrostatic potential. It is customary to define the coordinate axis for the system and $V_{zz} = eq$ is the maximum value of the field gradient. The orientation of the nuclear quantized axis with respect to the principal axis, z , is quantized. There is an interaction energy between Q and eq which is different for each possible orientation of the nucleus.

The Laplace equation requires that the electric field gradient is traceless tensor, so that

$$V_{xx} + V_{yy} + V_{zz} = 0. \quad (2.35)$$

Consequently, only two independent parameters are needed to specify the electric field gradient completely, and the two, which are usually chosen, are V_{zz} and an asymmetry parameter η , defined as

$$\eta = \frac{V_{xx} - V_{yy}}{V_{zz}}. \quad (2.36)$$

Using the relationships of $|V_{zz}| > |V_{yy}| \geq |V_{xx}|$ ensures that $0 \leq \eta \leq 1$.

The Hamiltonian of the quadrupole interaction can be written as

$$H_{\text{quad}} = \frac{eQ}{2I(2I-1)} (V_{zz} \hat{I}_z^2 + V_{xx} \hat{I}_x^2 + V_{yy} \hat{I}_y^2), \quad (2.37)$$

where \hat{I}_z , \hat{I}_x and \hat{I}_y are the nuclear spin operators. Using Eq. (2.36), the Hamiltonian becomes

$$H_{\text{quad}} = \frac{eQ}{2I(2I-1)} \left\{ 3\hat{I}_z^2 - I(I+1) + \eta(\hat{I}_+^2 + \hat{I}_-^2) \right\}. \quad (2.38)$$

where \hat{I}_+ and \hat{I}_- are shift operators. The calculated matrix elements of H_{quad} are

$$\langle \psi_{I, I_z} | H_{\text{quad}} | \psi_{I, I_z} \rangle = \frac{e^2 q Q}{4I(2I-1)} \{ 3I_z^2 - I(I+1) \} \quad (2.39)$$

and

$$\langle \psi_{I, I_z \pm 2} | H_{\text{quad}} | \psi_{I, I_z} \rangle = \frac{e^2 q Q}{8I(2I-1)} \eta \{ (I \mp I_z)(I \pm I_z + 1)(I \mp I_z - 1)(I \pm I_z + 2) \}^{1/2}, \quad (2.40)$$

and the other matrix elements are equal to zero. The eigenvalues of H_{quad} are obtained by calculating the determinant,

$$\left| \langle \psi_{I, I_z'} | H_{\text{quad}} | \psi_{I, I_z} \rangle - E \delta_{I_z, I_z'} \right| = 0. \quad (2.41)$$

As an example, a typical energy level scheme with the quadrupole interaction for ^{151}Eu ($I = 5/2 \rightarrow I = 7/2$) Mössbauer spectrum is shown in Fig. 2.3.

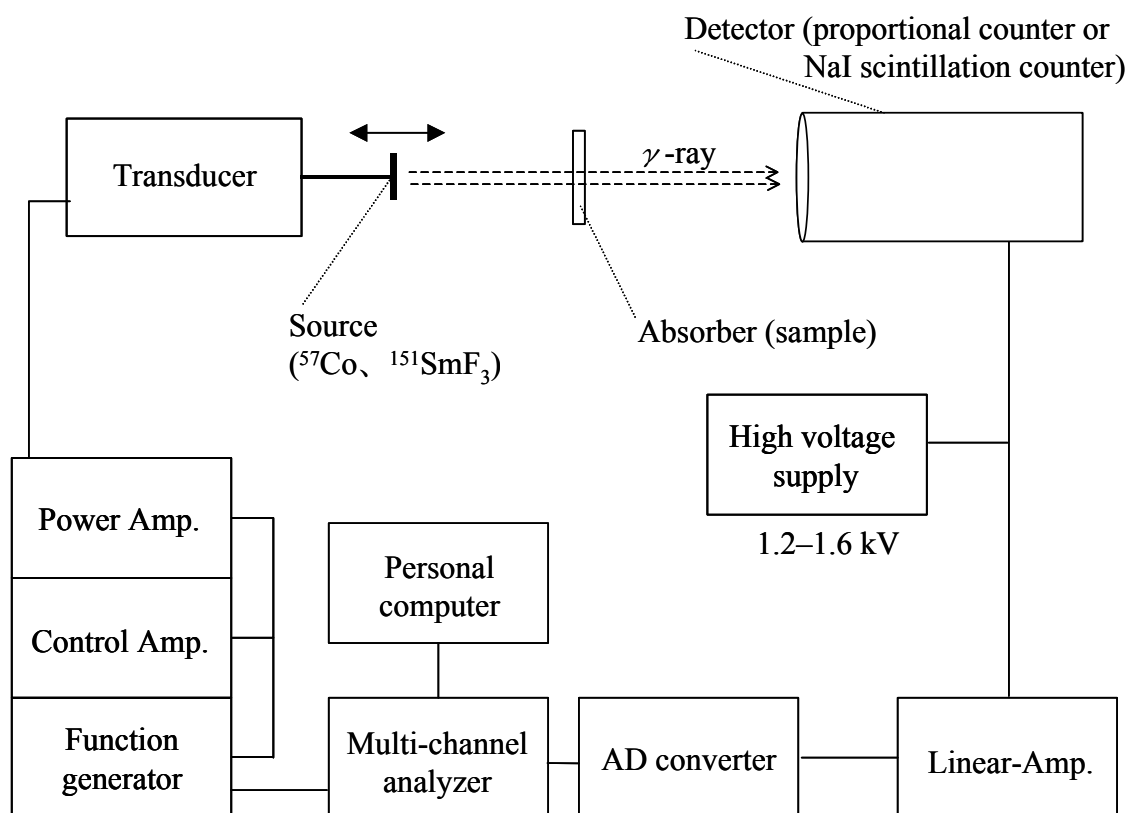


Figure 2.2 Schematic drawing of the Mössbauer measurement.

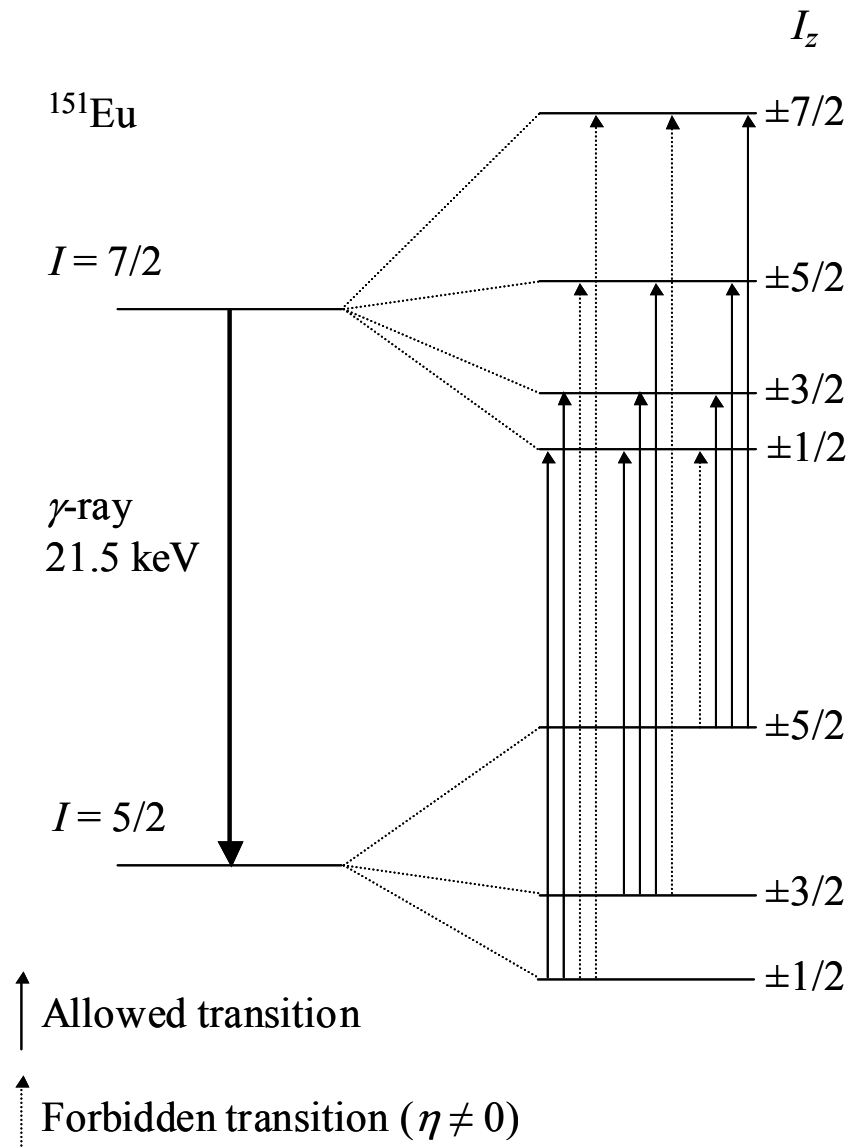


Figure 2.3 Typical energy level scheme for ^{151}Eu Mössbauer transition with quadrupole interaction.

2.8 References

- [2.1] Y. Morii, *J. Cryst. Soc. Jpn.* **34**, 62 (1992).
- [2.2] K. Ohoyama, T. Kanouchi, K. Nemoto, M. Ohashi, T. Kajitani, and Y. Yamaguchi, *Jpn. J. Appl. Phys.* **37**, 3319 (1998).
- [2.3] G. E. Bacon, “Neutron Diffraction”, Clarendon Press, Oxford (1975).
- [2.4] R. A. Young, Ed., “The Rietveld Method”, Oxford Univ. Press, Oxford (1993).
- [2.5] K. D. Rouse, M. J. Cooper, E. J. York, and A. Chakera, *Acta Crystallogr. Sec. A* **26**, 682 (1970).
- [2.6] K. -H. Hellwege and A. M. Hellwege, Landolt-Börnstein, New Series, Vol. II/11, Springer, Berlin (1981).
- [2.7] R. M. Mahesh, *Phys. Status Solidi b* **61**, 695 (1974).
- [2.8] N. N. Greenwood and T. C. Gibb, “Mössbauer Spectroscopy”, Chapman and Hall (1975).
- [2.9] R. M. Housley and F. Hess, *Phys. Rev.* **146**, 517 (1966).

Chapter 3.

Crystal structures and magnetic properties of the ordered perovskites $\text{Sr}_2\text{LnRuO}_6$

3.1 Introduction

3.1.1 Double perovskites $\text{A}_2\text{BB}'\text{O}_6$ [3.1, 2]

As described in section 1.1.1, the perovskite-type oxides allow much combination of ionic species, ionic valence, and ionic size, and they can adopt many derivative structures. Double perovskites are a compound group belonging to the family of perovskite-type compounds. The double perovskites have a general formula $\text{A}_2\text{BB}'\text{O}_6$, in which B and B' represent different ions. The study of the double perovskites has started in the 1950s; by present, many compounds have been discovered [3.1]. The group of double perovskite compounds contains many interesting materials, which show the dielectric (ferro/antiferroelectric) properties, magnetic (ferro/ferri/antiferromagnetic) properties, metallic electrical conductivity, and colossal magnetoresistance, etc. Therefore, double perovskites have attracted a great deal of interest in both sides of the basic and applied research.

To understand the physical properties of any material, the arrangement and position of the ions must be elucidated. In the case of the double perovskites, it is important to know the arrangement of the B (B') cations because the B cations generally determine the physical properties of perovskites ABO_3 . Three sublattice types for the B cations in the double perovskites are known: random, rock salt, and layered. The schematic structures are shown in Fig. 3.1.1. The random type is a disorder arrangement of the B cations, and the latter two types are ordered arrangements. Among three sublattice types, the layered type arrangement is a very rare case. It is known that only $\text{Ln}_2\text{CuSnO}_6$ ($\text{Ln} = \text{La, Pr, Nd, and Sm}$) [3.3,4] and $\text{La}_2\text{CuZrO}_6$ [3.4] adopt this arrangement, hence, the B cation arrangements in most double perovskites are random or rock salt types. Hereafter,

the double perovskites with the rock salt type arrangement will be called the ordered perovskites. The main factors determining the order or disorder arrangements in the double perovskites are the differences between B cations in the size and charge. The rock salt sublattice becomes more stable compared to the random sublattice as the size and charge difference of the B cations increase.

3.1.2 Magnetic interaction in ordered perovskites

Due to their structural feature, the ordered perovskites $\text{A}_2\text{BB}'\text{O}_6$ are convenient compounds to study the 180° magnetic superexchange interactions. In the case that both B and B' ions are magnetic, the 180° B–O–B' superexchange pathway is dominant in the magnetic ordering. Perovskite compounds, in which both B and B' ions are d block magnetic ions, have been synthesized over much combination of B and B' ions; their magnetic properties have been well investigated. Depending on the electronic configuration of B site ions, they show the antiferromagnetic, ferromagnetic, and ferrimagnetic ordering by the strong magnetic interaction between d electrons [3.5]. On the other hand, when B ions are magnetic and B' ions are nonmagnetic, the magnetic ordering of B ions occurs at low temperatures through long superexchange pathways of 90° and 180° B–O–B'–O–B, or a bending pathway B–O–O–B. This magnetic interaction is much weaker than that in ordered perovskites with magnetic B and B' ions belonging to the d block element.

For another case, there are ordered perovskites containing the lanthanide ions, i.e., A_2LnBO_6 . If the remaining B ion is a d block magnetic ion, the magnetic interaction between d and f electrons may be important. Considering the order of the strength for the magnetic interactions, $d-d > d-f > f-f$, the magnetic interaction between d–d electrons via long superexchange pathways, B–O–Ln–O–B and B–O–O–B, also may contribute to the magnetic properties of A_2LnBO_6 . It is predicted that the A_2LnBO_6 shows more complex and interesting magnetic properties by these two kinds of magnetic interactions. In addition, because of the similarity in chemical nature of lanthanides, a series of A_2LnBO_6 with different lanthanide ions can be synthesized as

long as the geometry conditions (e.g. the tolerance factor) are met. This makes it possible to change every one number of the 4f electron, which characterizes the magnetic properties of lanthanide ions. Therefore, the $A_2\text{LnBO}_6$ is a convenient system to investigate the magnetic interaction between d and f electrons.

This Chapter describes the crystal structures and magnetic properties of the ordered perovskites $\text{Sr}_2\text{LnRuO}_6$ and related ordered perovskites. As is mentioned above and in section 1.2, these compounds are interesting subjects of magnetic research. Previously, the magnetic properties of some compounds are reported; they sometimes show a long range magnetic ordering at low temperatures: Sr_2YRuO_6 ($T_N = 26$) [3.6, 7], $\text{Sr}_2\text{LuRuO}_6$ ($T_N = 30$) [3.8], and $\text{Sr}_2\text{ErRuO}_6$ ($T_N = \sim 40$ K) [3.9]. However, previous works are limited to a few compounds of this series, and the magnetic nature of this series with other lanthanides is unknown in spite of the possibility of fascinating magnetic properties depending upon the difference in the number of 4f electrons. Additionally, very recent reports show that the copper-doping Sr_2YRuO_6 shows the superconductivity [3.10-12]. Therefore, it is interesting to study systematically the magnetic properties of ordered perovskites $\text{Sr}_2\text{LnRuO}_6$ and related compounds.

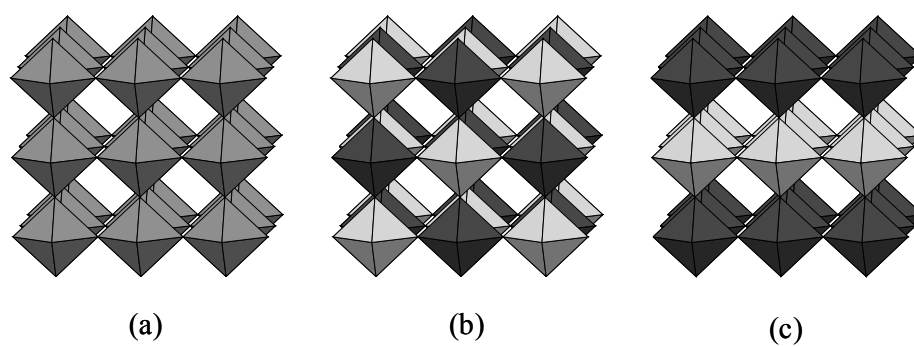


Figure 3.1.1 The schematic structures of perovskites with (a) random, (b) rock salt, and (c) layered arrangements of B-site cations. A-site cations are omitted.

3.2 Crystal structures and magnetic properties of ordered perovskites $\text{Sr}_2\text{LnRuO}_6$ ($\text{Ln} = \text{Eu-Lu}$)

3.2.1 Introduction

This section discusses the crystal structures and magnetic properties of $\text{Sr}_2\text{LnRuO}_6$ ($\text{Ln} = \text{Eu-Lu}$). These compounds are expected to adopt an ordered arrangement because the difference in ionic radii between Ru^{5+} and Ln^{3+} is large, (for instance, the six-coordinate ionic radii of Ru^{5+} , Eu^{3+} and Lu^{3+} are 0.565 Å, 0.947 Å and 0.861 Å, respectively). In addition, they are expected to show various magnetic behavior and magnetic transitions at low temperatures, which are thought to reflect the different electronic properties of lanthanide ions. Through study of the structurally ordered perovskites $\text{Sr}_2\text{LnRuO}_6$ ($\text{Ln} = \text{Eu-Lu}$), it is expected to obtain systematic information not only on the change of the crystal structure but also on the variation of the magnetic properties with the change of Ln^{3+} ions. In the latter case, an interesting magnetic phenomenon due to the magnetic interaction between d and f electrons will be observed.

3.2.2 Experimental

Polycrystalline samples of $\text{Sr}_2\text{LnRuO}_6$ were prepared by firing the appropriate amounts of strontium carbonate SrCO_3 , lanthanide sesquioxide Ln_2O_3 ($\text{Ln} = \text{Eu, Gd, Dy-Lu}$) or Tb_4O_7 , and ruthenium dioxide RuO_2 , first at 1173 K for 12 h and then 1473 K for 108 h with grinding and pelleting at regular intervals. The products were shown to be perovskite-like single-phase materials by powder X-ray diffraction measurements. Their magnetic susceptibility data were measured in a magnetic field of 0.1 T over the temperature range $6 \text{ K} < T < 300 \text{ K}$ using a SQUID magnetometer (Quantum Design, MPMS5S); magnetic susceptibility data were collected after cooling the sample from room temperature in zero applied field (ZFC) and after cooling in the measuring field (FC). The magnetization measurements were performed at 10 K over the magnetic field range $-5 \text{ T} < H < 5 \text{ T}$.

3.2.3 Results and discussion

3.2.3.1 Crystal structure

Figure 3.2.1(a) shows the X-ray diffraction profile for $\text{Sr}_2\text{DyRuO}_6$ as an example, and Figure 3.2.1(b) shows the profiles for $\text{Sr}_2\text{LnRuO}_6$ ($\text{Ln} = \text{Eu-Lu}$) in a higher angle range. X-ray diffraction data were analyzed by the Rietveld method with the program RIETAN97 β [3.13]. It is found that all the compounds $\text{Sr}_2\text{LnRuO}_6$ prepared in this study have a distorted perovskite-type structure, which is monoclinic with space group $P2_1/n$. The unit cell is related to the primitive perovskite unit cell (a_p) in the following way: $a \approx \sqrt{2} a_p$, $b \approx \sqrt{2} a_p$, and $c \approx 2a_p$. The Ln^{3+} and Ru^{5+} ions are arranged alternately at the B sites of the ABO_3 perovskite-type structure, i.e., they are structurally ordered over the six-coordinated sites of the $\text{Sr}_2\text{LnRuO}_6$. This crystal structure is illustrated in Fig. 3.2.2.

Each lattice parameter and reliability factors (R_{wp} , R_{I} , R_{F} , R_{e}) are listed in Table 3.2.1. The variation of lattice parameters for the $\text{Sr}_2\text{LnRuO}_6$ with the ionic radius of Ln^{3+} is displayed in Fig. 3.2.3. The lattice parameters a , b , and c increase with the Ln^{3+} ionic radius. The lattice parameter β increases and the differences among a , b and $c/\sqrt{2}$ spread with increase of the Ln^{3+} ionic radius. This fact indicates that from $\text{Ln} = \text{Lu}$ to Eu the crystal structures of $\text{Sr}_2\text{LnRuO}_6$ are more distorted from the cubic symmetry. Figure 3.2.4 shows the variation of the average Ru–O bond length, Ln–O bond length and Ln–O–Ru angle as a function of the Ln^{3+} ionic radius. The Ln–O bond length is monotonously increases with the Ln^{3+} ionic radius, while the Ru–O bond length does not change much. This result indicates that the charge configuration of these compounds is $\text{Sr}_2\text{Ln}^{3+}\text{Ru}^{5+}\text{O}_6$. The Ln–O–Ru angle decreases remarkably with the increase of Ln^{3+} ionic radius. This decreasing in the Ln–O–Ru angle can be explained by the tilting of linkage of the LnO_6 and RuO_6 octahedra which is due to the distortion of the double perovskite $\text{Sr}_2\text{LnRuO}_6$ from the cubic symmetry.

3.2.3.2 Magnetic properties

The molar magnetic susceptibilities of $\text{Sr}_2\text{LnRuO}_6$ ($\text{Ln} = \text{Eu-Lu}$) are plotted as a

function of temperature in Figs. 3.2.5 and 3.2.6. The Curie-Weiss law is valid for the magnetic susceptibilities of $\text{Sr}_2\text{LnRuO}_6$ in higher temperature range ($T > 150$ K) except for those of $\text{Sr}_2\text{EuRuO}_6$. The effective magnetic moments (μ_{eff}) and Weiss constants (θ) obtained by the Curie-Weiss fitting to the higher temperature susceptibility data are listed in Table 3.2.2. In this table, the calculated moments for the Ln^{3+} ion (free ion), μ_{Ln} , are also listed. It is found that the effective magnetic moments for $\text{Sr}_2\text{LnRuO}_6$ are close to the values for the Ln^{3+} ion, in spite of the fact that there exist two kinds of magnetic ions, Ln^{3+} and Ru^{5+} , in the $\text{Sr}_2\text{LnRuO}_6$ except for $\text{Ln} = \text{Lu}$. This result indicates that the contribution of the magnetic moment of the Ru^{5+} ion to the paramagnetic behavior of the $\text{Sr}_2\text{LnRuO}_6$ is small compared with that of the Ln^{3+} ion.

The $\text{Sr}_2\text{LnRuO}_6$ compounds show a variety of temperature dependences of magnetic susceptibilities at low temperatures as depicted in Figs. 3.2.5 and 3.2.6. From these measurements, it is found that the magnetic transition occurs in all of these compounds. Previous neutron diffraction experiments at 4.2 K report that $\text{Sr}_2\text{LuRuO}_6$ [3.8] shows an antiferromagnetic ordering of Ru^{5+} ions and that in the $\text{Sr}_2\text{ErRuO}_6$ [3.9] both Er^{3+} and Ru^{5+} ions order antiferromagnetically. The present magnetic susceptibility measurements on $\text{Sr}_2\text{LuRuO}_6$ and $\text{Sr}_2\text{ErRuO}_6$ show maxima in the susceptibility (ZFC) vs. temperature curves at 32 and 42 K, respectively. The negative Weiss constants (θ) listed in Table 3.2.2 indicate that the predominant magnetic interactions in these compounds are antiferromagnetic. It is considered that the magnetic interactions between Ru^{5+} ions should operate significantly because the transition temperatures do not exhibit so much difference among compounds. Generally, the antiferromagnetic ordering of Ru^{5+} ions in the Sr_2BRuO_6 (where B is a trivalent diamagnetic ion) is due to the superexchange interaction between nearest neighboring Ru^{5+} ions, i.e., the pathway is Ru-O-O-Ru or Ru-O-B-O-Ru . In the present $\text{Sr}_2\text{LnRuO}_6$, two kinds of the magnetic ions exist; therefore, it is thought that not only the magnetic interaction between Ru^{5+} ions but also the interaction between Ln^{3+} and Ru^{5+} ions (the pathway is Ln-O-Ru) should contribute to the magnetic properties of these compounds. Since the interactions between Ln^{3+} ions are generally very weak, they will not participate in the

magnetic ordering. The Néel temperatures for the compounds $\text{Sr}_2\text{LnRuO}_6$ (Ln = Tb–Tm) are a little higher than that for $\text{Sr}_2\text{LuRuO}_6$ ($T_N = 32$ K, Lu^{3+} is diamagnetic). This fact indicates that the magnetic interactions between Ru^{5+} and Ln^{3+} ions greatly contribute to the antiferromagnetic ordering in the $\text{Sr}_2\text{LnRuO}_6$ compounds. The Néel temperature for $\text{Sr}_2\text{EuRuO}_6$ is close to that for $\text{Sr}_2\text{LuRuO}_6$. Since the ground state of Eu^{3+} ion is $^7\text{F}_0$, the magnetic interaction between Eu^{3+} and Ru^{5+} ions is negligible for this antiferromagnetic transition.

For all compounds, the field dependence of the magnetization were measured at 10 K over the magnetic field range $-5 \text{ T} < H < 5 \text{ T}$. Figure 3.2.7 shows the variation of magnetization as a function of magnetic field for the $\text{Sr}_2\text{TbRuO}_6$ and $\text{Sr}_2\text{YbRuO}_6$. Small magnetic hysteresis was found for all compounds. In addition to this, the large divergence between the FC and ZFC susceptibilities was found for all compounds. These experimental results indicate that $\text{Sr}_2\text{LnRuO}_6$ are not ideal antiferromagnets. It is considered that this is due to the contribution of the weak ferromagnetic component to the magnetic property. In the case of the compounds with a low crystal symmetry such as monoclinic symmetry, the Dzyaloshinsky-Moriya (D-M) interaction can exist between the ordered elements which results in the existence of a weak ferromagnetic component in their susceptibilities.

The $\text{Sr}_2\text{EuRuO}_6$ compound shows that the temperature dependence of magnetic susceptibility (Fig. 3.2.6) does not obey the Curie-Weiss law. The ground state $^7\text{F}_0$ of Eu^{3+} is nonmagnetic, and the excited states $^7\text{F}_J$ ($J = 1, 2, \dots, 6$) are close enough to give energy differences comparable to $k_B T$ at room temperature. The excitation to the upper state affects sufficiently the magnetic susceptibility at room temperature. Thus, the molar magnetic susceptibility for Eu^{3+} can be expressed by the following equation [3.14]:

$$\chi(\text{Eu}^{3+}) = \frac{N_A \mu_B^2}{3k_B T} \frac{24 + (13.5\gamma - 1.5)e^{-\gamma} + (67.5\gamma - 2.5)e^{-3\gamma} + (189\gamma - 3.5)e^{-6\gamma}}{1 + 3e^{-\gamma} + 5e^{-3\gamma} + 7e^{-6\gamma}}, \quad (3.1)$$

where the parameter $\gamma = \lambda / k_{\text{B}}T$ is the ratio of the multiplet width (the spin-orbit coupling constant, λ) and the thermal energy ($k_{\text{B}}T$), and it is 1/21 for the Eu^{3+} ion. If the magnetic behavior of Eu^{3+} ion and Ru^{5+} ion is independent each other in the paramagnetic region, the susceptibility of $\text{Sr}_2\text{EuRuO}_6$ will be given by the sum of the susceptibilities of each paramagnetic ion. In that case, the total magnetic susceptibility of $\text{Sr}_2\text{EuRuO}_6$ is given by

$$\chi_{\text{M}} = \chi(\text{Eu}^{3+}) + \chi(\text{Ru}^{5+}) + \chi_{\text{TIP}}, \quad (3.2)$$

where $\chi(\text{Ru}^{5+}) = \frac{C}{T - \theta}$,

and χ_{TIP} is the temperature-independent susceptibility of $\text{Sr}_2\text{EuRuO}_6$. In order to explain the behavior of magnetic susceptibility and to estimate the effective magnetic moment and Weiss constant of Ru^{5+} , the experimental susceptibility was fitted using this equation (3.2). For preventing the parameters from converging meaningless values, the λ value was fixed on 363 cm^{-1} , which is a theoretical value (when the screening number σ is 34). This theoretical value is very close to the values reported for other ordered perovskites, for example, 352 cm^{-1} ($\text{Cs}_2\text{NaEuCl}_6$) obtained from the luminescence spectra [3.15] and 364 cm^{-1} ($\text{Ba}_2\text{EuIrO}_6$) from the magnetic susceptibilities [3.16]. By this fitting, the effective magnetic moment and Weiss constant were estimated to be $\mu_{\text{eff}} = 3.1(1) \mu_{\text{B}}$ and $\theta = -399(16) \text{ K}$, respectively. The negative Weiss constant indicates the existence of the antiferromagnetic interaction of Ru^{5+} ions.

The magnetic susceptibility of $\text{Sr}_2\text{YbRuO}_6$ compound shows unusual temperature dependence, namely the ZFC magnetic susceptibility is larger than the FC magnetic susceptibility below the transition temperature and the maximum in the susceptibility vs. temperature curve is found only in the FC susceptibility. The large negative Weiss constant ($\theta = -225(23) \text{ K}$) indicates the existence of the antiferromagnetic interaction.

3.2.4 Summary

In this section, the perovskite-type compounds $\text{Sr}_2\text{LnRuO}_6$ ($\text{Ln} = \text{Eu-Lu}$) have been synthesized, and their crystal structures and magnetic properties have been studied. Powder X-ray diffraction measurements and the Rietveld analysis show that they are

monoclinic with space group $P2_1/n$ and that Ln^{3+} and Ru^{5+} ions are structurally ordered. By the magnetic susceptibility measurements, it is found that $\text{Sr}_2\text{LnRuO}_6$ show an antiferromagnetic transition at 30–46 K and they show complex magnetic behavior below the magnetic transition temperature. These facts are ascribable to the magnetic coupling between 4d electrons of Ru^{5+} ions and 4f electrons of Ln^{3+} ions. Some of $\text{Sr}_2\text{LnRuO}_6$ compounds have been investigated furthermore using such as specific heat and neutron diffraction measurements. Those results will be discussed in the following sections.

Table 3.2.1 Unit cell parameters and reliability factors for $\text{Sr}_2\text{LnRuO}_6$ ($\text{Ln} = \text{Eu-Lu}$)

Ln	$a / \text{\AA}$	$b / \text{\AA}$	$c / \text{\AA}$	β / deg	R_{wp}	R_{I}	R_{F}	R_{e}
Eu	5.8055(2)	5.8455(2)	8.2302(2)	90.360(2)	8.53	1.58	2.04	6.58
Gd	5.7978(2)	5.8317(2)	8.2165(3)	90.325(2)	9.71	2.13	2.59	8.03
Tb	5.7885(6)	5.8114(4)	8.2008(8)	90.257(6)	11.61	2.90	3.79	9.31
Dy	5.7777(6)	5.7974(4)	8.1821(8)	90.270(6)	12.54	2.35	3.35	10.49
Ho	5.7719(6)	5.7784(5)	8.1651(9)	90.200(5)	10.89	1.77	2.61	9.13
Er	5.7611(6)	5.7644(5)	8.1449(8)	90.180(5)	11.33	1.96	2.41	8.95
Tm	5.7517(6)	5.7535(6)	8.1231(6)	90.204(6)	11.79	1.96	2.49	9.23
Yb	5.7430(5)	5.7431(5)	8.1046(5)	90.210(5)	12.99	2.00	3.20	10.03
Lu	5.7334(5)	5.7347(5)	8.0968(5)	90.176(5)	13.18	2.46	2.62	10.05

Table 3.2.2 Calculated magnetic moments for free Ln^{3+} ions (μ_{Ln}), effective magnetic moments (μ_{eff}) and Weiss constants (θ) for $\text{Sr}_2\text{LnRuO}_6$ ($\text{Ln} = \text{Gd-Lu}$)

Ln^{3+}	$\mu_{\text{Ln}} / \mu_{\text{B}}$	$\mu_{\text{eff}} / \mu_{\text{B}}$	θ / K
Gd^{3+} ($4f^7$)	7.94	7.1(2)	-8(1)
Tb^{3+} ($4f^8$)	9.72	9.1(1)	-15(3)
Dy^{3+} ($4f^9$)	10.63	10.4(2)	-20(3)
Ho^{3+} ($4f^{10}$)	10.58	10.6(2)	-20(3)
Er^{3+} ($4f^{11}$)	9.59	9.8(1)	-22(3)
Tm^{3+} ($4f^{12}$)	7.55	8.1(1)	-47(4)
Yb^{3+} ($4f^{13}$)	4.54	6.6(3)	-225(23)
Lu^{3+} ($4f^{14}$)	—	3.2(1)	-205(15)

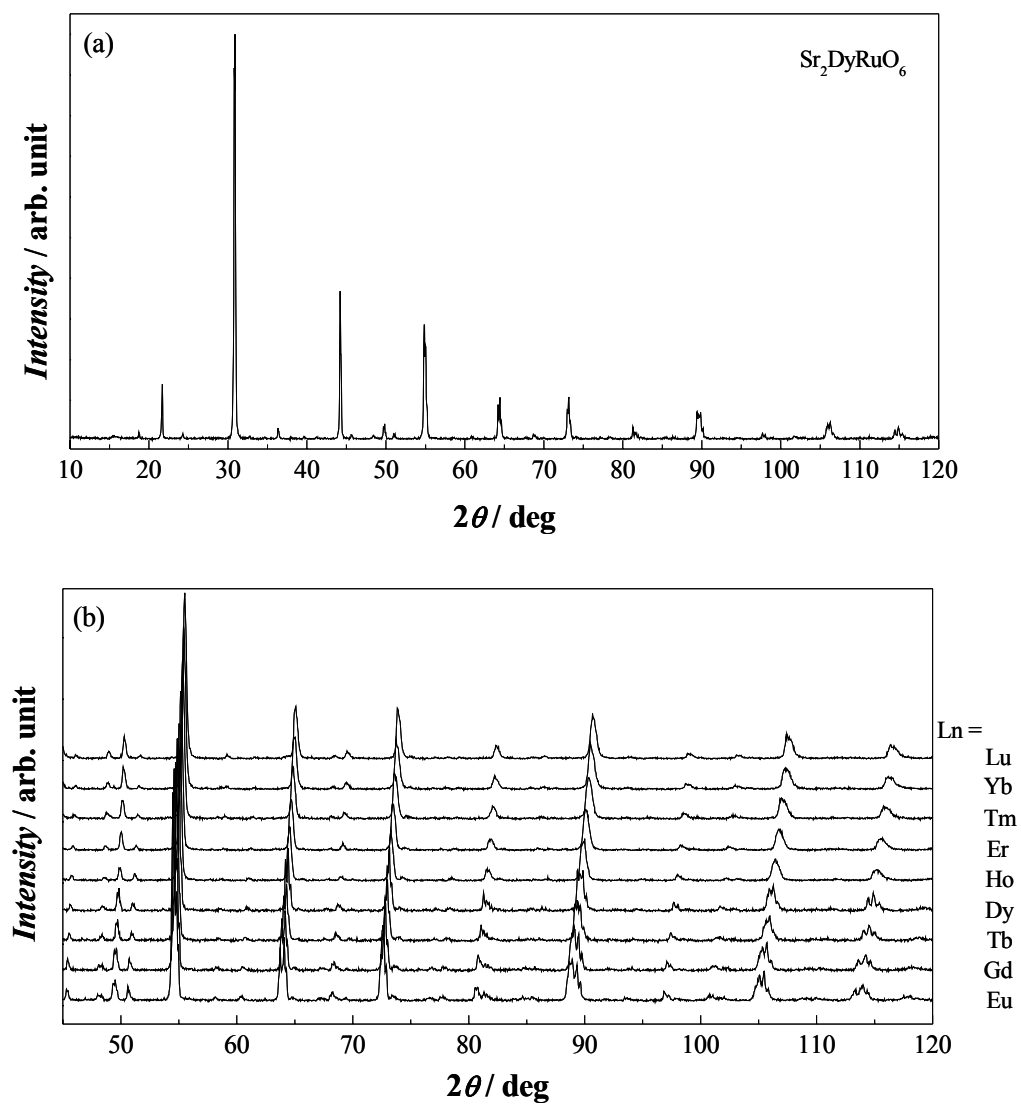


Figure 3.2.1 X-ray diffraction profiles of $\text{Sr}_2\text{LnRuO}_6$: (a) $\text{Sr}_2\text{DyRuO}_6$, (b) $\text{Sr}_2\text{LnRuO}_6$ (Ln = Eu–Lu).

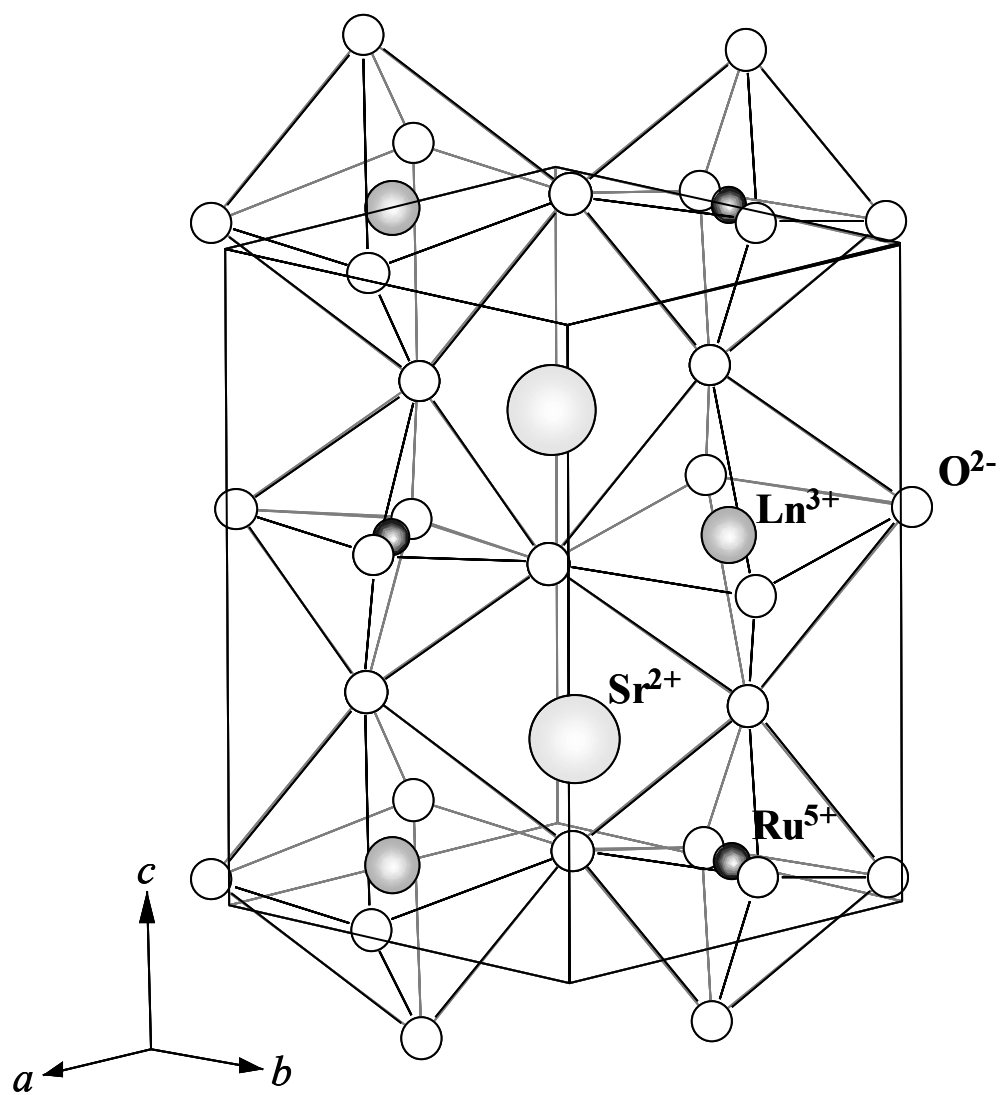


Figure 3.2.2 Crystal structure of $\text{Sr}_2\text{LnRuO}_6$ ($\text{Ln} = \text{Eu-Lu}$).

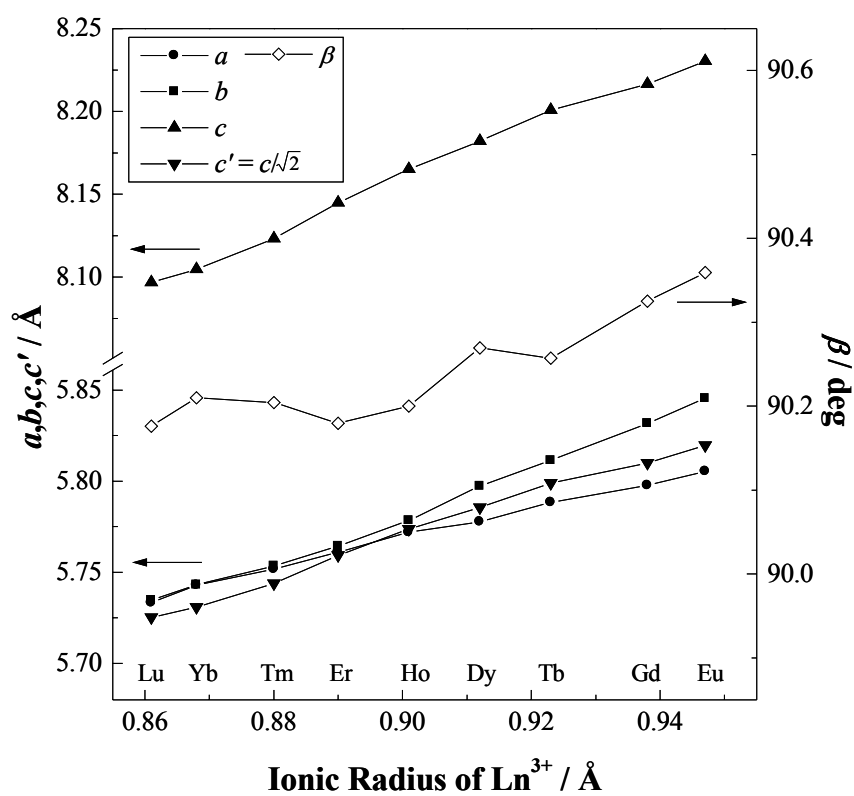


Figure 3.2.3 Variation of lattice parameters for $\text{Sr}_2\text{LnRuO}_6$ ($\text{Ln} = \text{Eu-Lu}$) with Ln^{3+} radius.

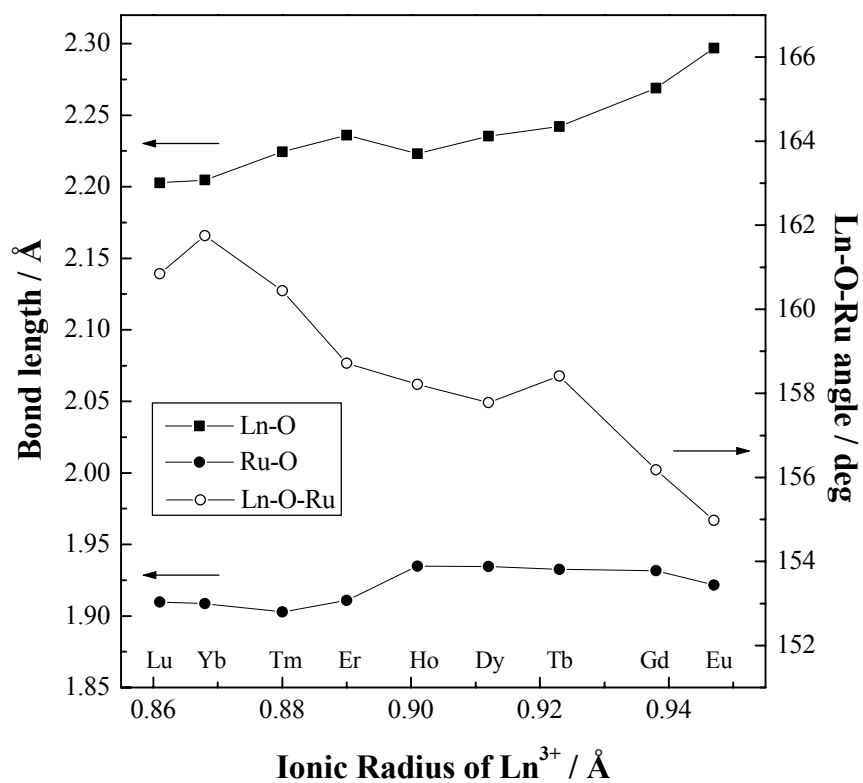


Figure 3.2.4 Average Ru-O bond length, Ln-O bond length, and Ln-O-Ru angle.

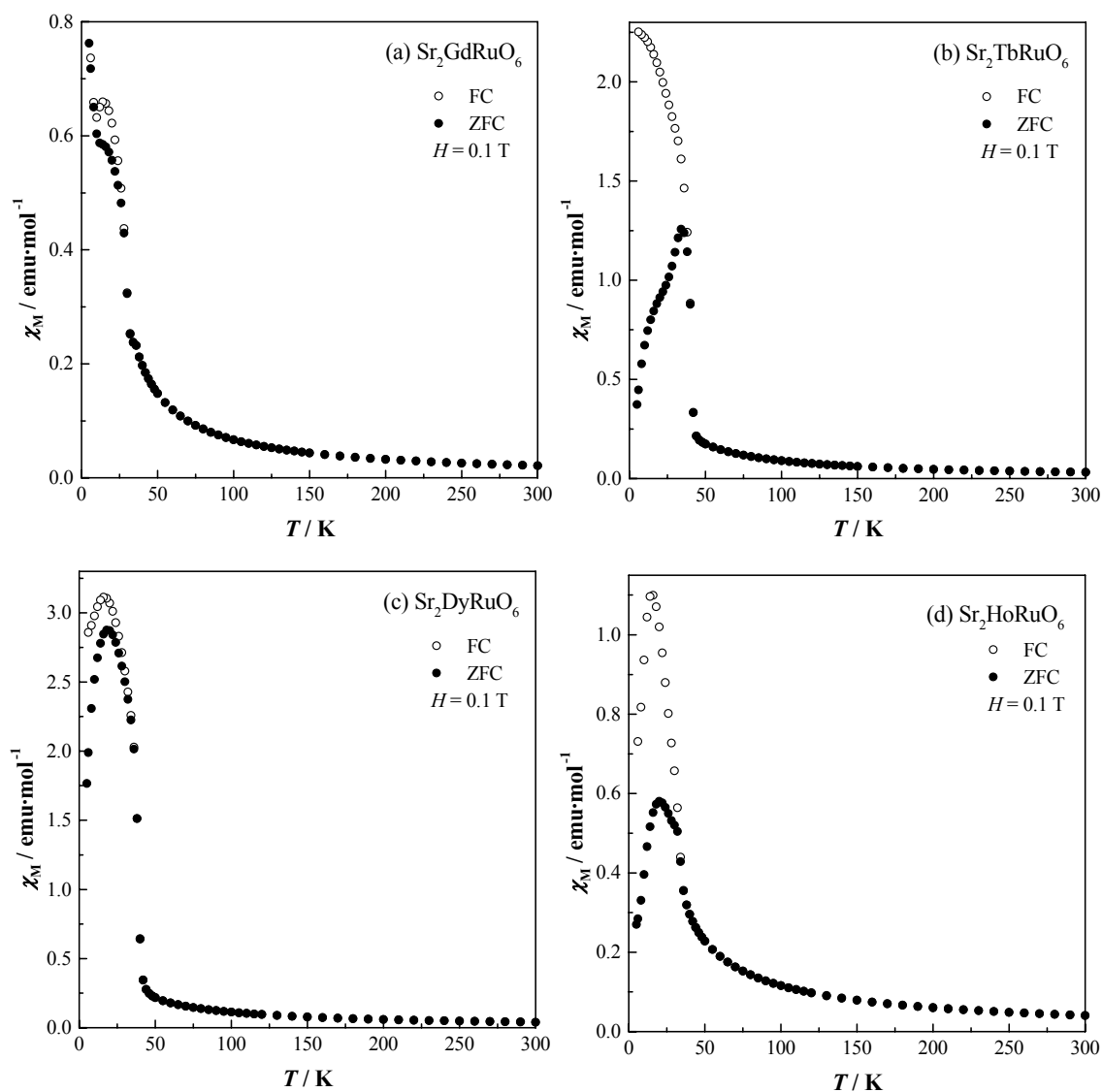


Figure 3.2.5 Temperature dependence of the ZFC (filled symbols) and FC (open symbols) molar magnetic susceptibilities for $\text{Sr}_2\text{LnRuO}_6$ (Ln = Gd–Lu).

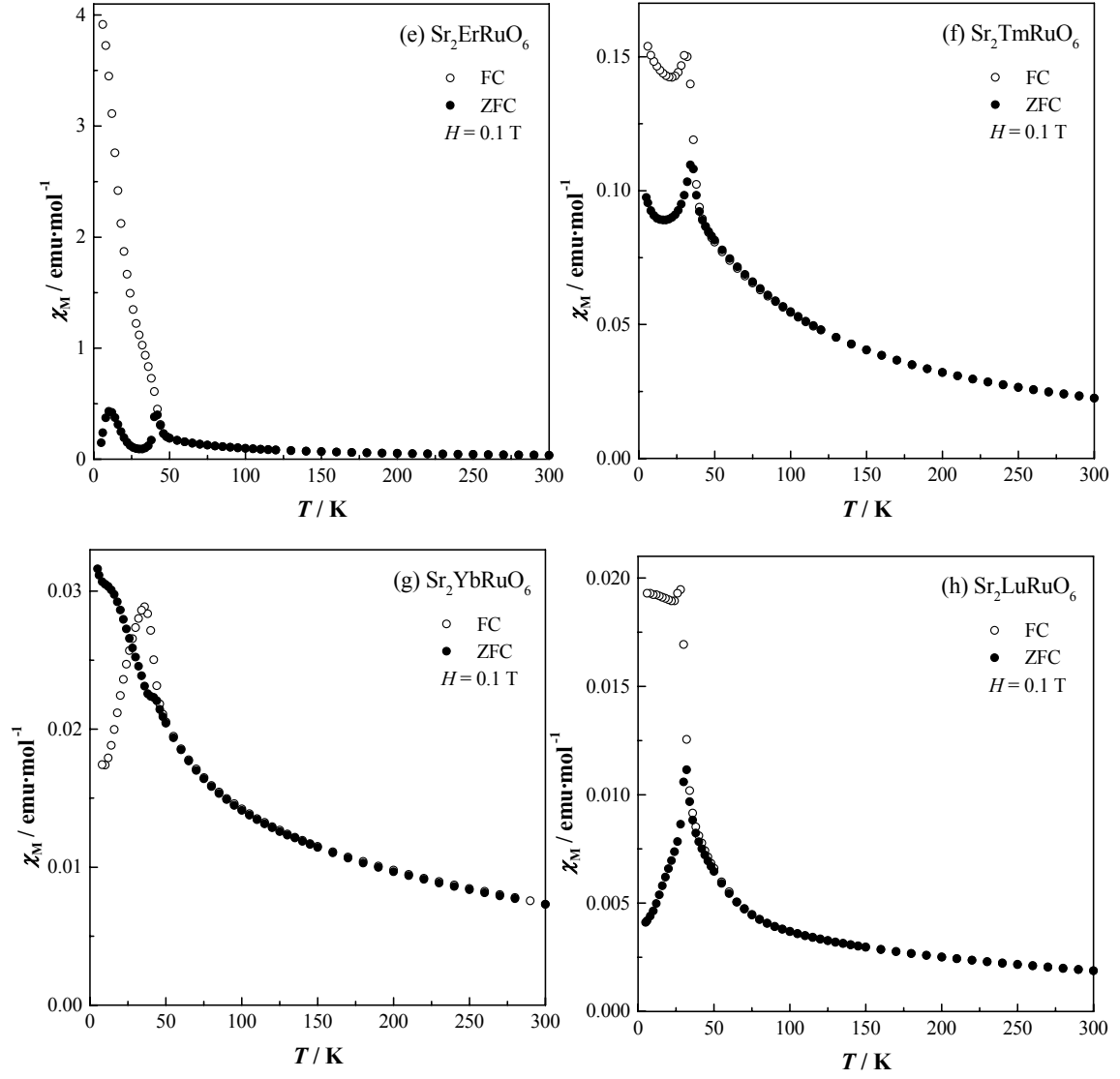


Figure 3.2.5 *continued*.

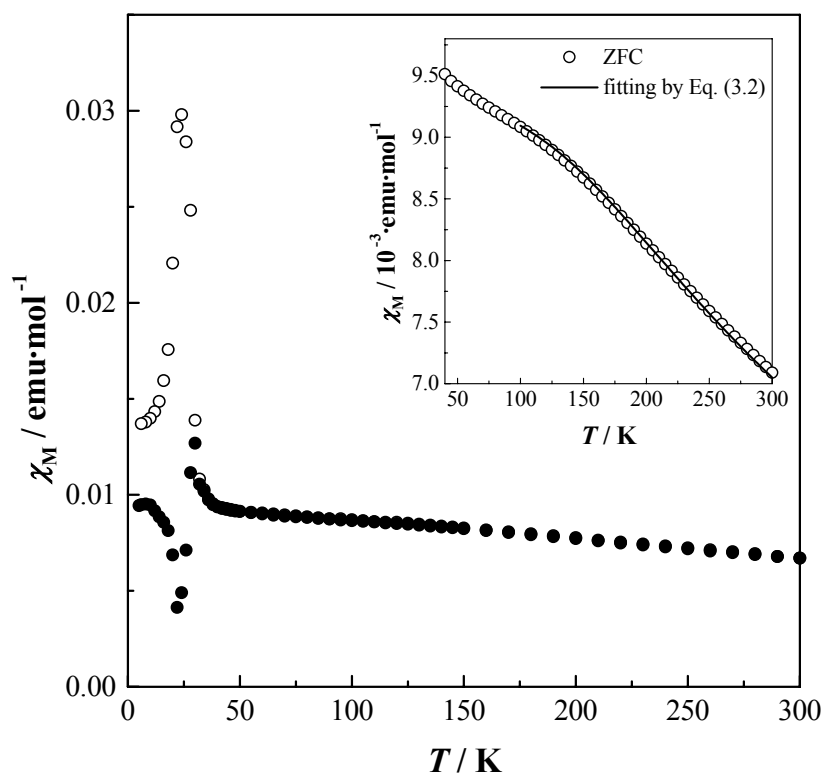


Figure 3.2.6 Temperature dependence of the ZFC (filled symbols) and FC (open symbols) molar magnetic susceptibilities for $\text{Sr}_2\text{EuRuO}_6$. The inset shows the susceptibility calculated by Eq. (3.2) (solid line).

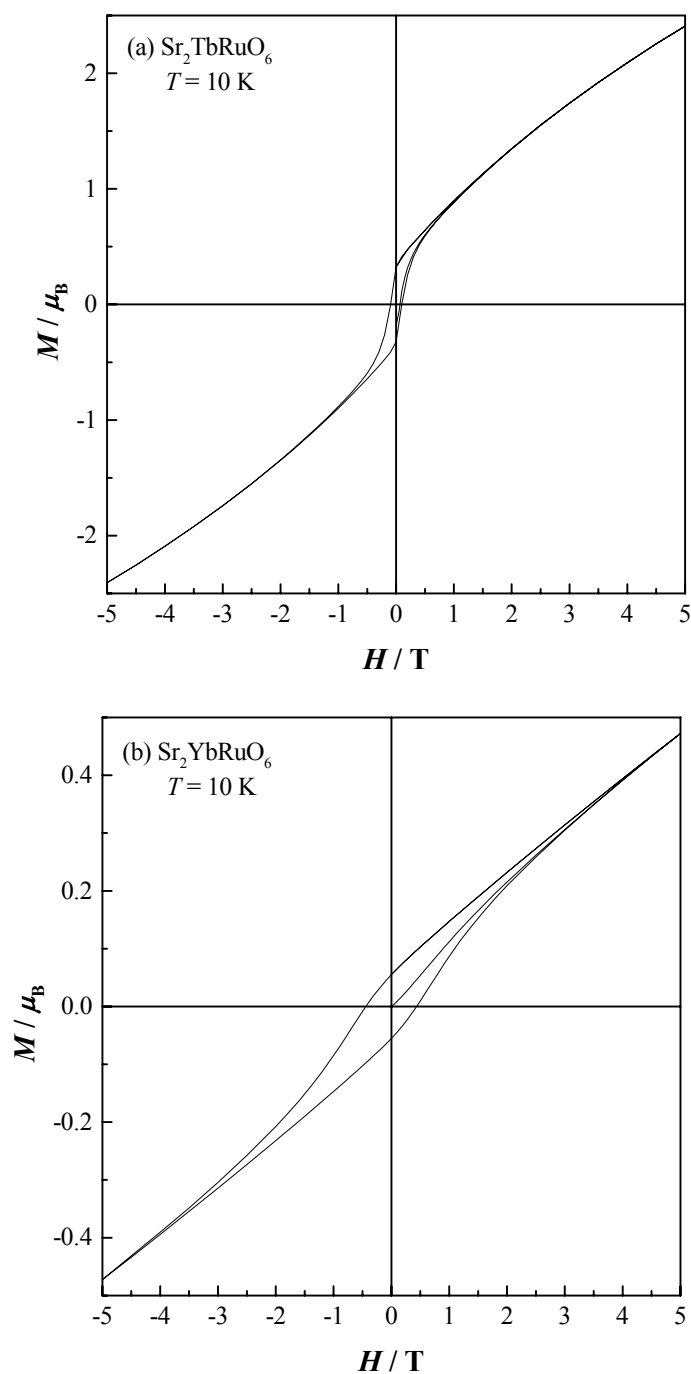


Figure 3.2.7 Variation of magnetization with the applied field at 10 K (a) for $\text{Sr}_2\text{TbRuO}_6$ and (b) for $\text{Sr}_2\text{YbRuO}_6$.

3.3 Magnetic and neutron diffraction study on ordered perovskite $\text{Sr}_2\text{HoRuO}_6$

3.3.1 Introduction

In section 3.2, the crystal structures and magnetic properties of the ordered perovskites $\text{Sr}_2\text{LnRuO}_6$ ($\text{Ln} = \text{Eu-Lu}$) were described. These compounds have the ordered perovskite-type structure and they become monoclinically distorted with an increase of ionic Ln^{3+} radius. These compounds showed a magnetic transition at 30–46 K and a complicated temperature dependence of magnetic susceptibilities below the transition temperatures. Furthermore, small magnetic hysteresis loops have been observed at low temperatures. In order to explain the complicated temperature dependence of the magnetic susceptibilities for $\text{Sr}_2\text{LnRuO}_6$ ($\text{Ln} = \text{Eu-Lu}$), the powder neutron diffraction, magnetic susceptibility and magnetization measurements were performed.

This section describes the crystal and magnetic structures and magnetic properties of $\text{Sr}_2\text{HoRuO}_6$ in detail. This compound shows two magnetic anomalies in the temperature dependence of the magnetic susceptibility (at ~20 and 36 K). In order to make clear the magnetic behavior of $\text{Sr}_2\text{HoRuO}_6$, the magnetic measurements were performed in each of the three temperature regions (below 20 K, 20–36 K and above 36 K).

3.3.2 Experimental

A polycrystalline sample of $\text{Sr}_2\text{HoRuO}_6$ was prepared by firing the appropriate amounts of SrCO_3 , Ho_2O_3 and RuO_2 , first at 1173 K for 12 h and then 1473 K for 60 h in air with interval regular grinding and pelleting. The progress of the reactions was monitored by powder X-ray diffraction measurements.

Powder neutron diffraction profiles were measured at 10 K, 25 K and room temperature using a high-resolution powder diffractometer (HRPD) [3.17] in the JRR-3M reactor (Japan Atomic Energy Research Institute), with a Ge (331)

monochromator ($\lambda = 1.8230 \text{ \AA}$) at both 10 and 25 K and with a Si (533) monochromator ($\lambda = 1.1624 \text{ \AA}$) at room temperature. The collimators used were 6'-20'-6', which were placed before and after the monochromator, and between the sample and each detector. The set of 64 detectors and collimators, which were placed every 2.5 degrees, rotate around the sample. Crystal and magnetic structures were determined by the Rietveld technique, using the program RIETAN98 β [3.13].

The field dependence of the magnetization was measured at 2, 5, 10, 15, 20, 25, 30, 40 and 100 K over the applied magnetic field range $-5 \text{ T} < H < 5 \text{ T}$, and the temperature dependence of the magnetic susceptibility was made in the applied field of 0.1 T over the temperature range 5–300 K, using a SQUID magnetometer (Quantum Design, MPMS5S). The magnetization (at 5 and 25 K) and all the susceptibility measurements were performed using both zero field cooling (ZFC) and field cooling (FC) conditions. Specific heat measurements were performed using relaxation technique with a commercial specific heat measuring system (Quantum Design, PPMS) in the temperature range 5–100 K.

3.3.3 Results and discussion

3.3.3.1 Crystal structure

It was ascertained that the $\text{Sr}_2\text{HoRuO}_6$ prepared in this study crystallized in a single phase by the X-ray diffraction measurement at room temperature. All the neutron diffraction data were analyzed by the Rietveld method. As a result of the structural refinement using data collected at room temperature, it was found that the crystal structure of $\text{Sr}_2\text{HoRuO}_6$ was a monoclinic perovskite of space group $P2_1/n$ (No. 14) with an ordered arrangement between Ru^{5+} and Ho^{3+} over the six-coordinate B sites. This unit cell is related to the primitive perovskite unit cell (a_p) by $a \approx \sqrt{2} a_p$, $b \approx \sqrt{2} a_p$, and $c \approx 2a_p$. The unit cell parameters were $a = 5.7710(3) \text{ \AA}$, $b = 5.7801(3) \text{ \AA}$, $c = 8.1640(4) \text{ \AA}$ and $\beta = 90.199(4)^\circ$ ($R_{wp} = 10.00 \%$, $R_l = 2.95 \%$, $R_F = 1.35 \%$, and $R_e = 7.30 \%$). The observed and calculated neutron diffraction profile is plotted in Fig. 3.3.1. The refined structural parameters and the bond lengths and angles, calculated from these

structural parameters, are listed in Tables 3.3.1 and 3.3.2, respectively.

3.3.3.2 Magnetic properties

The temperature dependence of the magnetic susceptibility and specific heat for $\text{Sr}_2\text{HoRuO}_6$ is shown in Fig. 3.3.2. It is found that the divergence in the magnetic susceptibilities between the FC and ZFC occurs at ~ 36 K and that the maximum of susceptibility appears at ~ 15 K (for FC) and ~ 20 K (for ZFC). The specific heat measurement also shows a λ -type anomaly at 36 K. We consider that the anomalies of magnetic susceptibility and specific heat at 36 K show an antiferromagnetic transition, and that the divergence in the magnetic susceptibility indicates the presence of a ferromagnetic moment or a spin glass transition. As will be described later, the possibility of the spin glass transition is denied from the results of magnetic hysteresis measurements. The fitting of the Curie-Weiss law to the temperature dependence of magnetic susceptibilities at higher temperatures ($T > 150$ K) gives an effective magnetic moment (μ_{eff}) and Weiss constant (θ) of $10.6 \mu_{\text{B}}$ and -20 K, respectively. Since the theoretical free-ion magnetic moments of Ru^{5+} and Ho^{3+} are $3.87 \mu_{\text{B}}$ and $10.58 \mu_{\text{B}}$, respectively, the observed effective magnetic moment (μ_{eff}) is lower than the expected value of $11.3 \mu_{\text{B}}$ [estimated from $(\mu_{\text{Ru}^{5+}}^2 + \mu_{\text{Ho}^{3+}}^2)^{1/2}$] which suggests that the magnetic ions in this compound are affected by the crystal field to some extent. The negative Weiss constant indicates that the predominant magnetic interaction in $\text{Sr}_2\text{HoRuO}_6$ is antiferromagnetic.

In order to study the origin of the divergence between FC and ZFC susceptibilities, the field dependence of the magnetization were measured at 2, 5, 10, 15, 20, 25, 30, 40 and 100 K, and the magnetization measurements under field-cooled condition were also performed at 5 and 25 K. The magnetic hysteresis curves (ZFC) measured at 10 and 25 K are shown in Fig. 3.3.3. The FC hysteresis curves agree entirely with the ZFC ones both at 10 and 25 K. This agreement indicates the absence of a spin glass phase. If the spin glass transition occurred, the FC magnetization should be larger than the ZFC magnetization because of freezing of the induced moment. In addition, a small magnetic

hysteresis loop at 5–30 K was observed, indicating the existence of a ferromagnetic moment in this $\text{Sr}_2\text{HoRuO}_6$. It is calculated to be 0.04–0.125 $\mu_{\text{B}}/\text{mol}$ at 5–30 K. For compounds with a low crystal symmetry such as monoclinic, a Dzyaloshinsky-Moriya (D-M) interaction can exist between the ordered elements, which results in the existence of a weak ferromagnetic moment associated with the antiferromagnetism. Metamagnetic behavior is found below 10 K (see Fig. 3.3.3(a)). This temperature is lower than the temperature at which another magnetic anomaly observed (15 K for FC; 20 K for ZFC).

3.3.3.3 Magnetic structure

Figure 3.3.4 shows the neutron diffraction profiles collected at 10 and 25 K. A number of low-angle peaks, which are not observed at room temperature, appear in these profiles and indicate the presence of an antiferromagnetic ordering. The author attempted to determine the magnetic structures by using the magnetic structural data of $\text{Sr}_2\text{ErRuO}_6$ [3.9], but this attempt failed. In that structural model, the magnetic moments were aligned along the a axis. The large (010) and (100) peaks ($2\theta \approx 18.2^\circ$) are observed in the profiles of $\text{Sr}_2\text{HoRuO}_6$ at 10 and 25 K, but the (001) peak ($2\theta \approx 12.8^\circ$) is not found. This fact indicates that the alignment of the magnetic moments of $\text{Sr}_2\text{HoRuO}_6$ is not in the a direction, but rather in the c direction. The magnetic structure of $\text{Sr}_2\text{HoRuO}_6$ determined is illustrated in Fig. 3.3.5. The refined structural parameters are listed in Table 3.3.3. In this magnetic structure, both the magnetic moments of Ho^{3+} and Ru^{5+} ions are ordered antiferromagnetically. Each of the ions orders in a type I arrangement. In the ab plane, the magnetic moments of Ho^{3+} and Ru^{5+} ions are coupled ferrimagnetically.

The only difference between 10 and 25 K data is in the intensity of the magnetic Bragg peaks, i.e., the peaks at 10 K are more intense than those at 25 K. The ordered magnetic moments are 2.74(9) μ_{B} for Ru^{5+} and 6.66(8) μ_{B} for Ho^{3+} at 10 K, and 2.19(10) μ_{B} for Ru^{5+} and 3.02(7) μ_{B} for Ho^{3+} at 25 K. This result is in accord with the tendency found for the ordered moments of $\text{Sr}_2\text{ErRuO}_6$ [3.9], i.e., the ordered magnetic moments of lanthanide ions increase with decreasing temperature and do not saturate

even at 4.2 K. The values of the ordered moments for Ru^{5+} are larger than those of other perovskite compounds containing Ru^{5+} [3, 6, 8, 9, 18, 19]. This may be attributable to the fact that the ordered magnetic moment of Ru^{5+} is estimated to be larger because of the similarity in the magnetic peak positions between Ru^{5+} and Ho^{3+} . Since the weak ferromagnetic components observed in the magnetization measurements are very small compared with the ordered magnetic moments of Ho^{3+} and Ru^{5+} ions, the magnitude of the moments cannot be estimated by this refinement of neutron diffraction profiles.

3.3.4 Summary

In this section, magnetic properties of the ordered perovskite $\text{Sr}_2\text{HoRuO}_6$ have been investigated in detail. The magnetic susceptibility and specific heat measurements show the existence of the magnetic transition at 36 K. Powder neutron diffraction measurements were performed at 10 K, 25 K, and room temperature. The neutron diffraction profile measured at 10 and 25 K and the resulting calculations indicate that there is a long range antiferromagnetic ordering involving both Ru^{5+} and Ho^{3+} . Each magnetic moment of these ions orders in a Type I arrangement and they are antiparallel with each other in the ab -plane. The direction of the magnetic moments is along the c axis. The ordered magnetic moments are $2.74(9) \mu_B$ for Ru^{5+} and $6.66(8) \mu_B$ for Ho^{3+} at 10 K, and $2.19(10) \mu_B$ for Ru^{5+} and $3.02(7) \mu_B$ for Ho^{3+} at 25 K.

Table 3.3.1 Crystallographic data for $\text{Sr}_2\text{HoRuO}_6$ at room temperature

Atom	Site	x	y	z	$B / \text{\AA}^2$
Sr	4e	0.0053(13)	0.0281(5)	0.2479(11)	0.79(4)
Ho	2d	1/2	0	0	0.13(5)
Ru	2c	1/2	0	1/2	0.48(6)
O(1)	4e	0.2663(11)	0.2966(13)	0.0357(9)	0.92(9)
O(2)	4e	0.2010(11)	-0.2280(12)	0.0354(8)	0.74(8)
O(3)	4e	-0.0642(11)	0.4852(10)	0.2334(8)	0.83(7)

Note. $a = 5.7710(3) \text{ \AA}$, $b = 5.7801(3) \text{ \AA}$, $c = 8.1640(4) \text{ \AA}$, $\beta = 90.200(3)^\circ$,
 $R_{\text{wp}} = 10.00 \%$, $R_{\text{I}} = 2.95 \%$, $R_{\text{F}} = 1.35 \%$, $R_{\text{e}} = 7.30 \%$.

Table 3.3.2 Bond lengths (\AA) and bond angles ($^\circ$) for $\text{Sr}_2\text{HoRuO}_6$ at room temperature

Ho–O(1)	2.201(6) $\times 2$	Ru–O(1)	1.956(6) $\times 2$
Ho–O(2)	2.191(7) $\times 2$	Ru–O(2)	1.974(7) $\times 2$
Ho–O(3)	2.208(6) $\times 2$	Ru–O(3)	1.944(6) $\times 2$
Sr–O(1)	2.576(10)	2.774(10)	2.911(11)
Sr–O(2)	2.547(11)	2.823(10)	2.843(10)
Sr–O(3)	2.563(9)	2.675(7)	
O(1)–Ho–O(2)	91.9(3)	O(1)–Ru–O(2)	90.2(4)
O(1)–Ho–O(3)	90.0(2)	O(1)–Ru–O(3)	91.2(4)
O(2)–Ho–O(3)	91.4(3)	O(2)–Ru–O(3)	90.3(3)

Table 3.3.3 Crystallographic data for $\text{Sr}_2\text{HoRuO}_6$ at 10 and 25 K

Atom	Site	x	y	z	$B / \text{\AA}^2$	μ / μ_{B}
10 K						
$a = 5.7628(2) \text{ \AA}$, $b = 5.7841(2) \text{ \AA}$, $c = 8.1468(3) \text{ \AA}$, $\beta = 90.244(2)^\circ$,						
$R_{\text{wp}} = 9.24 \%$, $R_{\text{I}} = 3.20 \%$, $R_{\text{F}} = 1.80 \%$, $R_{\text{e}} = 5.41 \%$.						
Sr	4e	0.0054(17)	0.0327(7)	0.2471(13)	0.20(8)	
Ho	2d	1/2	0	0	0.10(9)	6.66(8)
Ru	2c	1/2	0	1/2	0.58(13)	2.74(9)
O(1)	4e	0.2702(14)	0.3059(14)	0.0308(11)	0.35(15)	
O(2)	4e	0.1966(14)	-0.2250(14)	0.0384(9)	0.11(10)	
O(3)	4e	-0.0696(13)	0.4840(13)	0.2346(9)	0.35(15)	
25 K						
$a = 5.7618(2) \text{ \AA}$, $b = 5.7819(1) \text{ \AA}$, $c = 8.1507(2) \text{ \AA}$, $\beta = 90.247(2)^\circ$,						
$R_{\text{wp}} = 6.81 \%$, $R_{\text{I}} = 2.64 \%$, $R_{\text{F}} = 1.54 \%$, $R_{\text{e}} = 5.44 \%$.						
Sr	4e	0.0071(11)	0.0314(5)	0.2485(8)	0.31(6)	
Ho	2d	1/2	0	0	0.13(9)	3.02(7)
Ru	2c	1/2	0	1/2	0.33(9)	2.19(10)
O(1)	4e	0.2673(9)	0.3012(10)	0.0352(7)	0.45(13)	
O(2)	4e	0.1973(9)	-0.2267(10)	0.0375(7)	0.22(11)	
O(3)	4e	-0.0689(9)	0.4828(9)	0.2343(6)	0.38(10)	

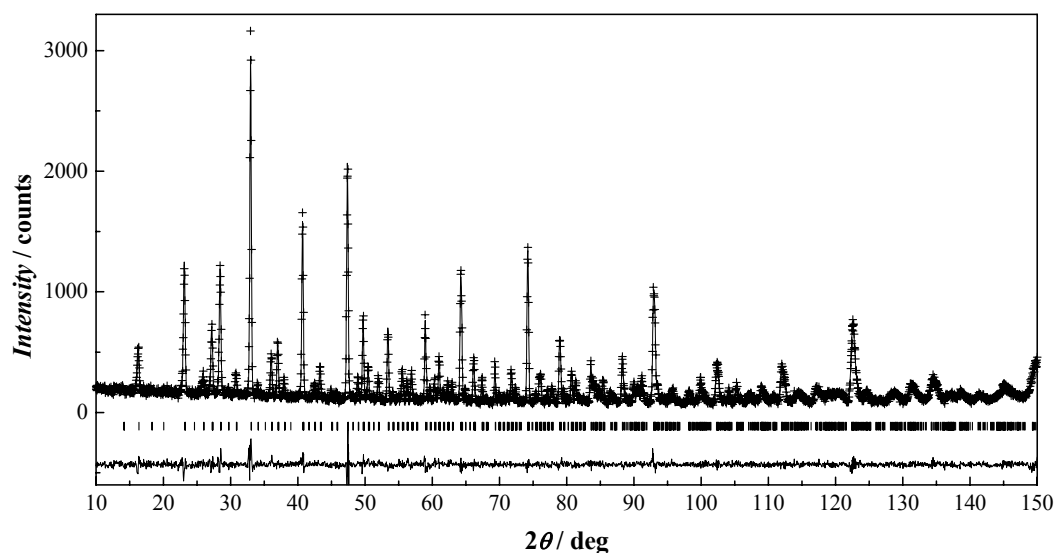


Figure 3.3.1 Powder neutron diffraction profiles for $\text{Sr}_2\text{HoRuO}_6$ at room temperature. The calculated and observed profiles are shown by the top solid line and cross markers, respectively. The vertical marks in the middle show positions calculated for Bragg reflections. The lower trace is a plot of the difference between the calculated and observed intensities.

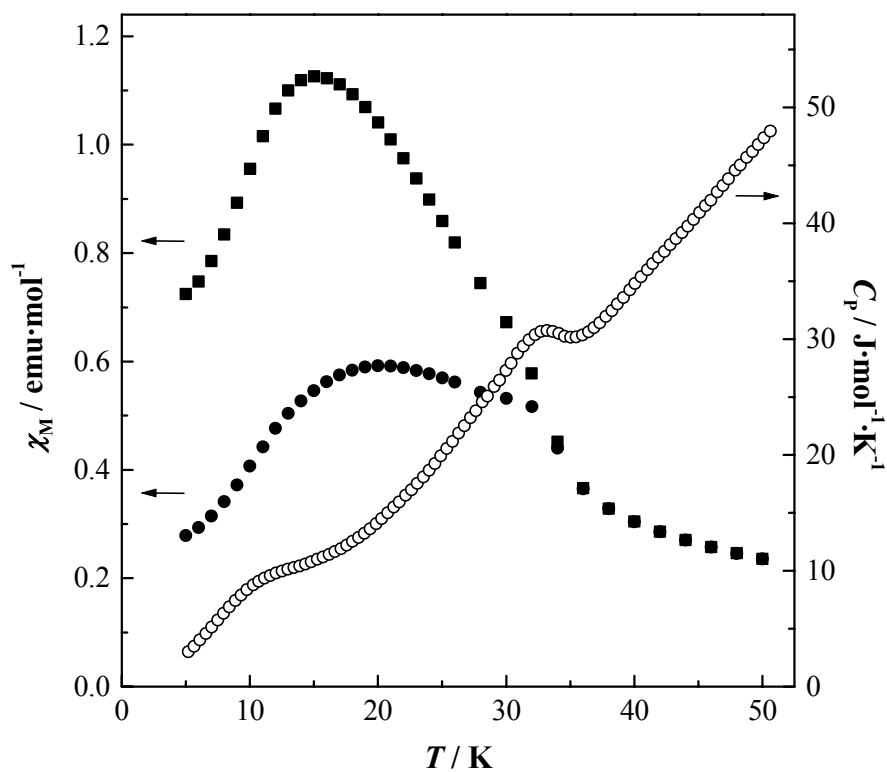


Figure 3.3.2 Temperature dependence of the specific heat (hollow circle) and the ZFC (filled circle) and FC (filled square) magnetic susceptibilities for $\text{Sr}_2\text{HoRuO}_6$.

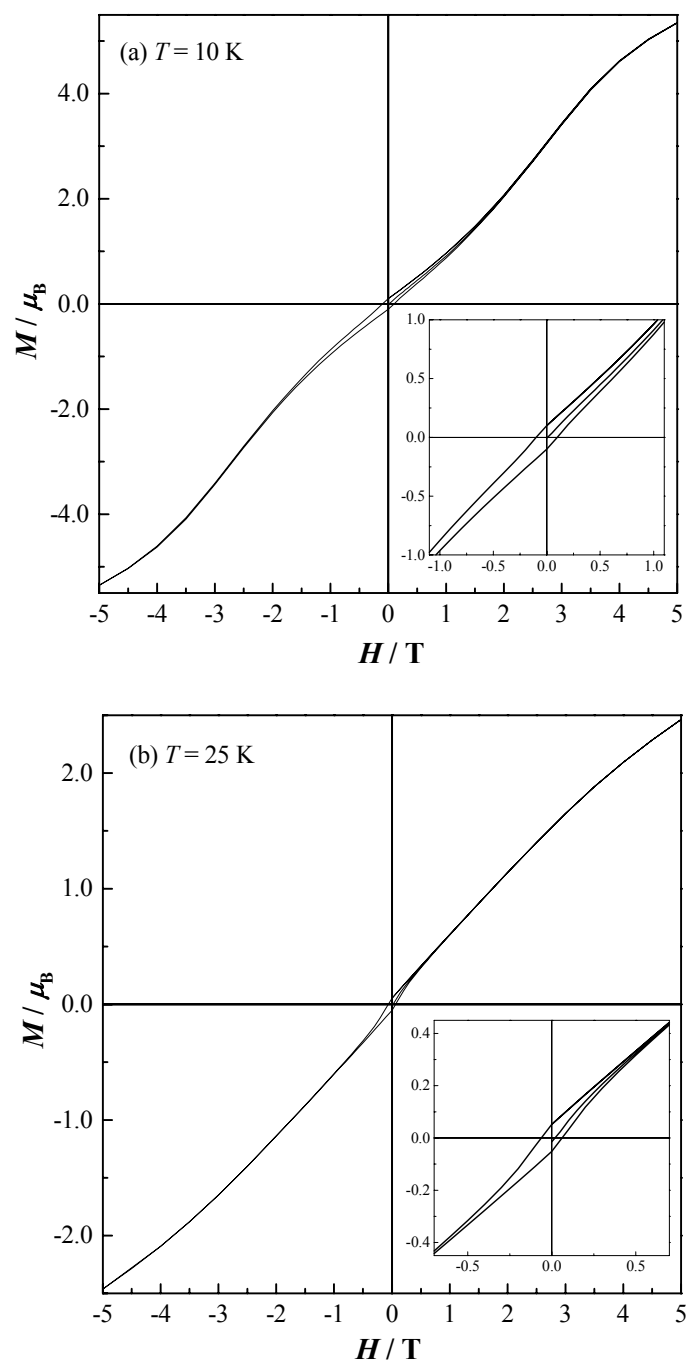


Figure 3.3.3 Field dependence of the ZFC magnetization at 10 K (a) and at 25 K (b).

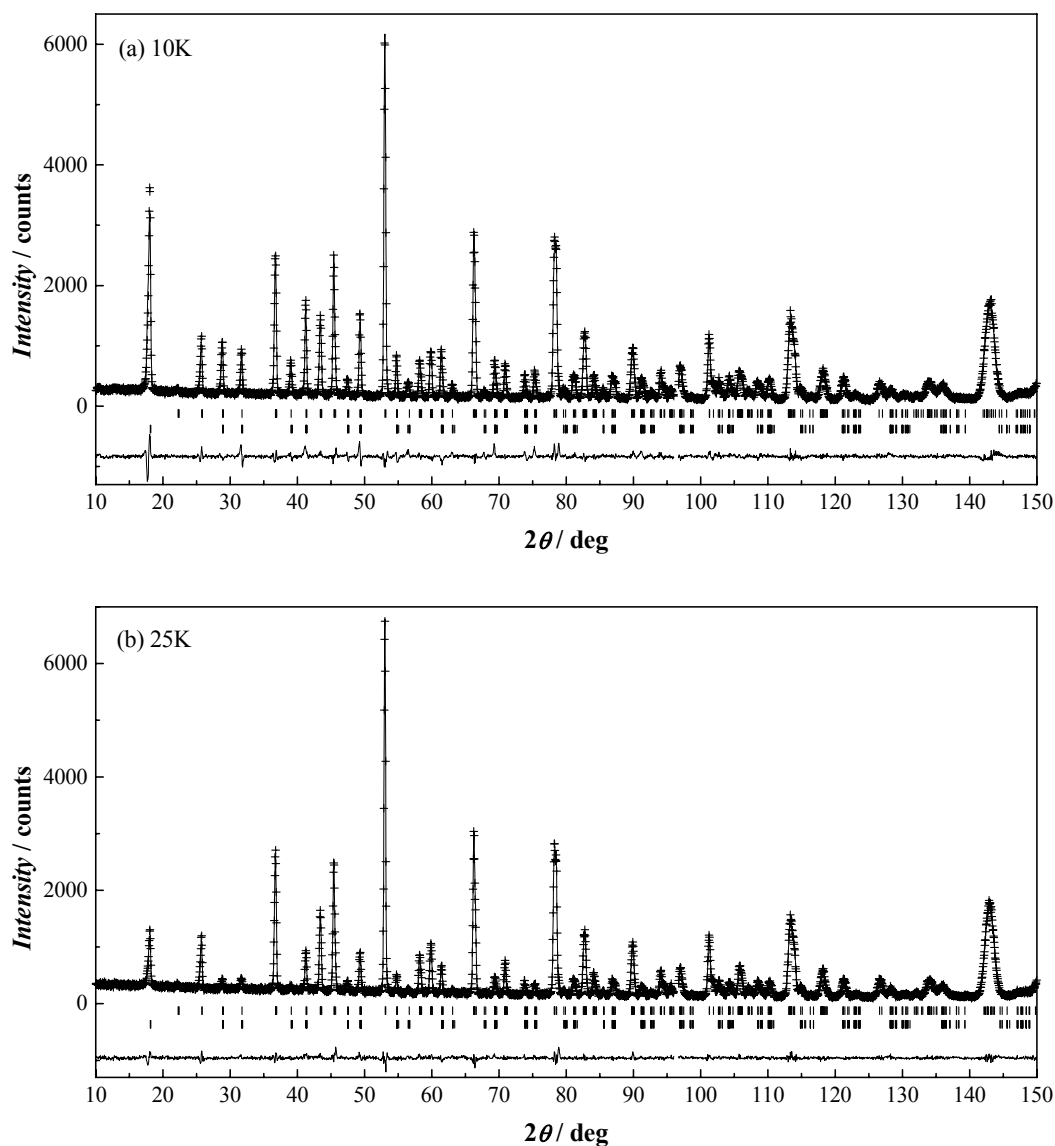


Figure 3.3.4 Powder neutron diffraction profiles for $\text{Sr}_2\text{HoRuO}_6$ at 10 K (a) and 25 K (b). The calculated and observed profiles are shown by the top solid line and cross markers, respectively. The nuclear reflection positions are shown as upper vertical marks and magnetic ones by lower vertical marks. The lower trace is a plot of the difference between the calculated and observed intensities.

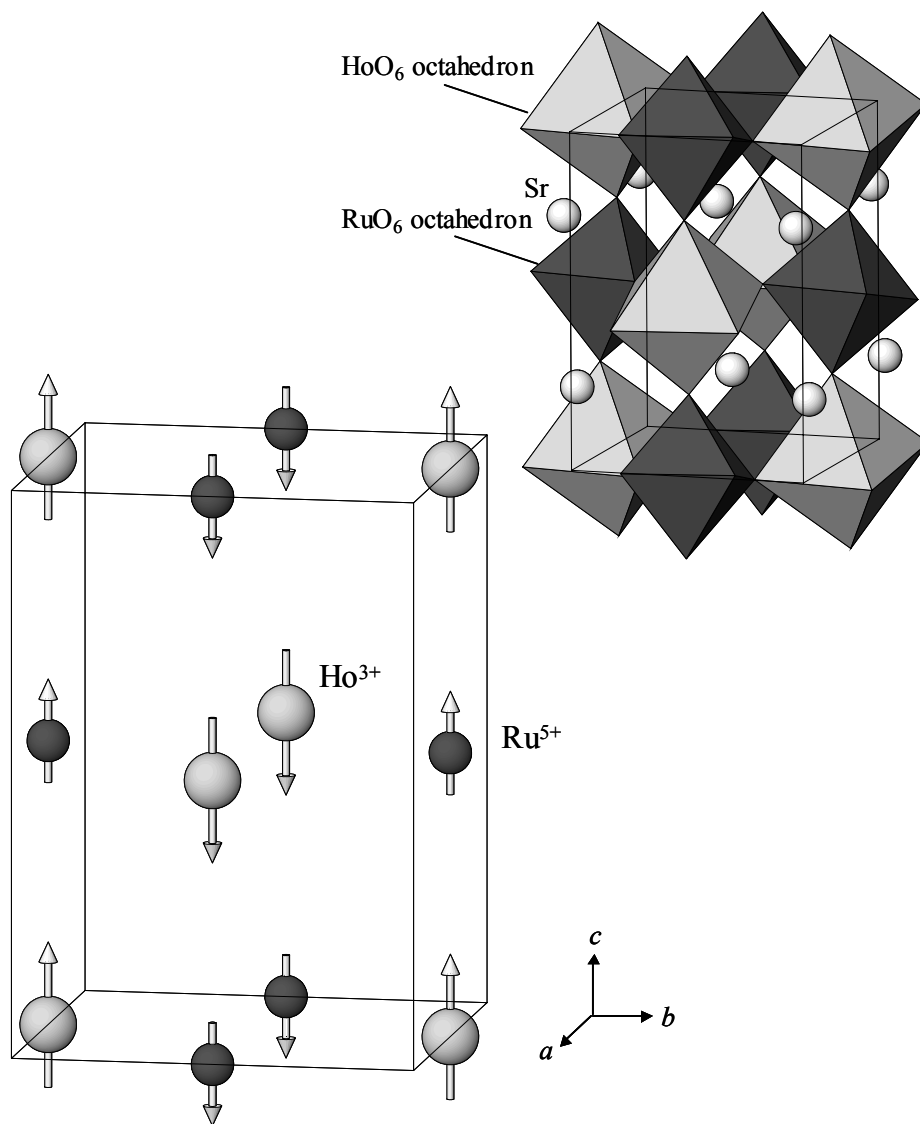


Figure 3.3.5 The crystal structure (right top) and magnetic structure (left bottom) of $\text{Sr}_2\text{HoRuO}_6$ at 10 K. The arrows indicate the directions of the magnetic moments.

3.4 Magnetic properties and crystal structures of ordered perovskites $\text{Sr}_2\text{TbRu}_{1-x}\text{Ir}_x\text{O}_6$

3.4.1 Introduction

In section 3.2, the crystal structures and magnetic properties of the ordered perovskites $\text{Sr}_2\text{LnRuO}_6$ ($\text{Ln} = \text{Eu-Lu}$) were described. These compounds have the ordered perovskite-type structure and they become monoclinically distorted with an increase of ionic Ln^{3+} radius. These compounds showed a magnetic transition at 30–46 K and a complicated temperature dependence of magnetic susceptibilities below the transition temperatures. Furthermore, small magnetic hysteresis loops have been observed at low temperatures. In order to explain the complicated temperature dependence of the magnetic susceptibilities for $\text{Sr}_2\text{LnRuO}_6$ ($\text{Ln} = \text{Eu-Lu}$), the powder neutron diffraction, magnetic susceptibility and magnetization measurements were performed.

In this section, the study on the crystal and magnetic structures and magnetic properties of $\text{Sr}_2\text{TbRuO}_6$ using powder neutron diffraction, magnetic susceptibility and specific heat measurements are described. In addition, the author will also discuss the crystal structures and magnetic properties of a solid solution of $\text{Sr}_2\text{TbRu}_{1-x}\text{Ir}_x\text{O}_6$ ($x = 0.0-1.0$). A series of ordered perovskites $\text{Sr}_2\text{LnIrO}_6$ containing both iridium and lanthanides ($\text{Ln} = \text{Ce, Sm-Lu}$) have similar crystal structures to that of $\text{Sr}_2\text{LnRuO}_6$. Among them, $\text{Sr}_2\text{TbIrO}_6$ has an ordered arrangement between Tb^{4+} and Ir^{4+} ions and shows two magnetic transitions at 27 and 51 K [3.20, 21]. Therefore, it is interesting to synthesize solid solutions between $\text{Sr}_2\text{Tb}^{3+}\text{Ru}^{5+}\text{O}_6$ and $\text{Sr}_2\text{Tb}^{4+}\text{Ir}^{4+}\text{O}_6$ in which the charge configurations of B site ions are different from each other, and to study the variation of the valence state of the B site ions with compositions and their magnetic properties.

3.4.2 Experimental

Polycrystalline samples of $\text{Sr}_2\text{TbRu}_{1-x}\text{Ir}_x\text{O}_6$ ($x = 0.0, 0.1, \dots 0.8, 0.85, 0.9, 0.95$ and

1.0) were prepared by firing the appropriate amounts of SrCO_3 , Tb_4O_7 , RuO_2 and Ir (metal) first at 1173 K for 12 h and then 1473 K for 60 h in air with intermediate regular grinding and pelleting. In addition, the specimens with $x = 0.8\text{--}0.95$ were also prepared by heating up to 1573 K for 48 h. The progress of the reactions was monitored by powder X-ray diffraction measurements.

Powder neutron diffraction profiles were measured at 10 K and room temperature for $\text{Sr}_2\text{TbRuO}_6$ using a high-resolution powder diffractometer (HRPD) [3.17] in the JRR-3M reactor (Japan Atomic Energy Research Institute), with a Ge (331) monochromator ($\lambda = 1.8230 \text{ \AA}$). The collimators used were 6'-20'-6', which were placed before and after the monochromator, and between the sample and each detector. The set of 64 detectors and collimators, which were placed every 2.5 degrees, rotate around the sample. Crystal and magnetic structures were determined by the Rietveld technique, using the program RIETAN97 β [3.13].

The field-dependence of the magnetization for $\text{Sr}_2\text{TbRuO}_6$ was measured at 10, 15, 20, 25, 38 and 100 K over the applied magnetic field range $-5 \text{ T} < H < 5 \text{ T}$, and the temperature-dependence of the DC magnetic susceptibility was recorded in an applied field of 0.1 T over the temperature range 5–300 K, using a SQUID magnetometer (Quantum Design, MPMS5S). The susceptibility measurements and the magnetization were performed under two sets of conditions, i.e., after zero field cooling (ZFC) and after field cooling (FC).

Specific heat measurements for $\text{Sr}_2\text{TbRuO}_6$ were performed using a relaxation technique by a commercial heat capacity measuring system (Quantum Design, PPMS) in the temperature range 2–100 K. The sample in the form of a pellet was mounted on a thin alumina plate with apiezon (N grease) for better thermal contact.

3.4.3 Results and discussion

3.4.3.1 Crystal structure of $\text{Sr}_2\text{TbRu}_{1-x}\text{Ir}_x\text{O}_6$

Almost all the reaction products $\text{Sr}_2\text{TbRu}_{1-x}\text{Ir}_x\text{O}_6$ were finally formed in a single phase with a perovskite-type structure. However, some samples which have

composition of $x = 0.8$ (prepared both at 1473 K and at 1573 K) and $x = 0.85\text{--}0.90$ (prepared at 1473 K) were obtained as two kinds of perovskite phases. Their X-ray diffraction patterns were indexed on a monoclinic unit cell (space group $P2_1/n$), and their structural analyses using the Rietveld method show that the Ln and Ru/Ir ions are arranged in an alternating manner.

Figure 3.4.1 shows the variation of lattice parameters for $\text{Sr}_2\text{TbRu}_{1-x}\text{Ir}_x\text{O}_6$ with the x value. It is found that the lattice parameters for the compounds with $x = 0.0\text{--}0.7$ are obviously larger than those for the compounds with $x = 0.85\text{--}1.0$, and that the order of the magnitude of a and b is different between these two sets of compounds, i.e., $a < b$ in the former compounds, and $a > b$ in the latter compounds. The average ionic radius of the B site ions is calculated to be ~ 0.74 Å for the case of Tb^{3+} and $\text{Ru}^{5+}/\text{Ir}^{5+}$, and it is ~ 0.69 Å for the case of Tb^{4+} and $\text{Ru}^{4+}/\text{Ir}^{4+}$. These results indicate that the compounds with $x = 0.0\text{--}0.7$ have an ordered arrangement between Tb^{3+} and $\text{Ru}^{5+}/\text{Ir}^{5+}$ and those with $x = 0.85\text{--}1.0$ have an ordered arrangement between Tb^{4+} and $\text{Ru}^{4+}/\text{Ir}^{4+}$ at B sites [3.20].

The diffraction pattern of a sample with $x = 0.8$ which was prepared by heating at 1473 K for 60 h shows the presence of two phases. They are $\text{Sr}_2\text{Tb}^{3+}(\text{Ru}_{1-x}\text{Ir}_x)^{5+}\text{O}_6$ and $\text{Sr}_2\text{Tb}^{4+}(\text{Ru}_{1-x}\text{Ir}_x)^{4+}\text{O}_6$. The ratio of these two phases could be estimated to be 59 : 41 from the Rietveld analysis. Heating at higher temperatures increases the ratio of the formation of the $\text{Sr}_2\text{Tb}^{3+}(\text{Ru}_{1-x}\text{Ir}_x)^{5+}\text{O}_6$ phase (to more than 90 %), but it could not be obtained as a single phase.

These results indicate that $\text{Sr}_2\text{TbRuO}_6$ and $\text{Sr}_2\text{TbIrO}_6$ do not form a complete solid solution. The borderline between these two phases is in the neighborhood of $x = 0.8$ for $\text{Sr}_2\text{TbRu}_{1-x}\text{Ir}_x\text{O}_6$, but this x value may be shifted to some extent by the heating conditions.

For the later magnetic measurements, the samples of $x = 0.0\text{--}0.7$, 1.0 (prepared by heating at 1473 K) and $x = 0.8\text{--}0.95$ (prepared by heating at 1573 K) were used.

3.4.3.2 Magnetic properties of $\text{Sr}_2\text{TbRuO}_6$ and $\text{Sr}_2\text{TbRu}_{1-x}\text{Ir}_x\text{O}_6$

The magnetic susceptibilities and specific heat of $\text{Sr}_2\text{TbRuO}_6$ are plotted as a function of temperature in Fig. 3.4.2. The magnetic susceptibility data show that a magnetic transition occurs at 41 K, and a rapid increase of the magnetic moment ($\sim 0.27 \mu_B$) is observed with decreasing temperature from 41 K to 32 K. The specific heat also shows a λ -type anomaly at 41 K. The field dependence of the magnetization at 25 and 36 K is plotted in Fig. 3.4.3. Magnetization measurements at 36 K show the existence of a small hysteresis, and the remnant magnetization is estimated to be about $0.15 \mu_B$ from the magnetic hysteresis curve. These results indicate that the magnetic transition observed at 41 K is an antiferromagnetic transition rather than a ferromagnetic one, and that the small remnant magnetization and the divergence between the FC and ZFC susceptibilities is derived from the weak ferromagnetic moment associated with this antiferromagnetism.

In addition, another broad peak may be observed at ~ 32 K in the specific heat vs. temperature curve. An anomaly of the magnetic susceptibility was also observed at ~ 31 K. However, the magnetic hysteresis curves measured at 25 and 36 K (Fig. 3.4.3) are very similar except for the difference in the remnant magnetization ($0.26 \mu_B$ at 25 K and $0.15 \mu_B$ at 36 K). This magnetic transition may be a reorientation of the magnetic moments [3.22].

Figure 3.4.4 shows the temperature dependence of the magnetic susceptibilities for $\text{Sr}_2\text{TbRu}_{1-x}\text{Ir}_x\text{O}_6$. The fitting of the Curie-Weiss law to the temperature-dependence of magnetic susceptibilities at higher temperatures ($T > 100$ K) gives the effective magnetic moment (μ_{eff}) and Weiss constant (θ), which are plotted as a function of x value in Fig. 3.4.5. The effective magnetic moments are $\sim 9.2 \mu_B$ for $x = 0.0$ – 0.7 and $\sim 8.0 \mu_B$ for $x = 0.85$ – 1.0 . This fact can be explained by the difference in the oxidation state of terbium ion in the solid solutions, i.e., the terbium ion is in the trivalent state ($9.72 \mu_B$) in the former solid solutions and that is in the tetravalent state ($7.94 \mu_B$) in the latter solid solutions. The results that the magnitudes of magnetic susceptibilities for $\text{Sr}_2\text{Tb}^{3+}(\text{Ru}_{1-x}\text{Ir}_x)^{5+}\text{O}_6$ ($x = 0.0$ – 0.7 , Fig. 3.4.4(a)) are much larger than those for

$\text{Sr}_2\text{Tb}^{4+}(\text{Ru}_{1-x}\text{Ir}_x)^{4+}\text{O}_6$ ($x = 0.85\text{--}1.0$, Fig. 3.4.4(b)) can be explained by the same reason, that is, these results are consistent with the valence configuration in the $\text{Sr}_2\text{TbRu}_{1-x}\text{Ir}_x\text{O}_6$ derived from the crystallographic data.

It is found that as the x value increases (i.e., the proportion of Ir increases), the magnetic transition temperature of $\text{Sr}_2\text{Tb}^{3+}(\text{Ru}_{1-x}\text{Ir}_x)^{5+}\text{O}_6$ decreases (see Fig. 3.4.4(a)). Many experimental results indicate that the magnetic interactions between the Ir^{5+} ([Xe]4f¹⁴5d⁴ electronic structure) ions are weaker than those between the Ru^{5+} ([Kr]4d³) ions. For example, the ordered perovskites $\text{Sr}_2\text{Ln}^{3+}\text{Ru}^{5+}\text{O}_6$ (Ln = Eu–Lu) show the magnetic transitions at low temperatures (30–46 K), while the ordered perovskites $\text{Sr}_2\text{Ln}^{3+}\text{Ir}^{5+}\text{O}_6$ (Ln = Sm–Gd, Dy–Lu) do not show any magnetic transition down to 5 K [3.20]. Hence, the decrease in the transition temperature with the increase of the x value would be due to the decreasing proportion of the Ru^{5+} ions.

On the other hand, the magnetic transition temperature for the $\text{Sr}_2\text{Tb}^{4+}(\text{Ru}_{1-x}\text{Ir}_x)^{4+}\text{O}_6$ ($x = 0.85\text{--}1.0$, Fig. 3.4.4(b)) increases with the x value. This can be explained by taking account of the fact that the Ru^{4+} ion has a similar electronic configuration (4d⁴) to that for the Ir^{5+} (5d⁴) ion, i.e., the magnetic exchange interaction between Ru^{4+} ions should be weak. The increase in the magnetic transition temperature with x is due to the increase in the proportion of Ir^{4+} ions (5d⁵) having strong interactions.

3.4.3.3 Neutron diffraction measurements for $\text{Sr}_2\text{TbRuO}_6$

It was ascertained, by the X-ray diffraction measurement at room temperature, that $\text{Sr}_2\text{TbRuO}_6$ crystallized in a single phase. The author carried out neutron diffraction measurements both at room temperature and at 10 K. Rietveld analysis of the data collected at room temperature indicated that the crystal structure of $\text{Sr}_2\text{TbRuO}_6$ is a monoclinic perovskite with the space group $P2_1/n$ (No.14) and has an ordered arrangement between Tb^{3+} and Ru^{5+} ions over the six-coordinate B sites. The unit cell parameters are $a = 5.7932(2)$ Å, $b = 5.8107(1)$ Å, $c = 8.2011(3)$ Å and $\beta = 90.249(2)^\circ$ ($R_{\text{wp}} = 6.26$ %, $R_{\text{I}} = 1.96$ %, $R_{\text{F}} = 1.39$ %, and $R_{\text{e}} = 5.54$ %). This result is consistent

with that of the previous X-ray diffraction measurements in section 3.2. The observed and calculated neutron diffraction profiles are shown in Fig. 3.4.6(a). The refined structural parameters, and the bond lengths and bond angles are listed in Tables 3.4.1 and 3.4.2, respectively.

Figure 3.4.6(b) shows the neutron diffraction profile measured at 10 K. A number of low angle peaks, which are not observed at room temperature, appear in this profile. This fact indicates the presence of antiferromagnetic ordering. The positions of these magnetic reflection peaks very closely resemble those for $\text{Sr}_2\text{HoRuO}_6$ measured at 10 K (section 3.3) except for the difference in the intensity of the (001) peak ($2\theta \approx 12.8^\circ$). In the case of $\text{Sr}_2\text{HoRuO}_6$, this magnetic peak was negligibly weak, indicating that the alignment of the magnetic moments was parallel to the c direction. On the other hand, the corresponding (001) peak observed for the present $\text{Sr}_2\text{TbRuO}_6$ has a significant intensity. The magnetic structure of $\text{Sr}_2\text{TbRuO}_6$ was refined using a model in which $\text{Sr}_2\text{TbRuO}_6$ has the same magnetic structure as $\text{Sr}_2\text{HoRuO}_6$ and that the alignment of the magnetic moments cants from the c axis to some extent. In this refinement, all the magnetic moments are assumed to be collinear.

Very good agreement between the observed and calculated intensities was obtained. The refined structural parameters are listed in Table 3.4.1. The observed and calculated neutron diffraction profiles are shown in Fig. 3.4.6(b). The crystal structure at 10 K is similar to that at room temperature, and the monoclinic distortion is a little larger than that at room temperature. The magnetic structure of $\text{Sr}_2\text{TbRuO}_6$ is illustrated in Fig.3.4.7. In this magnetic structure, the magnetic moments of both Tb^{3+} and Ru^{5+} ions are ordered antiferromagnetically. Each of these orders in a Type I arrangement. The gradient of the magnetic moments against the c axis is about 20° , but the exact direction of them could not be determined. The ordered magnetic moments are $2.99(11) \mu_B$ (for Ru^{5+}) and $4.98(12) \mu_B$ (for Tb^{3+}). The ordered moment for the Tb^{3+} is much smaller than the value of gJ ($9 \mu_B$). This may be explained by the following reason. The magnetic moments of Tb^{3+} ions do not saturate at 10 K. This tendency has been experimentally found for the $\text{Sr}_2\text{HoRuO}_6$ ($6.68 \mu_B$ at 10 K) and $\text{Sr}_2\text{ErRuO}_6$ ($4.59 \mu_B$ at 4.2 K) [3.9].

3.4.4 Summary

In this section, magnetic properties of the ordered perovskite $\text{Sr}_2\text{TbRuO}_6$ have been investigated in detail. The magnetic susceptibility and specific heat measurements show the existence of the magnetic transition at 41 K. Powder neutron diffraction measurements were performed at 10 K and room temperature. The neutron diffraction profile measured at 10 K and the resulting calculations indicate that there is a long range antiferromagnetic ordering involving both Ru^{5+} and Tb^{3+} . Each magnetic moment of these ions orders in a Type I arrangement and they are antiparallel with each other in the ab -plane. The direction of the magnetic moments cant by about 20° against the c axis. The ordered magnetic moments at 10 K are $2.99(11) \mu_B$ for Ru^{5+} and $4.98(12) \mu_B$ for Tb^{3+} .

The magnetic properties of $\text{Sr}_2\text{TbRu}_{1-x}\text{Ir}_x\text{O}_6$ ($0 \leq x \leq 1$) have been also studied. The structural data and the value of the effective magnetic moment indicate that these compounds adopt the valence configuration of $\text{Sr}_2\text{Tb}^{3+}(\text{Ru}_{1-x}\text{Ir}_x)^{5+}\text{O}_6$ ($x = 0.0\text{--}0.7$) or $\text{Sr}_2\text{Tb}^{4+}(\text{Ru}_{1-x}\text{Ir}_x)^{4+}\text{O}_6$ ($x = 0.85\text{--}1.0$). Evidence for the presence of a mixed valence state was not found. The magnetic transition temperature for $\text{Sr}_2\text{Tb}^{3+}(\text{Ru}_{1-x}\text{Ir}_x)^{5+}\text{O}_6$ decreases with increasing x . On the other hand, that for $\text{Sr}_2\text{Tb}^{4+}(\text{Ru}_{1-x}\text{Ir}_x)^{4+}\text{O}_6$ increases with x .

Table 3.4.1 Crystallographic data for $\text{Sr}_2\text{TbRuO}_6$ at 10 K and room temperature

Atom	Site	x	y	z	$B / \text{\AA}^2$	μ / μ_B
room temperature						
$a = 5.7932(2) \text{ \AA}$, $b = 5.8107(1) \text{ \AA}$, $c = 8.2011(3) \text{ \AA}$, $\beta = 90.249(2)^\circ$						
$R_{\text{wp}} = 6.26 \%$, $R_{\text{I}} = 1.96 \%$, $R_{\text{F}} = 1.39 \%$, $R_{\text{e}} = 5.54 \%$.						
Sr	4e	0.0071(11)	0.0291(5)	0.2488(8)	0.8(1)	
Tb	2d	1/2	0	0	0.3(1)	
Ru	2c	1/2	0	1/2	0.3(1)	
O(1)	4e	0.2683(8)	0.2988(9)	0.0360(7)	0.5(1)	
O(2)	4e	0.1967(9)	-0.2301(9)	0.0387(6)	0.8(1)	
O(3)	4e	-0.0696(8)	0.4847(8)	0.2332(6)	0.9(1)	
10 K						
$a = 5.7805(2) \text{ \AA}$, $b = 5.8072(1) \text{ \AA}$, $c = 8.1853(3) \text{ \AA}$, $\beta = 90.314(2)^\circ$						
$R_{\text{wp}} = 7.02 \%$, $R_{\text{I}} = 2.65 \%$, $R_{\text{F}} = 1.52 \%$, $R_{\text{e}} = 5.38 \%$.						
Sr	4e	0.0058(10)	0.0330(5)	0.2494(7)	0.4(1)	
Tb	2d	1/2	0	0	0.2(1)	4.98(12)
Ru	2c	1/2	0	1/2	0.4(1)	2.99(11)
O(1)	4e	0.2697(8)	0.3027(9)	0.0374(7)	0.5(1)	
O(2)	4e	0.1939(8)	-0.2270(9)	0.0397(6)	0.2(1)	
O(3)	4e	-0.0714(8)	0.4824(8)	0.2319(6)	0.4(1)	

Table 3.4.2 Bond lengths (\AA) and bond angles ($^\circ$) for $\text{Sr}_2\text{TbRuO}_6$ at room temperature

Tb-O(1)	$2.215(5) \times 2$	Ru-O(1)	$1.966(5) \times 2$
Tb-O(2)	$2.225(5) \times 2$	Ru-O(2)	$1.964(5) \times 2$
Tb-O(3)	$2.232(5) \times 2$	Ru-O(3)	$1.958(5) \times 2$
.....			
Sr-O(1)	2.565(8)	2.796(7)	2.913(7)
Sr-O(2)	2.542(8)	2.813(8)	2.880(8)
Sr-O(3)	2.552(7)	2.688(6)	
.....			
O(1)-Tb-O(2)	91.6(2)	O(1)-Ru-O(2)	90.4(3)
O(1)-Tb-O(3)	90.4(2)	O(1)-Ru-O(3)	90.4(3)
O(2)-Tb-O(3)	91.4(2)	O(2)-Ru-O(3)	90.0(2)

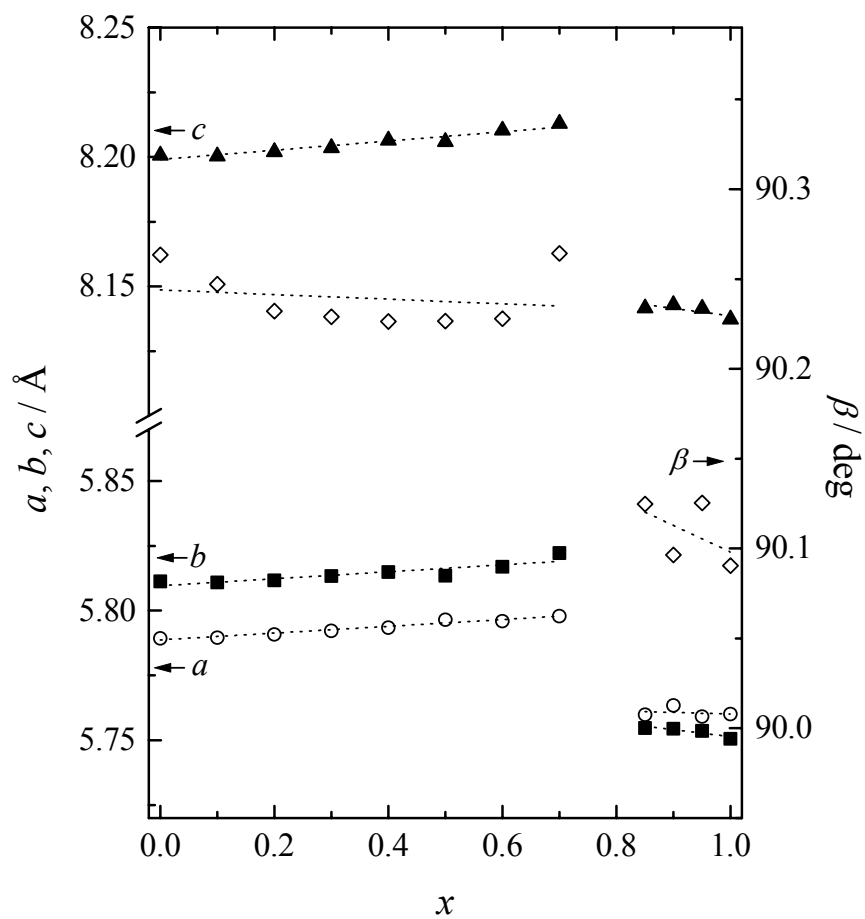


Figure 3.4.1 Variation of lattice parameters for $Sr_2TbRu_{1-x}Ir_xO_6$ with x value.

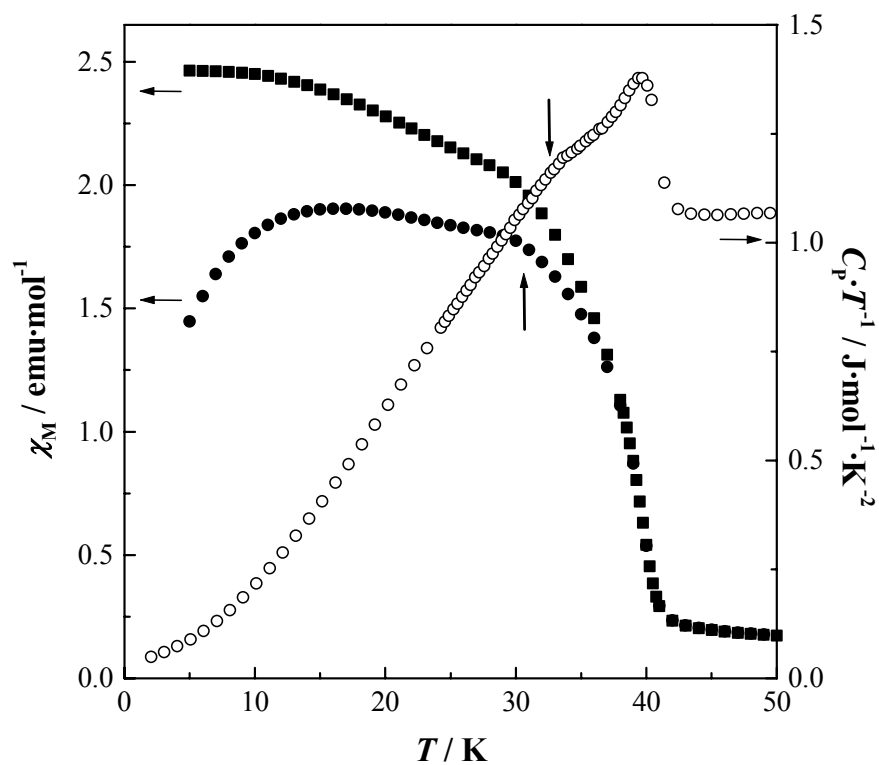


Figure 3.4.2 Temperature dependence of the specific heat deviated by temperature (○) and the ZFC (●) and FC (■) magnetic susceptibilities for $\text{Sr}_2\text{HoRuO}_6$. Two vertical arrows at 32 K and 31 K show specific heat and magnetic susceptibility anomalies, respectively.

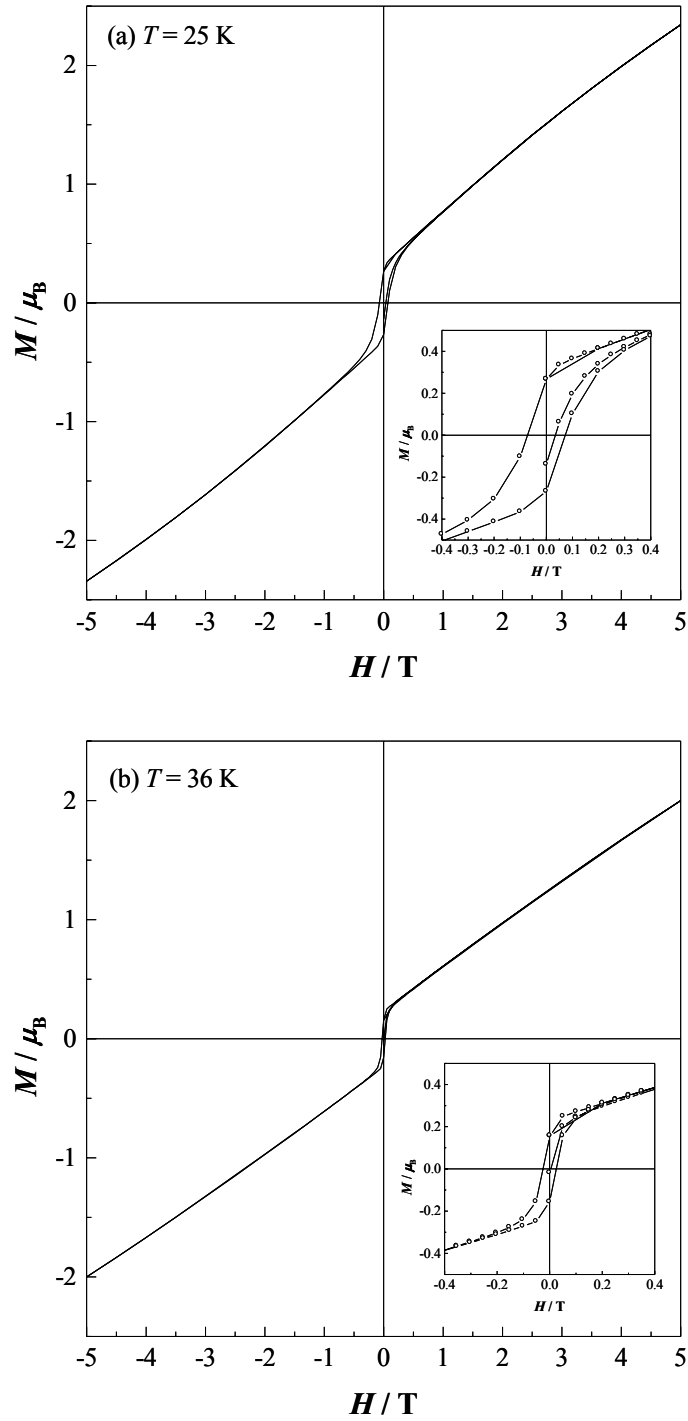


Figure 3.4.3 Variation of magnetization with the applied field for $\text{Sr}_2\text{TbRuO}_6$ (a) at 25 K and (b) at 36 K.

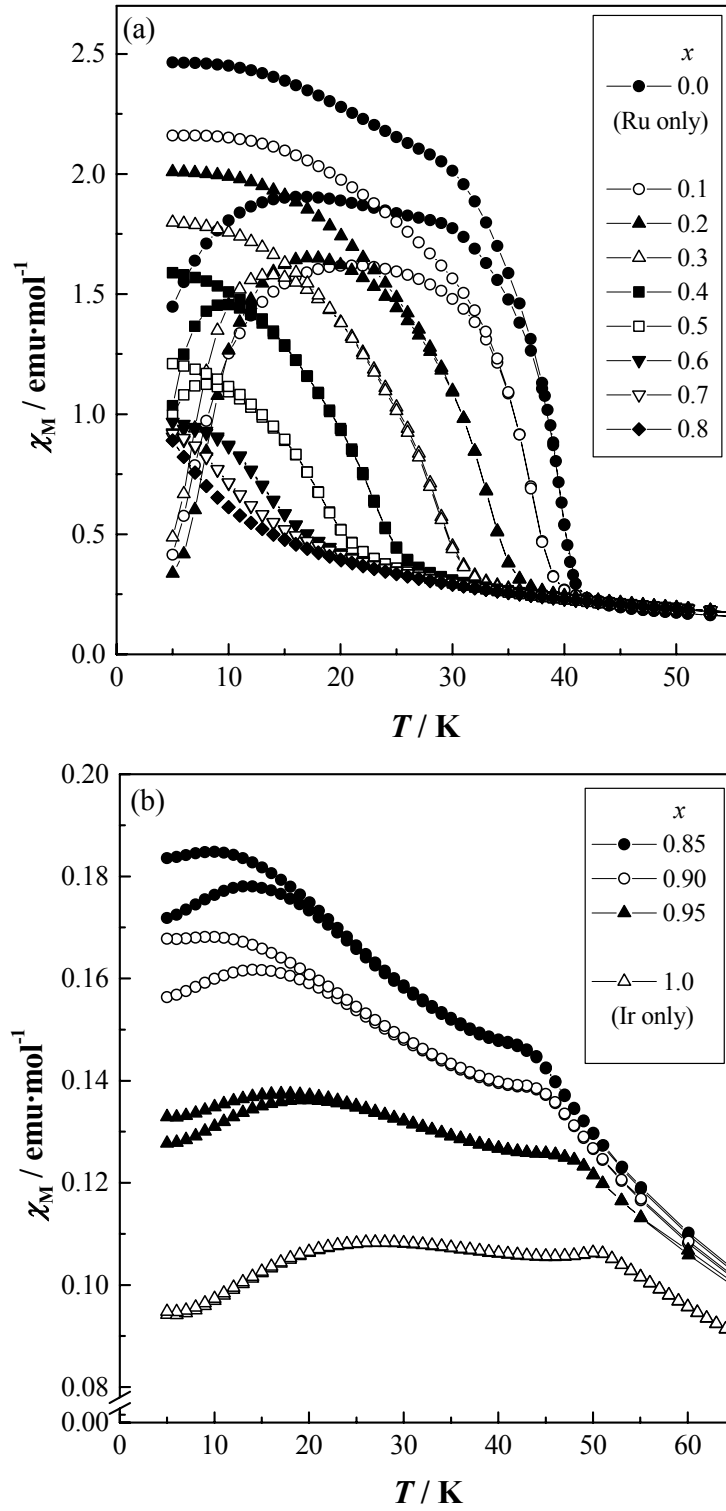


Figure 3.4.4 Temperature dependence of the ZFC and FC magnetic susceptibilities for $\text{Sr}_2\text{TbRu}_{1-x}\text{Ir}_x\text{O}_6$: (a) $x = 0.0$ – 0.8 and (b) 0.85 – 1.0 .

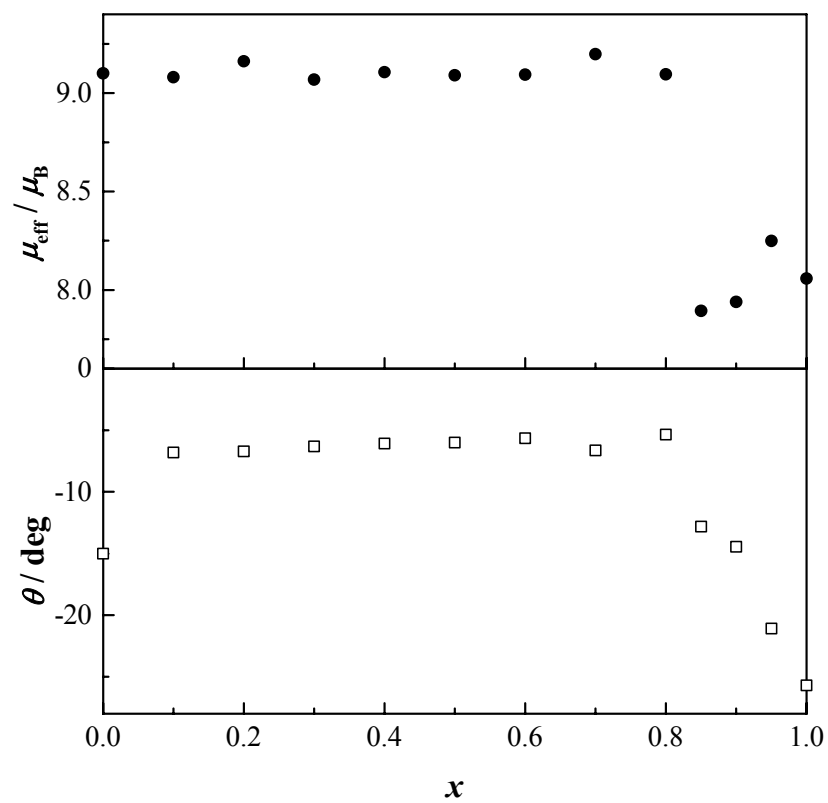


Figure 3.4.5 Variation of the effective magnetic moment μ_{eff} (●) and Weiss constant θ (□) for $\text{Sr}_2\text{TbRu}_{1-x}\text{Ir}_x\text{O}_6$ with x value.

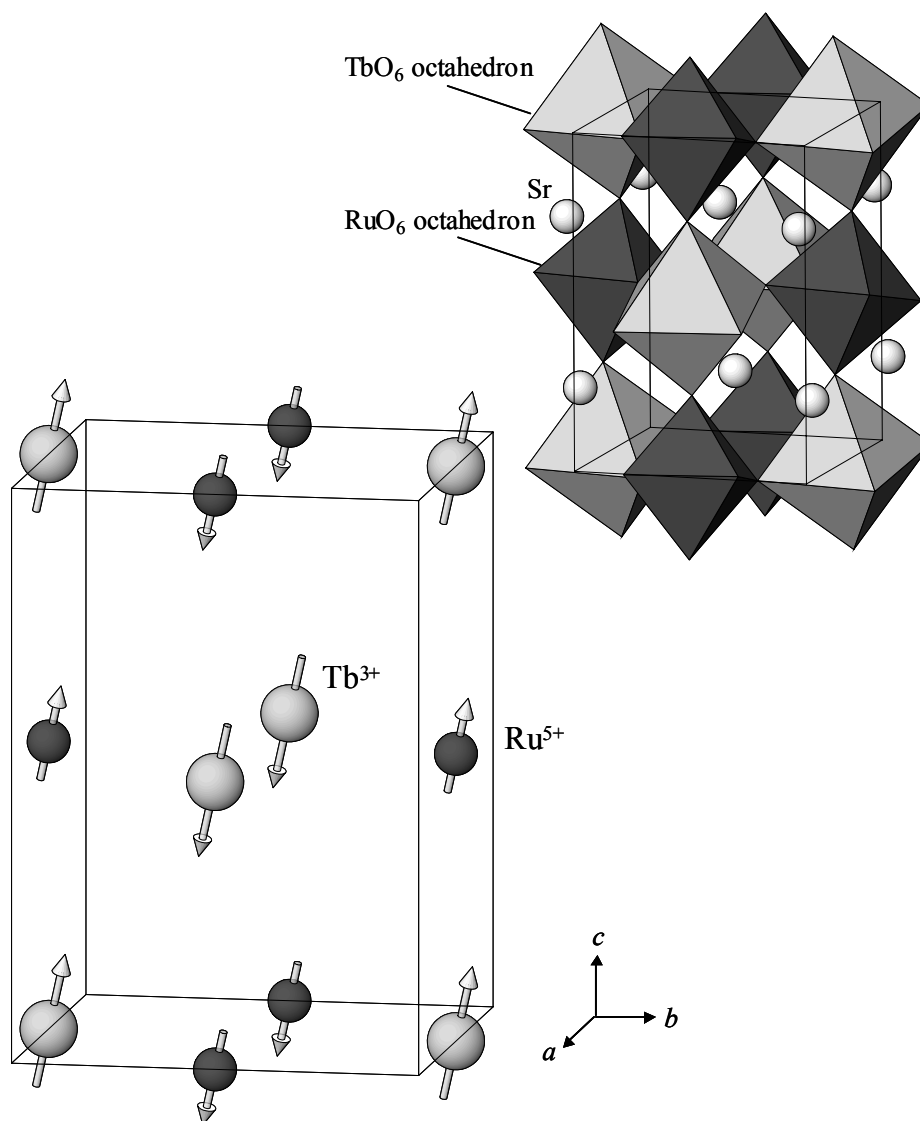


Figure 3.4.7 The crystal structure (right top) and magnetic structure (left bottom) of Sr_2TbRuO_6 at 10 K. The arrows indicate the directions of the magnetic moments. The direction of the magnetic moments cant by about 20° against the c axis.

3.5 Magnetic properties of ordered perovskites Ba_2LnTaO_6 ($Ln = Y$, Lanthanides)

3.5.1 Introduction

A series of the perovskites, Ba_2LnTaO_6 ($Ln = Y$ or lanthanide elements), has an ordered arrangement of the Ln and Ta ions [3.23, 24]. According to Galasso et al. [3.24], these compounds have an orthorhombic unit cell (for a La compound), a tetragonal cell (for a Gd compound), and cubic cells (for Y , $Dy - Lu$ compounds). Recently, Taira et al. reported the magnetic susceptibilities of Ba_2YbTaO_6 and the EPR spectrum of Yb^{3+} doped in $BaLuTaO_6$ [3.25]. They determined the energy level of the ground state and two excited states for the Yb^{3+} ion, and suggested the existence of the covalency in the Yb^{3+} ion in the octahedral symmetry. The valences of the Ln and Ta ions in the $BaLnTaO_6$ are $+3$ ($[Xe]4f^n$) and $+5$ ($[Xe]4f^{14}5d^0$), respectively. Only Ln^{3+} ions contribute to the magnetic behavior of this series of compounds. Therefore, this system is appropriate for the study of the magnetic properties on f electrons in the B sites of ordered perovskites.

In this section, the author will discuss the structural and magnetic properties of Ba_2LnTaO_6 ($Ln = Y$ or lanthanides) in detail. Their crystal structures at room temperature were refined by the Rietveld analysis of the powder X-ray diffraction data. Their magnetic susceptibility measurements were performed in the temperature range between 5 and 300 K. In addition, ^{151}Eu Mössbauer spectra for Ba_2EuTaO_6 were measured at 12, 100, 200 and 300 K.

3.5.2 Experimental

A series of Ba_2LnTaO_6 compounds was synthesized by the solid-state reaction method. Starting materials were $BaCO_3$, Ln_2O_3 ($Ln = Y, La, Nd, Sm-Gd, Dy-Lu$), Pr_6O_{11} , Tb_4O_7 and Ta_2O_5 . These reagents were weighed in appropriate metal ratios and ground intimately in an agate mortar. The mixtures were pressed into pellets and were calcined at 1173 K. The calcined materials were reground and sintered in air at 1573 K

for several days with intermediate regrinding and repelletizing.

X-ray diffraction measurements were carried out at room temperature in the range $10^\circ < 2\theta < 120^\circ$ using an angle step of 0.02° with Cu- $K\alpha$ radiation on a MultiFlex diffractometer (Rigaku). The X-Ray diffraction patterns were analyzed by the Rietveld method, using the program RIETAN2000 [3.26].

The temperature dependence of magnetic susceptibilities was measured under a zero-field-cooled condition (ZFC) in the temperature range 5–300 K (5–400 K for Sm and Eu compounds) using a SQUID magnetometer (Quantum Design, MPMS-5S). The magnetic field, which was applied after the sample was cooled from 300 K to 5 K in zero field, was 0.1 T.

The ^{151}Eu Mössbauer spectrum was measured with a Mössbauer spectrometer VT-6000 (Laboratory Equipment Co.) in the constant acceleration mode. The spectrometer was calibrated with a spectrum of $\alpha\text{-Fe}$ at room temperature. A $^{151}\text{SmF}_3$ radiation source (1.85 GBq) was used and the γ -rays were detected with a NaI scintillation counter. EuF_3 was used as a reference standard for the chemical isomer shift. The average surface density of the sample was $14.0 \text{ mg (Eu) / cm}^2$. Mössbauer measurements were conducted at 12, 100, 200, and 300 K, using a cryostat system CryoMini (Iwatani Industrial Gases Co.).

3.5.3 Results and discussion

3.5.3.1 Crystal structures

The results of the X-ray diffraction measurements show that $\text{Ba}_2\text{LnTaO}_6$ compounds have a single phase. The X-ray diffraction patterns for $\text{Ba}_2\text{LnTaO}_6$ ($\text{Ln} = \text{Y, Dy-Lu}$) were indexed with a cubic unit cell, whereas $\text{Ln} = \text{La, Pr, Nd, Sm-Tb}$ compounds were monoclinically distorted. Figure 3.5.1 shows the X-ray diffraction profiles for $\text{Ba}_2\text{LaTaO}_6$ and $\text{Ba}_2\text{LuTaO}_6$. The diffraction reflection at $2\theta \approx 18^\circ$ was found for any compound. The presence of this reflection indicates the ordered arrangements between the B site ions. Therefore, it is considered that they have an ordered perovskite-type structure with rock salt sublattice. This structure generally adopts a

cubic unit cell (space group: $Fm\bar{3}m$; $2a_p \times 2a_p \times 2a_p$) or a monoclinic one (space group: $P2_1/n$; $\sqrt{2} a_p \times \sqrt{2} a_p \times 2a_p$) [3.1]. The Rietveld analysis for the X-ray diffraction profiles of these compounds was carried out. The crystal structure of Ba_2LnTaO_6 is illustrated in Fig. 3.5.2. The crystallographic data for Ba_2LaTaO_6 and Ba_2LuTaO_6 are shown in Table 3.5.1. The unit cell parameters and the reliability factors for Ba_2LnTaO_6 are listed in Table 3.5.2.

Figure 3.5.3 shows the variation of lattice parameters for Ba_2LnTaO_6 with the ionic radius of Ln^{3+} in the six coordination. The lattice parameters, a_m , b_m , c_m (for the monoclinic cell), and a_c (for the cubic cell) increase with the Ln^{3+} ionic radius. In the monoclinic region, the lattice parameter β_m increases and the differences among a_m , b_m and $c_m/\sqrt{2}$ spread with increase of the Ln^{3+} ionic radius. This fact indicates that the crystal structures of Ba_2LnTaO_6 are more distorted from the cubic symmetry as the size of Ln^{3+} ion becomes larger. This agrees with the tendency found in other ordered perovskites, Sr_2LnRuO_6 (section 3.2), Ba_2LnNbO_6 [3.27], and A_2LnIrO_6 ($A = Sr, Ba$) [3.20, 28, 29].

Figure 3.5.4 shows the variation of the average Ln–O and Ta–O bond lengths for the Ba_2LnTaO_6 compounds against the ionic radius of Ln^{3+} . It is found that the average Ln–O bond length increases with the ionic radius of Ln^{3+} , while the average Ta–O bond length is nearly constant (~ 1.99 Å). This value is close to the $Ta^{5+}-O^{2-}$ bond length calculated from Shannon's ionic radii (2.04 Å), rather than the $Ta^{4+}-O^{2-}$ bond length (2.08 Å) [3.30]. Therefore, it is considered that the tantalum ions in Ba_2LnTaO_6 are in the pentavalent state and all the lanthanide ions are in the trivalent state.

3.5.3.2 Magnetic properties

Ba_2LnTaO_6 ($Ln = Nd, Gd-Yb$)

Figure 3.5.5 shows the temperature dependence of the inverse magnetic susceptibilities for Ba_2LnTaO_6 ($Ln = Nd, Gd-Yb$). The Ta^{5+} ions are nonmagnetic; hence only Ln^{3+} ions contribute to the magnetic behavior of Ba_2LnTaO_6 . These compounds are paramagnetic down to 5 K. The susceptibilities were fitted with a

Curie-Weiss law in the whole temperature range (for Gd) or in higher temperature ranges (above 50 K for Nd, Tb–Er; above 100 K for Tm). The effective magnetic moments and Weiss constants determined are listed in Table 3.5.3. The effective magnetic moments are comparable to the values found in Ba_2LnNbO_6 [3.27]. These values are consistent with the free-ion ones, assuming that $\Delta E \ll k_B T$, where ΔE is the energy difference between the excited and ground states of the electronic multiplet. The Weiss constants are negative except for the Gd compound. This fact may indicate the existence of a Ln^{3+} – Ln^{3+} antiferromagnetic interaction.

At lower temperatures, the susceptibilities of some compounds departed from the Curie-Weiss law. These departures may be due to the crystal field splitting. In the Yb compound, for example, the ground state $^2F_{7/2}$ of Yb^{3+} is split into two doublets (Γ_6 and Γ_7) and one quartet (Γ_8) in the octahedral symmetry. Taira et al. determined the energy level of this splitting (the ground state is Γ_6 ; the first excited state is Γ_8 and $E_{\Gamma_8} - E_{\Gamma_6} = 429.7 \text{ cm}^{-1}$; the second excited state is Γ_7 and $E_{\Gamma_7} - E_{\Gamma_6} = 1225.4 \text{ cm}^{-1}$) and the effective magnetic moment $4.41 \mu_B$ from the fitting of the magnetic susceptibilities [3.25].

Ba₂PrTaO₆

Figure 3.5.6 shows the temperature dependence of the magnetic susceptibility measured for Ba_2PrTaO_6 . This compound is paramagnetic down to 5 K. The ground state 3H_4 of Pr^{3+} ion is split into one singlet (Γ_1), one doublet (Γ_3) and two triplets (Γ_4 and Γ_5) in the octahedral symmetry. It is expected that the ground state and the first excited state are Γ_1 and Γ_4 , respectively and that the upper excited states are Γ_3 and Γ_5 , which is analogous with the results for $Cs_2NaPrBr_6$ [3.31]. The wave functions of these states are given by Lea et al. [3.32], and they are as follows:

$$\begin{array}{ll}
 \text{ground state} & \Gamma_1: \quad \sqrt{5/24}|+4\rangle + \sqrt{7/12}|0\rangle + \sqrt{5/24}|-4\rangle \\
 \text{1st excited state} & \Gamma_4: \quad \sqrt{1/8}|\pm 3\rangle + \sqrt{7/8}|\mp 1\rangle \\
 & \quad \sqrt{1/2}|+4\rangle - \sqrt{1/2}|-4\rangle
 \end{array}$$

$$\begin{aligned}
 \text{2nd excited state } \Gamma_5: & \quad \sqrt{7/8}|\pm 3\rangle - \sqrt{1/8}|\mp 1\rangle \\
 & \quad \sqrt{1/2}|+2\rangle - \sqrt{1/2}|-2\rangle \\
 \text{3rd excited state } \Gamma_3: & \quad \sqrt{7/24}|+4\rangle - \sqrt{5/12}|0\rangle + \sqrt{7/24}|-4\rangle \\
 & \quad \sqrt{1/2}|+2\rangle + \sqrt{1/2}|-2\rangle
 \end{aligned} \tag{3.3}$$

In order to explain the temperature dependence of the magnetic susceptibility, these wave functions were used as a first approximation, although the crystal structure of Ba_2PrTaO_6 is distorted from the cubic symmetry to some extent. The magnetic susceptibility of the Pr^{3+} ion is calculated by the Van Vleck equation [3.14]:

$$\chi(Pr^{3+}) = \frac{N_A g_J^2 \mu_B^2 J(J+1)}{3k_B T} F(T), \tag{3.4}$$

where

$$\begin{aligned}
 F(T) = & \left[3e^{-\Delta_{41}/k_B T} + 75e^{-\Delta_{51}/k_B T} + \frac{80k_B T}{\Delta_{41}}(1 - e^{-\Delta_{41}/k_B T}) \right. \\
 & + \frac{112k_B T}{\Delta_{41} - \Delta_{31}}(e^{-\Delta_{31}/k_B T} - e^{-\Delta_{41}/k_B T}) + \frac{42k_B T}{\Delta_{51} - \Delta_{41}}(e^{-\Delta_{41}/k_B T} - e^{-\Delta_{51}/k_B T}) \\
 & \left. + \frac{48k_B T}{\Delta_{51} - \Delta_{31}}(e^{-\Delta_{31}/k_B T} - e^{-\Delta_{51}/k_B T}) \right] / 40(1 + 2e^{-\Delta_{31}/k_B T} + 3e^{-\Delta_{41}/k_B T} + 3e^{-\Delta_{51}/k_B T})
 \end{aligned}$$

and N_A , μ_B and k_B are Avogadro number, Bohr magneton and Boltzmann constant, respectively. Δ_{31} , Δ_{41} and Δ_{51} are the energies of Γ_3 , Γ_4 and Γ_5 states above the ground state (Γ_1), respectively. By fitting this equation to the experimental magnetic susceptibility over the temperature range 50–300 K, the effective magnetic moment for Ba_2PrTaO_6 was obtained to be $3.4 \mu_B$. This value is close to the free-ion value ($3.58 \mu_B$). The estimated energy levels are $\Delta_{41} = 459 \text{ cm}^{-1}$, $\Delta_{51} \approx 1600 \text{ cm}^{-1}$ and $\Delta_{31} \approx 1800 \text{ cm}^{-1}$. The fitting curve is shown in Fig. 3.5.6. The increase in the susceptibility at low temperatures may be due to the existence of the paramagnetic Ta^{4+} ion formed from a slight oxygen deficiency.

Ba_2SmTaO_6

The temperature dependence of the magnetic susceptibility for Ba_2SmTaO_6 is shown in Fig. 3.5.7. The ground state of the Sm^{3+} ion is $^6H_{5/2}$. At low temperatures, only this magnetic $^6H_{5/2}$ ground multiplet is populated. However, the energy difference between the ground state ($^6H_{5/2}$) and the first excited state ($^6H_{7/2}$) is not very large compared with $k_B T$. Hence, the population to the excited state must be taken into consideration in the calculation of magnetic susceptibility at higher temperature (300–400 K). The temperature dependence of the susceptibility is given by reference [3.33],

$$\chi(Sm^{3+}) = \frac{C_1}{T} + \alpha_1 + \frac{C_2}{T} e^{-\Delta/T}, \quad (3.5)$$

where Δ is the energy difference between the ground state and the first excited state, and C_i and α_1 are the Curie and Van Vleck constant, respectively. Δ and α_1 are not independent since $\alpha_1 = 1.07 / \Delta$, if Δ is given in Kelvin. C_2 is fixed at $1.34 \text{ emu} \cdot \text{K} \cdot \text{mol}^{-1}$, which is calculated for the first excited state $^6H_{7/2}$. The fit to the experimental data gives $C_1 = 0.0588 \text{ emu} \cdot \text{K} \cdot \text{mol}^{-1}$ and $\Delta = 1005 \text{ cm}^{-1}$. The effective magnetic moment for the ground state is $0.69 \mu_B$, and is smaller than the free-ion moment ($0.845 \mu_B$), which is probably due to the effect of the crystal field. The obtained spin-orbit coupling constant λ is 287 cm^{-1} .

Ba_2EuTaO_6

Figure 3.5.8 shows the temperature dependence of the magnetic susceptibility for Ba_2EuTaO_6 . The susceptibility increases with decreasing temperature down to $\sim 100 \text{ K}$; below this temperature it flattens out. At lower temperatures ($< 20 \text{ K}$) it increases again. This feature may indicate a small quantity of paramagnetic Ta^{4+} ion, which is similar to the case of Ba_2PrTaO_6 . Below 100 K only the non-magnetic ground state (7F_0) is populated, and the susceptibility plateau is due to the temperature-independent term of the Van Vleck formula. The molar magnetic susceptibility for Eu^{3+} taken into account the contribution from the excited states 7F_J ($J = 1, 2, \dots, 6$) can be written by the

following equation [3.14],

$$\chi(\text{Eu}^{3+}) = \frac{N_A \mu_B^2}{3k_B T} \times \frac{24 + (13.5\gamma - 1.5)e^{-\gamma} + (67.5\gamma - 2.5)e^{-3\gamma} + (189\gamma - 3.5)e^{-6\gamma} + \dots}{1 + 3e^{-\gamma} + 5e^{-3\gamma} + 7e^{-6\gamma} + \dots}, \quad (3.6)$$

where $\gamma = \lambda / k_B T$ is 1 / 21 of the ratio of the overall multiplet width to $k_B T$. By fitting this equation to the experimental magnetic susceptibility above 50 K, the spin-orbit coupling constant λ was obtained to be 332 cm^{-1} . This value is close to the values reported in other ordered perovskites, for example, 339 cm^{-1} ($Ba_2\text{EuNbO}_6$) [3.27] and 364 cm^{-1} ($Ba_2\text{EuIrO}_6$) [3.28].

3.5.3.3 ^{151}Eu Mössbauer spectrum

^{151}Eu Mössbauer spectra for $Ba_2\text{EuTaO}_6$ measured at 12, 100, 200 and 300 K are shown in Fig. 3.5.9. Because of the low symmetry of the europium site in $Ba_2\text{EuTaO}_6$ (point symmetry: $\bar{1}$), an electric field gradient tensor should exist at this site. The quadrupole Hamiltonian is given by

$$H_{\text{quad}} = \frac{e^2 q Q}{4I(2I-1)} \left[3I_z^2 - I(I+1) + \eta(I_x^2 - I_y^2) \right], \quad (3.7)$$

where Q is the quadrupole moment, I is the nuclear spin, $eq = V_{zz}$, and $\eta = (V_{xx} - V_{yy}) / V_{zz}$ (V_{ii} is the electric field gradient tensor). The asymmetry parameter η is not equal to zero, because the symmetry at the Eu site is not axially symmetric. Then, the 12 possible transitions (eight allowed transitions and four forbidden transitions) due to a quadrupole interaction were taken into account. The observed data were fitted with the sum of these Lorentzian lines. In order to derive these Lorentzian equations, the results by Shenoy and Dunlap [3.34] were used and the ratio of the excited and ground state quadrupole moments ($R_Q = Q_e / Q_g$) were taken as 1.312 [3.35]. Therefore, the fitting parameters are isomer shift (δ), quadrupole coupling constant ($eV_{zz}Q_g$), asymmetry parameter (η), and two common parameters for 12 Lorentzian, *i.e.*, linewidth (Γ) and

peak intensity (I_0).

The calculated spectra are shown in Fig. 3.5.9, and the obtained fitting parameters are listed in Table 3.5.4. The isomer shifts are $1.441\text{--}1.536\text{ mm}\cdot\text{s}^{-1}$, which confirms that the europium ions are in the trivalent state. The quadrupole coupling constants and asymmetry parameters were determined to be $4.6\text{--}5.3\text{ mm}\cdot\text{s}^{-1}$ and $0.60\text{--}0.93$, respectively. This fact indicates the existence of the electric field gradient at the Eu nuclei. The sign of $eV_{zz}Q_g$ is positive in this case, which is the same result as those for other analogous compounds measured at room temperature: $4.96\text{ mm}\cdot\text{s}^{-1}$ for $\text{Ba}_2\text{EuNbO}_6$ [3.27] and $4.92\text{ mm}\cdot\text{s}^{-1}$ for $\text{Ba}_2\text{EuIrO}_6$ [3.28].

Figure 3.5.10 shows the temperature dependence of the absorption area of the intensity curves (A) and isomer shifts (δ). The area of the intensity is proportional to the recoil-free fraction f . The recoil-free fraction is represented by the following equation [3.36],

$$f = \exp \left[\frac{-6E_R}{k_B \Theta_D} \left\{ \frac{1}{4} + \left(\frac{T}{\Theta_D} \right)^2 \int_0^{\Theta_D/T} \frac{x dx}{(e^x - 1)} \right\} \right], \quad (3.8)$$

where Θ_D is the Debye temperature, and E_R is the free-atom recoil energy. The theoretical curve with $\Theta_D = 335\text{ K}$ (a solid line in Fig. 3.5.10) is in good agreement with the experimental data. The isomer shift decreases with increasing temperature. This decrease should be due to the second-order Doppler shift and the change in the electron density at the Eu nuclei. According to the Debye model, the temperature dependence of the second-order Doppler shift ($\Delta\delta_{\text{SOD}}$) can be expressed by the following equation [3.37],

$$\Delta\delta_{\text{SOD}} = \frac{-9k_B T}{2Mc} \left\{ \frac{1}{8} \frac{\Theta_D}{T} + \left(\frac{T}{\Theta_D} \right)^3 \int_0^{\Theta_D/T} \frac{x^3 dx}{(e^x - 1)} \right\}, \quad (3.9)$$

where M and c are the mass of isotope and the speed of light, respectively. The temperature dependence of $\Delta\delta_{\text{SOD}}$ ($\Theta_D = 335\text{ K}$) is calculated using this equation and it is shown in Fig. 3.5.10 (a broken line). The difference in the isomer shifts between 12 and 300 K ($0.096\text{ mm}\cdot\text{s}^{-1}$) is larger than that in the second-order Doppler shifts (0.053

$\text{mm}\cdot\text{s}^{-1}$). This difference is probably attributable to the decrease of the electron densities at the Eu nuclei caused by the increase of Eu–O bond length [3.38, 39]. This increase may be derived from the thermal expansion of the lattice.

3.5.4 Summary

In this section, the crystal structures and magnetic properties of the ordered perovskites Ba_2LnTaO_6 ($Ln = Y, \text{lanthanides}$) have been investigated. Their X-ray diffraction measurements and Rietveld analysis show that they have an ordered perovskite structure and monoclinic ($Ln = \text{La–Tb}$) with space group $P2_1/n$ or cubic ($Ln = Y, \text{Dy–Lu}$) with space group $Fm\bar{3}m$. All the compounds are paramagnetic down to 5 K. Ba_2SmTaO_6 and Ba_2EuTaO_6 show Van Vleck paramagnetism; their spin-orbit coupling constants are determined to be 287 cm^{-1} and 331 cm^{-1} , respectively. ^{151}Eu Mössbauer measurements for Ba_2EuTaO_6 were carried out at 12, 100, 200, and 300 K. The Eu ion is in the trivalent state, and the symmetry of the Eu site is distorted from the octahedral symmetry. The Debye temperature of Eu^{3+} was determined to be 335 K from the temperature dependence of the absorption area of intensity curves.

Table 3.5.1 Unit cell parameters and reliability factors for Ba_2LnTaO_6

Ln	$a / \text{\AA}$	$b / \text{\AA}$	$c / \text{\AA}$	$\beta / ^\circ$	$R_{wp} / \%$	$R_I / \%$	$R_e / \%$
Y	8.4368(1)	–	–	–	12.61	1.53	7.86
La	6.1453(2)	6.0946(2)	8.6091(4)	90.335(1)	11.52	1.40	9.08
Pr	6.0919(2)	6.0561(2)	8.5545(2)	90.157(1)	11.62	1.51	9.52
Nd	6.0808(2)	6.0476(2)	8.5425(2)	90.142(1)	11.41	1.40	9.14
Sm	6.0468(3)	6.0225(3)	8.5107(3)	90.038(6)	11.43	1.22	9.08
Eu	6.0191(7)	6.0152(6)	8.4964(2)	90.00(4)	11.50	1.35	9.03
Gd	6.015(3)	6.013(2)	8.4852(2)	90.00(3)	13.80	1.93	7.79
Tb	5.993(3)	5.993(3)	8.4651(1)	90.00(2)	10.80	2.06	7.55
Dy	8.4571(2)	–	–	–	13.34	1.56	8.92
Ho	8.4427(2)	–	–	–	13.57	1.91	8.04
Er	8.4240(1)	–	–	–	12.09	1.44	7.91
Tm	8.4064(1)	–	–	–	11.12	1.47	7.31
Yb	8.3894(1)	–	–	–	11.86	1.20	7.64
Lu	8.3760(1)	–	–	–	12.85	1.49	7.76

Table 3.5.2 Structural parameters for Ba_2LnTaO_6 ($Ln = La$ and Lu)

Atom	Site	x	y	z	$B / \text{\AA}^2$
Ba_2LaTaO_6 space group: $P2_1/n$					
Ba	$4e$	0.002(1)	0.002(1)	0.248(1)	0.55(3)
La	$2d$	1/2	0	0	0.12(5)
Ta	$2c$	1/2	0	1/2	0.10(4)
O(1)	$4e$	0.232(6)	0.279(5)	0.035(7)	1.0(3)
O(2)	$4e$	0.206(5)	-0.243(5)	0.034(7)	1.0(3)
O(3)	$4e$	-0.061(3)	0.517(9)	0.224(2)	1.0(3)
Ba_2LuTaO_6 space group: $Fm\bar{3}m$					
Ba	$8c$	1/4	1/4	1/4	0.58(2)
Lu	$4b$	1/2	1/2	1/2	0.23(6)
Ta	$4a$	0	0	0	0.24(6)
O	$24e$	0.237(1)	0	0	0.8(1)

Table 3.5.3 The calculated magnetic moments for Ln^{3+} (μ_{Ln}) and the experimental effective magnetic moments (μ_{eff}) and Weiss constants (θ) for Ba_2LnTaO_6

Compounds	μ_{Ln} / μ_B	μ_{eff} / μ_B	θ / K
Ba_2NdTaO_6	3.62	3.21(1)	-19.5(3)
Ba_2GdTaO_6	7.94	7.83(1)	0.37(5)
Ba_2TbTaO_6	9.72	9.49(1)	-10.3(2)
Ba_2DyTaO_6	10.63	10.26(1)	-6.68(6)
Ba_2HoTaO_6	10.58	10.17(1)	-3.73(12)
Ba_2ErTaO_6	9.59	9.44(1)	-7.73(5)
Ba_2TmTaO_6	7.55	7.83(2)	-35.7(6)

Table 3.5.4 Mössbauer spectrum parameters for $\text{Ba}_2\text{EuTaO}_6$

T / K	$\delta / \text{mm}\cdot\text{s}^{-1}$	$eV_{zz}Q_g / \text{mm}\cdot\text{s}^{-1}$	η	$\Gamma / \text{mm}\cdot\text{s}^{-1}$	$I_0 / \%$
300	1.441(10)	5.2(3)	0.76(10)	2.15(7)	10.6(2)
200	1.466(8)	4.6(3)	0.60(13)	2.25(6)	11.3(2)
100	1.532(8)	5.3(2)	0.79(8)	2.21(6)	12.7(2)
12	1.536(8)	5.1(3)	0.93(8)	2.21(6)	12.9(2)

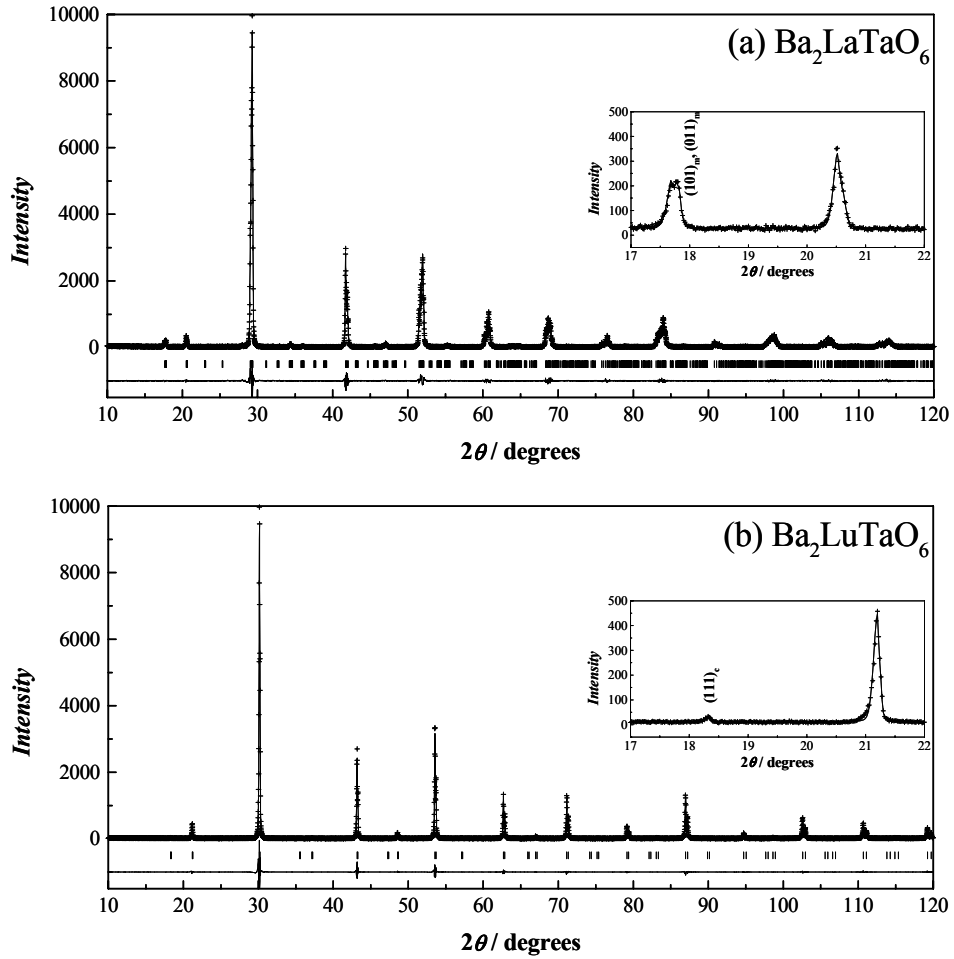


Figure 3.5.1 X-ray diffraction profiles for Ba_2LaTaO_6 (a) and Ba_2LuTaO_6 (b). The calculated and observed diffraction profiles are shown on the top solid line and cross markers, respectively. The vertical marks in the middle show positions calculated from Bragg reflections. The bottom trace is a plot of the difference between calculated and observed intensities. The insets show the enlargement of the profiles at low angles.

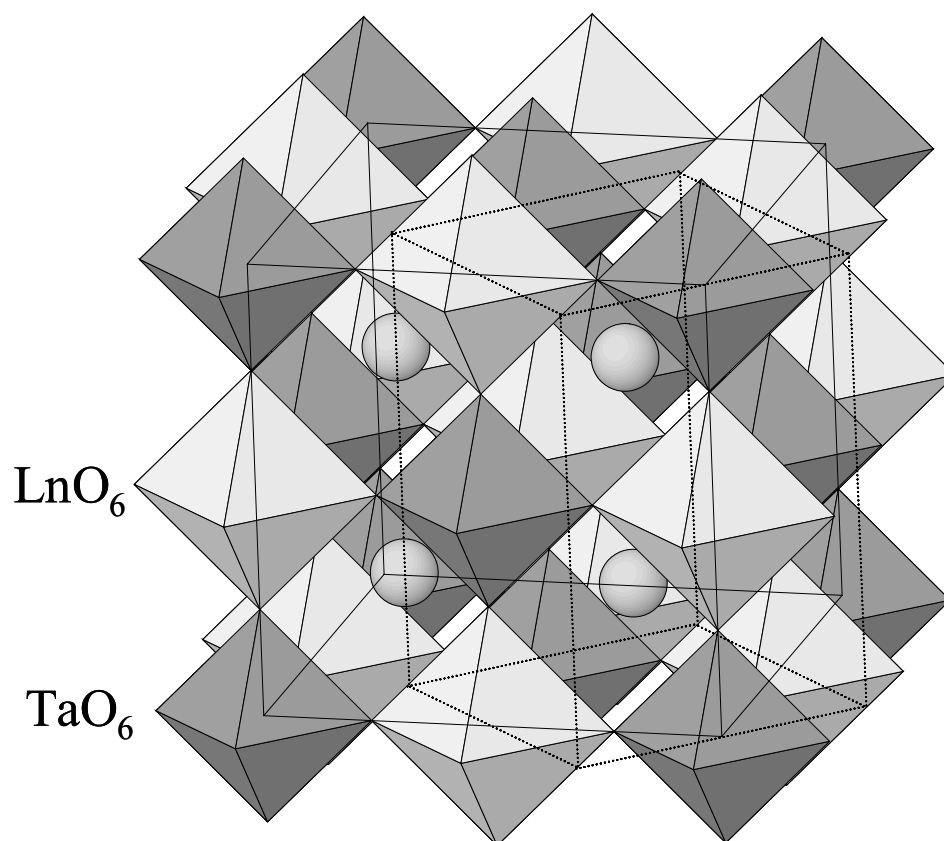


Figure 3.5.2 The crystal structure of Ba_2LnTaO_6 . The solid and dashed lines indicate the cubic and monoclinic unit cells, respectively.

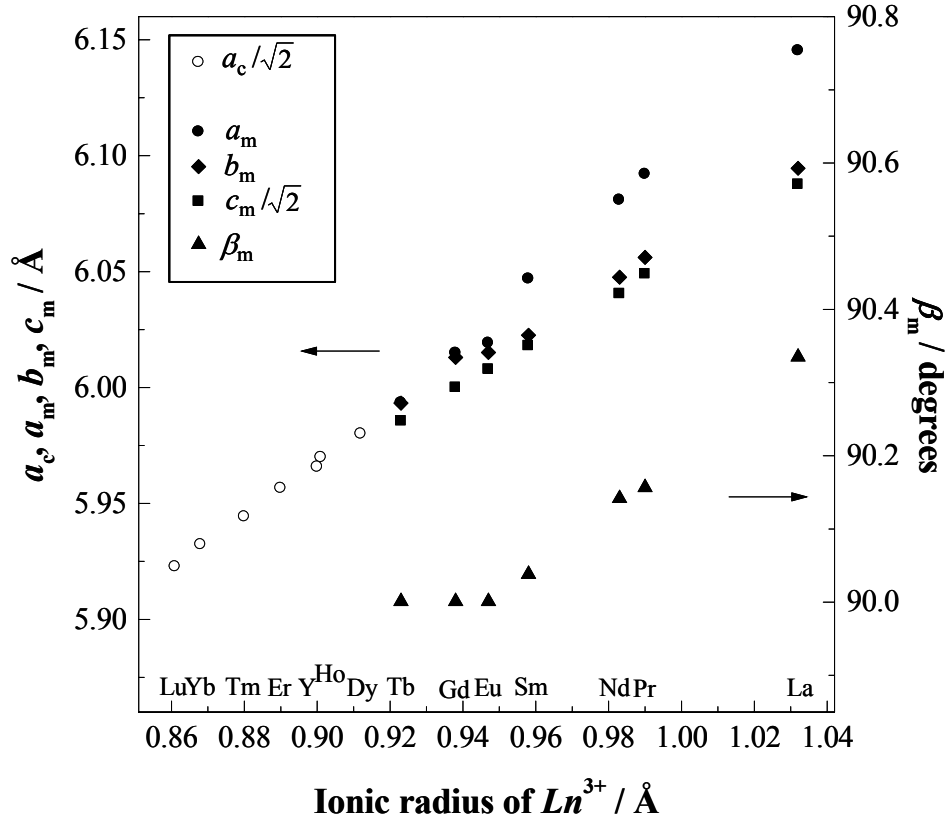


Figure 3.5.3 Variation of lattice parameters for Ba_2LnTaO_6 with the ionic radius of Ln^{3+} .

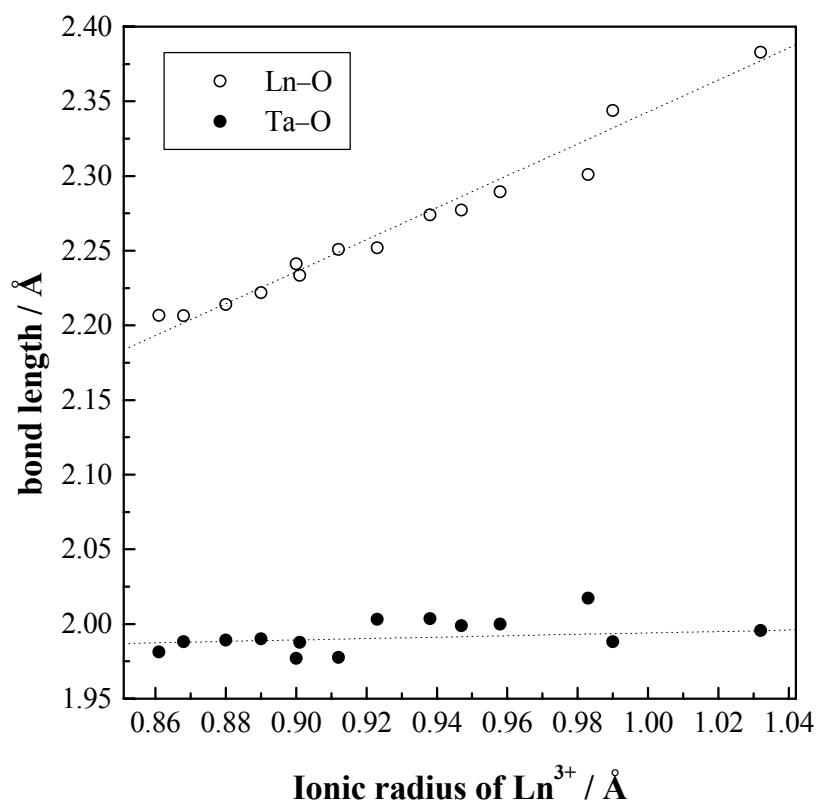


Figure 3.5.4 Variation of average bond lengths $Ln-O$ and $Ta-O$ for Ba_2LnTaO_6 with the ionic radius of Ln^{3+} .

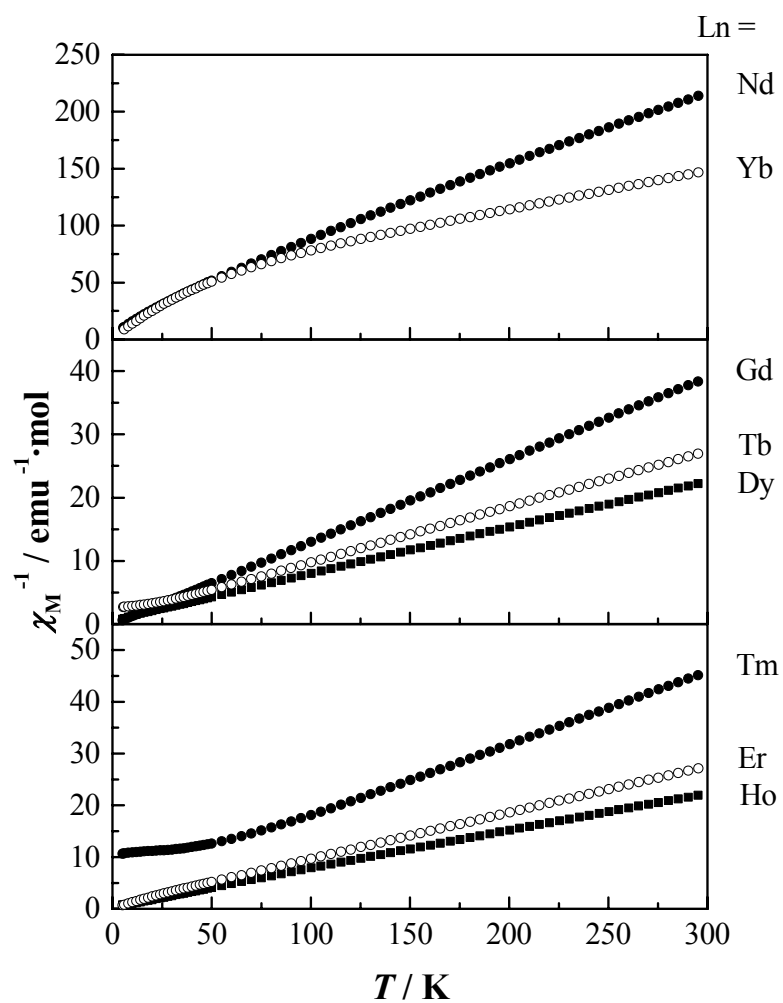


Figure 3.5.5 Temperature dependence of the inverse magnetic susceptibilities of Ba_2LnTaO_6 ($Ln = Nd, Gd\text{--}Yb$).

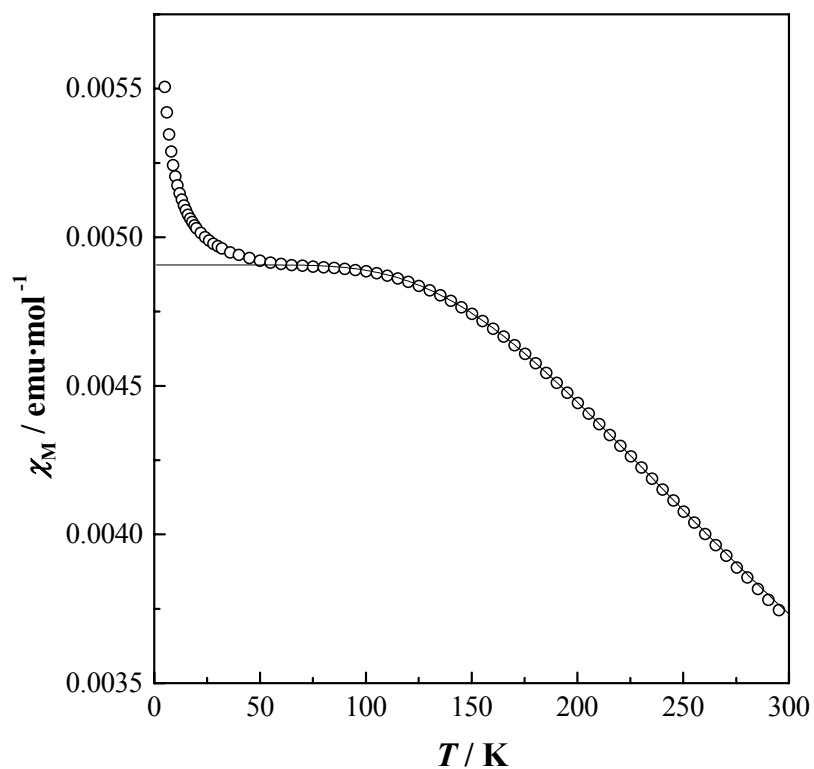


Figure 3.5.6 Temperature dependence of the magnetic susceptibility of Ba_2PrTaO_6 . A solid line is calculated with Eq. (3.4).

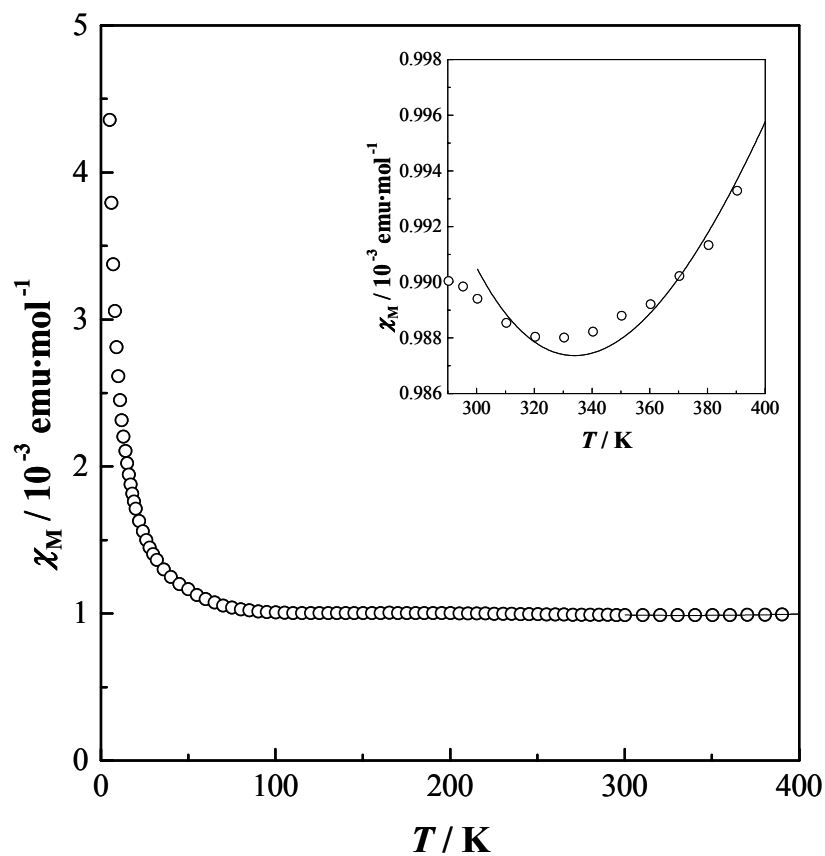


Figure 3.5.7 Temperature dependence of the magnetic susceptibility of Ba_2SmTaO_6 . A solid line is calculated with Eq. (3.5) in the temperature range of 300–400 K.

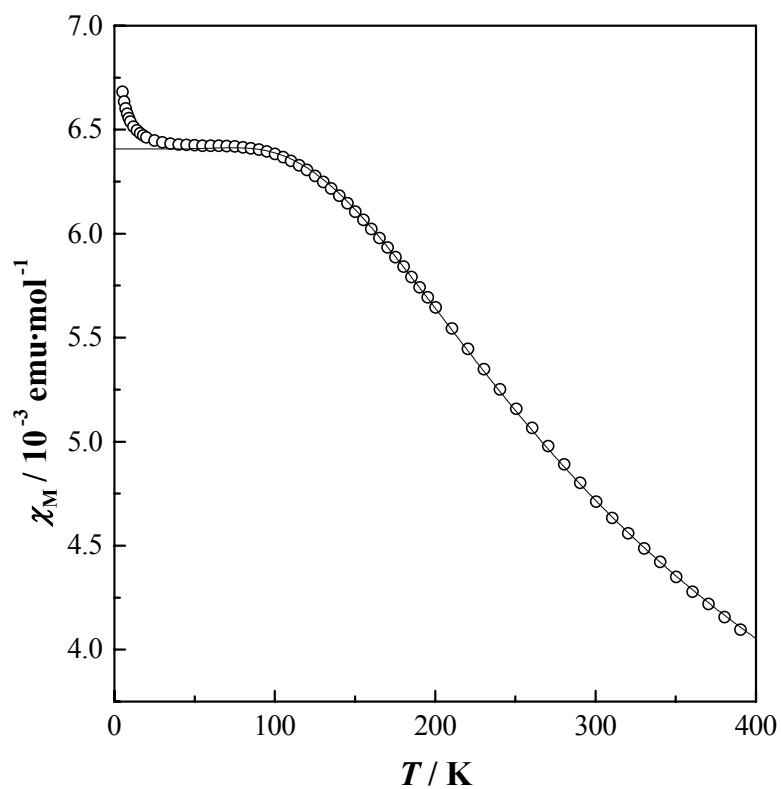


Figure 3.5.8 Temperature dependence of the magnetic susceptibility of Ba_2EuTaO_6 . A solid line is calculated with Eq. (3.6).

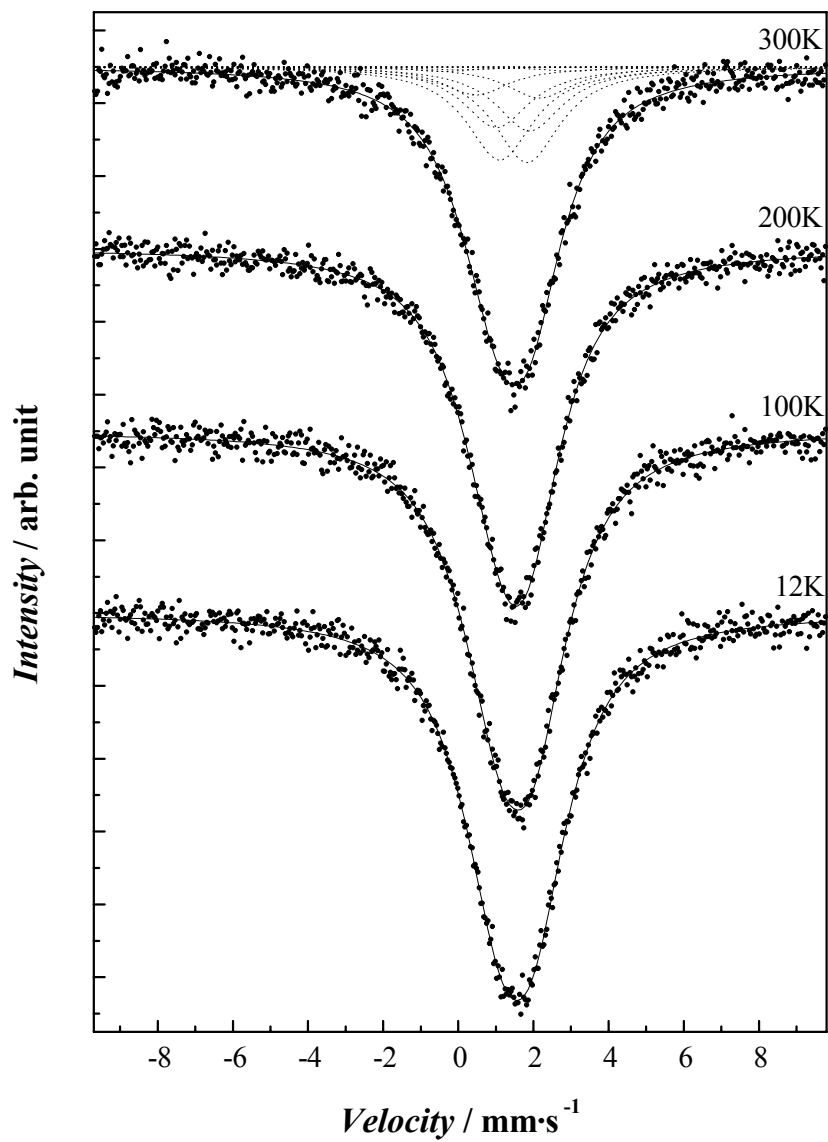


Figure 3.5.9 ^{151}Eu Mössbauer spectra of $Ba_2\text{EuTaO}_6$ at 12, 100, 200, and 300 K.

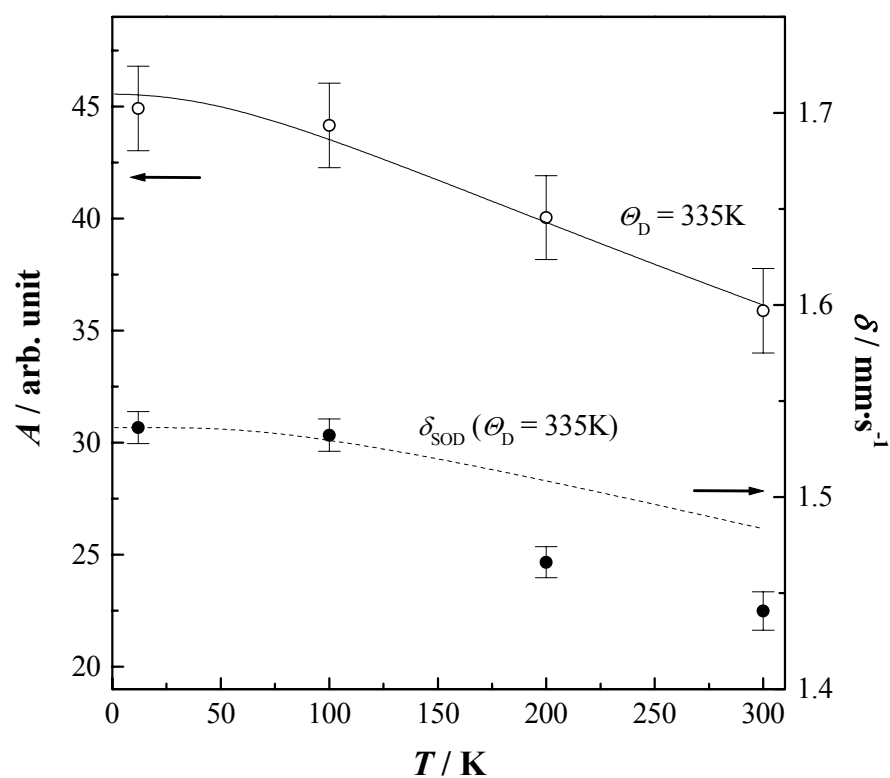


Figure 3.5.10 Temperature dependence of absorption area of intensity curves (A) and the isomer shift (δ) of $\text{Ba}_2\text{EuTaO}_6$. A solid line is the theoretical curve of the recoil-free fraction (Eq. (3.8); $\Theta_D = 335 \text{ K}$) normalized to A ; a broken line is the theoretical curve of the second-order Doppler shift with $\Theta_D = 335 \text{ K}$ (Eq. (3.9)).

3.6 References

- [3.1] M. T. Anderson, K. B. Greenwood, G.A. Taylor, and K. R. Poeppelmeier, *Prog. Solid State Chem.*, **22**, 197-233 (1993).
- [3.2] S. Nomura and K. Uchino, *kotai butsuri* **18**, 71 (1982) (in Japanese).
- [3.3] M.T. Anderson and K.R. Poeppelmeier, *Chem. Mater.*, **3**, 476-482 (1991).
- [3.4] M. Azuma, S. Kaimori, and M. Takano, *Chem. Mater.*, **10**, 3124-3130 (1998).
- [3.5] J. Longo and R. Ward, *J. Am. Chem. Soc.* **83**, 2816 (1961).
- [3.6] P. D. Battle and W. J. Macklin, *J. Solid State Chem.* **52**, 138 (1984).
- [3.7] G. Cao, Y. Xin, C. S. Alexander, and J. E. Crow, *Phys. Rev. B* **63**, 184432 (2001).
- [3.8] P. D. Battle and C. W. Jones, *J. Solid State Chem.* **78**, 108 (1989).
- [3.9] P. D. Battle, C. W. Jones, and F. Studer, *J. Solid State Chem.* **90**, 302 (1991).
- [3.10] M. K. Wu, D. Y. Chen, F. Z. Chien, S. R. Sheen, D. C. Ling, C. Y. Tai, G. Y. Tseng, D. H. Chen, and F. C. Zhang, *Z. Phys. B* **102**, 37 (1997).
- [3.11] M. DeMarco, H. A. Blackstead, J. D. Dow, M. K. Wu, D. Y. Chen, M. Haka, S. Toorongian, and J. Fridmann, *Phys. Rev. B* **62**, 14301 (2000).
- [3.12] H. A. Blackstead, J. D. Dow, D. R. Harshman, W. B. Yelon, M. X. Chen, M. K. Wu, D. Y. Chen, F. Z. Chien, and D. B. Pulling, *Phys. Rev. B* **63**, 214412-1 (2001).
- [3.13] F. Izumi, "The Rietveld Method" (R.A.Young, Ed.), Chap. 13. Oxford Univ. Press, Oxford, 1993.
- [3.14] J. H. Van Vleck, "The Theory of Electric and Magnetic Susceptibilities", Oxford Univ. Press, Oxford (1931).
- [3.15] C. D. Flint and F. L. Stewart-Darling, *Mol. Phys.* **44**, 61 (1981).
- [3.16] M. Wakeshima, D. Harada, Y. Hinatsu, and N. Masaki, *J. Solid State Chem.* **147**, 618-623 (1999).
- [3.17] Y. Morii, *J. Cryst. Soc. Jpn.* **34**, 62 (1992).

- [3.18] P. D. Battle, J. B. Goodenough, and R. Price, *J. Solid State Chem.* **46**, 234 (1983).
- [3.19] P. D. Battle and W. J. Macklin, *J. Solid State Chem.* **54**, 245 (1984).
- [3.20] D. Harada, M. Wakeshima, and Y. Hinatsu, *J. Solid State Chem.* **145**, 356 (1999).
- [3.21] D. Harada, M. Wakeshima, Y. Hinatsu K. Ohoyama, and Y. Yamaguchi, *J. Phys.: Condens. Matter* **12**, 3229 (2000).
- [3.22] K. Tezuka, Y. Hinatsu, K. Oikawa, Y. Shimojo, and Y. Morii, *J. Phys.: Condens. Matter* **12**, 4151 (2000).
- [3.23] V. S. Filip'ev and E. G. Fesenko, *Kristallografiya* **6**, 770 (1961).
- [3.24] F. S. Galasso, G. K. Layden, and D. E. Flinchbaugh, *J. Chem. Phys.* **44**, 2703 (1966).
- [3.25] N. Taira and Y. Hinatsu, *J. Solid State Chem.* **150**, 31 (2000).
- [3.26] F. Izumi and T. Ikeda, *Mater. Sci. Forum* **321-324**, 198 (2000).
- [3.27] K. Henmi and Y. Hinatsu, *J. Solid State Chem.* **148**, 353 (1999).
- [3.28] M. Wakeshima, D. Harada, Y. Hinatsu, and N. Masaki, *J. Solid State Chem.* **147**, 618 (1999).
- [3.29] M. Wakeshima, D. Harada, and Y. Hinatsu, *J. Mater. Chem.* **10**, 419 (2000).
- [3.30] R. D. Shannon, *Acta Crystallogr. Sect. A* **32**, 751 (1976).
- [3.31] A. Furrer and H. Güdel, *Phys. Rev. B* **56**, 15062 (1997).
- [3.32] K. R. Lea, M. J. M. Leask, and W. P. Wolf, *J. Phys. Chem. Solids* **23**, 1381 (1962).
- [3.33] C. F. Goya, R. C. Mercader, M. T. Causa, and M. Tovar, *J. Phys.: Condens. Matter* **8**, 8607 (1996).
- [3.34] G. K. Shenoy and B. D. Dunlap, *Nucl. Instrum. Methods* **71**, 285 (1969).
- [3.35] J. G. Stevens, "Handbook of Spectroscopy", edited by J. W. Robinson (CRC Press, Boca Raton, Florida, 1981), Vol. III, p464.
- [3.36] K. Mahesh, *Phys. Stat. Sol. (b)* **61**, 695 (1974).
- [3.37] R. M. Housley and F. Hess, *Phys. Rev.* **146**, 517 (1996).

- [3.38] S. Tanabe, K. Hirao, and N. Soga, *J. Non-Cryst. Solids* **113**, 178 (1989).
- [3.39] A. Nakamura, N. M. Masaki, M. Nakada, M. Saeki, K. Tomimoto, and J. Akimitsu, *Ceramic Transactions* **71**, 295 (1996).

Chapter 4.

Crystal structures and magnetic properties of 6H-perovskites Ba₃LnRu₂O₉

4.1 Introduction

4.1.1 6H-perovskites Ba₃LnRu₂O₉

This chapter describes the crystal structures and magnetic properties of the perovskite-related compounds Ba₃LnRu₂O₉ (Ln = Y, In, lanthanides). In Chapter 3, the crystal structures and magnetic properties of ordered perovskites Sr₂LnRuO₆, which contain Ln and Ru ions as B site ions at a 1:1 ratio, have been discussed, and it is found that these compounds show interesting and complex magnetic behavior at low temperatures. The Ba₃LnRu₂O₉ also contains both Ln and Ru ions as B site ions, and its ratio is 1:2. The increase in the proportion of smaller Ru ions makes the tolerance factor t (Eq. (1.1)) large. As a result, the tolerance factor becomes ~ 1 or exceeds 1 in some cases. Therefore, as is mentioned in section 1.1.1.2, it is expected that Ba₃LnRu₂O₉ adopts a hexagonal perovskite structure; the 6H-BaTiO₃ type structure [4.1] is most prospective.

This 6H-BaTiO₃ type structure has two kinds of sites for the B ions: the corner-sharing octahedral site and the face-sharing octahedral site. Generally, the B site ion with a low oxidation state and large size occupies the former site, and that with a high oxidation state and small size occupies the latter site. In the case of Ba₃LnRu₂O₉, Ln and Ru ions occupy the corner-sharing and face-sharing sites, respectively, and form the LnO₆ octahedron and the Ru₂O₉ polyhedron. This Ru₂O₉ polyhedron consists of face-sharing two RuO₆ octahedra and is called “Ru₂O₉ dimer”. The magnetic behavior of this Ru₂O₉ dimer is attractive because of a very short Ru–Ru distance (2.5–2.7 Å) in the dimer. Therefore, it is expected to find the strong magnetic interaction between Ru ions in the dimer, i.e., the formation of the magnetic dimer.

Previously, it was reported that the magnetic susceptibilities of $\text{Ba}_3\text{M}^{2+}\text{Ru}^{5+}_2\text{O}_9$ ($\text{M} = \text{Mg}, \text{Ca}, \text{Cd}, \text{and Sr}$) showed a broad maximum at 400–500 K and approached zero with decreasing temperature [4.2]. These features were explained by the antiferromagnetic coupling of Ru^{5+} ions in the dimer isolated magnetically by diamagnetic M^{2+} ions, which has the singlet ground state and the exchange integral $J = \sim -170$ K.

Since the most stable oxidation state of lanthanide ions is trivalent, the expected electronic configuration of $\text{Ba}_3\text{LnRu}_2\text{O}_9$ is $\text{Ba}_3\text{Ln}^{3+}\text{Ru}^{4.5+}_2\text{O}_9$. If the magnetic moments of Ru ions in the dimer couple antiferromagnetically, each dimer has one unpaired electron at sufficiently low temperatures. In addition, if the lanthanide ions are magnetic, there exists a 180° Ru–O–Ln superexchange magnetic interaction. Therefore, this series of $\text{Ba}_3\text{LnRu}_2\text{O}_9$ compounds is considered to bring about interesting magnetic behavior due to the Ru_2O_9 dimer itself and the magnetic interaction between Ru and Ln ions.

4.1.2 Magnetic susceptibilities of the magnetic dimer [4.3, 4]

This section describes briefly the magnetic susceptibilities of the magnetic dimer for the later discussion of magnetic properties of $\text{Ba}_3\text{LnRu}_2\text{O}_9$.

The Hamiltonian in use for metal-metal exchange interaction in magnetic insulators is of the form

$$H = -2 \sum J_{ij} \mathbf{S}_i \cdot \mathbf{S}_j \quad (4.1)$$

where \mathbf{S}_i and \mathbf{S}_j are the spin operators and J is the exchange integral, and the sum is taken over all pair-wise interactions of spins i and j in a lattice. For the dimeric magnetic unit, this summation is limited to two magnetic ions 1 and 2, so that

$$H = -2J \mathbf{S}_1 \cdot \mathbf{S}_2. \quad (4.2)$$

This is called an isotropic or Heisenberg Hamiltonian. The negative J refers to antiferromagnetic interactions, and positive J refers to ferromagnetic interactions. Taking into account an external magnetic field applied along the z -axis of the pair, the Hamiltonian is taken as

$$H = g\mu_B \mathbf{S}'_z H_z - 2J \mathbf{S}_1 \cdot \mathbf{S}_2 \quad (4.3)$$

where \mathbf{S}'_z is the operator for the z -component of total spin of the pair ($\mathbf{S}'_z = \mathbf{S}_1 + \mathbf{S}_2$). For a pair of $S_1 = S_2 = 1/2$ ions, an antiferromagnetic interaction gives a spin-singlet ground state ($S' = 0$) and a spin-triplet excited state ($S' = 1$) with $-2J$ in energy above the singlet (Fig. 4.1.1). Each state splits into $(2S' + 1)$ -levels by the external magnetic field.

Magnetic susceptibility per mole of dimers is obtained by the application of Van Vleck's equation to the energy level situation of the dimer:

$$\chi_{\text{dimer}} = \frac{N_A g^2 \mu_B^2}{3k_B T} \times \frac{\sum S'(S' + 1)(2S' + 1)e^{-E/k_B T}}{\sum (2S' + 1)e^{-E/k_B T}} \quad (4.4)$$

where $E = E_{S'} - E_g$, and $E_{S'}$ and E_g are the energy of the state of S' and that of the ground state, respectively. For example, the magnetic susceptibility of the $S_1 = S_2 = 1/2$ dimer is given by this equation:

$$\chi_{\text{dimer}} = \frac{N_A g^2 \mu_B^2}{3k_B T} \times \frac{6}{x^2 + 3}, \quad (4.5)$$

where x is $e^{-J/k_B T}$. Magnetic susceptibilities of other dimers ($S_1 = S_2 = 1, 3/2, 2, 5/2$ etc.) also can be obtained by the same way. The temperature dependence of some dimers is plotted in Fig. 4.1.2. Note that, for negative J (antiferromagnetic interaction), χ has a maximum and approaches zero below this maximum temperature.

Above treatment has been applied to magnetic susceptibilities of many dinuclear complexes. One of the most famous examples is the study concerning the hydrated copper acetate $[\text{Cu}(\text{OAc})_2 \cdot (\text{H}_2\text{O})]_2$ [4.5]. This compound has a short Cu–Cu distance (2.616 Å), and each Cu ion has an $S = 1/2$ spin. Its magnetic susceptibility shows a maximum near room temperature and then decreases so rapidly with decreasing temperature, and apparently becomes zero at ~ 50 K. This magnetic behavior was explained by the isolated dimer model, i.e., a pair-wise exchange interaction between Cu ions yields a singlet ground state and a triplet excited state. One result of this success is that Eq. (4.5) is now referred to regularly as the “Bleaney-Bowers equation”.

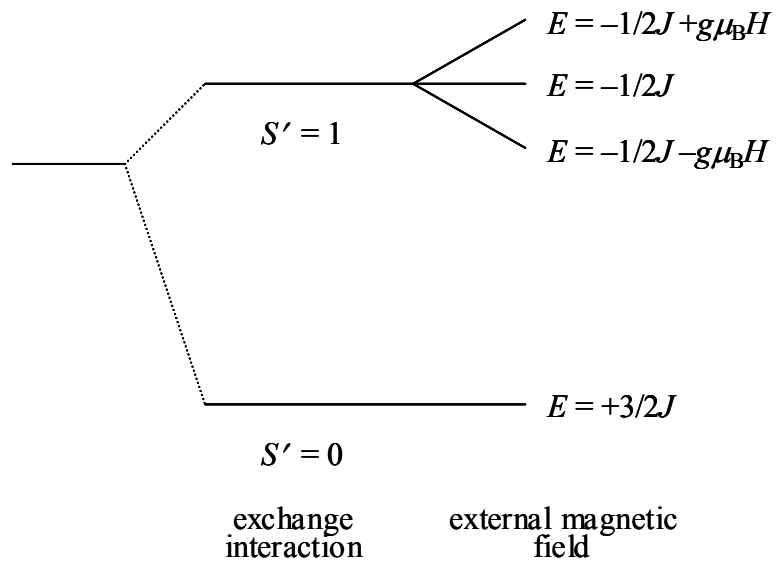


Figure 4.1.1 Energy levels for a pair of $S = 1/2$ ions undergoing antiferromagnetic exchange. The $S' = 1$ level is $-2J$ in energy above the $S' = 0$ level.

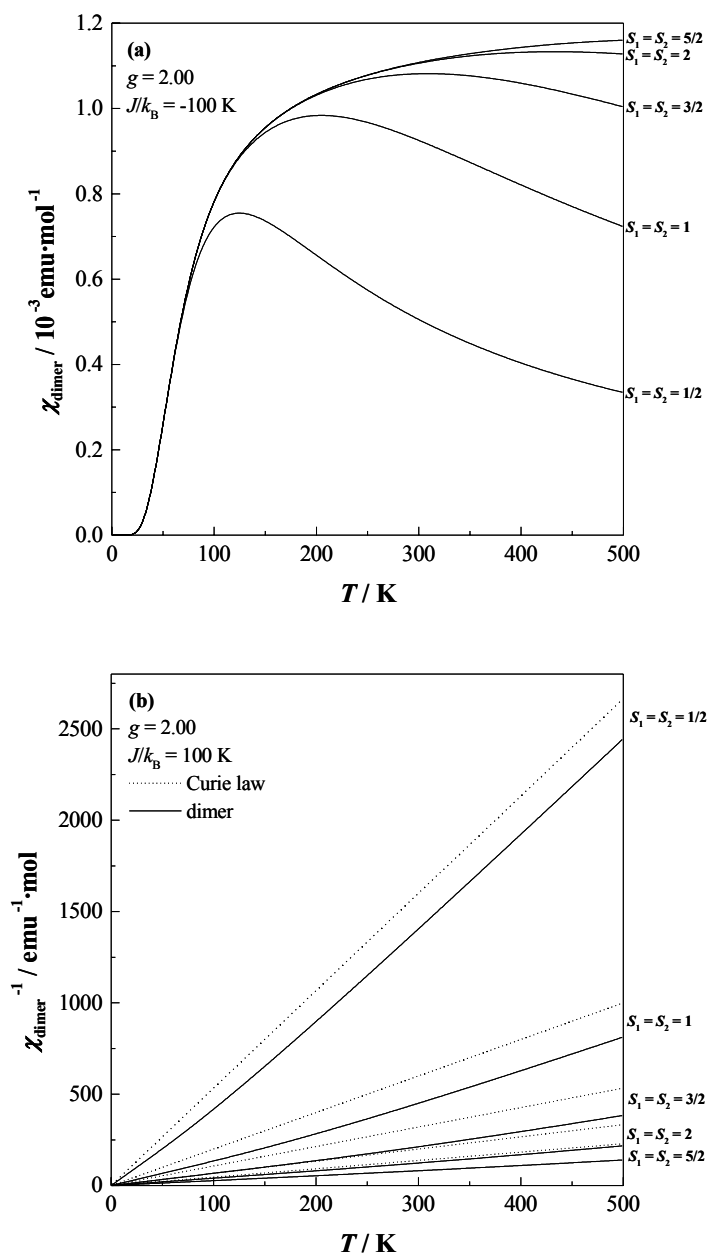


Figure 4.1.2 Calculated magnetic susceptibilities for antiferromagnetically (a), and ferromagnetically (b) coupled dimers with $S = 1/2, 1, 3/2, 2$, and $5/2$.

4.2 Crystal structures and electrical resistivity of $Ba_3LnRu_2O_9$

4.2.1 Experimental

4.2.1.1 Sample preparation

Polycrystalline samples of $Ba_3LnRu_2O_9$ were prepared by the conventional solid-state reaction. As starting materials, $BaCO_3$, RuO_2 , Ln_2O_3 ($Ln = Y, La, Nd, Sm-Gd, Dy-Lu$), CeO_2 , Pr_6O_{11} , Tb_4O_7 , In_2O_3 were used. Before use, La_2O_3 , Nd_2O_3 , and In_2O_3 were dried in air at 1173 K (La_2O_3 and Nd_2O_3) or 1073 K (In_2O_3) for a day. The samples were weighed in an appropriate metal ratio and well mixed in an agate mortar. The mixtures were pressed into pellets and then calcined at 1173 K for 12 h. The calcined materials were fired in air at 1373–1573 K for 60–108 h with several interval grindings and pelletings. The heating rate was 100 K / h. The progress of the reaction was monitored by powder X-ray diffraction measurements.

A diamagnetic $Ba_3SrNb_2O_9$, which is isomorphous with $Ba_3LnRu_2O_9$, was also prepared. As will be described later, this compound is needed to estimate the lattice contribution of the specific heat to the total specific heat of $Ba_3NdRu_2O_9$. As starting materials, $BaCO_3$, $SrCO_3$, and Nb (metal) were used. The stoichiometric mixtures were calcined in air, first at 1123 K for 12×2 h and then at 1623 K for 48 h, and finally, were heated at 1573 K for 48 h in a flow of helium gas. The XRD measurements showed that $Ba_3SrNb_2O_9$ was formed as a single phase and that its crystal structure agreed with a previous report [4.6].

4.2.1.2 X-ray diffraction measurements

The powder X-ray diffraction profile at room temperature was measured in the range $10^\circ \leq 2\theta \leq 120^\circ$ using a 2θ step size of 0.02° with Cu- $K\alpha$ radiation on a Rigaku MultiFlex diffractometer. Crystal structures were determined by the Rietveld technique, using the program RIETAN2000 [4.7].

4.2.1.3. Electrical resistivity measurements

The temperature dependence of the resistivity for $Ba_3LnRu_2O_9$ was measured in

the temperature range 100–400 K (for both cooling and heating process) using a DC four-probe technique with the same measurement system (PPMS model). The sintered samples were cut into pieces having sizes of approximately $5.0 \times 2.5 \times 1.2 \text{ mm}^3$. Four contact wires were painted onto the samples using silver paste.

4.2.2 Results and discussion

4.2.2.1 Crystal structure of $Ba_3LnRu_2O_9$

The results of the X-ray diffraction measurements show that $Ba_3LnRu_2O_9$ ($Ln = Y, In, La-Nd, Sm-Lu$) are formed as single-phase materials. The X-ray diffraction patterns of La and Lu compounds are shown in Fig. 4.2.1. The data have been analyzed by the Rietveld method. The results indicate that their crystal structures are a 6H-perovskite structure with space group $P6_3/mmc$ (No. 194). The cation sites within the face-sharing octahedra of this structure are occupied by Ru ions and those within the corner-sharing octahedra are occupied by Ln ions. The schematic structure of $Ba_3LnRu_2O_9$ is illustrated in Fig. 4.2.2. The structural parameters and reliability factors are summarized in Table 4.2.1. Their crystal structures are the same as those of other $Ba_3MRu_2O_9$ type compounds [4.8-10]. Neither the cation disorder between these two sites nor oxygen defect were found within the error of these analyses.

The variation of lattice parameters for $Ba_3LnRu_2O_9$ with the ionic radius of Ln^{3+} is shown in Fig. 4.2.3. The lattice parameters for $Ba_3LnRu_2O_9$ increase monotonously with the ionic radius of Ln^{3+} from Lu to La, while those for the Ce, Pr and Tb compounds deviate substantially from this trend. Some selected bond lengths and angles are listed in Table 4.2.2. Figure 4.2.4 plots the variation of the refined Ln–O(2) bond lengths with the ionic radius of Ln^{3+} . Except for the Ce, Pr and Tb compounds, it is found that the Ln–O(2) bond length increases with the ionic radius of Ln^{3+} . The refined Ce–O, Pr–O and Tb–O bond lengths are 2.213(8), 2.195(5) and 2.132(3) Å, respectively. They are close to $Ln^{4+}-O^{2-}$ lengths calculated from Shannon's ionic radii [4.11]: 2.27 (for Ce), 2.25 (for Pr) and 2.16 Å (for Tb). These results indicate that the Ce, Pr and Tb ions are in the tetravalent state. This conclusion agrees with previous discussions by

Müller-Buschbaum et al. (for Ce compound) [4.12] and Treiber et al. (for Pr compound) [4.8].

Figure 4.2.5 shows the variation of the Ru–O(1), Ru–O(2), and average Ru–O bond lengths with the ionic radius of Ln^{3+} . The O(1) atoms are on the shared-face in the Ru_2O_9 dimer, and O(2) atoms are on the top or bottom face of the Ru_2O_9 dimer. The Ru–O(1) and Ru–O(2) bond lengths are 2.002–2.046 Å and 1.908–1.982 Å, respectively, indicating that two octahedra in this Ru_2O_9 dimer are distorted in shape. The Ru–O(1) length increases with increasing the ionic radius of Ln^{3+} , while the Ru–O(2) length decreases, therefore, this tendency clearly indicates that the shape of Ru_2O_9 dimers is more distorted with increasing the ionic radius of Ln^{3+} .

For the Ce, Pr and Tb compounds, the Ru–O(1) and Ru–O(2) bond lengths deviate substantially from this trend. The average Ru–O bond lengths of these three compounds are 1.989–1.993 Å, and they are in the middle between 1.965 Å for $Ru^{5+}-O^{2-}$ and 2.020 Å for $Ru^{4+}-O^{2-}$ calculated from the Shannon's ionic radii [4.11]. However, it is considered that the ruthenium ions are most likely tetravalent in the Ce, Pr, and Tb compounds, because the obtained lengths are very close to the $Ru^{4+}-O^{2-}$ lengths found in other perovskites, for example, $CaRuO_3$: 1.99 Å [4.13, 14] $SrRuO_3$: 1.984 Å [4.13, 15], and $BaRuO_3$: 1.993 Å [4.16]. On the other hands, the average Ru–O bond lengths of the other compounds are 1.971–1.985 Å, and they are shorter than those of the Ce, Pr, and Tb compounds and longer than $Ru^{5+}-O^{2-}$ length (1.965 Å) found in $Ba_3M^{2+}Ru^{5+}_2O_9$ ($M = Zn$ and Ni) [4.9]. This fact indicates that the average valency of Ru ions is +4.5, as is expected from the trivalent oxidation state of Ln ions and the stoichiometry in the oxygen content.

The difference in the interatomic distance between two ruthenium ions in the Ru_2O_9 dimer supports the above discussion. The Ru–Ru distance of $Ba_3LnRu_2O_9$ and other $Ba_3MRu_2O_9$ -type compounds are also listed in Table 4.2.3. This Ru–Ru distance increase with the average valence of Ru ions: 2.481–2.515 Å for Ru^{4+} ions, 2.517–2.582 Å for $Ru^{4.5+}$ ions (if it is limited only in this study, 2.524–2.563 Å), and 2.649–2.701 Å for Ru^{5+} ions. This tendency is explained by the difference in the strength of the

electrostatic repulsion between ruthenium, i.e., the Ru–Ru distance becomes larger with increasing the average valence of ruthenium ions.

In Table 4.2.2, two bond angles, Ru–O(2)–Ln and Ru–O(1)–Ru angles, are listed. These angles are important for the criteria of the magnetic interactions observed in the Ba₃LnRu₂O₉. The Ru–O(2)–Ln angles are very near to 180° and the Ru–O(1)–Ru angles are ~77°. The Ru–O(2)–Ln pathway in the 6H-perovskites Ba₃LnRu₂O₉ is comparable with that of the ordered perovskites Sr₂LnRuO₆.

4.2.2.2 Electrical resistivity

The resistivity of Ba₃LnRu₂O₉ is plotted as a function of reciprocal temperature in Figs. 4.2.6(a) (Ln = Y, La, Sm, Eu, and Lu) and 4.2.7(a) (Ln = Ce, Pr, and Tb). They are nonmetallic at least in the range 100 < *T* < 400 K, showing the increasing resistance with decreasing temperature. Attempts to fit the observed data to a simple Arrhenius model were unsuccessful. The Mott variable-range hopping (VRH) model [4.22],

$$\rho \propto \exp((T_0/T)^\nu), \quad (4.6)$$

was taken into account. When the parameter ν is 1/3, i.e., the variable range hopping in two dimensions, experimental data show good linearity (Figs. 4.2.6(b) and 4.2.7(b)). The resistivity of the isostructural compounds Ba₃MRu₂O₉ (M = Fe, Co, Ni, Cu, and In) was reported previously, and it was found that the plots of $\log \rho$ vs. $T^{-1/3}$ are linear [4.23]. These results also suggest that the semiconducting behavior of Ba₃LnRu₂O₉ may be attributed to the variable range hopping in two dimensions [4.22].

The crystal structure of Ba₃LnRu₂O₉ (Fig. 4.2.2) can be expressed by the alternate stacking of two kinds of two-dimensional layers which consist of the LnO₆ octahedra or Ru₂O₉ polyhedra. This structural feature may account for the observed resistivity behavior.

4.2.3 Summary

In this section, the perovskite-related compounds Ba₃LnRu₂O₉ (Ln = Y, In, La–Nd, Sm–Lu) have been synthesized, and their crystal structures have been determined by the

X-ray diffraction measurements. The Rietveld analysis of the X-ray diffraction data show that they have the 6H- BaTiO_3 type structure with space group $P6_3/mmc$ and that the two kinds of B cation sites, the face-sharing and corner-sharing octahedral sites, are occupied by Ru and Ln ions, respectively. For the Ce, Pr, and Tb compounds, the oxidation states of both Ru and Ln ions are tetravalent. On the other hand, other compounds adopt a valence configuration of $\text{Ba}_3\text{Ln}^{3+}\text{Ru}^{4.5+}_2\text{O}_9$.

In addition, the electrical resistivity measurement has been performed for the Y, In, La, Ce, Pr, Sm, Eu, Tb, and Lu compounds. These compounds are semiconductors over the temperature range 100–400 K. The temperature dependence of the resistivity obeys the Mott variable-range hopping model rather than the Arrhenius one.

Table 4.2.1 Structural parameters for $Ba_3LnRu_2O_9$

	Y	In	La	Ce	Pr	Nd*	Sm	Eu
$a / \text{\AA}$	5.8816(2)	5.8185(3)	5.9579(3)	5.8894(2)	5.8855(1)	5.9319(1)	5.9192(3)	5.9133(3)
$c / \text{\AA}$	14.5010(4)	14.3145(7)	15.0058(8)	14.6476(4)	14.6071(2)	14.7589(3)	14.6788(7)	14.6346(6)
Ba(1) $B/\text{\AA}^2$	0.32(4)	0.48(9)	0.15(5)	0.75(6)	0.51(4)	0.34(7)	0.70(8)	0.95(8)
Ba(2) z	0.9061(1)	0.9101(1)	0.8947(1)	0.9025(1)	0.9036(1)	0.8994(2)	0.9029(1)	0.9041(1)
Ba(2) $B/\text{\AA}^2$	0.74(3)	0.47(4)	0.52(4)	0.61(3)	0.51(2)	0.86(5)	0.70(5)	1.01(4)
Ln $B / \text{\AA}^2$	0.05(6)	0.07(8)	0.1	0.19(5)	0.04(4)	0.10(5)	0.10(8)	0.10(7)
Ru z	0.1624(1)	0.1605(1)	0.1649(1)	0.1653(1)	0.1649(1)	0.1645(1)	0.1636(1)	0.1634(1)
Ru $B / \text{\AA}^2$	0.08(3)	0.04(5)	0.1	0.10(3)	0.10(3)	0.63(3)	0.09(5)	0.10(4)
O(1) x	0.4885(7)	0.4865(9)	0.4882(9)	0.4901(10)	0.4882(7)	0.4885(2)	0.4884(11)	0.4882(9)
O(1) $B/\text{\AA}^2$	0.7(2)	0.1(3)	0.3(3)	1.2(3)	1.1(2)	0.70(3)	1.0(4)	1.0(3)
O(2) x	0.1763(6)	0.1704(10)	0.1794(7)	0.1765(8)	0.1754(6)	0.1779(2)	0.1777(9)	0.1773(8)
O(2) z	0.4125(3)	0.4148(6)	0.4055(4)	0.4122(4)	0.4128(4)	0.4084(1)	0.4090(6)	0.4101(5)
O(2) $B/\text{\AA}^2$	0.8(1)	0.9(2)	1.1(2)	1.2(2)	0.8(1)	1.04(3)	1.0(2)	1.0(2)
$R_{wp} / \%$	11.86	15.94	13.06	13.35	10.82	7.65	15.69	13.73
$R_I / \%$	1.89	2.82	2.43	2.56	1.66	2.64	3.85	3.32
$R_F / \%$	1.08	2.03	1.77	2.01	1.29	1.69	2.28	2.02
$R_e / \%$	9.24	12.38	11.31	10.79	7.55	5.82	10.38	9.71

Note. Space group $P6_3/mmc$; $z = 2$. The atomic positions: Ba(1) $2b(0,0,1/4)$; Ba(2) $4f(1/3,2/3,z)$; Ru $4f(1/3,2/3,z)$; O(1) $6h(x,2x,1/4)$; O(2) $12k(x,2x,z)$.

* Neutron diffraction data at room temperature.

Table 4.2.1 *continued*

	Gd	Tb*	Dy	Ho	Er	Tm	Yb	Lu
$a / \text{\AA}$	5.9097(2)	5.8365(5)	5.8904(2)	5.8838(2)	5.8764(2)	5.8686(2)	5.8616(2)	5.8542(2)
$c / \text{\AA}$	14.6101(3)	14.4257(9)	14.5299(4)	14.5064(5)	14.4794(4)	14.4537(5)	14.4321(4)	14.4163(4)
Ba(1) $B/\text{\AA}^2$	0.42(5)	0.59(12)	0.40(5)	0.74(3)	0.67(2)	0.23(3)	0.29(4)	0.40(5)
Ba(2) z	0.9040(1)	0.9066(3)	0.9058(1)	0.9063(1)	0.9068(1)	0.9072(1)	0.9076(1)	0.9077(1)
Ba(2) $B/\text{\AA}^2$	0.88(3)	0.58(11)	0.86(3)	0.74	0.67	0.23	0.86(3)	0.61(3)
Ln $B / \text{\AA}^2$	0.23(5)	0.51(9)	0.22(5)	0.10(5)	0.10(4)	0.20(4)	0.33(4)	0.08(4)
Ru z	0.1635(1)	0.1636(2)	0.1630(1)	0.1622(1)	0.1621(1)	0.1620(1)	0.1618(1)	0.1616(1)
Ru $B / \text{\AA}^2$	0.18(3)	0.48(7)	0.23(3)	0.18(3)	0.10(3)	0.20(4)	0.15(3)	0.10(3)
O(1) x	0.4891(7)	0.4883(4)	0.4885(7)	0.4884(7)	0.4876(7)	0.4882(7)	0.4875(7)	0.4878(9)
O(1) $B/\text{\AA}^2$	0.9(2)	0.68(7)	0.8(2)	0.9(1)	0.8(1)	0.7(1)	0.6(2)	1.0(3)
O(2) x	0.1772(6)	0.1727(3)	0.1762(6)	0.1758(7)	0.1754(5)	0.1751(5)	0.1748(5)	0.1746(6)
O(2) z	0.4105(4)	0.4151(1)	0.4120(4)	0.4125(4)	0.4127(4)	0.4125(4)	0.4124(4)	0.4135(4)
O(2) $B/\text{\AA}^2$	1.1(2)	0.90(6)	1.3(2)	0.9	0.8	0.7	1.2(2)	1.0(2)
$R_{wp} / \%$	11.75	7.88	11.44	11.98	10.83	10.78	11.25	13.32
$R_l / \%$	2.00	2.37	1.73	2.58	2.04	2.35	1.76	1.91
$R_F / \%$	1.39	1.54	1.20	1.65	1.27	1.63	1.09	1.40
$R_e / \%$	8.42	6.31	8.44	8.69	7.58	8.10	7.64	9.58

Table 4.2.2 Selected bond lengths (Å) and angles (°) for $Ba_3LnRu_2O_9$

	Y	In	La	Ce	Pr	Nd*	Sm	Eu
Ba(1)–O(1)	×6	2.912(1)	2.981(1)	2.946(5)	2.945(5)	2.967(1)	2.959(1)	2.962(1)
Ba(1)–O(2)	×6	2.963(6)	2.918(9)	2.979(7)	2.974(5)	2.968(1)	2.964(8)	2.960(9)
Ba(2)–O(1)	×3	2.901(4)	2.924(6)	2.847(6)	2.888(4)	2.867(2)	2.903(6)	2.894(7)
Ba(2)–O(2)	×6	2.944(1)	2.910(1)	2.986(1)	2.950(5)	2.971(1)	2.960(1)	2.963(1)
Ba(2)–O(2)	×3	3.078(5)	2.997(9)	3.393(6)	3.150(7)	3.255(2)	3.154(8)	3.190(9)
Ru–O(1)	×3	2.028(5)	2.006(7)	2.046(7)	2.024(8)	2.033(2)	2.030(7)	2.034(9)
Ru–O(2)	×3	1.934(5)	1.964(9)	1.908(7)	1.962(8)	1.926(2)	1.926(8)	1.918(9)
Ru–O (average)		1.981(5)	1.985(8)	1.977(7)	1.993(8)	1.979(2)	1.978(7)	1.976(9)
Ru–Ru		2.540(2)	2.563(4)	2.554(3)	2.481(3)	2.486(2)	2.536(3)	2.537(4)
Ln–O(2)	×6	2.199(5)	2.107(9)	2.332(7)	2.213(8)	2.273(1)	2.243(8)	2.260(9)
Ru–O(2)–Ln		179.0(3)	177.9(5)	176.2(4)	179.9(4)	177.5(1)	178.0(4)	177.5(5)
Ru–O(1)–Ru		77.5(3)	79.4(4)	77.2(3)	75.6(4)	76.5(3)	77.3(3)	77.2(4)

Note. * Neutron diffraction data at room temperature.

Table 4.2.2 *continued*

	Gd	Tb*	Dy	Ho	Er	Tm	Yb	Lu
Ba(1)–O(1)	×6	2.957(1)	2.921(2)	2.948(1)	2.944(1)	2.941(1)	2.937(1)	2.930(1)
Ba(1)–O(2)	×6	2.964(6)	2.953(3)	2.962(6)	2.960(7)	2.956(6)	2.947(6)	2.948(6)
Ba(2)–O(1)	×3	2.893(5)	2.890(4)	2.903(5)	2.905(5)	2.911(4)	2.907(5)	2.908(6)
Ba(2)–O(2)	×6	2.958(1)	2.921(2)	2.948(1)	2.944(1)	2.941(1)	2.936(1)	2.929(1)
Ba(2)–O(2)	×3	3.147(6)	3.042(4)	3.095(6)	3.081(7)	3.068(6)	3.063(6)	3.039(6)
Ru–O(1)	×3	2.034(6)	2.002(4)	2.026(6)	2.029(6)	2.021(5)	2.024(6)	2.019(7)
Ru–O(2)	×3	1.929(6)	1.982(3)	1.939(6)	1.937(6)	1.938(5)	1.935(6)	1.940(6)
Ru–O (average)		1.982(6)	1.992(3)	1.982(6)	1.983(6)	1.980(5)	1.980(6)	1.980(6)
Ru–Ru		2.527(3)	2.493(6)	2.530(3)	2.547(3)	2.545(3)	2.543(3)	2.549(3)
Ln–O(2)	×6	2.237(6)	2.132(3)	2.206(6)	2.196 (7)	2.188(5)	2.184(6)	2.166(6)
Ru–O(2)–Ln		178.3(3)	179.9(2)	178.8(3)	178.7(4)	178.7(3)	178.4(3)	178.8(3)
Ru–O(1)–Ru		76.8(3)	77.0(2)	77.3(3)	77.7(3)	78.0(3)	77.9(3)	78.3(3)

Table 4.2.3 Ru–Ru distance in the Ru_2O_9 dimer for $Ba_3MRu_2O_9$

	Compounds	Ru–Ru distance	Reference
Ru^{4+}	$Ba_3TiRu_2O_9$	2.515	[4.17] ^{*1}
	$Ba_3CeRu_2O_9$	2.483	[4.12]
		2.481	this study
	$Ba_3PrRu_2O_9$	2.486	this study
	$Ba_3TbRu_2O_9$	2.493	this study ^{*1}
$Ru^{4.5+}$	$Ba_3YRu_2O_9$	2.526	[4.18]
		2.540	this study
	$Ba_3InRu_2O_9$	2.517	[4.10] ^{*1}
		2.582	[4.19]
		2.563	this study
	$Ba_3LaRu_2O_9$	2.554	this study
	$Ba_3NdRu_2O_9$	2.524	this study ^{*1}
	$Ba_3SmRu_2O_9$	2.533	[4.12]
		2.583	[4.19]
		2.537	this study
	$Ba_3EuRu_2O_9$	2.536	this study
	$Ba_3GdRu_2O_9$	2.534	[4.18]
		2.527	this study
	$Ba_3DyRu_2O_9$	2.527	[4.12]
		2.530	this study
	$Ba_3HoRu_2O_9$	2.547	this study
	$Ba_3ErRu_2O_9$	2.534	[4.12]
		2.545	this study
	$Ba_3TmRu_2O_9$	2.543	this study
	$Ba_3YbRu_2O_9$	2.541	[4.18]
		2.547	this study
	$Ba_3LuRu_2O_9$	2.549	this study
Ru^{5+}	$Ba_3MgRu_2O_9$	2.68	[4.2]
	$Ba_3CoRu_2O_9$	2.677	[4.9] ^{*1}
		2.684	[4.10] ^{*1}
	$Ba_3NiRu_2O_9$	2.681	[4.9] ^{*1}
		2.686	[4.10] ^{*1}
	$Ba_3CuRu_2O_9$	2.701	[4.10] ^{*1, *2}
	$Ba_3ZnRu_2O_9$	2.685	[4.9] ^{*1}
	$Ba_3CaRu_2O_9$	2.649	[4.20]
	$Ba_3SrRu_2O_9$	2.676	[4.21] ^{*1, *3}

Note. ^{*1} Neutron diffraction data at room temperature,
^{*2} orthorhombic structure, and ^{*3} monoclinic structure.

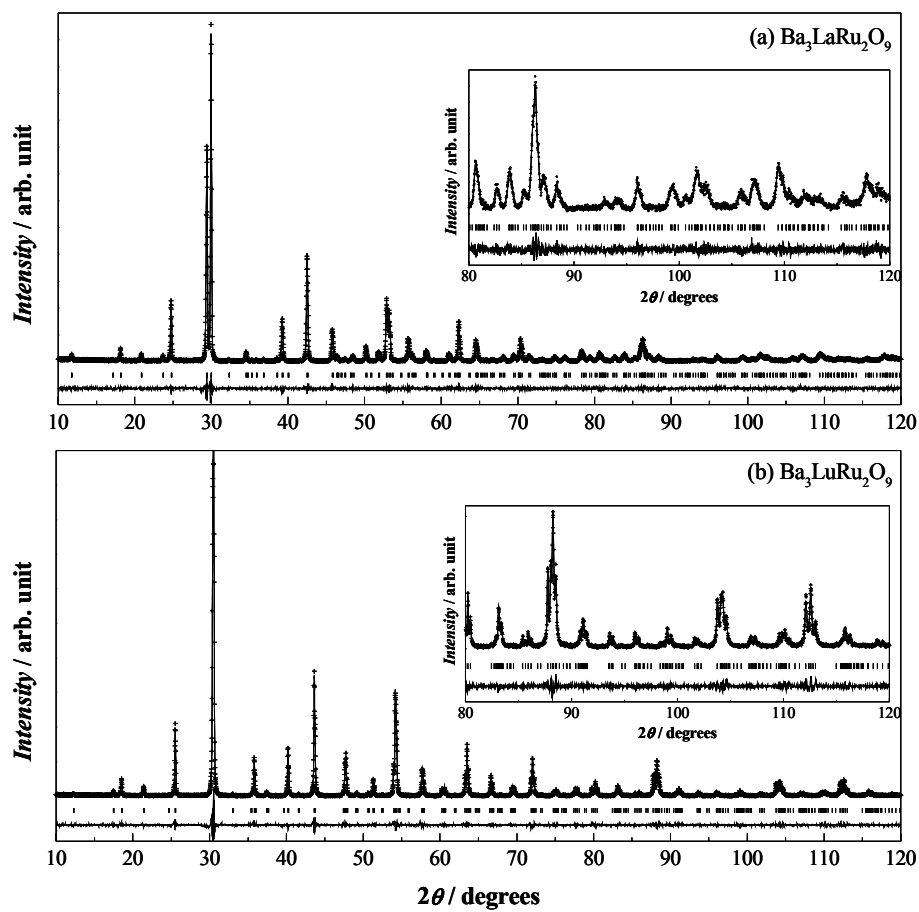


Figure 4.2.1 X-ray diffraction profiles for (a) $\text{Ba}_3\text{LaRu}_2\text{O}_9$ and (b) $\text{Ba}_3\text{LuRu}_2\text{O}_9$.

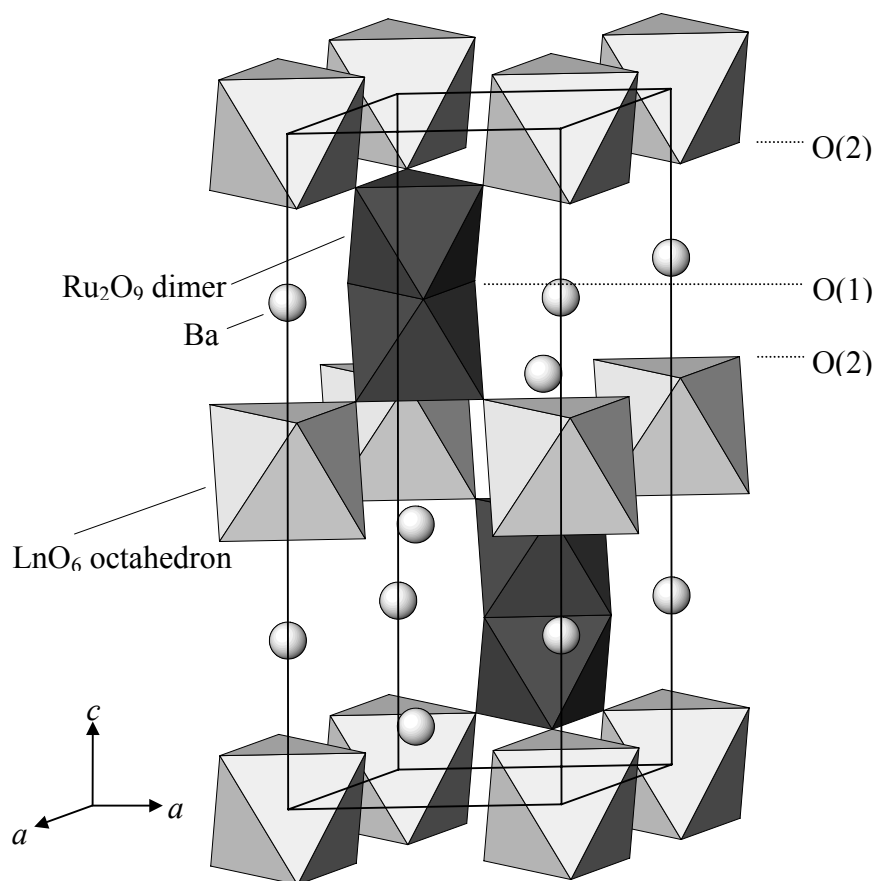


Figure 4.2.2 The crystal structure of $Ba_3LnRu_2O_9$.

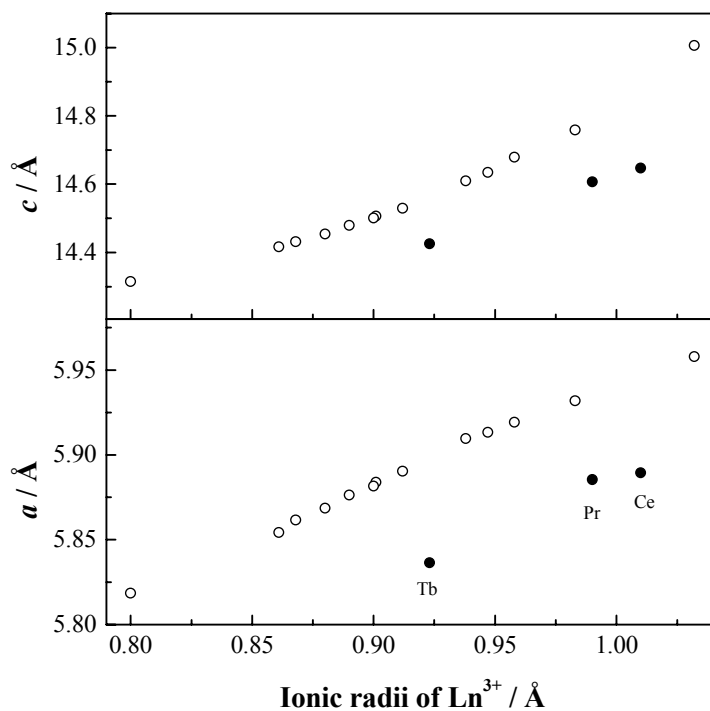


Figure 4.2.3 Variation of lattice parameters of $Ba_3LnRu_2O_9$ with the ionic radius of Ln^{3+} .

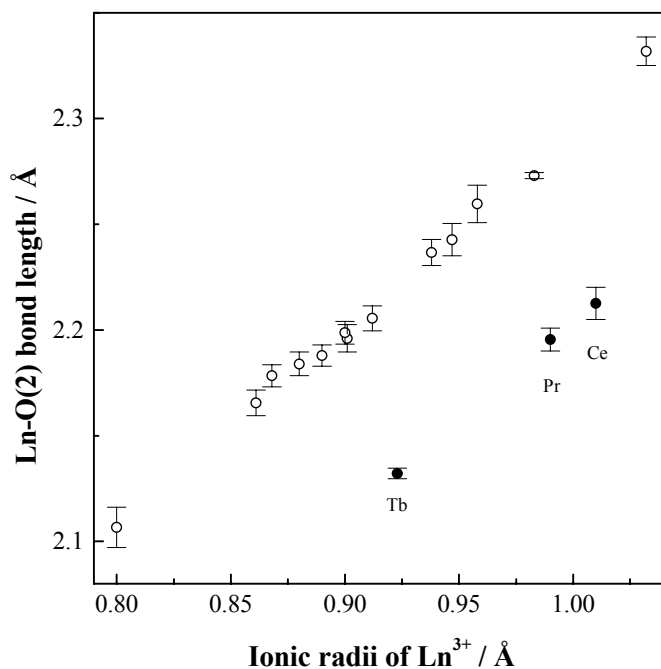


Figure 4.2.4 Variation of the Ln-O(2) bond lengths of $Ba_3LnRu_2O_9$ with the ionic radius of Ln^{3+} .

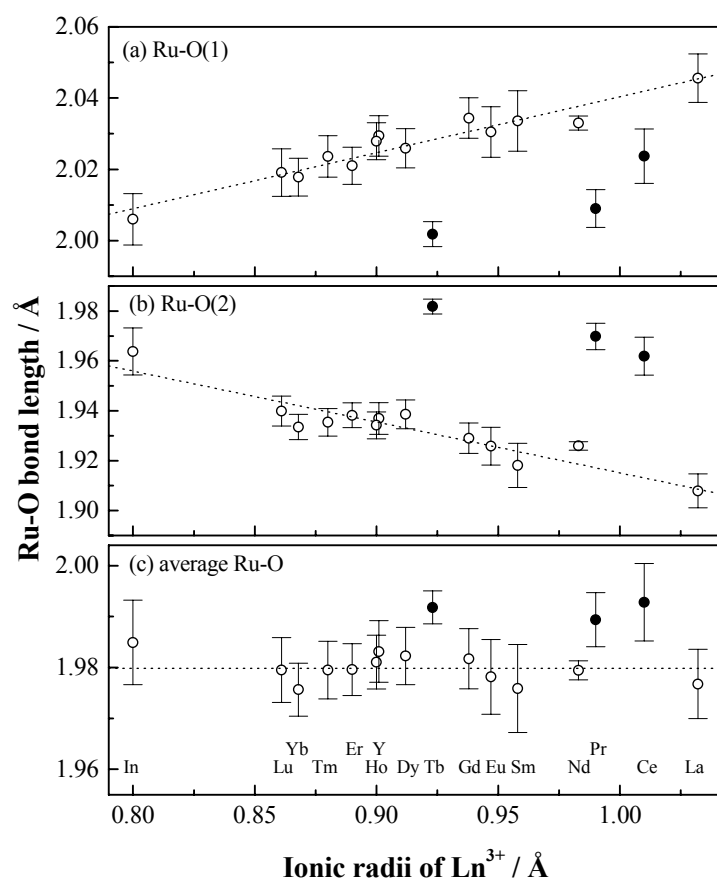


Figure 4.2.5 Variation of the Ru–O bond lengths of $Ba_3LnRu_2O_9$: (a) Ru–O(1), (b) Ru–O(2), and (c) average Ru–O lengths.

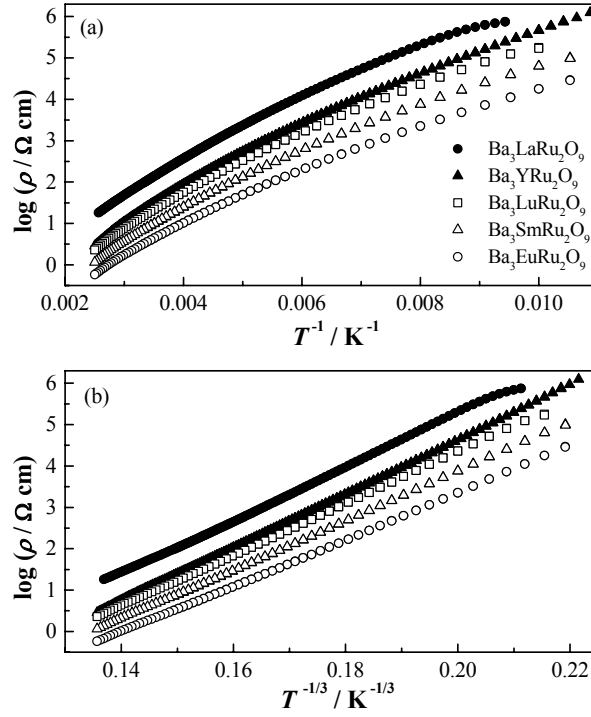


Figure 4.2.6 Temperature dependence of the resistivity for $\text{Ba}_3\text{LnRu}_2\text{O}_9$ (Ln = Y, La, Sm, Eu, and Lu). (a) $\log \rho$ vs. T^{-1} plot; (b) $\log \rho$ vs. $T^{-1/3}$ plot.

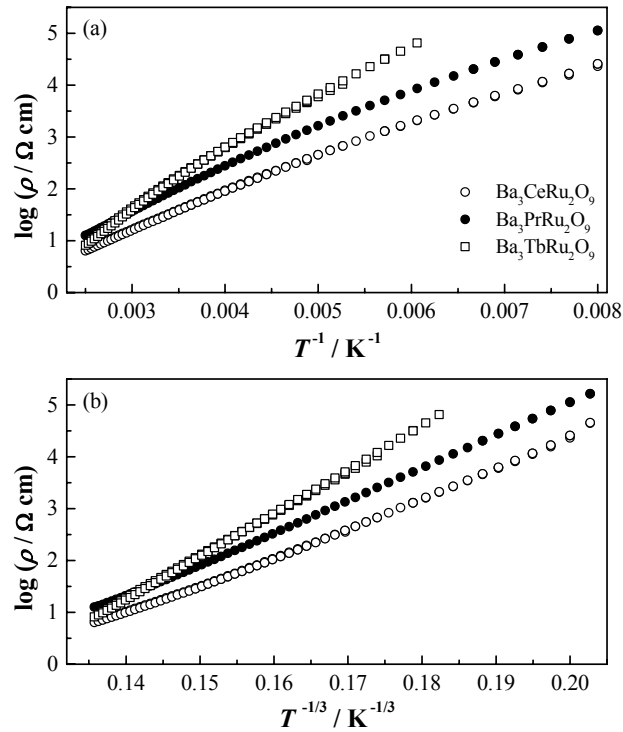


Figure 4.2.7 Temperature dependence of the resistivity for $\text{Ba}_3\text{LnRu}_2\text{O}_9$ (Ln = Ce, Pr, and Tb). (a) $\log \rho$ vs. T^{-1} plot; (b) $\log \rho$ vs. $T^{-1/3}$ plot.

4.3 Magnetic properties of 6H-perovskites Ba₃LnRu₂O₉ (Ln = Y, In, La, Sm, Eu, and Lu)

4.3.1 Introduction

The magnetic properties of 6H-perovskites Ba₃LnRu₂O₉ (Ln = Y, In, La, Sm, Eu, and Lu) will be discussed in this section. As described in section 4.2, these compounds have a hexagonal unit cell, and two kinds of the B site ions, Ru and Ln, occupy the face-sharing octahedral sites (Ru₂O₉ dimer) and the corner-sharing octahedral ones (LnO₆ octahedron), respectively. It is also shown that the Ru ions in the Ru₂O₉ dimer in these compounds have a valence state of +4.5. When this Ru^{4.5+}₂O₉ dimer adopts a charge configuration of Ru⁴⁺Ru⁵⁺O₉, the total spin of a dimer may be $S = 1/2$ at sufficiently low temperatures. In that case, it is expected that not only the intra-dimer magnetic interaction but also the interaction between the dimers contribute to the magnetic properties of Ba₃Ln³⁺Ru^{4.5+}₂O₉. However, there are few researches on this system, and their magnetic properties at low temperatures are not well known. In order to elucidate the magnetic behavior of Ru^{4.5+}₂O₉ dimer, the magnetic susceptibility and specific heat of the Ba₃LnRu₂O₉, in which the Ln³⁺ ions are nonmagnetic or weak magnetic (Ln = Y, In, La, Sm, Eu, and Lu), are performed.

4.3.2 Experimental

The samples of Ba₃LnRu₂O₉ (Ln = Y, In, La, Sm, Eu, and Lu) were prepared by the solid-state reaction. As starting materials, BaCO₃, RuO₂, and Ln₂O₃ were used. The samples were fired in air first at 1173 K for 12 h, and then at 1373 K (for Ln = In) or at 1473 K (for other samples) for 60–108 h. The progress of the reaction of both samples was monitored by powder X-ray diffraction measurements.

The temperature dependence of the magnetic susceptibilities was measured under both zero-field-cooled (ZFC) and field-cooled (FC) conditions in an applied field of 0.1 T over the temperature range 1.8–400 K using a SQUID magnetometer (Quantum Design, MPMS-5S).

Specific heat measurements were performed using a relaxation technique with a commercial heat capacity measurements system (Quantum Design, PPMS model) in the temperature range 1.8–300 K. The sintered sample in the form of a pellet was mounted on a thin alumina plate with grease for better thermal contact.

4.3.3 Results and discussion

4.3.3.1 Magnetic susceptibility

The temperature dependence of the magnetic susceptibilities (χ_M) for $Ba_3LnRu_2O_9$ is plotted in Fig. 4.3.1. Except for the La compound, they show a broad maximum at 290 K (for $Ln = Y$), 370 K (In), 180 K (Sm), 135 K (Eu), and 345 K (Lu). The magnetic susceptibility of $Ba_3LaRu_2O_9$ shows a plateau around 22 K. None of these compounds obey the Curie-Weiss law. In addition, it is found that they show another magnetic anomaly at low temperatures: 4.5 K (for $Ln = Y$), 4.5 K (In), 6.0 K (La), 12.5 K (Sm), 9.5 K (Eu), and 9.5 K (Lu).

The observed broad maxima above 100 K are similar to that found in the magnetic susceptibility vs. temperature curves for $Ba_3M^{2+}Ru^{5+}_2O_9$ ($M = Mg, Ca, Sr, \text{ and } Cd$) reported by Darriet et al. [4.2]. They explained this behavior using a dimer model, in which two spins of Ru^{5+} ions in the Ru_2O_9 dimer couple antiferromagnetically. The effective magnetic moments per molecule are calculated from the equation $\mu_{\text{eff}} = 2.828 (\chi_M T)^{1/2}$, and their temperature dependence is illustrated in Fig. 4.3.2(a). They decrease gradually with decreasing temperature down to 0.24–0.45 μ_B at 1.8 K. Therefore, the magnetic interaction between Ru ions in the dimer is antiferromagnetic rather than ferromagnetic.

Since the average valency of ruthenium ions is +4.5 in the title compounds, the dimer model (see section 4.1.2) is applied to the observed magnetic susceptibilities; in this model, it is assumed that all dimers adopt a valence state of $Ru^{4+}Ru^{5+}O_9$ (i.e. d^4-d^3 dimer):

$$\chi_{45low} = \frac{N_A g^2 \mu_B^2}{3k_B T} \times \frac{3}{4} \times \frac{x^8 + 10x^5 + 35}{x^8 + 2x^5 + 3} \quad (4.7)$$

or

$$\chi_{45high} = \frac{N_A g^2 \mu_B^2}{3k_B T} \times \frac{3}{4} \times \frac{x^{15} + 10x^{12} + 35x^7 + 84}{x^{15} + 2x^{12} + 3x^7 + 4}. \quad (4.8)$$

Equations (4.7) and (4.8) express the magnetic susceptibility for the low-spin ($S_{Ru4+} = 1$) dimers and that for the high-spin ($S_{Ru4+} = 2$) dimers, respectively. The temperature dependence of the effective magnetic moments calculated from the Eqs. (4.7) and (4.8) (for $g = 2$; $J = 50, 200, -50, -100, -150$, and -200 K) are plotted in Fig. 4.3.2(b). The curves calculated for the positive J values do not match the experimental data. In the case of the negative J values, the temperature dependence of the calculated effective magnetic moments resembles the experimental data in the higher temperature region. They approach $1.732 \mu_B$ (i.e., $S = 1/2$ per dimer) with decreasing temperature; however, the experimental data are still smaller than this value. This result indicates that there exist the antiferromagnetic orderings of Ru_2O_9 dimers in these $Ba_3LnRu_2O_9$ compounds. Measurements of the magnetic susceptibility and specific heat (as will be described later) show the anomalies at low temperatures due to these antiferromagnetic interactions.

4.3.3.2 Specific heat

Figure 4.3.3 shows the variation of the specific heat divided by temperature (C_p/T) as a function of temperature. An anomaly has been observed for each compound, which corresponds to the anomaly found at low temperatures in the magnetic susceptibility. For $Ba_3LaRu_2O_9$, a small specific heat anomaly has been found at 22 K, which is consistent with the slight plateau observed in the susceptibility vs. temperature curve at the same temperature. For $Ba_3SmRu_2O_9$, another broad anomaly has been observed at around 4 K.

The total entropy is calculated by $S_{total} = \int C_p/T dT$. In order to estimate the entropy below 1.8 K, the extrapolated curve of $C_p/T \propto T^2$ was used (see the dotted curves in Figure 4.3.3). The temperature dependence of the total entropy is shown in Figure 4.3.4. The magnetic entropy change derived from this magnetic anomaly is estimated to be

approximately $3.0 \text{ J}\cdot\text{mol}^{-1}\cdot\text{K}^{-1}$ (for $Ln = Y, In, Eu, Lu$), $6.0 \text{ J}\cdot\text{mol}^{-1}\cdot\text{K}^{-1}$ (for $Ln = Sm$), and $0.3 \text{ J}\cdot\text{mol}^{-1}\cdot\text{K}^{-1}$ (for $Ln = La$). These magnetic entropy changes correspond to the antiferromagnetic orderings of Ru_2O_9 dimers. The value of $3.0 \text{ J}\cdot\text{mol}^{-1}\cdot\text{K}^{-1}$ is smaller than the expected value $R \ln (2S + 1) = R \ln 2 = 5.76 \text{ J}\cdot\text{mol}^{-1}\cdot\text{K}^{-1}$. This may be due to the occurrence of the short-range magnetic ordering at higher temperatures than the respective magnetic transition temperatures. The entropy change for $Ba_3SmRu_2O_9$ is larger than those for the others. It contains two entropy changes for the anomalies at 12.5 and 4 K observed in the C_p/T vs. temperature curve. The anomaly at 12.5 K is due to the antiferromagnetic ordering between Ru_2O_9 dimers and that at 4 K is possibly a Schottky-type one which is caused by the energy level splitting of the ground doublet Γ_7 of Sm^{3+} ions in the internal magnetic field made by the magnetic ordering of the Ru_2O_9 dimers. For $Ba_3EuRu_2O_9$, the entropy change is very close to that of $Ba_3LnRu_2O_9$ ($Ln = \text{nonmagnetic } Y^{3+}, In^{3+} \text{ and } Lu^{3+} \text{ ions}$). This fact indicates that the Eu^{3+} is a nonmagnetic ion with the $J = 0$ ground state.

The temperature dependence of the magnetic susceptibility and specific heat for $Ba_3LaRu_2O_9$ is different from that for the other $Ba_3LnRu_2O_9$, i.e., its magnetic susceptibility has a slight plateau around 22 K without showing any maximum, and the entropy change for the magnetic anomaly estimated from the specific heat measurements is much smaller than those for the other $Ba_3LnRu_2O_9$ compounds. These differences in the magnetic behavior may arise from the distortion of the Ru_2O_9 polyhedron. The $Ba_3LaRu_2O_9$ has the most distorted Ru_2O_9 polyhedron, i.e., the difference between $Ru-O(1)$ and $Ru-O(2)$ bond lengths is the largest among the series of $Ba_3LnRu_2O_9$ (see Fig. 4.2.5).

4.3.4 Summary

In this section, magnetic properties of $Ba_3LnRu_2O_9$ in which the Ln^{3+} ions are nonmagnetic or weak magnetic ($Ln = Y, In, La, Sm, Eu, \text{ and } Lu$) have been studied. The magnetic susceptibilities show a broad maximum at 135–370 K except for the La compound, which shows a plateau around 22 K. In addition, another magnetic anomaly

is found at 4.5–12.5 K by the magnetic susceptibility and specific heat measurements for any compound. It is considered that this magnetic behavior is ascribable to the antiferromagnetic coupling between two Ru ions in a Ru_2O_9 dimer and to the magnetic interaction between the Ru_2O_9 dimers.

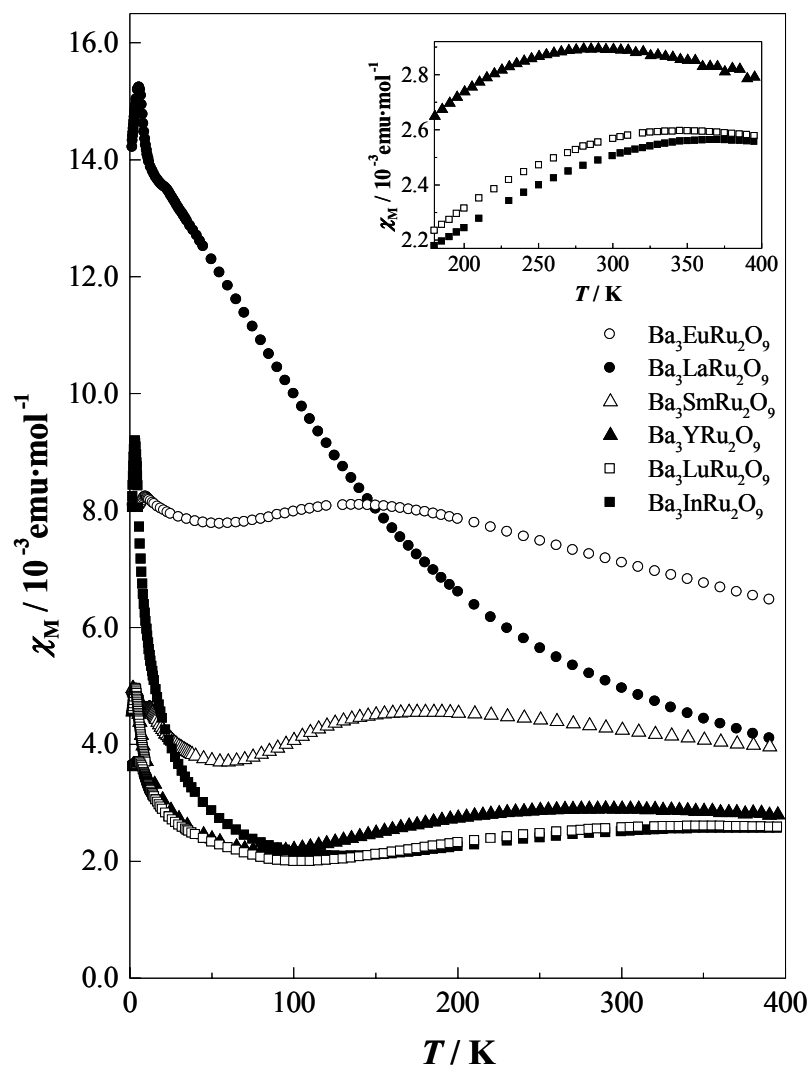


Figure 4.3.1 Temperature dependence of the magnetic susceptibility for $Ba_3LnRu_2O_9$ ($Ln = Y, In, La, Sm, Eu, \text{ and } Lu$).

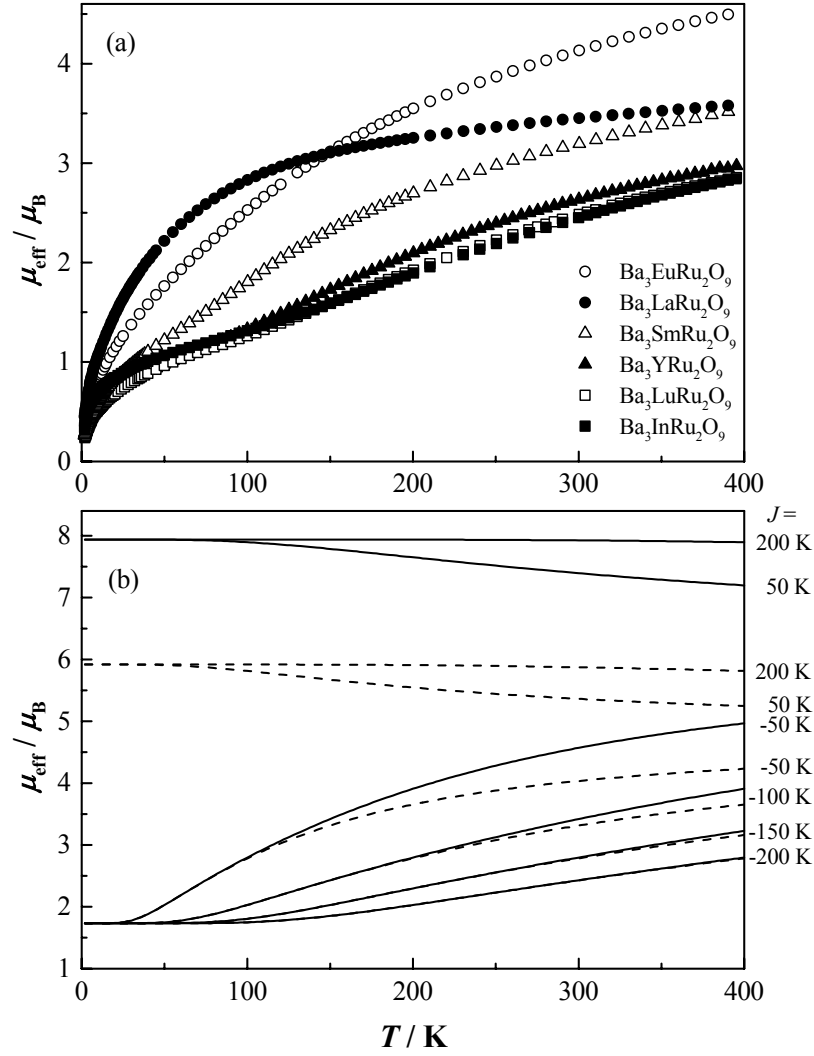


Figure 4.3.2 (a) Temperature dependence of the effective magnetic moment of $Ba_3LnRu_2O_9$. (b) The dashed and solid lines are the effective magnetic moments calculated by Eqs. (4.7) and (4.8), respectively.

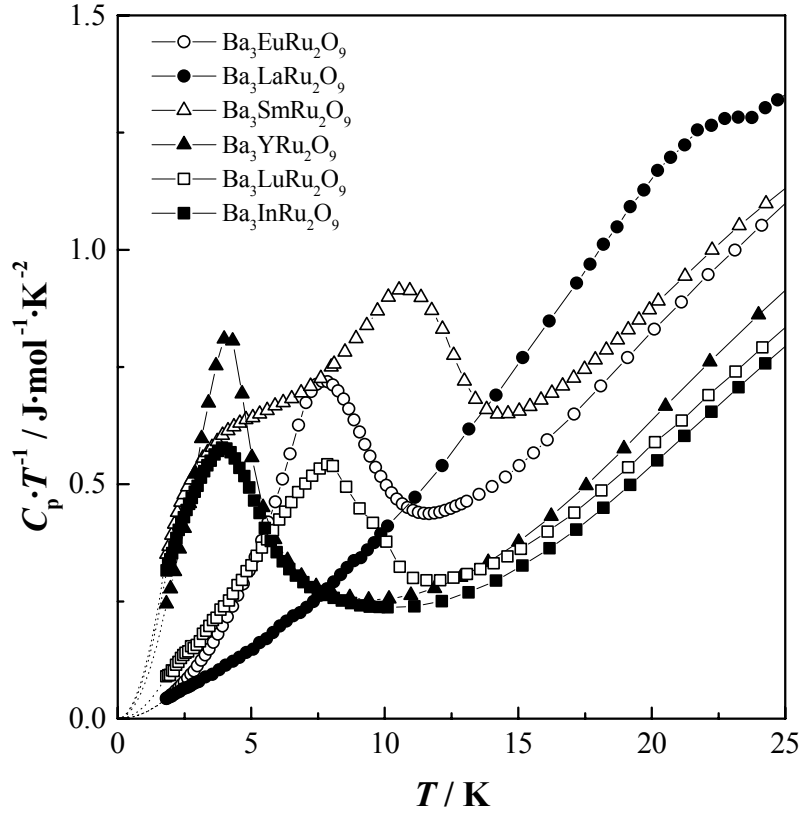


Figure 4.3.3 Temperature dependence of the specific heat divided by temperature (C_p/T) for $Ba_3LnRu_2O_9$. The dotted lines at low temperatures are the extrapolated curves of $C_p/T \propto T^2$.

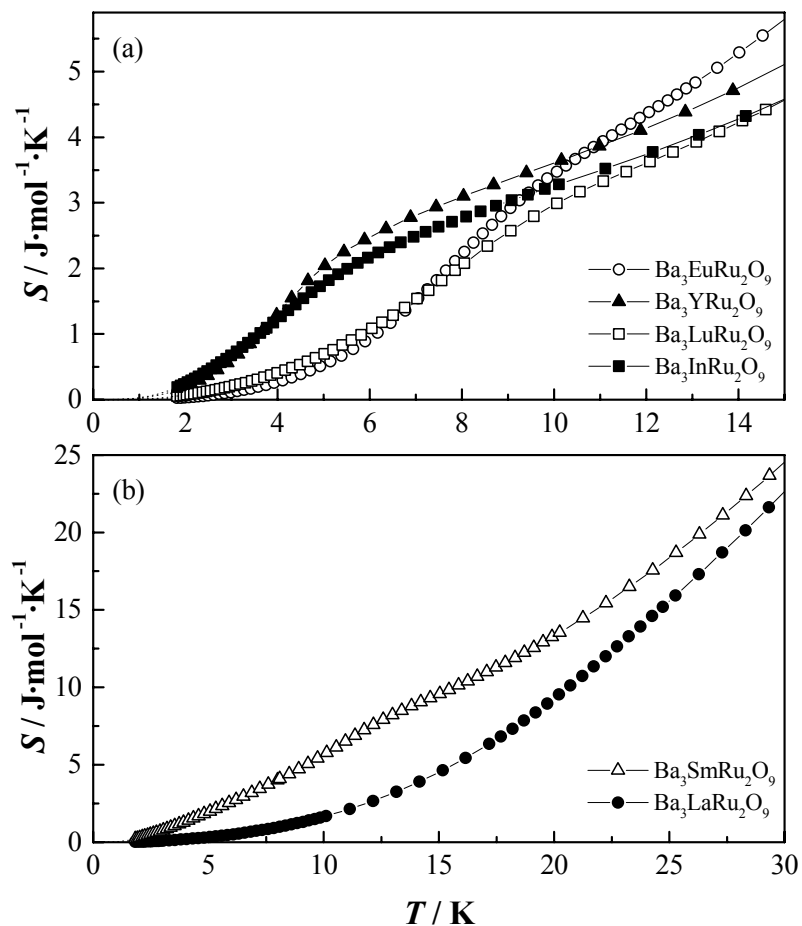


Figure 4.3.4 Temperature dependence of the total entropy of $Ba_3LnRu_2O_9$: (a) $Ln = Y, In, Eu, \text{ and } Lu$, (b) $Ln = La \text{ and } Sm$.

4.4 Magnetic and neutron diffraction studies on 6H-perovskites $Ba_3Ln^{4+}Ru^{4+}_2O_9$ ($Ln = Ce, Pr, \text{ and } Tb$)

4.4.1 Introduction

This section describes the magnetic properties of 6H-perovskites $Ba_3LnRu_2O_9$ with $Ln = Ce, Pr, \text{ or } Tb$. These three compounds have a valence configuration of $Ba_3Ln^{4+}Ru^{4+}_2O_9$ (section 4.2). Therefore, it is expected that they will show many interesting magnetic properties due to the magnetic behavior of the $Ru^{4+}_2O_9$ dimer and to the magnetic interactions between the Ru^{4+} and Ln^{4+} ions. In order to elucidate their magnetic properties, their magnetic susceptibility and specific heat measurements are carried out. In addition, the magnetic structure of the Tb compound is determined by the neutron diffraction measurement.

4.4.2 Experimental

The samples of $Ba_3LnRu_2O_9$ ($Ln = Ce, Pr, \text{ and } Tb$) were prepared by the solid-state reaction. As starting materials, $BaCO_3$, RuO_2 , CeO_2 , Pr_6O_{11} , and Tb_4O_7 were used. The samples were fired in air first at 1173 K for 12 h, and then at 1473 K for 24×4 h ($Ln = Ce$) or at 1473 K for 24×2 h and at 1573 K for 24×4 h ($Ln = Pr, Tb$). The progress of the reaction of both samples was monitored by powder X-ray diffraction measurements.

Powder neutron diffraction profiles for $Ba_3TbRu_2O_9$ were measured at 2 and 15 K, and at room temperature in the range $3^\circ \leq 2\theta \leq 153^\circ$ at intervals of 0.1° with the wavelength of 1.8196 Å. Measurements were performed on the Kinken powder diffractometer for High Efficiency and high Resolution MEaSurements, HERMES, of the Institute for Materials Research (IMR), Tohoku University [2.24], installed at the JRR-3M Reactor in the Japan Atomic Research Institute (JAERI), Tokai. Crystal and magnetic structures were determined by the Rietveld technique, using the program RIETAN2000 [4.7].

The magnetic measurements were carried out using a SQUID magnetometer (Quantum Design, MPMS-5S). The temperature dependence of the magnetic susceptibilities was measured under both zero-field-cooled (ZFC) and field-cooled (FC)

conditions in an applied field of 0.1 T over the temperature range 1.8–400 K.

Specific heat measurements were performed using a relaxation technique with a commercial heat capacity measurement system (Quantum Design, PPMS model) in the temperature range 1.8–300 K. The sintered sample in the form of a pellet was mounted on a thin alumina plate with grease for better thermal contact.

4.4.3 Results and discussion

4.4.3.1 Crystal structure of Ba₃TbRu₂O₉ at low temperatures

Powder neutron diffraction (ND) measurements for Ba₃TbRu₂O₉ were performed at 2 and 15 K, and at room temperature. Their diffraction profiles are shown in Fig. 4.4.1. The Rietveld analyses of data collected at 15 K and room temperature indicate that Ba₃TbRu₂O₉ adopts the 6H-perovskite structures, which is consistent with the conclusions from the XRD data. No evidence for cation disorder or oxygen defects was found. The refined structural parameters, and some selected bond lengths and angles are summarized in Tables 4.4.1 and 4.4.2. The data collected at 2 K show a number of low angle peaks, which are not observed at 15 K and room temperature. They are due to an antiferromagnetic ordering of the Tb⁴⁺ ions. The crystal and magnetic structures at 2 K have been determined by the Rietveld method. The crystal structure at 2 K has the same symmetry as that at 15 K and room temperature, i.e., Ba₃TbRu₂O₉ does not show any structural phase transition down to 2 K. The magnetic structure will be discussed later.

4.4.3.2 Magnetic susceptibilities

The temperature dependence of the ZFC and FC magnetic susceptibilities for Ba₃PrRu₂O₉ are plotted in Fig. 4.4.2. The magnetic susceptibilities of Ba₃PrRu₂O₉ increase gradually above 100 K. In addition, they show an anomaly at 10.5 K and the divergence between the ZFC and FC susceptibilities is observed below this temperature. Both the Ru⁴⁺ ions (4d⁴) and Pr⁴⁺ ions (4f¹) should contribute to the magnetic susceptibility of Ba₃PrRu₂O₉. The Ru⁴⁺ ions form Ru₂O₉ dimers in this compound. The magnetic behavior above 100 K resembles that found in Ba₃M²⁺Ru⁵⁺₂O₉ (M²⁺ is nonmagnetic) reported by Darriet et al. [4.2]. Therefore, the author attempted to apply

the dimer model to the present results. The temperature dependence of the magnetic susceptibility for $Ru^{4+}_2O_9$ dimers should be represented by

$$\chi_{\text{dimer}} = \frac{N_A g^2 \mu_B^2}{3k_B T} \times \frac{6(x^4 + 5)}{x^6 + 3x^4 + 5} \quad (4.9)$$

or

$$\chi_{\text{dimer}} = \frac{N_A g^2 \mu_B^2}{3k_B T} \times \frac{6(x^{18} + 5x^{14} + 14x^8 + 30)}{x^{20} + 3x^{18} + 5x^{14} + 7x^8 + 9}. \quad (4.10)$$

The Eqs. (4.9) and (4.10) express the magnetic susceptibility for the low spin ($S_1 = S_2 = 1$) and high spin ($S_1 = S_2 = 2$) dimers, respectively. The observed susceptibilities of $Ba_3PrRu_2O_9$ show Curie-Weiss-like behavior at low temperatures. The Curie-Weiss term

$$\chi_{\text{CW}} = \frac{C}{T - \theta} \quad (4.11)$$

is added to the equations for dimers, χ_{dimer} (Eq. (4.9) or (4.10)):

$$\chi = \chi_{\text{dimer}} + \chi_{\text{CW}} + \chi_{\text{TIP}}, \quad (4.12)$$

where C , θ and χ_{TIP} are the Curie constant, the Weiss temperature, and the temperature independent paramagnetic susceptibility, respectively. In order to explain the temperature dependency of the magnetic susceptibility, Eq. (4.12) was fitted to the experimental data above 30 K. The solid lines in Fig. 4.4.2 represent the fitting results, and the following parameter values are determined from these fits:

	g	J/k_B [K]	C [emu·K·mol ⁻¹]	θ [K]	χ_{TIP} [10 ⁻⁴ emu·mol ⁻¹]
low spin model	1.98(2)	-281(1)	0.096(8)	-38(4)	9.2(4)
high spin model	1.98(2)	-280(1)	0.10(1)	-40(4)	9.0(4)

Both calculated susceptibilities are in comparatively good agreement with the experimental data. There is not a large difference between the two calculated curves in this temperature range; accordingly, it cannot be determined whether the high spin or low spin state is adopted.

The Curie-Weiss term of Eq. (4.12) would be due to the paramagnetism of the Pr⁴⁺ ions. The effective magnetic moment is about 0.9 μ_B , which is much smaller than that expected for a free f¹ ion (2.54 μ_B). This indicates that the crystal field with octahedral symmetry has a significant effect on the magnetic properties of Pr⁴⁺. A comparably small magnetic moment has been reported for the perovskites Ba_{1-x}Sr_xPrO₃ [4.25]. The value of J is ~ -280 K, which indicates the presence of an antiferromagnetic interaction in the dimers. The magnitude of this J value is larger than that for the most of the Ru⁵⁺₂O₉ dimers ($S_1 = S_2 = 3/2$; $J \sim -170$ K) [4.2, 26]. This means that the magnetic interaction in the Ru⁴⁺₂O₉ dimers is stronger than that in the Ru⁵⁺₂O₉ dimers. The difference in the Ru–Ru distance may be one of the causes for this phenomenon. The Ru–Ru distance in the Ru⁴⁺₂O₉ dimers is ~ 2.48 Å, which is much shorter than that in the Ru⁵⁺₂O₉ dimers (2.649–2.701 Å) (See Table 4.2.3).

The temperature dependence of the magnetic susceptibilities for Ba₃CeRu₂O₉ is also shown in Fig. 4.4.2. No divergency between the ZFC and FC susceptibilities has been found throughout the experimental temperature range. At low temperatures, no magnetic anomalies have been observed, that is, the susceptibilities of Ba₃CeRu₂O₉ decrease with increasing temperature. However, they increase slightly with temperature above 200 K. Only the Ru⁴⁺₂O₉ (4d⁴) dimers should contribute to the magnetic susceptibility of this compound, because the other ions are nonmagnetic. The author tried to fit the observed susceptibility data by using the same dimer model [Eq. (4.12)]. However, a good agreement between the observed and calculated susceptibilities was not obtained. This result means that the magnetic properties of Ba₃CeRu₂O₉ do not obey the simple dimer model. In order to explain this magnetic behavior, further magnetic measurements in the higher temperature range are needed.

The temperature dependence of the magnetic susceptibility of Ba₃TbRu₂O₉ is plotted in Fig. 4.4.3. The susceptibility shows a maximum at 9.5 K and decreases rapidly with decreasing temperature below this point, indicating the occurrence of an antiferromagnetic transition. Below the transition temperature, the ZFC and FC susceptibilities diverge. Attempts to fit the observed susceptibility using the same dimer

model [Eq. (4.12)] were unsuccessful. One reason for this may come from the fact that the magnetic susceptibility of the paramagnetic Tb^{4+} ions should be much larger than that of the dimers. The higher temperature data ($T > 100$ K) can be fitted using the Curie-Weiss law. The obtained effective magnetic moment and Weiss constant are $7.93(1) \mu_B$ and $-2.8(3)$ K, respectively. This effective magnetic moment is close to that for Tb^{4+} ions ($7.94 \mu_B$) rather than that for Tb^{3+} ions ($9.72 \mu_B$). The field dependence of the magnetization was measured at 5 and 20 K. A small hysteresis loop was observed at 5 K, and it has a remnant magnetization of $\sim 0.01\mu_B$. Generally, when the antiferromagnetically ordered spins on the two sublattices (up and down) are not exactly antiparallel and have a small canting angle, this canting gives rise to a small net moment and the weak ferromagnetism occurs. This may explain the observed small ferromagnetic moment.

4.4.3.3 Specific heat

Figure 4.4.4(a) shows the variation of the specific heat for $Ba_3LnRu_2O_9$ ($Ln = Ce, Pr \text{ and } Tb$) as a function of temperature. The specific heat measurements for $Ba_3PrRu_2O_9$ and $Ba_3TbRu_2O_9$ show λ -type anomalies at 10.5 K and 9.5 K, respectively, which correspond to the magnetic anomalies found in the magnetic susceptibilities. These facts indicate that an Ln^{4+} antiferromagnetic transition occurs at these temperatures. The temperature dependence of the total entropy has been calculated from the specific heat data, and it is shown in Fig. 4.4.4(b). If it is assumed that the electronic and lattice contributions to the specific heat are equal among these three compounds, the difference in the total entropy between the Ce and Pr compounds (or between the Ce and Tb compounds) should be equal to the magnetic entropy of Pr^{4+} (or Tb^{4+}). The magnetic entropies of Pr^{4+} and Tb^{4+} estimated at 15 K are 3.2 and $9.5 \text{ J}\cdot\text{mol}^{-1}\cdot\text{K}^{-1}$, respectively. The ground state $^2F_{5/2}$ of the Pr^{4+} ion is split into a doublet (Γ_7) and a quartet (Γ_8) in the octahedral symmetry. The magnetic entropy change of $Ba_3PrRu_2O_9$ is close to $R \ln 2 = 5.76 \text{ J}\cdot\text{mol}^{-1}\cdot\text{K}^{-1}$ rather than $R \ln 4 = 11.53 \text{ J}\cdot\text{mol}^{-1}\cdot\text{K}^{-1}$, which suggests that the ground state is Γ_7 . The effective magnetic moment obtained from the

experimental data ($\sim 0.9 \mu_B$) is close to that expected from this ground state:

$$g_J \sqrt{J_z(J_z + 1)} = \frac{6}{7} \sqrt{\frac{5}{6}(\frac{5}{6} + 1)} = 1.06 \mu_B.$$

The magnetic entropy change of $Ba_3TbRu_2O_9$ is $9.5 \text{ J} \cdot \text{mol}^{-1} \cdot \text{K}^{-1}$, which is smaller than that expected from $R \ln (2S + 1) = R \ln 8 = 17.29 \text{ J} \cdot \text{mol}^{-1} \cdot \text{K}^{-1}$. The cause of this discrepancy is not clear at present. There may be a short range magnetic ordering of Tb^{4+} ions above the magnetic transition temperature.

4.4.3.4 Magnetic structure of $Ba_3TbRu_2O_9$

As has been mentioned earlier, some magnetic reflection peaks were observed in the neutron diffraction data collected at 2 K (see Fig. 4.4.1). All magnetic peaks are indexed in the crystallographic unit cell with odd values of l ; however, the (001) peak ($2\theta = \sim 7.2^\circ$) and other (00 l) peaks are negligibly weak. These facts indicate that two Tb^{4+} ions occupying the $2a$ Wyckoff positions have antiparallel magnetic moments with each other, and that the direction of ordered moments is parallel to the c axis. On the other hand, the ordered moments of Ru ions were not determined. This may be due to an absence of long range magnetic ordering of the Ru_2O_9 dimers. The magnetic structure of $Ba_3TbRu_2O_9$ is illustrated in Fig. 4.4.5. In this magnetic structure, the magnetic moments of the Tb^{4+} ions order ferromagnetically in the xy plane, and these ferromagnetic sheets are stacked antiferromagnetically along the c axis. The direction of ordered moments is parallel to the c axis. The ordered magnetic moment of Tb^{4+} ions is $6.84(4) \mu_B$. This value is reasonable for Tb^{4+} ($4f^7$) and comparable to those of other perovskites containing Tb^{4+} ions: $6.76 \mu_B$ ($SrTbO_3$) and $6.5 \mu_B$ ($BaTbO_3$) at 10 K [4.27].

4.4.4 Summary

In this section, magnetic properties of $Ba_3LnRu_2O_9$ ($Ln = Ce, Pr, \text{ or } Tb$) with a valence configuration of $Ba_3Ln^{4+}Ru^{4+}_2O_9$ have been studied. The magnetic susceptibility and specific heat measurements show that the Ln^{4+} antiferromagnetic transition occurs at 9.5 K for $Ba_3TbRu_2O_9$ and at 10.5 K for $Ba_3PrRu_2O_9$. It was found that the temperature dependence of the magnetic susceptibility of $Ba_3PrRu_2O_9$ obeys the dimer model. Powder neutron diffraction measurements for $Ba_3TbRu_2O_9$ were

performed at 2 K, 15 K, and room temperature. The magnetic structure of $Ba_3TbRu_2O_9$ was determined by the Rietveld analysis of data collected at 2 K. The magnetic moments of Tb^{4+} ions order antiferromagnetically, while the ordered moments of Ru ions were not determined in this experiment. The direction of the magnetic moments for Tb^{4+} is along the c axis, and the ordered magnetic moment is $6.84(4) \mu_B$.

Table 4.4.1 Structural parameters for $Ba_3TbRu_2O_9$ determined by the neutron diffraction measurements

Atom	Site	x	y	z	$B / \text{\AA}^2$
space group: $P6_3/mmc$ (No. 194); $z = 2$					
room temperature					
$a = 5.8365(5) \text{\AA}$, $c = 14.4257(9) \text{\AA}$, $R_{wp} = 7.88 \%$, $R_I = 2.37 \%$, $R_F = 1.54 \%$, $R_e = 6.31 \%$					
Ba(1)	$2b$	0	0	1/4	0.59(12)
Ba(2)	$4f$	1/3	2/3	0.9066(3)	0.58(11)
Tb	$2a$	0	0	0	0.51(9)
Ru	$4f$	1/3	2/3	0.1636(2)	0.48(7)
O(1)	$6h$	0.4883(4)	0.9766	1/4	0.68(7)
O(2)	$12k$	0.1727(3)	0.3454	0.4151(1)	0.90(6)
15 K					
$a = 5.8236(4) \text{\AA}$, $c = 14.4096(7) \text{\AA}$, $R_{wp} = 5.98 \%$, $R_I = 1.68 \%$, $R_F = 1.02 \%$, $R_e = 3.60 \%$					
Ba(1)	$2b$	0	0	1/4	0.02(8)
Ba(2)	$4f$	1/3	2/3	0.9063(2)	0.11(7)
Nd	$2a$	0	0	0	0.18(6)
Ru	$4f$	1/3	2/3	0.1639(1)	0.24(5)
O(1)	$6h$	0.4896(3)	0.9792	1/4	0.41(5)
O(2)	$12k$	0.1728(2)	0.3456	0.4150(1)	0.46(4)
2 K					
$a = 5.8238(2) \text{\AA}$, $c = 14.4088(4) \text{\AA}$, $R_{wp} = 6.47 \%$, $R_I = 1.39 \%$, $R_F = 0.82 \%$, $R_e = 3.62 \%$					
Ba(1)	$2b$	0	0	1/4	0.04(8)
Ba(2)	$4f$	1/3	2/3	0.9063(2)	0.20(7)
Nd	$2a$	0	0	0	0.33(5)
Ru	$4f$	1/3	2/3	0.1640(2)	0.28(4)
O(1)	$6h$	0.4890(3)	0.9780	1/4	0.49(4)
O(2)	$12k$	0.1726(2)	0.3452	0.4150(1)	0.56(3)
Magnetic moment of Tb: $6.84(4) \mu_B$					
Direction of moment: [001]					

Table 4.4.2 Selected bond lengths (Å) and angles (°) for $Ba_3TbRu_2O_9$

	300 K	15 K	2 K
Ba(1)–O(1) × 6	2.921(2)	2.914(2)	2.914(2)
Ba(1)–O(2) × 6	2.953(3)	2.948(2)	2.946(2)
Ba(2)–O(1) × 3	2.890(4)	2.875(3)	2.878(3)
Ba(2)–O(2) × 6	2.921(2)	2.915(2)	2.915(2)
Ba(2)–O(2) × 3	3.042(4)	3.042(3)	3.043(3)
Ru–O(1) × 3	2.002(4)	2.006(3)	2.000(3)
Ru–O(2) × 3	1.982(3)	1.978(2)	1.981(2)
Ru–O (average)	1.992(3)	1.992(2)	1.991(3)
Ru–Ru	2.493(6)	2.482(4)	2.480(2)
Tb–O(2) × 6	2.132(3)	2.131(2)	2.129(2)
Ru–O(2)–Tb	179.9(2)	179.9(1)	179.9(1)
Ru–O(1)–Ru	77.0(2)	76.4(1)	76.6(1)

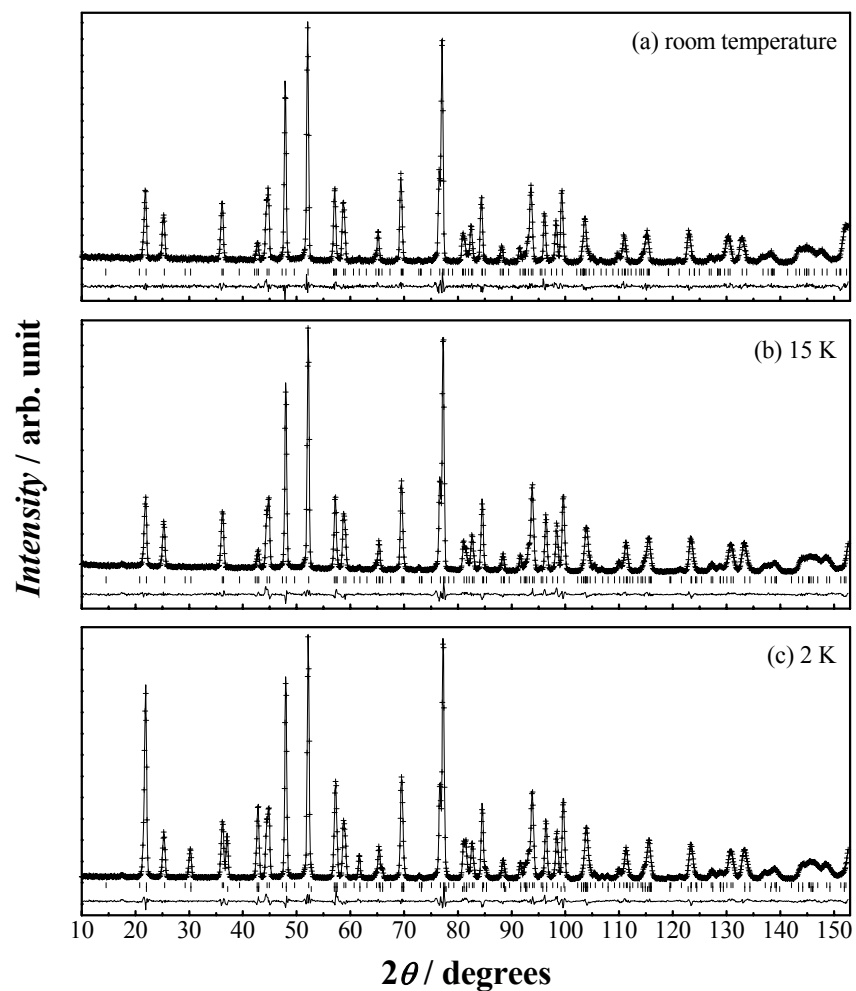


Figure 4.4.1 Powder neutron diffraction profiles for $Ba_3TbRu_2O_9$ at room temperature (a), at 15 K (b) and at 2 K (c). The calculated and observed diffraction profiles are shown on the top solid line and cross markers, respectively. The vertical marks show positions calculated from Bragg reflections. In (c), the magnetic reflection positions are shown as lower vertical marks. The bottom trace is a plot of the difference between calculated and observed intensities.

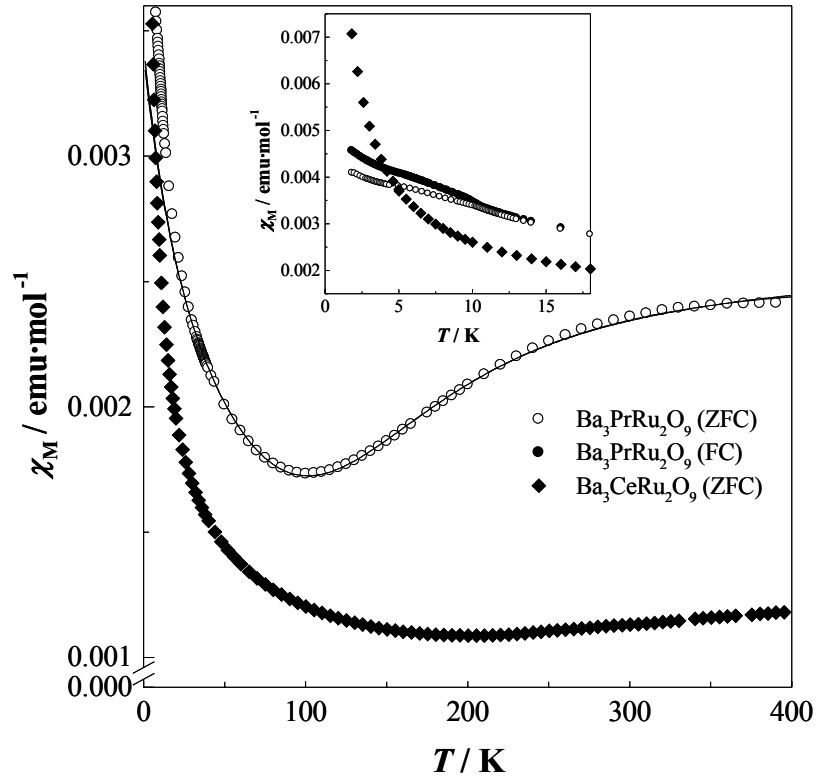


Figure 4.4.2 Temperature dependence of magnetic susceptibilities of $Ba_3CeRu_2O_9$ and $Ba_3PrRu_2O_9$. The applied field is 0.1 T. Inset shows the magnetic susceptibilities at low temperatures. The solid lines are the susceptibilities calculated by Eq. (4.12). These are for the low spin model and for the high spin model. In this figure, they overlap.

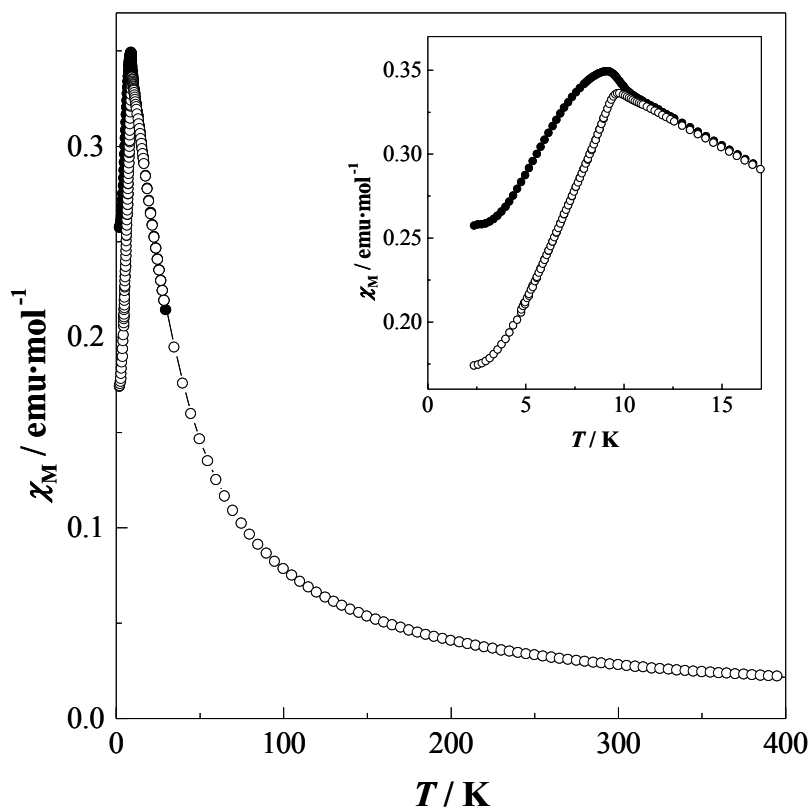


Figure 4.4.3 Temperature dependence of magnetic susceptibilities of $Ba_3TbRu_2O_9$. The open and filled symbols show the ZFC and FC susceptibilities, respectively. The applied field is 0.1 T.

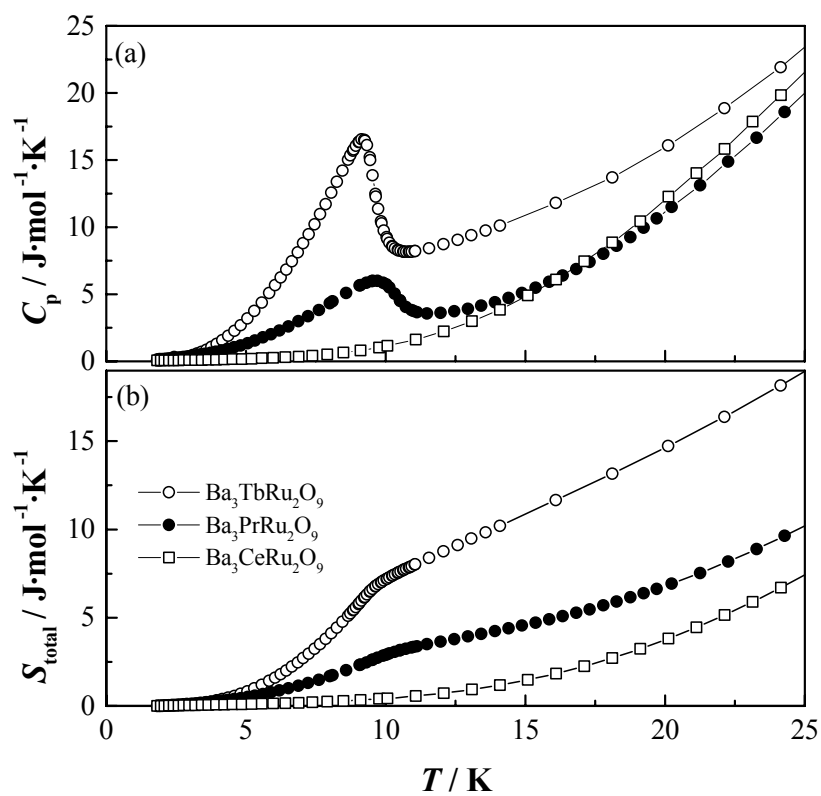


Figure 4.4.4 Temperature dependences of the specific heat (a) and the total entropy (b) for $Ba_3LnRu_2O_9$.

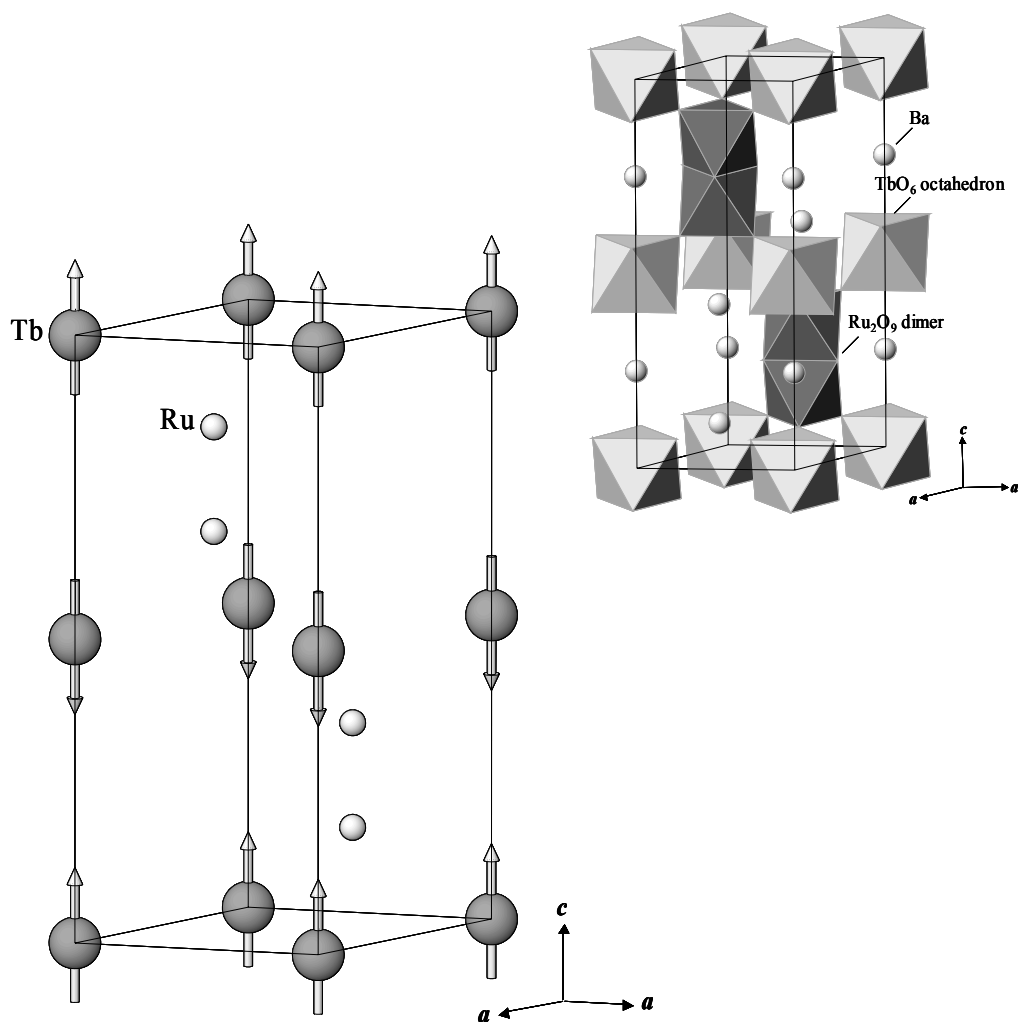


Figure 4.4.5 The crystal structure (right top) and magnetic structure (left bottom) of $Ba_3TbRu_2O_9$ at 2 K. The arrows indicate the direction of the magnetic moments. The ordered magnetic moment of Tb^{4+} : $6.84(4) \mu_B$; the direction of the magnetic moments: $[001]$.

4.5 Ferromagnetic transition and structural phase transition of $\text{Ba}_3\text{NdRu}_2\text{O}_9$

4.5.1 Introduction

This chapter describes the crystal structure and magnetic properties of $\text{Ba}_3\text{Nd}^{3+}\text{Ru}^{4.5+}_2\text{O}_9$. As shown later, this compound shows peculiar structural and magnetic properties among a series of $\text{Ba}_3\text{LnRu}_2\text{O}_9$ compounds, i.e., the structural phase transition and ferromagnetic transition are observed only in this compound. In order to elucidate the origin of these transitions, following measurements have been performed: the magnetic susceptibility, magnetization, and specific heat measurements in the temperature range 1.8–300 K, and its neutron diffraction measurements at 10, 60 and 180 K and room temperature. Their results will be discussed here.

4.5.2. Experimental

4.5.2.1 Sample preparation

The sample of $\text{Ba}_3\text{NdRu}_2\text{O}_9$ was prepared by the solid-state reaction. As starting materials, BaCO_3 , RuO_2 , and Nd_2O_3 were used. The sample was fired in air firstly at 1173 K for 12 h, secondly 1473 K for 12×2 h, and finally 1573 K for 12×5 h. A diamagnetic $\text{Ba}_3\text{SrNb}_2\text{O}_9$ was also prepared. This compound is isomorphous with $\text{Ba}_3\text{LnRu}_2\text{O}_9$ and is needed to estimate the lattice contribution of the specific heat to the total specific heat of $\text{Ba}_3\text{NdRu}_2\text{O}_9$. As starting materials, BaCO_3 , SrCO_3 , and Nb (metal) were used. The stoichiometric mixtures were calcined in air, first at 1123 K for 12×2 h and then at 1623 K for 48 h, and finally, were heated at 1573 K for 48 h in a flow of helium gas. The progress of the reaction of both samples was monitored by powder X-ray diffraction measurements.

4.5.2.1 X-ray and neutron diffraction measurements

The powder X-ray diffraction profiles at 13–200 K were measured in the range $10^\circ \leq 2\theta \leq 120^\circ$ using a 2θ step size of 0.02° with $\text{Cu-K}\alpha$ radiation on a Rigaku RINT2200 diffractometer. A sample was cooled by a variable temperature cryostat system,

CryoMini (Iwatani Industrial Gases Co.).

Powder neutron diffraction measurements were performed at 10, 60, 180, and 300 K using a high-resolution powder diffractometer (HRPD) [4.28] at the JRR3-M reactor (Japan Atomic Energy Research Institute), with a Ge(331) monochromator ($\lambda = 1.82268$ Å). The collimators used were 6'-20'-6' and were placed before and after the monochromator, and between the sample and each detector. The set of 64 detectors and collimators, which were placed every 2.5°, rotates around the sample. Crystal and magnetic structures were determined by the Rietveld technique, using the program RIETAN2000 [4.7].

4.5.2.3 Magnetic and thermal measurements

The magnetic measurements were carried out using a SQUID magnetometer (Quantum Design, MPMS-5S). The temperature dependence of the magnetic susceptibilities was measured under both zero-field-cooled (ZFC) and field-cooled (FC) conditions in an applied field of 0.1 T over the temperature range 1.8–400 K. The magnetization measurements were performed at 2, 10, 21, and 25 K over the magnetic field $0 \leq H \leq 5$ T.

The remnant magnetization measurements were also performed. The sample was cooled to 5 K in a zero field. The magnetic field was applied up to 5 T and then reduced to zero, and the magnetization measurements were performed in the temperature range from 5 to 30 K.

Specific heat measurements were performed using a relaxation technique with a commercial heat capacity measurement system (Quantum Design, PPMS model) in the temperature range 1.8–300 K. The sintered sample in the form of a pellet was mounted on a thin alumina plate with grease for better thermal contact.

4.5.3 Results and discussion

4.5.3.1 Crystal structure at low temperatures

Neutron diffraction data collected at room temperature indicates that Ba₃NdRu₂O₉ is formed as a single phase and has a hexagonal symmetry at room temperature. The

data have been analyzed by the Rietveld method, and the results show that the crystal structure of this compound is the 6H-perovskite structure with space group $P6_3/mmc$.

Neutron diffraction measurements were also performed at 10, 60, and 180 K to check whether the crystal phase transition occurred or not, and to determine the crystal structures at low temperatures. Their diffraction profiles are shown in Fig. 4.5.1, and the results were analyzed by the Rietveld method. The crystal structure at 180 K is the same as that at room temperature (space group $P6_3/mmc$). The diffraction data collected at 10 and 60 K indicate that the crystal structures at these temperatures have a lower symmetry than that at 180 K. Initially, we attempted to analyze these profiles by assuming a structure model in which the crystal symmetry is orthorhombic with space group $Cmcm$ ($a_{ortho} \approx a_{hex}$, $b_{ortho} \approx \sqrt{3} b_{hex}$, $c_{ortho} \approx c_{hex}$) which is the same as that for $Ba_3CoRu_2O_9$ at 2 K [4.9, 10]. However, this assumption gave an unsatisfactory result. Therefore, the author has lowered the symmetry of the crystal structure model from orthorhombic to monoclinic. It has been found that the analysis using a structure model which has a monoclinic symmetry with space group $C2/c$ (No. 15), gives a good agreement with experimental data. The crystal structure of $Ba_3NdRu_2O_9$ at 60 K is illustrated in Fig. 4.5.2. The unit cell parameters (a_{mono} , b_{mono} , c_{mono} and β_{mono}) at 60 K are 5.9173(3), 10.2425(5), 14.7663(9) Å, and 90.819(2)°, respectively. The structural parameters of both phases are summarized in Tables 4.5.1 and 4.5.2, and their bond lengths and angles are listed in Tables 4.5.3 and 4.5.4.

The neutron diffraction profile at 10 K indicates that there exist some magnetic reflection peaks due to a ferromagnetic ordering of Nd^{3+} ions, as will be described later. The crystal and magnetic structures at 10 K have been determined by the Rietveld method. The crystal structure at 10 K has the same symmetry as that at 60 K. The magnetic structure will be discussed later.

Powder X-ray diffraction measurements were also performed in the temperature range of 13 to 200 K. The diffraction profiles collected at 13–110 K are indexed in a monoclinic unit cell ($C2/c$), and those collected at 130–200 K are indexed in a hexagonal unit cell ($P6_3/mmc$). Therefore, it is considered that the structural phase

transition occurs around 120 K.

4.5.3.2 Magnetic properties of $Ba_3NdRu_2O_9$

(a) Magnetization measurements. The temperature dependence of the magnetic susceptibility (M/H) of $Ba_3NdRu_2O_9$ is plotted in Fig. 4.5.3. The magnetic susceptibility shows a rapid increase when the temperature is decreased through 24 K, and the large divergence between the ZFC and FC susceptibilities is found below this temperature. These results indicate that a ferromagnetic or a ferrimagnetic transition has occurred at 24 K. Some analogous compounds $Ba_3LnRu_2O_9$ ($Ln = Y, In, La, Lu$) in which only Ru ions are magnetic, have been prepared, and their magnetic susceptibilities have been measured (section 4.3). They show antiferromagnetic transitions below 15 K. Hence, the Nd ions should contribute to the magnetic transition of $Ba_3NdRu_2O_9$ observed at 24 K. The temperature dependence of the inverse susceptibility (H/M) is shown in an inset graph in Fig. 4.5.3. A linear relationship between the inverse susceptibility vs. temperature is observed above 120 K. Below this temperature, the susceptibility deviates from this relationship, which is due to the structural phase transition. The higher temperature data ($T > 200$ K) are fitted using the Curie-Weiss law. The obtained effective magnetic moment and Weiss constant are $5.82(3) \mu_B$ and $-85(3)$ K, respectively.

The temperature dependence of the remnant magnetization is plotted in Fig. 4.5.4. The remnant magnetization is constant ($\sim 1.05 \mu_B$) below 15 K and decreases with increasing temperature between 15 and 24 K and is zero above 24 K. The field dependence of the magnetization at 2, 10, 21, and 25 K is shown in Fig. 4.5.5. Data collected below 21 K show a hysteresis loop, which means that there exists a ferromagnetic moment.

(b) Specific heat measurements. Figure 4.5.6 shows the variation of the specific heat for $Ba_3NdRu_2O_9$ as a function of temperature. Two anomalies have been observed at 17 and 24 K. The λ -type anomaly at 24 K corresponds to the magnetic

transition found in the magnetic susceptibility. No anomaly corresponding to the structural phase transition at *ca.* 120 K has been found in this measurement.

The specific heat data for $\text{Ba}_3\text{SrNb}_2\text{O}_9$ are also plotted in Fig. 4.5.6. The crystal structure of this compound is analogous to that of $\text{Ba}_3\text{NdRu}_2\text{O}_9$ at room temperature (space group $P6_3/mmc$), and it has no magnetic ions. If it is assumed that the electronic and lattice contributions to the specific heat are equal between $\text{Ba}_3\text{NdRu}_2\text{O}_9$ and $\text{Ba}_3\text{SrNb}_2\text{O}_9$, the magnetic specific heat for $\text{Ba}_3\text{NdRu}_2\text{O}_9$ is obtained by subtracting the specific heat of $\text{Ba}_3\text{SrNb}_2\text{O}_9$ from that of $\text{Ba}_3\text{NdRu}_2\text{O}_9$.

The temperature dependence of the magnetic specific heat divided by temperature (C_M/T) and of the magnetic entropy (S_M) is shown in Fig. 4.5.7. The magnetic entropy change (ΔS_M) between 1.8 and 24 K is $\sim 11.1 \text{ J}\cdot\text{mol}^{-1}\cdot\text{K}^{-1}$. This value is the sum of the entropy changes for two anomalies at 17 and 24 K. It seems that the entropy changes of these anomalies are equal; in that case, each entropy change is very close to $R \ln W = R \ln 2 = 5.76 \text{ J}\cdot\text{mol}^{-1}\cdot\text{K}^{-1}$. Above 24 K, the entropy increases with temperature. This may indicate the occurrence of a short-range magnetic ordering.

(c) Magnetic structure at 10 K. As mentioned in section 4.5.3.1, some magnetic reflection peaks are observed in the neutron diffraction data collected at 10 K. The positions of the magnetic diffraction lines are in accordance with those of the nuclear ones. The Rietveld analysis determines the magnetic structure of $\text{Ba}_3\text{NdRu}_2\text{O}_9$, which is illustrated in Fig. 4.5.8. In this magnetic structure, the magnetic moments of Nd^{3+} ions order ferromagnetically and are aligned along the *c*-axis. The ordered magnetic moment is $1.65(8) \mu_B$ / Nd^{3+} ion. The ordered moments of Ru ions have not been determined in this study, and this will be discussed in the following section.

4.5.3.3 Discussion on the magnetic properties of $\text{Ba}_3\text{NdRu}_2\text{O}_9$

The results of the magnetization, specific heat, and neutron diffraction measurements for $\text{Ba}_3\text{NdRu}_2\text{O}_9$ show that a ferromagnetic ordering of Nd^{3+} ions occurs at 24 K. $\text{Ba}_3\text{NdRu}_2\text{O}_9$ is considered to be nonmetallic because it shows the magnetic

behavior of the localized electrons, and because the analogous compounds Ba₃LnRu₂O₉ (Ln = Y, La–Pr, Sm, Eu, Tb, and Lu) (section 4.2.2.2) and Ba₃MRu₂O₉ (M = Fe, Co, Ni, Cu, and In) [4.23] are semiconductors. The neutron diffraction data at 10 K show that the crystal structure of Ba₃NdRu₂O₉ is distorted monoclinically and that the magnetic structure is described by a ferromagnetic ordering of Nd³⁺ ions; the ordered magnetic moment is 1.65(8) μ_B / Nd³⁺ ion and the direction of ordered moments is parallel to the *c*-axis. The magnetic entropy change of the magnetic transition at 24 K is close to $R \ln 2$. Therefore, it is considered that this magnetic entropy is due to the ground Kramer's doublet of Nd³⁺ ions.

In contrast, the ordered moments of Ru ions have not been determined from the present neutron diffraction data. However, the author believes that Ru ions are not in the paramagnetic state at low temperatures. If the Ru ions are paramagnetic down to 10 K, the magnetic transition found at 24 K should be due to only the ordering of Nd ions. We consider that this transition temperature is exceptionally high, because it is known that the magnetic interaction between the *f* electrons is generally very weak compared with that between the *d* electrons, and because the main pathway of the magnetic exchange interaction between Nd ions is a long superexchange pathway of Nd–O–O–Nd. The magnetic susceptibility measurements described in earlier sections (sections 4.3 and 4.4) show that magnetic moments of Ru ions in Ba₃LnRu₂O₉ (Ln = Y, In, La, Ce, Pr, Sm, Eu, Tb, and Lu) are coupled antiferromagnetically in the Ru₂O₉ dimer. Taking into account that the average valency of ruthenium ions in the Nd compound is +4.5, there may exist Ru⁴⁺Ru⁵⁺O₉ dimers. Each dimer has a total spin $S_{dimer} = 1/2$. If the magnetic ordering between dimers occurs at low temperatures, the entropy change $\Delta S_M = R \ln (2S_{dimer} + 1) = R \ln 2$ should be observed. The entropy change for an anomaly at 17 K, which is close to $R \ln 2$, may be due to the magnetic ordering of these Ru₂O₉ dimers. Our failure to detect the ordered magnetic moments of Ru ions may be due to the short-range ordering and/or the unsaturation of magnetic moments of Ru ions.

4.5.4 Summary

In this section, the crystal structure and magnetic properties of $\text{Ba}_3\text{NdRu}_2\text{O}_9$ have been studied. The X-ray and neutron diffraction measurements were carried out at some temperatures between 10 K and room temperature. It was found that this compound shows the crystal phase transition at ~ 120 K. The crystal structure at low temperatures was determined to be monoclinic with space group $C2/c$. The temperature dependence of the magnetic susceptibility and specific heat were measured. A ferromagnetic transition at 24 K was found, and the neutron diffraction measurement at 10 K shows that $\text{Ba}_3\text{NdRu}_2\text{O}_9$ has a long-range ferromagnetic ordering of Nd^{3+} ions with the ordered magnetic moment of $1.65(8) \mu_B$, and that the direction of the ordered moments is parallel to the c -axis.

Table 4.5.1 Structural parameters for $Ba_3NdRu_2O_9$ (hexagonal phase) determined by the neutron diffraction measurements

Atom	Site	x	y	z	$B / \text{\AA}^2$
space group: $P6_3/mmc$ (No. 194); $z = 2$					
room temperature					
$a = 5.9319(1) \text{ \AA}$, $c = 14.7589(3) \text{ \AA}$					
$R_{wp} = 7.65 \%$, $R_I = 2.64 \%$, $R_F = 1.69 \%$, $R_e = 5.82 \%$					
Ba(1)	$2b$	0	0	1/4	0.34(7)
Ba(2)	$4f$	1/3	2/3	0.8994(2)	0.86(5)
Nd	$2a$	0	0	0	0.10(5)
Ru	$4f$	1/3	2/3	0.1645(1)	0.63(3)
O(1)	$6h$	0.4885(2)	0.9769	1/4	0.70(3)
O(2)	$12k$	0.1779(2)	0.3557	0.4084(1)	1.04(3)
180 K					
$a = 5.9245(2) \text{ \AA}$, $c = 14.7643(6) \text{ \AA}$					
$R_{wp} = 11.58 \%$, $R_I = 3.80 \%$, $R_F = 2.41 \%$, $R_e = 9.58 \%$					
Ba(1)	$2b$	0	0	1/4	0.42(11)
Ba(2)	$4f$	1/3	2/3	0.8998(3)	0.48(8)
Nd	$2a$	0	0	0	0.31(7)
Ru	$4f$	1/3	2/3	0.1645(2)	0.41(5)
O(1)	$6h$	0.4881(3)	0.9762	1/4	0.51(6)
O(2)	$12k$	0.1787(2)	0.3573	0.4078(1)	0.73(5)

Table 4.5.2 Structural parameters for $Ba_3NdRu_2O_9$ (monoclinic phase) determined by the neutron diffraction measurements

Atom	Site	x	y	z	$B / \text{\AA}^2$
space group: $C2/c$ (No. 15); $z = 4$					
60 K					
$a = 5.9173(3) \text{ \AA}$, $b = 10.2425(5) \text{ \AA}$, $c = 14.7663(9) \text{ \AA}$, $\beta = 90.819(2)^\circ$					
$R_{wp} = 11.73 \%$, $R_I = 3.48 \%$, $R_F = 1.94 \%$, $R_e = 9.61 \%$					
Ba(1)	$4e$	0	$-0.0030(12)$	$1/4$	$0.10(7)$
Ba(2)	$8f$	$0.0038(9)$	$0.3313(8)$	$0.0989(3)$	$0.10(7)$
Nd	$4a$	0	0	0	$0.19(9)$
Ru	$8f$	$-0.0060(6)$	$0.3317(7)$	$0.8360(3)$	$0.31(7)$
O(1)	$4e$	0	$0.5147(9)$	$1/4$	$0.30(10)$
O(2)	$8f$	$0.2654(13)$	$0.2417(7)$	$0.2446(5)$	$0.40(10)$
O(3)	$8f$	$0.0188(12)$	$0.8210(6)$	$0.0926(4)$	$0.29(13)$
O(4)	$8f$	$0.2835(11)$	$0.0920(7)$	$0.0830(4)$	$0.57(11)$
O(5)	$8f$	$0.7536(12)$	$0.0891(6)$	$0.0988(4)$	$0.45(12)$
10 K					
$a = 5.9138(3) \text{ \AA}$, $b = 10.2352(4) \text{ \AA}$, $c = 14.7633(8) \text{ \AA}$, $\beta = 90.847(2)^\circ$					
$R_{wp} = 10.00 \%$, $R_I = 2.00 \%$, $R_F = 1.16 \%$, $R_e = 7.09 \%$					
Ba(1)	$4e$	0	$-0.0031(10)$	$1/4$	$0.04(6)$
Ba(2)	$8f$	$0.0037(7)$	$0.3323(7)$	$0.0995(3)$	$0.04(6)$
Nd	$4a$	0	0	0	$0.20(7)$
Ru	$8f$	$-0.0075(5)$	$0.3326(6)$	$0.8353(2)$	$0.44(6)$
O(1)	$4e$	0	$0.5131(7)$	$1/4$	$0.20(8)$
O(2)	$8f$	$0.2625(11)$	$0.2426(6)$	$0.2440(4)$	$0.63(8)$
O(3)	$8f$	$0.0212(10)$	$0.8219(5)$	$0.0927(4)$	$0.25(11)$
O(4)	$8f$	$0.2829(9)$	$0.0913(6)$	$0.0828(4)$	$0.75(9)$
O(5)	$8f$	$0.7506(10)$	$0.0906(6)$	$0.0975(4)$	$0.53(11)$
Magnetic moment of Nd: $1.65(8) \mu_B$					
Direction of moment: $[001]$					

Table 4.5.3 Selected bond lengths (Å) and angles (°) for $Ba_3NdRu_2O_9$ (hexagonal phase)

	room temperature	180 K
Nd–O(2) × 6	2.273(1)	2.284(2)
Ru–O(1) × 3	2.033(2)	2.029(3)
–O(2) × 3	1.926(2)	1.912(3)
Ru–O (average)	1.979(2)	1.971(3)
Ru–Ru	2.524(4)	2.525(6)
Ru–O(2) – Nd	177.5(1)	177.3(1)
Ru–O(1) – Ru	76.8(1)	77.0(2)

Table 4.5.4 Selected bond lengths (Å) and angles (°) for $Ba_3NdRu_2O_9$ (monoclinic phase)

	60 K	10 K
Nd–O(3) × 2	2.290(6)	2.282(5)
–O(4) × 2	2.267(6)	2.260(6)
–O(5) × 2	2.269(6)	2.274(5)
Nd–O (average)	2.276(6)	2.272(5)
Ru–O(1)	2.023(9)	2.021(7)
–O(2)	2.014(8)	2.028(7)
–O(2)	2.042(8)	2.051(7)
–O(3)	1.888(8)	1.907(7)
–O(4)	1.931(7)	1.946(6)
–O(5)	1.942(7)	1.926(6)
Ru–O (average)	1.973(8)	1.980(7)
Ru–Ru	2.542(8)	2.522(7)
Ru–O(3)–Nd × 2	174.3(4)	173.7(3)
Ru–O(4)–Nd × 2	174.3(4)	174.2(3)
Ru–O(5)–Nd × 2	169.4(4)	171.3(4)
Ru–O–Nd (average)	172.7(4)	173.1(3)
Ru–O(1)–Ru	77.9(4)	77.2(4)
Ru–O(2)–Ru × 2	77.6(3)	76.4(3)
Ru–O–Ru (average)	77.7(4)	76.7(3)

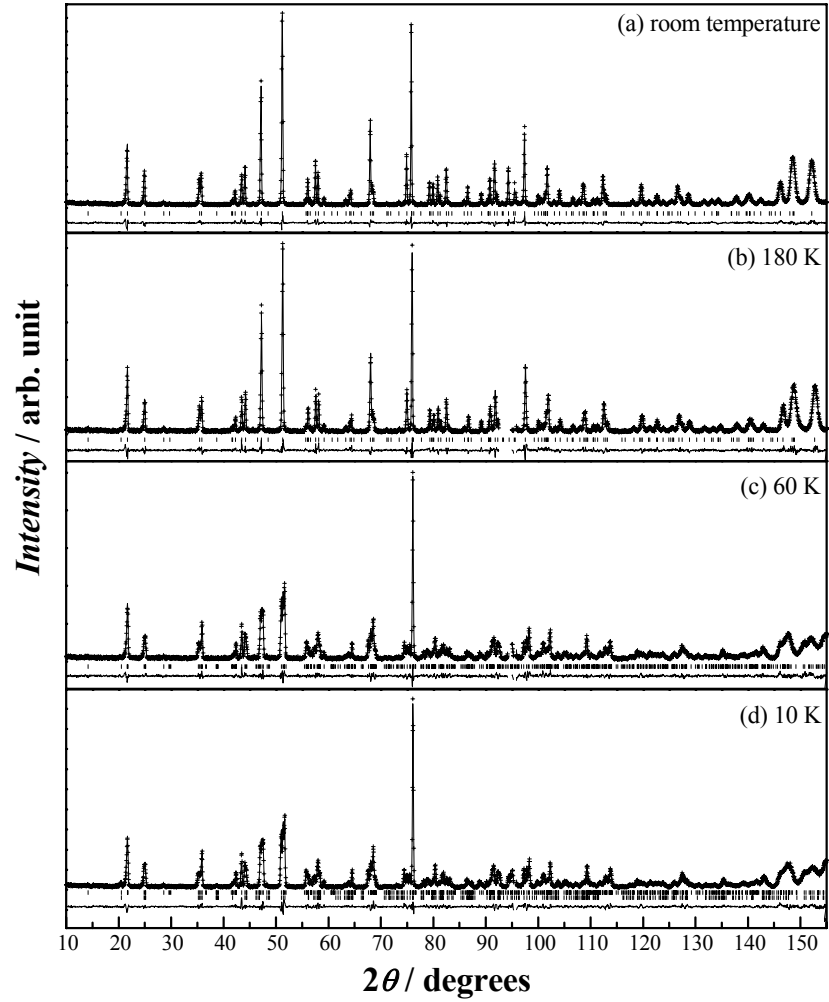


Figure 4.5.1 Powder neutron diffraction profiles for $\text{Ba}_3\text{NdRu}_2\text{O}_9$. The calculated and observed diffraction profiles are shown with the top solid line and cross markers, respectively. The vertical marks show positions calculated from Bragg reflections. In (d), the lower vertical marks show the magnetic reflection positions. The bottom trace is a plot of the difference between calculated and observed intensities.

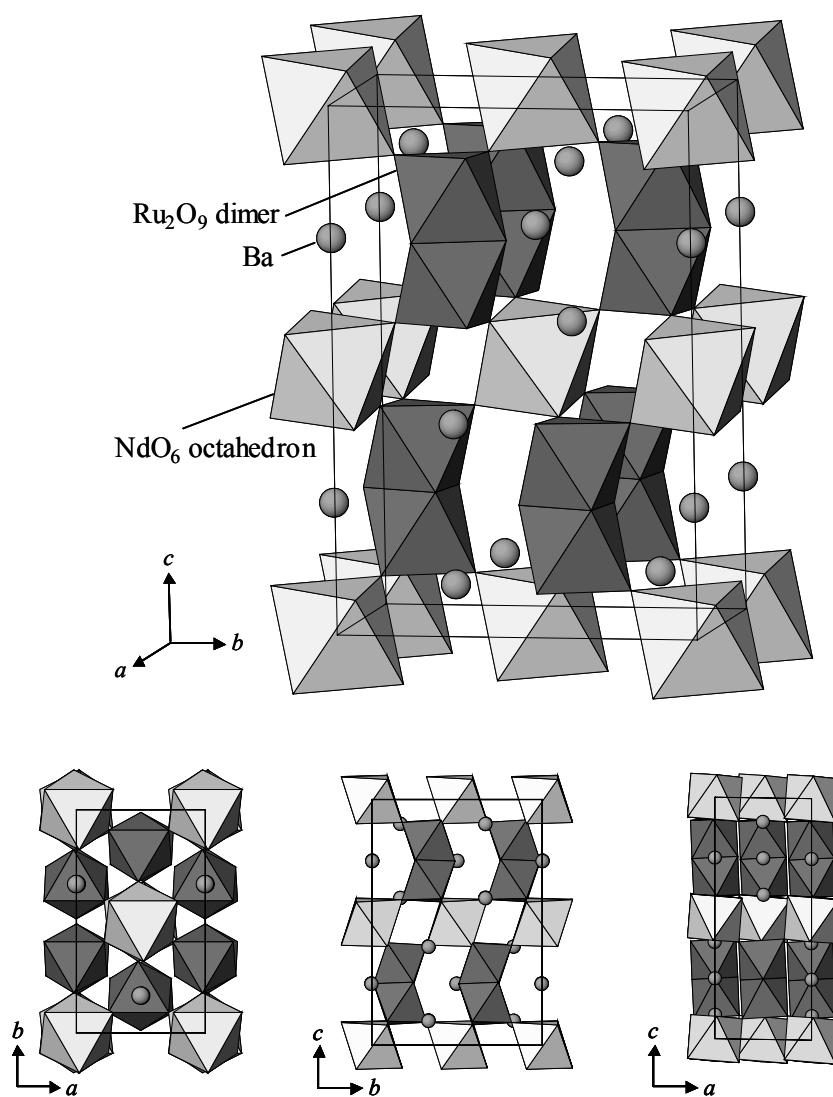


Figure 4.5.2 The crystal structure of $Ba_3NdRu_2O_9$ at 60 K.

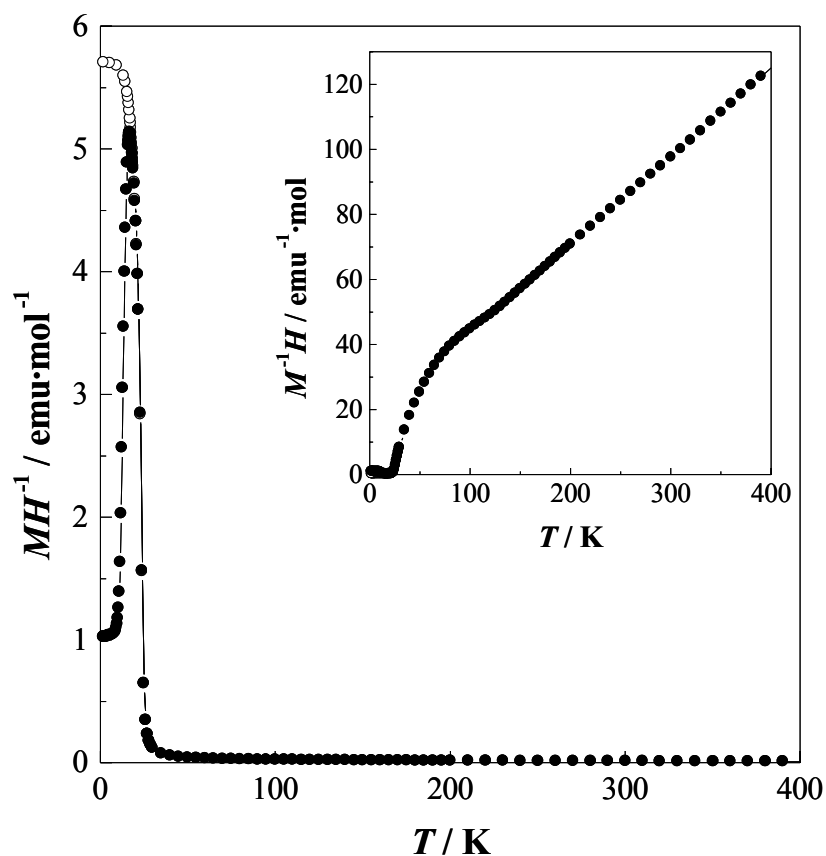


Figure 4.5.3 Magnetic susceptibilities (M/H) of $\text{Ba}_3\text{NdRu}_2\text{O}_9$. The filled and open symbols show the ZFC and FC susceptibilities, respectively. The applied field is 0.1 T. Inset shows the inverse susceptibility.

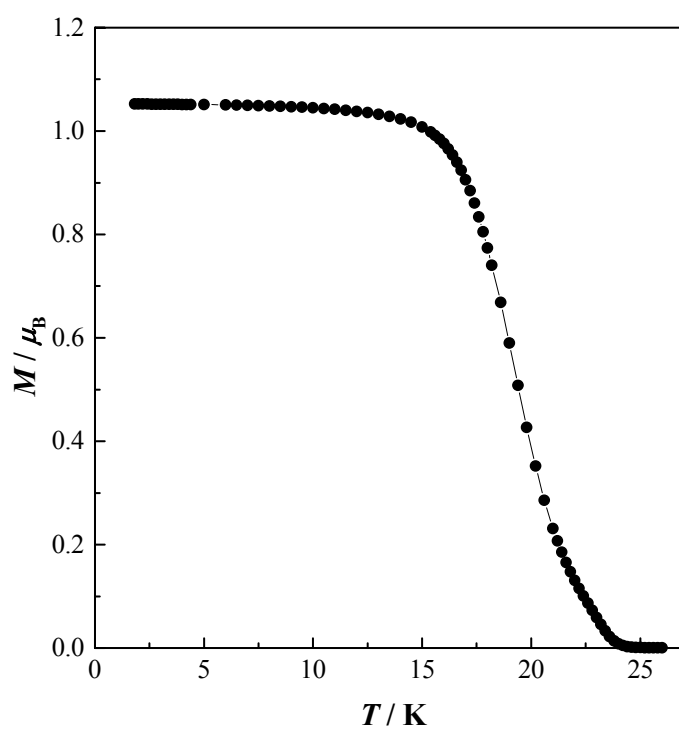


Figure 4.5.4 Temperature dependence of the remnant magnetization of $Ba_3NdRu_2O_9$.

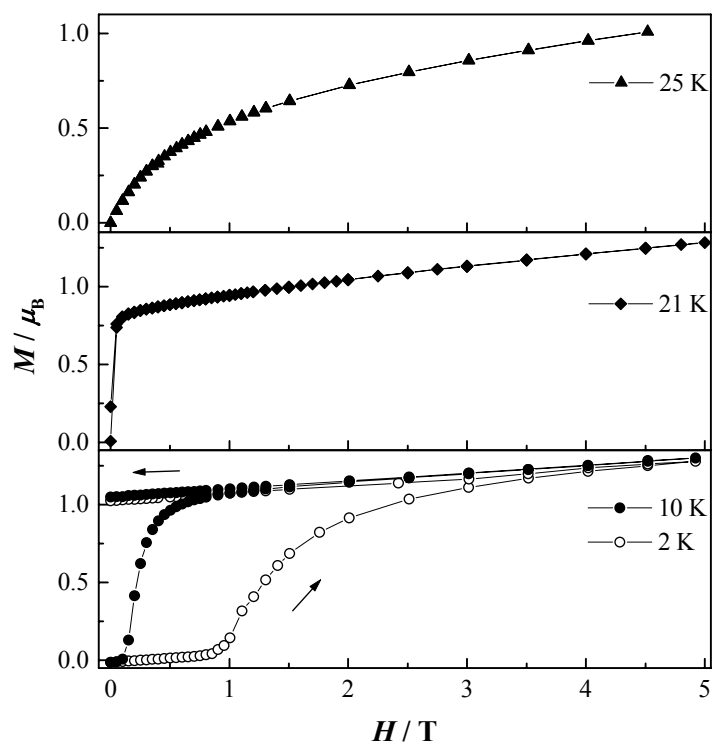


Figure 4.5.5 Field dependence of the magnetization of $Ba_3NdRu_2O_9$.

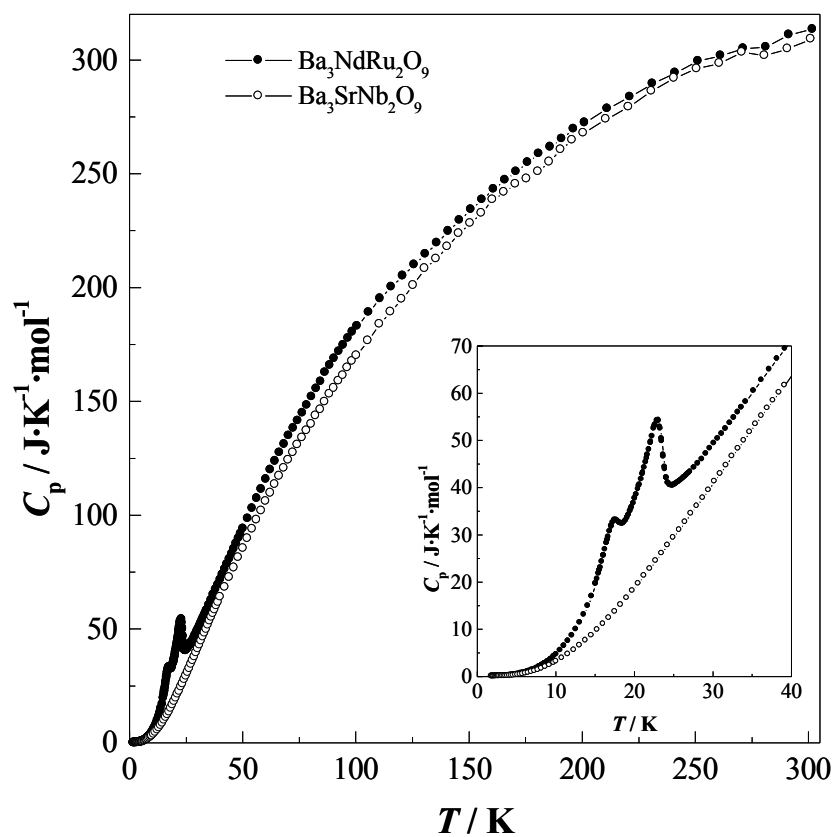


Figure 4.5.6 Temperature dependence of the specific heat for $\text{Ba}_3\text{NdRu}_2\text{O}_9$ and $\text{Ba}_3\text{SrNb}_2\text{O}_9$.

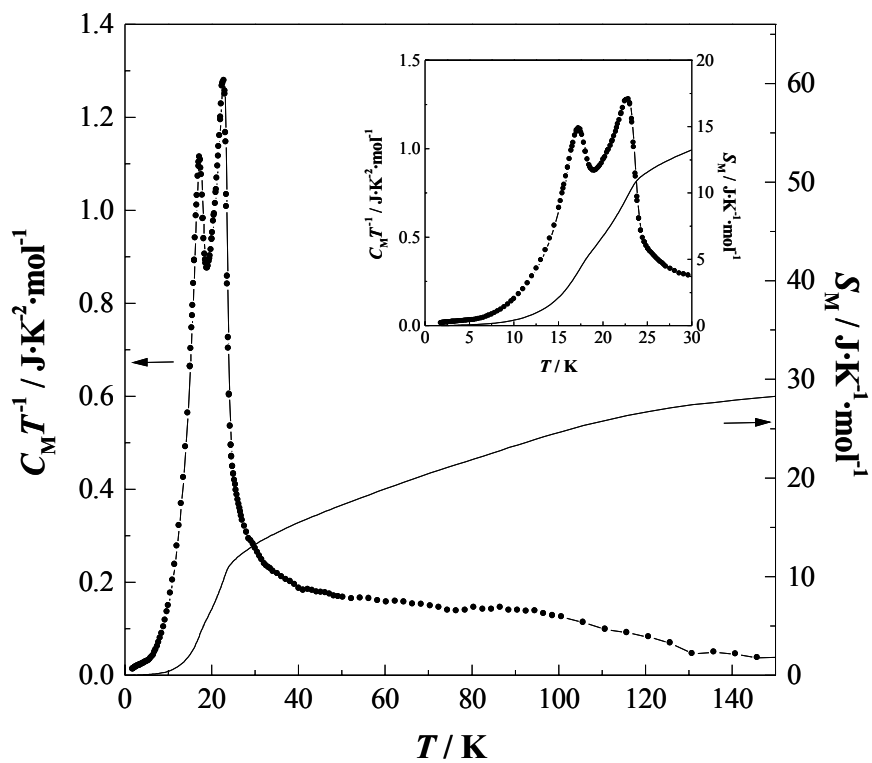


Figure 4.5.7 The magnetic specific heat divided by temperature (C_M/T) and magnetic entropy (S_M) of $Ba_3NdRu_2O_9$.

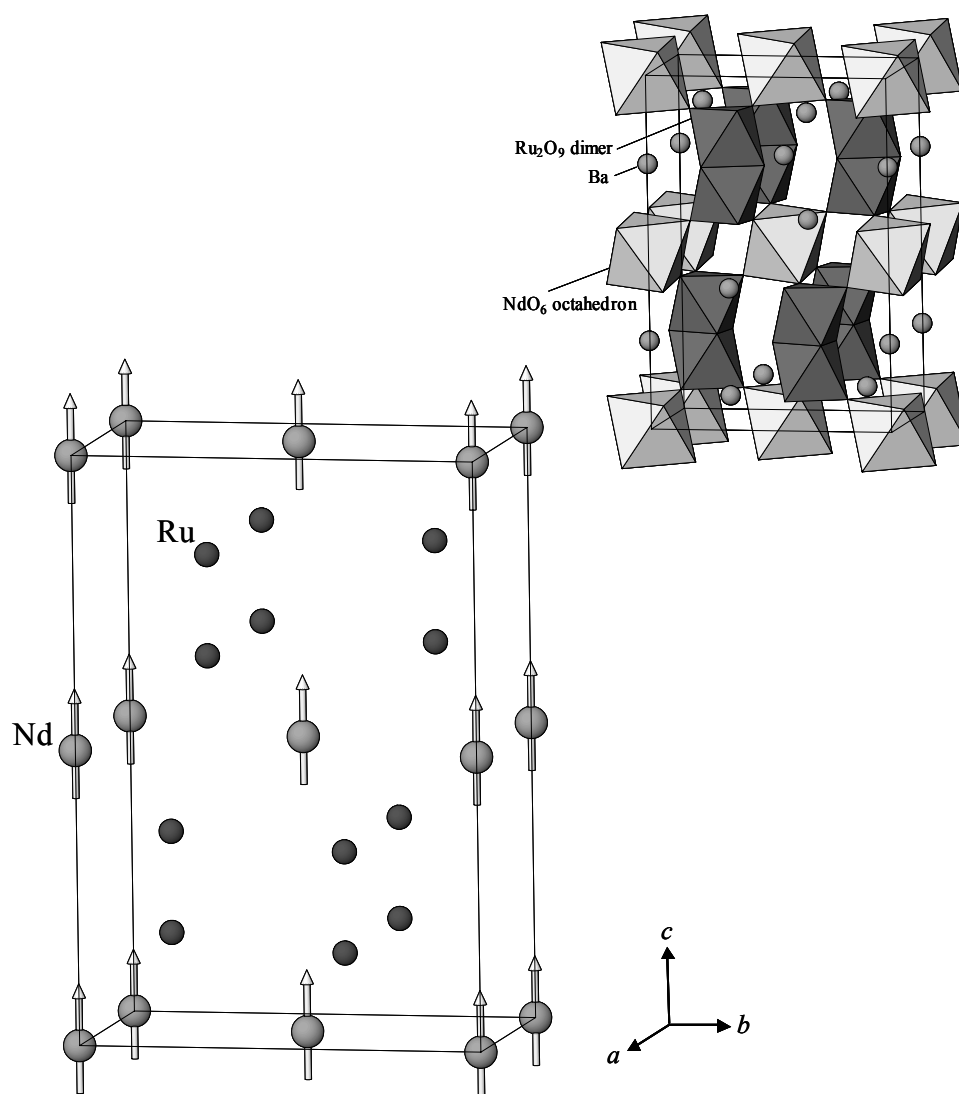


Figure 4.5.8 The crystal structure (right top) and magnetic structure (left bottom) of $\text{Ba}_3\text{NdRu}_2\text{O}_9$ at 10 K. The arrows indicate the direction of the magnetic moments.

4.6 Magnetic and calorimetric studies on Ba₃LnRu₂O₉ (Ln = Gd, Ho–Yb)

4.6.1 Introduction

This section describes the magnetic properties of 6H-perovskites Ba₃LnRu₂O₉ with Ln = Gd, Ho–Yb. As is shown in section 4.2, these compounds have a hexagonal unit cell, and two kinds of the B site ions, Ru and Ln, occupy the face-sharing octahedral sites (Ru₂O₉ dimer) and the corner-sharing octahedral ones (LnO₆ octahedron), respectively. In the case that both Ru and Ln ions are magnetic, these compounds may show magnetic cooperative phenomena due to the interaction between d and f electrons at sufficiently low temperatures. In fact, Ba₃NdRu₂O₉ shows a ferromagnetic transition of Nd³⁺ ions at 24 K (section 4.5), and antiferromagnetic transitions in Ba₃PrRu₂O₉ and Ba₃TbRu₂O₉ are observed at 10.5 K and 9.5 K, respectively (section 4.4). Now, we turn our attention to the lanthanides Ln = Gd, and Ho–Yb. These elements have large magnetic moments. So, the Ln ions should greatly contribute to the magnetic properties of Ba₃LnRu₂O₉.

In order to elucidate their magnetic behavior, the magnetic susceptibility and specific heat measurements for the Ba₃LnRu₂O₉ (Ln = Gd, Ho–Yb) are performed.

4.6.2 Experimental

The samples of Ba₃LnRu₂O₉ (Ln = Gd, Ho–Yb) were prepared by the solid-state reaction. As starting materials, BaCO₃, RuO₂, and Ln₂O₃ were used. The samples were initially fired in air at 1173 K for 12 h, and then at 1473 K for 12×2 h and at 1473 K for 12×5 h. The progress of the reaction of both samples was monitored by powder X-ray diffraction measurements.

Magnetic susceptibility measurements were carried out using a SQUID magnetometer (Quantum Design, MPMS-5S). Temperature dependence of the magnetic susceptibilities was measured under both zero-field-cooled (ZFC) and field-cooled (FC) conditions in an applied field of 0.1 T over the temperature range 1.8–400 K.

Specific heat measurements were performed using a relaxation technique with a commercial heat capacity measurement system (Quantum Design, PPMS model) in the temperature range 1.8–300 K. The sintered sample in the form of a pellet was mounted on a thin alumina plate with grease for better thermal contact.

4.6.3 Results and discussion

4.6.3.1 Magnetic susceptibilities

The temperature dependence of reciprocal magnetic susceptibilities for $Ba_3LnRu_2O_9$ ($Ln = Gd, Ho-Yb$) is shown in Fig. 4.6.1. The susceptibility data in the higher temperature region ($T > 150$ K) are fitted with the Curie-Weiss law; the effective magnetic moments μ_{eff} and Weiss constants θ are listed in Table 4.6.1. The Weiss constants are negative; therefore, the predominant magnetic interactions in these compounds are antiferromagnetic. The effective magnetic moments are obviously close to those for the free Ln^{3+} ions ($\mu_{Ln^{3+}}$) rather than the values calculated from

$$\mu_{\text{cal}} = \sqrt{\mu_{Ln^{3+}}^2 + \mu_{Ru^{4+}}^2 + \mu_{Ru^{5+}}^2}. \quad (4.13)$$

This fact indicates that the contribution of Ru ions to the effective magnetic moment is very small. Therefore, the Ru ions should be no longer in the paramagnetic state in this temperature range; the magnetic moments of two Ru ions in each Ru_2O_9 dimer are coupled antiferromagnetically. The similar antiferromagnetic coupling was found in the analogous 6H-perovskites $Ba_3LnRu_2O_9$ ($Ln = Y, In, La-Nd, Sm, Eu, Tb, Lu$) (sections 4.3–4.5).

Figures 4.6.2–4.6.6(a) show the temperature dependence of the magnetic susceptibility for each compound at low temperatures. It is found that the $Ba_3LnRu_2O_9$ show magnetic anomalies at 14.8 K ($Ln = Gd$), 10.2 K (Ho), 6.0 K (Er), 8.3 K (Tm), and 4.5 K (Yb). In order to clarify these magnetic anomalies, the specific heat measurements have been performed

4.6.3.2 Specific heats

Figures 4.6.2–4.6.6(b) show the variation of the specific heats (C_p) as a function of temperature. The specific heat of any compound shows a λ -type anomaly at the same temperature at which the magnetic anomaly is observed in the susceptibility vs. temperature curve. This result indicates that these anomalies are an antiferromagnetic transition.

The specific heat mainly consists of the lattice, electronic, and magnetic specific heats. In order to estimate the lattice and electronic contributions, we used a polynomial function of the temperature, $f(T) = aT^3 + bT^5 + cT^7$, in which the constants were determined by fitting this function to the observed specific heat data between 20 and 40 K. Each calculated curve is shown in Fig. 4.6.2–4.6.6(b) as a dotted curve. The magnetic specific heat (C_m) for $Ba_3LnRu_2O_9$ is obtained by subtracting the lattice and electronic contributions from the total specific heat, i.e., $C_m(T) = C_p(T) - f(T)$.

The temperature dependence of the magnetic entropy calculated by $S_m = \int C_m/T dT$ is shown in Figs. 4.6.2–4.6.6(c). As will be described later, the magnetic transitions observed for these $Ba_3LnRu_2O_9$ compounds are due to the magnetic ordering of Ln^{3+} ions, because the estimated magnetic entropy changes are large enough for the Ln^{3+} ordering. In addition, there may be a contribution of the magnetic interaction between antiferromagnetically coupled $Ru^{4.5+}_2O_9$ dimers, which have one unpaired electron per dimer at sufficiently low temperatures, to the magnetic entropy change. In section 4.3, the magnetic susceptibility and specific heat for $Ba_3Ln^{3+}Ru^{4.5+}_2O_9$ ($Ln = Y, In, La$ and Lu) in which only Ru ions are magnetic, have been measured. They show antiferromagnetic transitions at about 4.5 K (for $Ln = Y$ and In), 6.0 K (La), and 9.5 K (Lu), and the magnetic entropy change for such magnetic transitions is about 3 $J \cdot mol^{-1} \cdot K^{-1}$ (Y, In, Lu) and 0.3 $J \cdot mol^{-1} \cdot K^{-1}$ (La).

The magnetic entropy change associated with the antiferromagnetic ordering for $Ba_3GdRu_2O_9$ is 17.5 $J \cdot mol^{-1} \cdot K^{-1}$ (Fig. 4.6.2); this value is close to $R \ln W = R \ln 8 = 17.3 J \cdot mol^{-1} \cdot K^{-1}$ (W : number of states for Ln^{3+} ion). This result is consistent with the fact that the ground state for Gd^{3+} ion is $^8S_{7/2}$ (the degeneracy of which is $W = 2S + 1 =$

8) and confirms that the magnetic anomaly at 14.8 K is due to the antiferromagnetic ordering of Gd^{3+} ions.

The magnetic entropy change for $Ba_3HoRu_2O_9$ is $14.7 \text{ J}\cdot\text{mol}^{-1}\cdot\text{K}^{-1}$ (Fig. 4.6.3). In an octahedral crystal field environment, the ground state of 5I_8 for the Ho^{3+} ion is a singlet state Γ_1 or a doublet state Γ_3 , and there exists a low lying excited state (Γ_4 ; triplet) [4.29]. If these three states degenerate or if the energy difference among them is very small, the expected entropy change due to the Ho^{3+} antiferromagnetic transition is $R \ln 6 = 14.9 \text{ J}\cdot\text{mol}^{-1}\cdot\text{K}^{-1}$. On the other hand, if the energy difference between Γ_3 and Γ_4 is small and the energy difference between Γ_3 and Γ_1 is large, the expected entropy change is $R \ln 5 = 13.4 \text{ J}\cdot\text{mol}^{-1}\cdot\text{K}^{-1}$. In this case, the excess entropy change may be due to the magnetic ordering of $Ru^{4.5+}_2O_9$ dimers.

The magnetic entropy change for $Ba_3ErRu_2O_9$ is $13.0 \text{ J}\cdot\text{mol}^{-1}\cdot\text{K}^{-1}$ (Fig. 4.6.4). The ground state of $^4I_{15/2}$ for the Er^{3+} ion is a quartet state Γ_8 or a doublet state Γ_7 in an octahedral crystal field [4.29]. In the case that the ground state is Γ_8 , the expected entropy change due to the Er^{3+} antiferromagnetic transition, $R \ln 4 = 11.5 \text{ J}\cdot\text{mol}^{-1}\cdot\text{K}^{-1}$, is close to the observed value. The excess entropy change may be due to the magnetic ordering of $Ru^{4.5+}_2O_9$ dimers.

The magnetic entropy change for $Ba_3TmRu_2O_9$ is $2.9 \text{ J}\cdot\text{mol}^{-1}\cdot\text{K}^{-1}$ (Fig. 4.6.5). The ground state of 3H_6 for the Tm^{3+} ion in $Ba_3TmRu_2O_9$ is singlet (i.e., Γ_1 or Γ_2) [4.29]. The observed small entropy change should be due to the magnetic ordering of $Ru^{4.5+}_2O_9$ dimers.

The magnetic entropy change for $Ba_3YbRu_2O_9$ is $7.6 \text{ J}\cdot\text{mol}^{-1}\cdot\text{K}^{-1}$ (Fig. 4.6.6). In an octahedral crystal environment, the ground state of the Yb^{3+} ion (the state $^2F_{7/2}$) is the Γ_6 doublet; the expected entropy change due to the Yb^{3+} antiferromagnetic transition is $R \ln 2 = 5.8 \text{ J}\cdot\text{mol}^{-1}\cdot\text{K}^{-1}$. We consider that the excess entropy change ($1.8 \text{ J}\cdot\text{mol}^{-1}\cdot\text{K}^{-1}$) is due to the magnetic ordering of $Ru^{4.5+}_2O_9$ dimers. Another small anomaly observed at 7.5 K may be understandable by the same reason.

4.6.4 Summary

In this section, the magnetic properties of $Ba_3LnRu_2O_9$ with paramagnetic Ln^{3+} ions ($Ln = Gd, Ho-Yb$) are studied. The magnetic susceptibility and specific heat measurements were carried out. It was found that these compounds show magnetic anomalies at 14.8 K ($Ln = Gd$), 10.2 K (Ho), 6.0 K (Er), 8.3 K (Tm), and 4.5 K (Yb). The magnetic entropy changes associated with these magnetic anomalies were estimated from the specific heat data. The results indicate that these anomalies are mainly due to the antiferromagnetic ordering of Ln^{3+} ions.

The magnetic properties of 6H-perovskites $Ba_3LnRu_2O_9$ ($Ln = Y, In, La-Nd, Sm-Lu$) observed in this section and previous sections (sections 4.2–4.5) are summarized in Table 4.6.2.

Table 4.6.1 The magnetic moments for free Ln^{3+} ion ($\mu_{Ln^{3+}}$), calculated magnetic moments for all ions (μ_{cal}), effective magnetic moments (μ_{eff}) and Weiss constants (θ) for $Ba_3LnRu_2O_9$ (Gd, Ho–Yb)

Ln^{3+}	$\mu_{Ln^{3+}} / \mu_B$	μ_{cal} / μ_B	μ_{eff} / μ_B	θ / K
Gd ³⁺	7.94	9.28	7.68(1)	–2.9(5)
Ho ³⁺	10.58	11.62	10.15(1)	–5.4(4)
Er ³⁺	9.59	10.72	9.45(2)	–9.9(7)
Tm ³⁺	7.55	8.94	7.35(1)	–24.5(5)
Yb ³⁺	4.54	6.60	5.26(1)	–178(2)

Note. $\mu_{cal} = \sqrt{\mu_{Ln^{3+}}^2 + \mu_{Ru^{4+} (lowspin)}^2 + \mu_{Ru^{5+}}^2}$

Table 4.6.2 The magnetic properties of 6H-perovskites $Ba_3LnRu_2O_9$

	Oxidation state of Ln ion	T_a	T_b	Neutron diffraction
Y	+3 ([Kr]4d ⁰)	290 K	4.5 K (AF)	–
In	+3 ([Kr]4d ¹⁰)	370 K	4.5 K (AF)	–
La	+3 ([Xe]4f ⁰)	22 K (plateau)	6.0 K (AF)	–
Ce	+4 ([Xe]4f ⁰)	> 400 K	–	–
Pr	+4 ([Xe]4f ¹)	> 380 K	10.5 K (AF)	–
Nd	+3 ([Xe]4f ³)	–	24.0 K (F)	Structural phase transition at 120 K (hex. → mono.) Ferromagnetic ordering of Nd ³⁺ , 1.65 μ_B /Nd (10 K)
Sm	+3 ([Xe]4f ⁵)	180 K	12.5 K (AF)	–
Eu	+3 ([Xe]4f ⁶)	135 K	9.5 K (AF)	–
Gd	+3 ([Xe]4f ⁷)	–	14.8 K (AF)	–
Tb	+4 ([Xe]4f ⁷)	–	9.5 K (AF)	Antiferromagnetic ordering of Tb ⁴⁺ , 6.84 μ_B /Tb (2 K)
Dy	+3 ([Xe]4f ⁹)	–	27.8 K (AF)	–
Ho	+3 ([Xe]4f ¹⁰)	–	10.2 K (AF)	–
Er	+3 ([Xe]4f ¹¹)	–	6.0 K (AF)	–
Tm	+3 ([Xe]4f ¹²)	–	8.3 K (AF)	–
Yb	+3 ([Xe]4f ¹³)	–	4.5 K (AF)	–
Lu	+3 ([Xe]4f ¹⁴)	345 K	9.5 K (AF)	–

Note. T_a : peak temperature of the broad maximum observed in the magnetic susceptibility, T_b : magnetic transition temperature, AF: antiferromagnetic, and F: ferromagnetic.

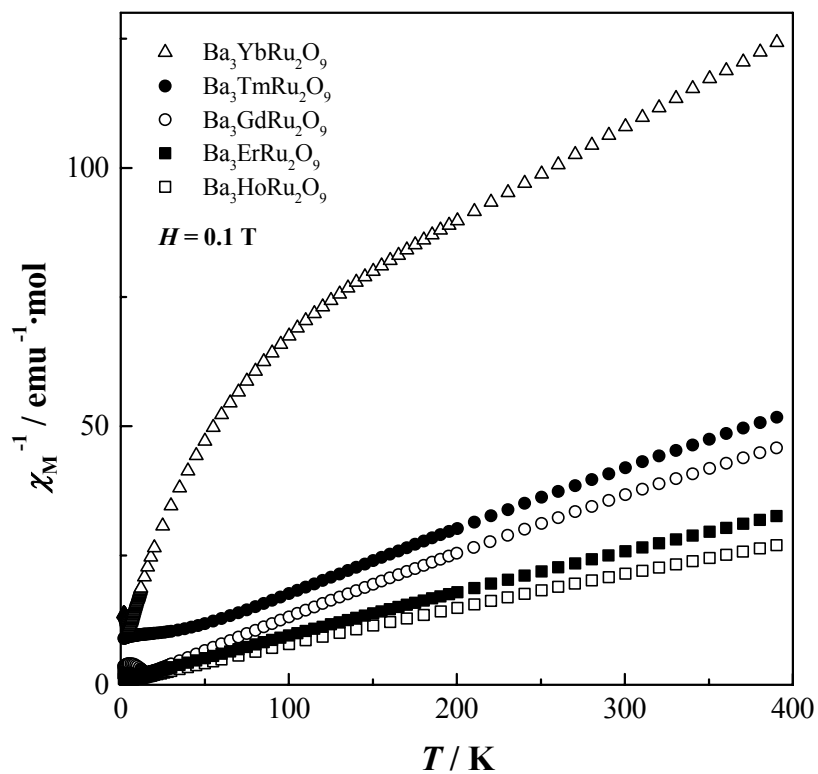


Figure 4.6.1 Temperature dependence of reciprocal magnetic susceptibilities for $Ba_3LnRu_2O_9$.

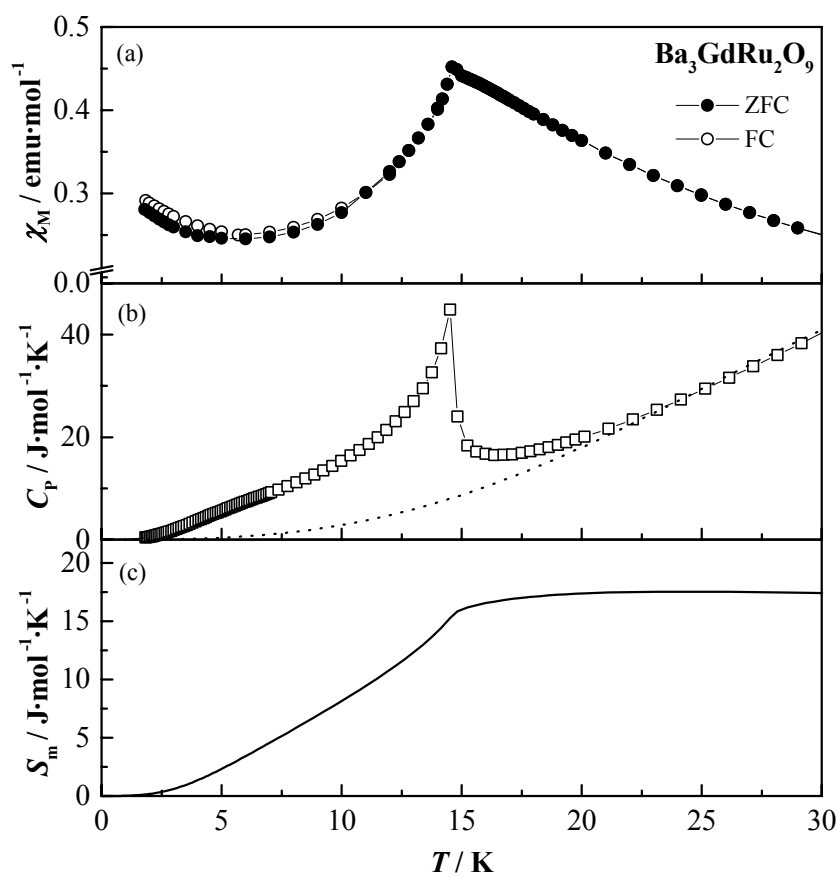


Figure 4.6.2 Temperature dependence of (a) the magnetic susceptibility, (b) specific heat and (c) magnetic entropy of $Ba_3GdRu_2O_9$.

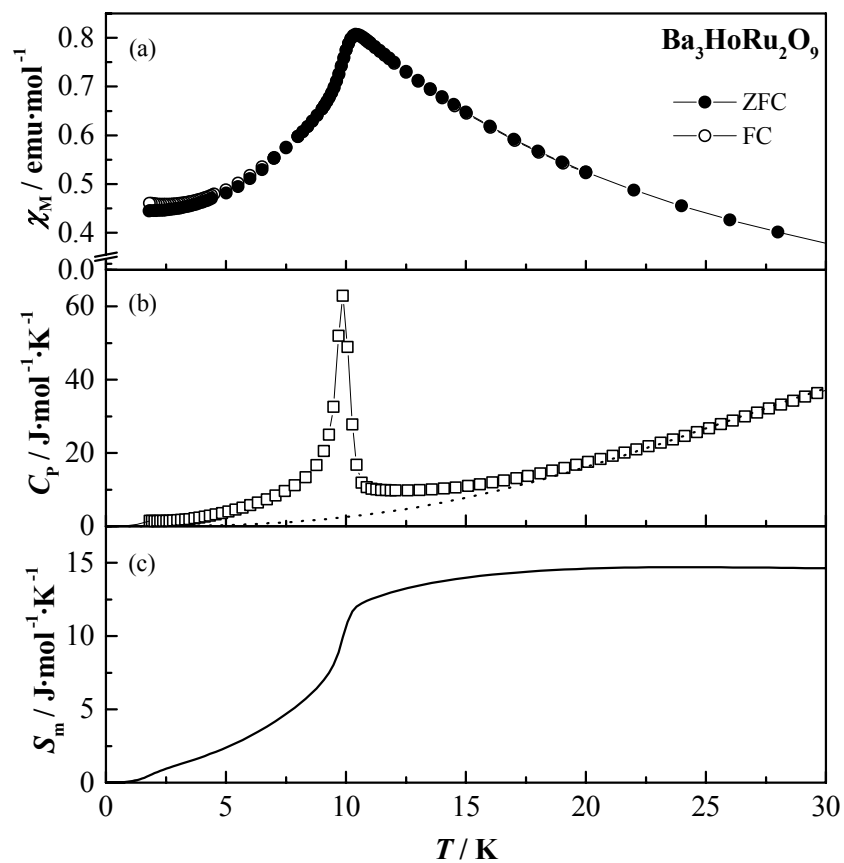


Figure 4.6.3 Temperature dependence of (a) the magnetic susceptibility, (b) specific heat and (c) magnetic entropy of $Ba_3HoRu_2O_9$.

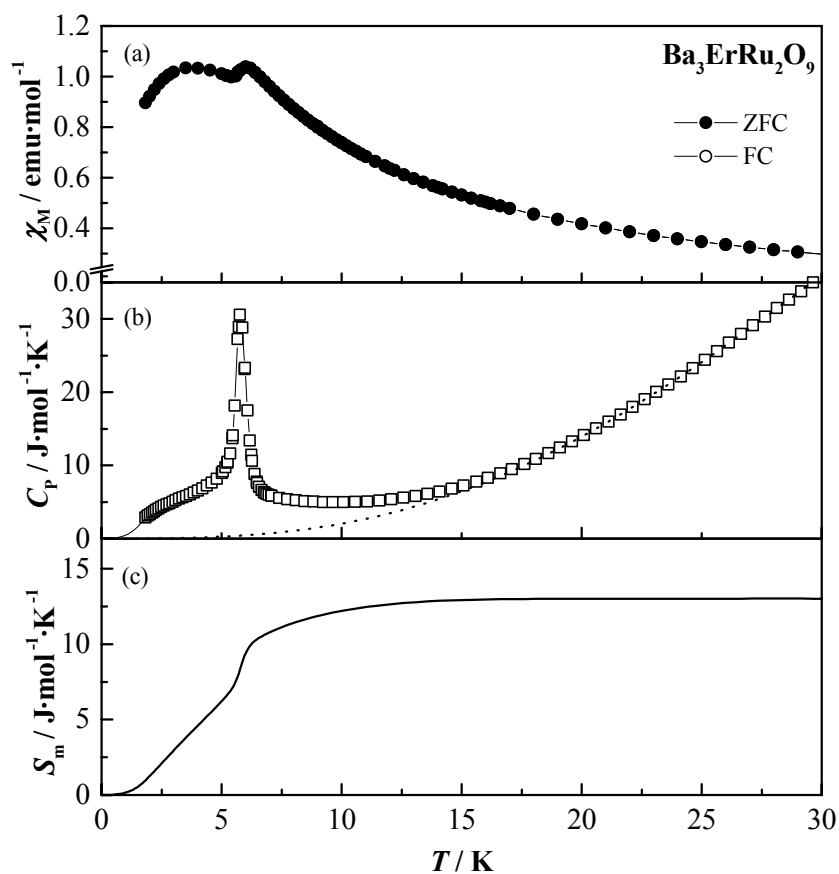


Figure 4.6.4 Temperature dependence of (a) the magnetic susceptibility, (b) specific heat and (c) magnetic entropy of $Ba_3ErRu_2O_9$.

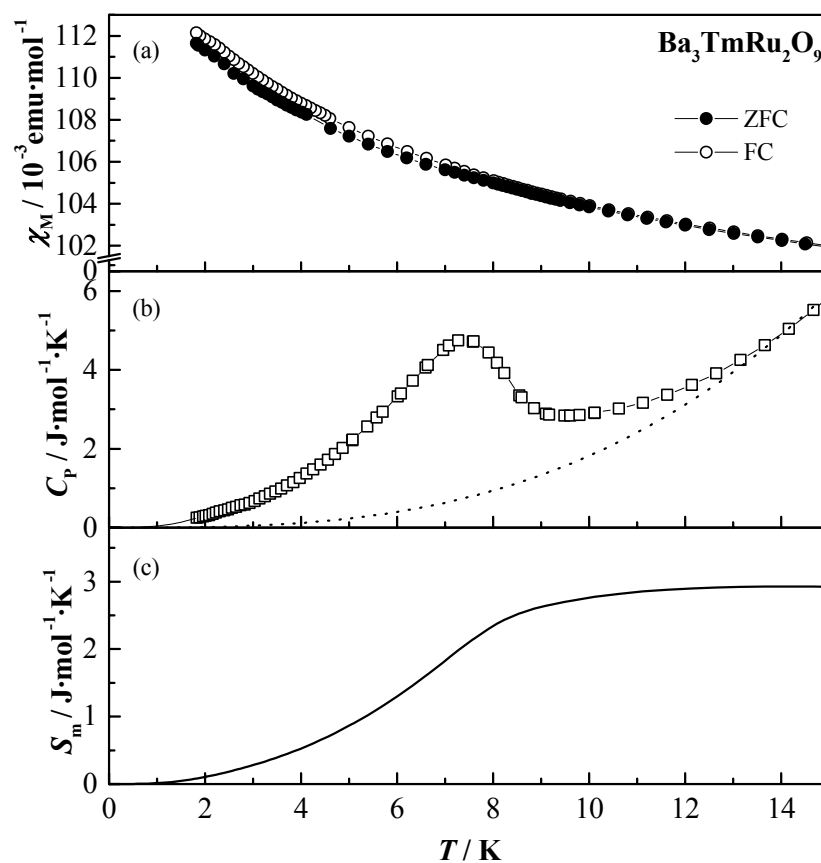


Figure 4.6.5 Temperature dependence of (a) the magnetic susceptibility, (b) specific heat and (c) magnetic entropy of $Ba_3TmRu_2O_9$.

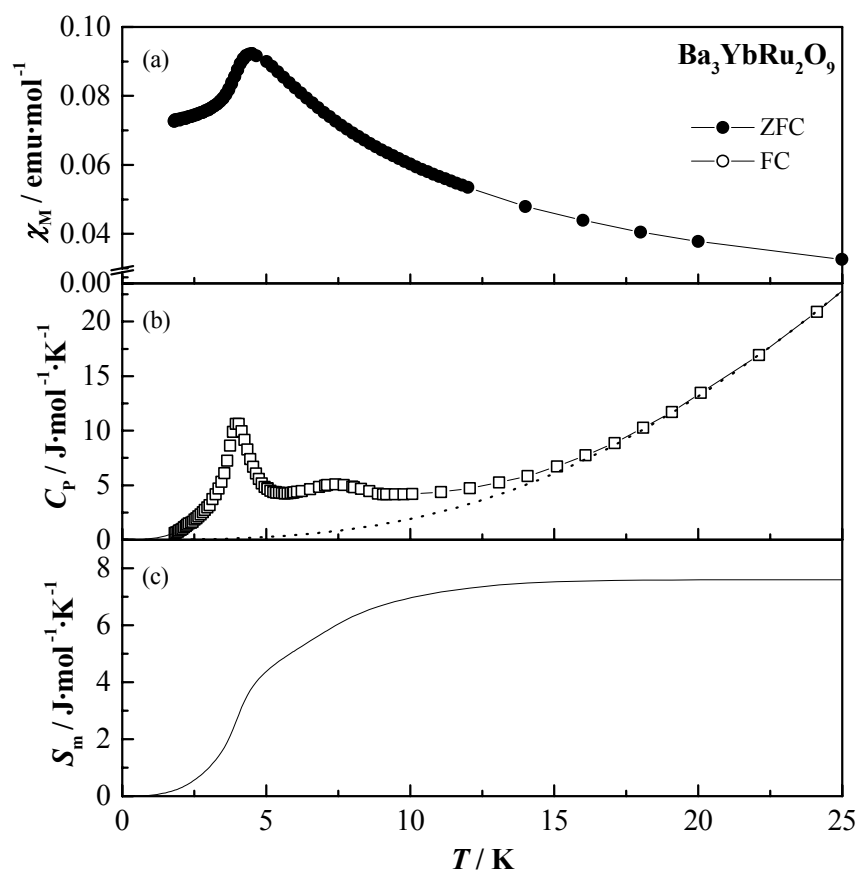


Figure 4.6.6 Temperature dependence of (a) the magnetic susceptibility, (b) specific heat and (c) magnetic entropy of $Ba_3YbRu_2O_9$.

4.7 References

- [4.1] R. D. Burbank and H. T. Evans, *Acta Crystallogr.* **1**, 330 (1948).
- [4.2] J. Darriet, M. Drillon, G. Villeneuve and P. Hagenmuller, *J. Solid State Chem.* **19**, 213 (1976).
- [4.3] R. L. Carlin, “Magnetochemistry”, Springer Verlag, Berlin (1986).
- [4.4] A. Earnshaw, “Introduction to magnetochemistry” Academic Press, London (1968).
- [4.5] B. Bleaney and K. D. Bowers, *Proc. Inorg. Soc. A* **214**, 451 (1952).
- [4.6] S. Kemmler-Sack, I. Thumm and M. Herrmann, *Z. Anorg. Allg. Chem.* **479**, 177 (1981).
- [4.7] F. Izumi and T. Ikeda, *Mater. Sci. Forum* **321-324**, 198 (2000).
- [4.8] U. Treiber, S. Kemmler-Sack, A. Ehmann, H. -U. Schaller, E. Dürschmidt, I. Thumm, and H. Bader, *Z. Anorg. Allg. Chem.* **481**, 143 (1981).
- [4.9] P. Lightfoot and P. D. Battle, *J. Solid State Chem.* **89**, 174 (1990).
- [4.10] J. T. Rijssenbeek, Q. Huang, R. W. Erwin, H. W. Zandbergen, and R. J. Cava, *J. Solid State Chem.* **146**, 65 (1999).
- [4.11] R. D. Shannon, *Acta Crystallogr. A* **32**, 751 (1976).
- [4.12] Hk. Müller-Buschbaum and B. Mertens, *Z. Naturforsch.* **51b**, 79 (1996).
- [4.13] H. Kobayashi, M. Nagata, R. Kanno, and Y. Kawamoto, *Mater. Res. Bull.* **29**, 1271 (1994).
- [4.14] W. Bensch, H. W. Schmalke, and A. Reller, *Solid State Ionics* **43**, 171 (1990).
- [4.15] C. W. Jones, P. D. Battle, and P. Lightfoot, *Acta Crystallogr. C* **45**, 365 (1989).
- [4.16] P. C. Donohue, L. Katz, and R. Ward, *Inorg. Chem.* **4**, 306 (1965).
- [4.17] D. Verdoes, H. W. Zandbergen, and D. J. W. Ijdo, *Acta. Crystallogr. C* **41**, 170 (1985).
- [4.18] M. Rath and Hk. Müller-Buschbaum, *J. Alloys Comp.* **210**, 119 (1994).
- [4.19] I. Thumm, U. Treiber and S. Kemmler-Sack, *Z. Anorg. Allg. Chem.* **477**, 161 (1981).

- [4.20] J. Willkens and Hk. Müller-Buschbaum, *Z. Anorg. Allg. Chem.* **619**, 517 (1993).
- [4.21] H. W. Zandbergen and D. J. W. Ijdo, *Acta. Crystallogr. C* **40**, 919 (1984).
- [4.22] N. F. Mott and E. A. Davis, “Electronic Processes in Non-Crystalline Materials”, 2nd ed, Clarendon Press, Oxford, (1979).
- [4.23] J. T. Rijssenbeek, P. Matl, B. Batlogg, N. P. Ong, and R. J. Cava, *Phys. Rev. B* **58**, No.16, 10315-10318 (1998).
- [4.24] K. Ohoyama, T. Kanouchi, K. Nemoto, M. Ohashi, T. Kajitani, and Y. Yamaguchi, *Jpn. J. Appl. Phys.* **37**, 3319 (1998).
- [4.25] Y. Hinatsu, *J. Solid State Chem.* **119**, 405 (1995).
- [4.26] J. Darriet, J. L. Soubeyroux and A. P. Murani, *J. Phys. Chem. Solids* **44**, 269 (1983).
- [4.27] K. Tezuka, Y. Hinatsu, Y. Shimojo and Y. Morii, *J. Phys.: Condens. Matter* **10**, 11703 (1998).
- [4.28] Y. Morii, *J. Cryst. Soc. Jpn.* **34**, 62 (1992).
- [4.29] K. R. Lea, M. J. M. Leask and W. P. Wolf, *J. Phys. Chem. Solids* **23**, 1381 (1962).

Chapter 5.

Concluding remarks

This dissertation presents the solid-state chemistry of some perovskite-related oxides containing both lanthanide and ruthenium ions. Their crystal structures were determined by the Rietveld analysis of both the X-ray and neutron diffraction profiles. The magnetic properties were investigated by the magnetic susceptibility, magnetic hysteresis, and specific heat measurements. Magnetic transitions were observed for some compounds, and their magnetic structures were determined from the neutron diffraction measurements.

Ordered-perovskites Sr_2LnRuO_6 and related compounds

The perovskites Sr_2LnRuO_6 ($Ln = Eu-Lu$) have the “ordered” perovskite structure in which Ln^{3+} and Ru^{5+} ions are arranged alternately at the B site of the ABO_3 . They have distorted crystal structures (monoclinic with space group $P2_1/n$), and the crystal structures are more distorted from the cubic symmetry with increasing the size of Ln ions. Sr_2LnRuO_6 shows an antiferromagnetic transition at 30–46 K and the complex magnetic behavior below the Néel temperature. A divergency between the ZFC and FC susceptibilities was observed for any compound below this temperature, which shows the onset of a small ferromagnetic moment. This ferromagnetic moment was explained by the weak ferromagnetism due to the lower symmetry of the crystal structures. (section 3.2)

In order to elucidate the magnetic properties of these compounds, the detailed magnetic susceptibility, specific heat, and neutron diffraction measurements were carried out for some compounds. For Sr_2HoRuO_6 , the results of these measurements indicate that there is a long range antiferromagnetic ordering involving both Ru^{5+} and Ho^{3+} . The magnetic structure of this compound was determined by the Rietveld analysis of the neutron diffraction data collected at 10 K. In this magnetic structure, each

magnetic moment of these ions orders in a Type I arrangement, and they are antiparallel with each other in the *ab*-plane, and the direction of the magnetic moments is along the *c* axis. (section 3.3)

For $\text{Sr}_2\text{TbRuO}_6$, the magnetic susceptibility and specific heat measurements show the existence of the magnetic transition at 41 K. Powder neutron diffraction measurements performed at 10 K indicate that there is a long range antiferromagnetic ordering involving both Ru^{5+} and Tb^{3+} , and the resulting calculation shows that the magnetic structure of $\text{Sr}_2\text{TbRuO}_6$ is similar to that of $\text{Sr}_2\text{HoRuO}_6$ except for the magnitude of the ordered magnetic moments and the direction of the magnetic moments (cant by about 20° against the *c* axis). (section 3.4)

In addition, the crystal structure and magnetic properties of a solid solution $\text{Sr}_2\text{TbRu}_{1-x}\text{Ir}_x\text{O}_6$ ($0 \leq x \leq 1$) were investigated. The structural data and the value of the effective magnetic moment indicate that these compounds adopt the valence configuration of $\text{Sr}_2\text{Tb}^{3+}(\text{Ru}_{1-x}\text{Ir}_x)^{5+}\text{O}_6$ ($x = 0.0-0.7$) or $\text{Sr}_2\text{Tb}^{4+}(\text{Ru}_{1-x}\text{Ir}_x)^{4+}\text{O}_6$ ($x = 0.85-1.0$). Their magnetic susceptibility measurements show the antiferromagnetic transition occurs at low temperatures for all the compounds. (section 3.4)

The crystal structures and magnetic properties of the ordered perovskites $\text{Ba}_2\text{LnTaO}_6$ ($\text{Ln} = \text{Y}$, lanthanides) were investigated. They have an ordered perovskite structure with monoclinic ($\text{Ln} = \text{La}-\text{Tb}$) or cubic symmetry ($\text{Ln} = \text{Y}$, $\text{Dy}-\text{Lu}$). All the compounds are paramagnetic down to 5 K. The magnetic susceptibilities of $\text{Ba}_2\text{SmTaO}_6$ and $\text{Ba}_2\text{EuTaO}_6$ were explained by the Van Vleck paramagnetism. ^{151}Eu Mössbauer measurements for $\text{Ba}_2\text{EuTaO}_6$ show that the Eu ion is in the trivalent state and that the symmetry of the Eu site is distorted from the octahedral symmetry. (section 3.5)

6H-perovskites $\text{Ba}_3\text{LnRu}_2\text{O}_9$

The perovskite-related compounds $\text{Ba}_3\text{LnRu}_2\text{O}_9$ ($\text{Ln} = \text{Y}$, In , $\text{La}-\text{Nd}$, $\text{Sm}-\text{Lu}$) have the 6H- BaTiO_3 type structure with space group $P6_3/mmc$. There exist two kinds of B cation sites, the face-sharing and corner-sharing octahedral sites, which are occupied by the Ru and Ln ions, respectively. For the Ce, Pr, and Tb compounds, the oxidation states

of both Ru and Ln ions are tetravalent, i.e., $\text{Ba}_3\text{Ln}^{4+}\text{Ru}^{4+}_2\text{O}_9$. On the other hand, other compounds adopt a valence configuration of $\text{Ba}_3\text{Ln}^{3+}\text{Ru}^{4.5+}_2\text{O}_9$. Electrical resistivity measurements indicate that these compounds are semiconductors over the temperature range 100–400 K. (section 4.2)

The temperature dependence of magnetic susceptibilities for $\text{Ba}_3\text{LnRu}_2\text{O}_9$ (Ln = Y, In, La, Sm, Eu, and Lu) was characteristic. They show a broad maximum above 135 K (for Ln = Y, In, Sm, Eu, and Lu) or a plateau around 22 K (for Ln = La). In addition, another magnetic anomaly is found at 4.5–12.5 K by the magnetic susceptibility and specific heat measurements for any compound. This magnetic behavior is ascribed to the antiferromagnetic coupling between two Ru ions in a Ru_2O_9 dimer and the magnetic interaction between the Ru_2O_9 dimers. (section 4.3)

$\text{Ba}_3\text{LnRu}_2\text{O}_9$ with Ln = Ce, Pr, or Tb adopts a valence configuration of $\text{Ba}_3\text{Ln}^{4+}\text{Ru}^{4+}_2\text{O}_9$. The antiferromagnetic transition was found at 9.5 K for $\text{Ba}_3\text{TbRu}_2\text{O}_9$ and at 10.5 K for $\text{Ba}_3\text{PrRu}_2\text{O}_9$, which was due to the antiferromagnetic ordering of Ln^{4+} ions. The temperature dependence of the magnetic susceptibility for $\text{Ba}_3\text{PrRu}_2\text{O}_9$ shows a broad maximum at $> \sim 380$ K, and this behavior was explained by the dimer model. The magnetic structure of $\text{Ba}_3\text{TbRu}_2\text{O}_9$ was determined by the powder neutron diffraction measurements. In this magnetic structure, the magnetic moments of Tb^{4+} ions order antiferromagnetically, and the direction of the magnetic moments for Tb^{4+} is along the c axis. The ordered moments of Ru ions were not determined in this experiment. (section 4.4)

$\text{Ba}_3\text{NdRu}_2\text{O}_9$ shows peculiar structural and magnetic properties among a series of $\text{Ba}_3\text{LnRu}_2\text{O}_9$ compounds, i.e., the structural phase transition and ferromagnetic transition are observed only in this compound. The X-ray and neutron diffraction measurements indicate that a crystal phase transition occurs at ~ 120 K and that its crystal structure at low temperatures is monoclinic with space group $C2/c$. A ferromagnetic transition was found at 24 K by magnetic susceptibility and specific heat measurements. The neutron diffraction measurement at 10 K shows that $\text{Ba}_3\text{NdRu}_2\text{O}_9$ has a long-range ferromagnetic ordering of Nd^{3+} ions with the ordered magnetic

moment of $1.65(8) \mu_B$, and that the direction of the ordered moments is parallel to the *c*-axis. (section 4.5)

The magnetic properties of $\text{Ba}_3\text{LnRu}_2\text{O}_9$ with the paramagnetic Ln^{3+} ions ($\text{Ln} = \text{Gd}, \text{Ho} - \text{Yb}$) were studied. It was found that these compounds show the magnetic anomalies at 14.8 K ($\text{Ln} = \text{Gd}$), 10.2 K (Ho), 6.0 K (Er), 8.3 K (Tm), and 4.5 K (Yb). The estimation of the magnetic entropy changes associated with these magnetic anomalies indicates that they are mainly due to the antiferromagnetic ordering of Ln^{3+} ions. (section 4.6)

The magnetic interactions between 4f electrons which characterize the magnetic properties of lanthanide ions are various and attractive. However, the 4f electrons are effectively shielded by the outer $5s^2 5p^6$ electron shells, which results in very weak magnetic interactions between 4f electrons. By introducing the ruthenium ions as the d electron system and by achieving the alternative arrangement of the lanthanide (4f) and ruthenium (4d) ions in the perovskite structure, the stronger magnetic interaction between f and d electrons becomes important.

For the ordered perovskites $\text{Sr}_2\text{LnRuO}_6$, antiferromagnetic transitions due to the magnetic cooperative phenomena between f and d electrons have been found at relatively high temperatures. In addition, by changing the number of 4f electrons, the systematical information concerning the d-f magnetic interaction has been obtained. For the 6H-perovskites $\text{Ba}_3\text{LnRu}_2\text{O}_9$, the peculiar temperature dependence of the magnetic susceptibilities has been observed. They have been explained by the d-f magnetic interaction and the magnetic coupling between Ru ions in the Ru_2O_9 dimer.

It is concluded that perovskite-related oxides containing both lanthanide and ruthenium ions show interesting magnetic properties, which are originated from both the characteristics of each magnetic ion and the magnetic interaction between them. These studies should contribute to the total understanding of the magnetic properties of the d-f electron system. In order to deepen this understanding and to find more

fascinating magnetic properties, a further investigation on compounds containing other metal ions such as 5d elements (osmium, rhenium, and iridium) and 5f elements (actinides) will be needed.

Acknowledgements

This dissertation has been carried out under the supervision of Professor Yukio Hinatsu at the Inorganic Chemistry Laboratory, the Division of Chemistry, Graduate School of Science, Hokkaido University. I have been helped by many people during the period of this thesis, and I would like to express my thanks to all of them.

Firstly, I would like to express my great appreciation and gratitude to Professor Yukio Hinatsu for his continuous guidance and stimulating criticism throughout the work of this thesis. Without his patient corrections of this manuscript, I would have never been able to publish anything.

I wish to express my gratitude to Professors Yoichi Sasaki and Tamotsu Inabe who acted as examiners of this dissertation and Professors Masaaki Miyashita and Michio Yazawa, for their helpful and useful suggestions.

I am deeply grateful to Drs. Makoto Wakeshima and Kazuyuki Matsuhira for many valuable discussions and constant encouragement. I also wish to thank all members of the Inorganic Chemistry Laboratory.

I especially wish to thank Dr. Akio Nakamura and Mr. Nobuyuki M. Masaki of Japan Atomic Energy Institute (JAERI) for their experimental support and fruitful discussion.

I would also like to thank Drs. Yukio Morii, Yoshinobu Ishii, Yutaka Shimojo, and Ken-ichi Oikawa of JAERI and Drs. Yasuo Yamaguchi, Kenji Ohoyama, and Aya Tobo of Tohoku University for the measurements and analysis of powder neutron diffraction data.

Finally, I sincerely thank my parents for their constant encouragement, understanding and support.

List of publications

[Thesis]

Original papers

- [1] Yoshihiro Doi and Yukio Hinatsu
"Crystal Structures and Magnetic Properties of Ordered Perovskites $\text{Sr}_2\text{LnRuO}_6$ (Ln = Eu–Lu)"
Journal of Physics: Condensed Matter, **11**, 4813–4820 (1999).
- [2] Yoshihiro Doi, Yukio Hinatsu, Ken-ichi Oikawa, Yutaka Shimojo, and Yukio Morii
"Magnetic and Neutron Diffraction Study on the Ordered Perovskite $\text{Sr}_2\text{HoRuO}_6$ "
Journal of Materials Chemistry, **10**, 797–800 (2000).
- [3] Yoshihiro Doi, Yukio Hinatsu, Ken-ichi Oikawa, Yutaka Shimojo, and Yukio Morii
"Magnetic Properties and Crystal Structures of Ordered Perovskites $\text{Sr}_2\text{TbRu}_{1-x}\text{Ir}_x\text{O}_6$ "
Journal of Materials Chemistry, **10**, 1731–1737 (2000).
- [4] Yuki Izumiyama, Yoshihiro Doi, Makoto Wakeshima, Yukio Hinatsu, Ken-ichi Oikawa, Yutaka Shimojo, and Yukio Morii
"Magnetic and Neutron Diffraction Studies of the Ordered Perovskite $\text{Ba}_2\text{NdRuO}_6$ "
Journal of Materials Chemistry, **10**, 2364–2367 (2000).
- [5] Yoshihiro Doi, Yukio Hinatsu, Yutaka Shimojo, and Yoshinobu Ishii
"Crystal Structure and Magnetic Properties of 6H-Perovskite $\text{Ba}_3\text{NdRu}_2\text{O}_9$ "
Journal of Solid State Chemistry, **161**, 113–120 (2001).
- [6] Yuki Izumiyama, Yoshihiro Doi, Makoto Wakeshima, Yukio Hinatsu, Yutaka Shimojo, and Yukio Morii
"Magnetic Properties of the Antiferromagnetic Double Perovskite $\text{Ba}_2\text{PrRuO}_6$ "
Journal of Physics: Condensed Matter, **13**, 1303–1313 (2001).
- [7] Yoshihiro Doi, Makoto Wakeshima, Yukio Hinatsu, Aya Tobo, Kenji Ohoyama, and Yasuo Yamaguchi
"Crystal Structures and Magnetic Properties of 6H-Perovskites $\text{Ba}_3\text{LnRu}_2\text{O}_9$ (Ln = Ce, Pr and Tb)"
Journal of Materials Chemistry, **11**, 3135–3140 (2001).
- [8] Yoshihiro Doi and Yukio Hinatsu
"Magnetic Properties of Ordered Perovskites $\text{Ba}_2\text{LnTaO}_6$ (Ln = Y, lanthanides)"
Journal of Physics: Condensed Matter, **13**, 4191–4202 (2001).

- [9] Makoto Wakeshima, Yuki Izumiyama, Yoshihiro Doi, and Yukio Hinatsu
"Valence Transition in Ordered Perovskites $\text{Ba}_2\text{PrRu}_{1-x}\text{Ir}_x\text{O}_6$ "
Solid State Communications, **120**, 273–278 (2001).
- [10] Yoshihiro Doi and Yukio Hinatsu
"Magnetic and Calorimetric Studies on $\text{Ba}_3\text{LnRu}_2\text{O}_9$ (Ln = Gd, Ho–Yb) with 6H-Perovskite Structure"
Journal of Materials Chemistry, **12**, 1792–1795 (2002).
- [11] Yoshihiro Doi, Kazuyuki Matsuhira, and Yukio Hinatsu
"Crystal Structures and Magnetic Properties of 6H-Perovskites $\text{Ba}_3\text{MRu}_2\text{O}_9$ (M = Y, In, La, Sm, Eu, and Lu)"
Journal of Solid State Chemistry, **165**, 317–323 (2002).
- [12] Yoshinori Sasaki, Yoshihiro Doi, and Yukio Hinatsu
"Magnetic and Calorimetric Studies of Double Perovskites $\text{Ba}_2\text{LnReO}_6$ (Ln = Y, Nd, Sm–Lu)"
Journal of Materials Chemistry, **12**, 2361–2366 (2002).

Other papers and proceedings

- [1] Yoshihiro Doi, Yukio Hinatsu, Yutaka Shimojo, and Yukio Morii
"Neutron Diffraction Study on Ordered Perovskites $\text{Sr}_2\text{LnRuO}_6$ (Ln = Ho, Tm)"
JAERI-Review 2000-005, 44 (2000).
- [2] Yoshihiro Doi, Yukio Hinatsu, Ken-ichi Oikawa, Yutaka Shimojo, and Yukio Morii
"Neutron Diffraction Study on Ordered Perovskites $\text{Sr}_2\text{TbRuO}_6$ "
JAERI-Review 2001-005, 44 (2001).
- [3] Yoshihiro Doi, Yukio Hinatsu, Ken-ichi Oikawa, Yutaka Shimojo, and Yukio Morii
"Magnetic Properties of $\text{Sr}_2\text{LnRuO}_6$ (Ln = Tb, Ho)"
The 1st International Symposium on Advanced Science Research, Advances in Neutron Scattering Research (ASR-2000), Proceedings.
Journal of the Physical Society of Japan, **70** Suppl. A. 151–153 (2001).
- [4] Yoshihiro Doi, Yukio Hinatsu, Ken-ichi Oikawa, Yutaka Shimojo, and Yukio Morii
"Magnetic and Neutron Diffraction Study on Ordered Perovskites $\text{Sr}_2\text{LnRuO}_6$ (Ln = Tb, Ho)"
4th International Conference on f-elements (ICFE'4), Proceedings.
Journal of Alloys and Compounds, **323-324**, 455–459 (2001).
- [5] Yoshihiro Doi and Yukio Hinatsu
"Antiferromagnetic Ordering in Hexagonal CoU_2O_6 and NiU_2O_6 "
Actinides-2001 International Conference, Proceedings.
Journal of Nuclear Science and Technology, in press.

- [6] Yoshihiro Doi, Makoto Wakeshima, Yukio Hinatsu, Aya Tobo, Kenji Ohoyama, and Yasuo Yamaguchi
"Magnetic and Calorimetric Studies on 6H-Perovskite $\text{Ba}_3\text{TbRu}_2\text{O}_9$ "
Rare Earths' – 2001, Proceedings.
Journal of Alloys and Compounds, in press.

[Others]

Original papers

- [1] Makoto Wakeshima, Yoshihiro Doi, Yukio Hinatsu, and Nobuyuki Masaki
"Mössbauer Effects and Magnetic Properties of Mixed Valent Europium Sulfide, EuPd_3S_4 "
Journal of Solid State Chemistry, **157**, 117–122 (2001).
- [2] Keitaro Tezuka, Yoshihiro Doi and Yukio Hinatsu
"Crystal Structures and Magnetic Properties of Zircon-type Compounds $\text{Lu}_{1-x}\text{Y}_x\text{CrO}_4$ "
Journal of Materials Chemistry, **12**, 1189–1193 (2002).